Production of charm and bottom quarks in $p + p$ collisions at 200GeV

Yuhei Morino

Center for Nuclear Study
Graduate School of Sience
The University of Tokyo

A Dissertation Submitted in Partial Fulllment of
the Requirements for the Degree of Doctor of Science

Abstract

The measurement of single electrons from semi-leptonic decay of heavy flavor in $p+p$ collisions at $\sqrt{s}$=200 GeV has been carried out with the PHENIX detector in the RHIC Year-2005 and Year-2006 run. Measured single electrons include contribution from both charm and bottom. This measurement provides a good test of the perturbative QCD. The separate measurement of p_T distribution about single electrons from bottom is important for a precise test of not only perturbative QCD but also fragmentation process.

The measurement of heavy flavor in $p+p$ collisions also provides an important base line to interpret the measurement of heavy flavor in Au+Au collisions at RHIC, since heavy flavor is only produced in the initial collisions. A strong suppression of the single electrons from heavy flavor at high p_T has been observed in central Au+Au collisions compared with $p+p$ collisions. The suppression indicates charm quarks lose a large fraction of their energy in the hot and dense medium, since the magnitude of energy loss of bottom in the medium is expected to be much smaller than that of charm due to the large difference of their masses. The contribution from bottom in the single electrons from heavy flavor must be determined for the discussion of the energy loss of bottom.

The first separate measurement of charm and bottom via a new method, partial reconstruction of $D/\bar{D} \to e^{\pm}K^{\mp}X$ decay, has been also carried out in $p+p$ collisions with the PHENIX detector in the RHIC Year-2005 and Year-2006 run. The measured contribution from bottom in the single electrons provides more precise test of perturbative QCD. It also provides the important base line to discuss at the behavior of bottom quarks in the medium created in Au+Au collisions.

It is found that there is the considerable contribution from bottom in the single electrons from heavy flavor above 3 GeV/c. The first separate spectra of the single electrons from charm and bottom are measured based on the fraction of bottom. The p_T distribution of the single electrons predicted in pQCD agrees with the measured spectra within its uncertainty and the ratio, (data/pQCD) is ~ 2 for charm production and ~ 1 for bottom production. The total cross section of bottom is also determined to $\sigma_{b\bar{b}} = 3.16^{+1.19}_{-1.07}(\mathrm{stat})^{+1.37}_{-1.27}(\mathrm{sys})\mu$b. The existence of energy loss of bottom quarks in the medium created in Au+Au collisions is found based on the measured $(b \to e)/(c \to e + b \to e)$ in $p+p$ collisions.

Contents

List of Figures

List of Tables

Chapter 1

Introduction

1.1 Quantum Chromodynamics

Quantum ChromoDynamics (QCD) is the theory of strong interactions between the quarks and gluons. QCD was developed as an extension of Quantum Electrodynamics (QED) via the imposition of a local SU(3) symmetry in 'color' space. The most important difference between QCD and QED is that QCD is the non-abelian gauge theory and as a consequence has gluon self-interaction. This nature of QCD leads 'asymptotic freedom' which is the most important feature of QCD. The strong coupling constant, α_s, can be expressed as a function of the momentum transfer, Q^2 as follows [1].

$$\alpha_s(Q^2) \sim \frac{12\pi}{(33 - 2N_f)\ln(Q^2/\lambda_{QCD}^2)},$$
(1.1)

where N_f is the number of quark flavors and $\lambda_{QCD} \sim 0.2$ GeV is the typical QCD scale. When the momentum transfer Q^2 is much larger than λ_{QCD}, α_s becomes small enough to allow us to use the perturbative method for QCD calculation (pQCD) as is the case in QED. On the other hand, when the momentum transfer Q^2 is not large, QCD is in non-perturbative regime and many approaches have been proposed to compute the non-perturbative effect.

Another important feature of QCD is 'confinement hypothese' that all observable states are color-singlets, implying directly the non-existence of colored free quarks and states. This hypothese is based on that particles with color content have never been observed.

1.2 Quark Gluon Plasma

The environment of extremely high temperature and/or density can also reduce α_s. The color confinement may be broken with increase of the temperature and/or density of a many body system consisted of hadrons. This results in a phase transition from the confined nuclear matter (ordered phase) to the deconfined state (disordered phase). The deconfined state is called 'Quark Gluon Plasma' (QGP) [2].

The existence and the thermodynamical properties of the QGP have been studied for long time using phenomenological models (Bag model, Hagedorn gas and so on) [3, 4]. Recently,

the lattice QCD calculation, which is numerical approach based on the first principle, show that a phase transition is realized from confined nuclear matter to the QGP at extreme high temperature $T_c \sim 170$ MeV and high energy density $\epsilon_c \sim 1$ GeV/fm^3 [5, 6, 7]. Figure 1.1
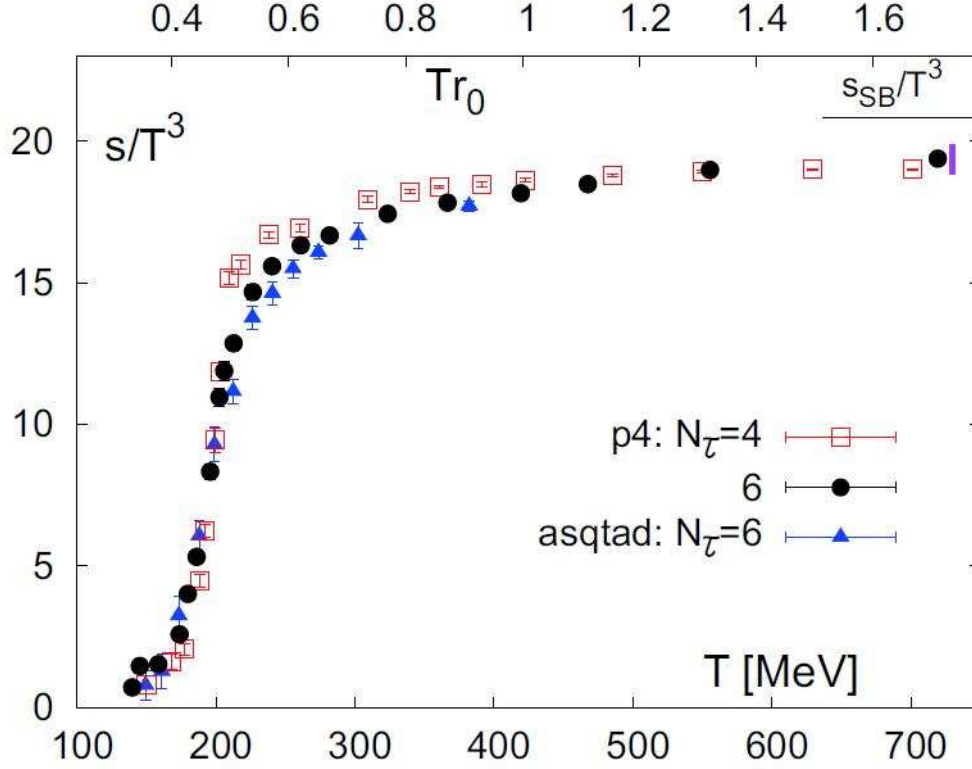
Figure 1.1: The entropy density ($s = \epsilon + p$) in units of T^3 as a function of T calculated by lattice QCD [7].

shows the entropy density ($s = \epsilon + p$) in units of T^3 as a function of T calculated by lattice QCD [7]. This calculation indicates that the entropy density increases rapidly around the critical temperature $T_c \sim 170$ MeV due to the increase of the degree of freedom, which is associated by the deconfinement of the matter.

Figure 1.2 shows a schematic picture of the expected phase diagram of hadronic matter including QGP [8, 9]. The horizontal axis is the baryon chemical potential, μ_{baryon} and the vertical axis is the temperature.

1.3   High Energy Heavy Ion Collisions

High energy heavy ion collision is a powerful and unique tool to realize high energy temperature enough to create QGP [10, 11]. Fixed target experiments with high-energy heavy-ion collisions began at Bevalac at Lawrence Berkeley with $\sim 2A$ GeV beams in the middle of 1970's. The Relativistic Heavy Ion Collider (RHIC) at the Brookhaven National Laboratory (BNL) is the

first colliding-type accelerator which can collide heavy nuclei up to gold (197Au) with the center of mass energy per nucleon pair of $\sqrt{s_{NN}} = 200$ GeV and started its operation in 2000. The energy density achieved by the collisions at RHIC is expected to be well above the critical temperature.

The most important feature of high energy heavy ion collisions is that the matter created in heavy ion collisions undergoes space-time evolution. Particles are produced at each stage in the space-time evolution and interact with the matter. Since all experimentally observables are particles after the space-time evolution, the integrated information of the interaction with the matter is only measured. This fact leads that it is important for the study of the QGP via high energy heavy ion collisions to know when the measured particles are produced. Remarkable features of high energy heavy ion collisions are summarized in Sec. 2.1 and important results measured in RHIC are summarized in Sec. 2.2.
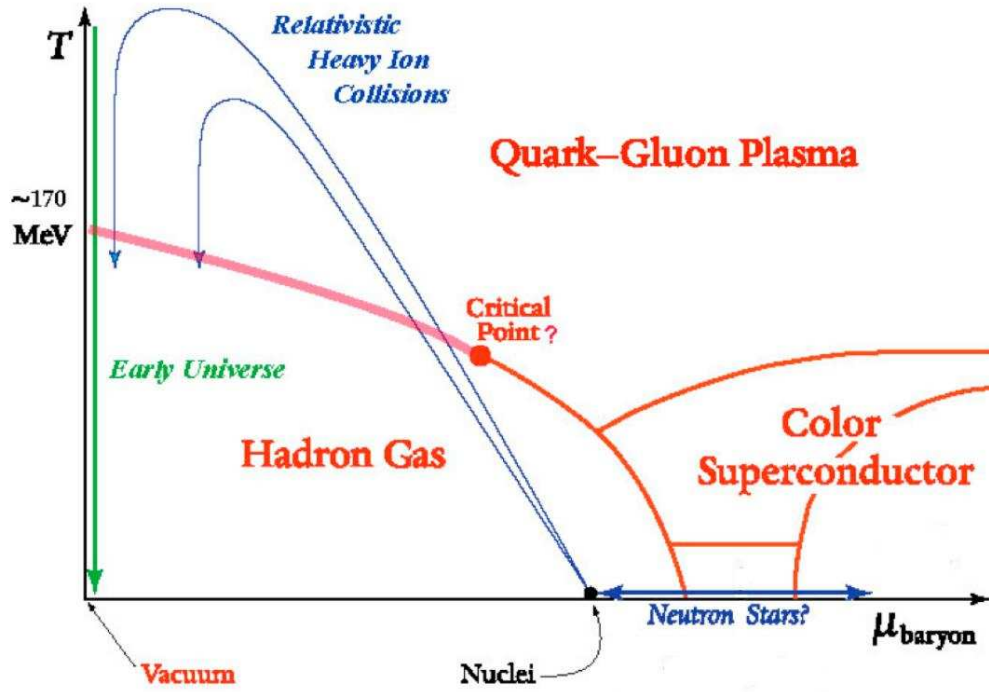
Figure 1.2: A predicted schematic phase diagram of hadronic matter including QGP [8, 9].

1.4 Heavy Flavor Produciton

Heavy quarks (charm, bottom) are primarily produced in hard partonic scattering in nucleon-nucleon collisions, since the initial content of heavy flavor in nuclei is negligibly small. The energy scale for the production of heavy quarks (charm and bottom) is significantly higher

than the typical QCD scale, $\lambda_{QCD} \sim 0.2$ GeV. This gives us a coupling constant of the order of $\alpha_s \sim 0.3$, which is small enough to apply pQCD calculation for the production of heavy quarks. Measurement of charm and bottom production in $p + p$ collisions provides a good test of the perturbative QCD calculations. The p_T distribution of bottomed hadrons in perturbative QCD calculations becomes compatible with the results at Tevatron because of the improvement of the fragmentation process recently. Therefore, measurement of p_T distribution of bottomed hadrons at RHIC also provides the important cross check for pQCD due to the large mass and a test of theoretical treatments of fragmentation process.

Heavy quarks are believed to be a special probe of the medium created in heavy ion collisions due to their large mass. Since heavy quarks are only produced in the initial stage in the heavy ion collision, heavy quark spectra in $p + p$ collisions provide a well defined initial state, even for low-momentum heavy quarks. Then, generated heavy quarks propagate through the hot and dense medium created in heavy ion collisions and their propagation probes characteristics of the medium.

Experiments at the RHIC has measured single electrons from semi-leptonic decay of heavy flavor at mid-rapidity ($| \eta | < 0.35$) in $p + p$ and Au+Au collisions at $\sqrt{s_{NN}} = 200$ GeV. A strong suppression at high p_T and azimuthal anisotropy of the single electrons have been observed in central Au+Au collisions [114]. Measured single electrons include contribution from both charm and bottom. The magnitude of energy loss of bottom in the hot and dense medium is expected to be much smaller than that of charm due to the large difference of their masses [26]. In addition, since the thermalization time of bottom should be larger than that of charm, the magnitude of flow of bottom is expected to be much smaller than that of charm. This fact indicates charm quarks lose a large fraction of their energy and flow in the matter created in Au+Au collisions. On the other hands, the existence of bottom modification (energy loss and flow) in the medium has been an open question without the determination of $(b \to e)/(c \to e + b \to e)$. Details of production of heavy flavor are summarized in Sec. 2.3.

1.5   Organization of This Thesis

Measurement of the fraction of bottom in single electrons from heavy flavor is crucial in $p + p$ collisions at RHIC for the pQCD test and the interpretation of results of single electrons in Au+Au collisions. For this purpose, production of charm and bottom quarks in $p + p$ collisions at $\sqrt{s} = 200$GeV at RHIC Year-2005 RUN and Year-2006 RUN has been studied via electrons from their semi-leptonic decay using PHENIX detectors at RHIC. At first, the p_T distribution of single electrons from heavy flavor in $p + p$ collisions is measured. In addition, a new analysis method using electron-hadron correlation is established to determine the fraction of bottom in the single electrons in this thesis. The new method provides the first result of the p_T distribution of single electrons from bottom quarks at RHIC.

The organization of this thesis is as follows.
Chapter 2 introduces the theoretical and experimental background for the heavy ion collisions and heavy flavor production at RHIC. The motivation to separate the contribution of charm and bottom quarks in electron measurement in $p + p$ collisions is also described here.

In chapter 3, the RHIC accelerator complex and the PHENIX detectors are described.

In chapter 4, the conditions of beam and trigger in the p + p runs in Year-2005 and Year-2006 are summarized.

In chapter 5, the analysis of measurement of the electrons from semi-leptonic decay of charm and bottom is explained. The analysis to separate the contribution of charm and bottom quarks in electron is also described here.

In chapter 6, the result of measurement of charm and bottom is shown.

Interpretations of the results are discussed in chapter 7.

Chapter 8 is the conclusion of this thesis.

Chapter 2

Theoretical and Experimental Background

In this chapter, theoretical and experimental approaches of relativistic heavy ion collision are summarized. The important feature and description of relativistic heavy ion collision are introduced in Sec. 2.1. Current experimental results about 'jet quenching' and 'azimuthal anisotropy' measured in RHIC, which are relevant to the motivation of this this thesis, are summarized in Sec. 2.2. Theoretical and experimental approaches of production of heavy quarks in nucleus-nucleus collisions are described in Sec. 2.3.

2.1 Relativistic Heavy Ion Collision

Relativistic heavy ion collisions provide a unique method to realize a high-temperature and high-density state which is required for QGP formation. Since there are many nucleons in a heavy nucleus, many nucleon-nucleon collisions are involved in heavy ion collisions. Longitudinal energies of the colliding nuclei are dissipated by the collisions and a huge amount of energy are released into a tiny colliding region. Then, the matter which has energy density large enough to form QGP will be created.

2.1.1 Collision Geometry

The number of hard scattering and nuclei participating in the collisions is largely determined by the collision geometry. The geometrical aspects of high-energy heavy-ion collisions play an important role in collision dynamics.

The Participant-Spectator Model

The participant-spectator model is a simple geometrical picture which describes the collision characteristics using the transverse distance between the colliding nuclei, impact parameter b. As schematically sketched in Figure 2.1, the colliding nuclei looks like thin pancakes in the center of mass frame because of the Lorentz contraction. Only the overlapping region of nuclei participate in the collision. The nucleons in this region are called participants. The nucleons

in other region of nuclei, which are called spectators or projectile fragments, do not participate in the collision and pass through the collision region with the same velocity as beam. The spectators are unstable and evaporate the nucleons which also have the almost same velocity as beam. Figure 2.2 illustrates a central collision and a peripheral collision of nuclei with radius of the nucleus R. Information about the impact parameter b is obtained by measurement of the observables related to the sizes of the spectators and/or the participants.
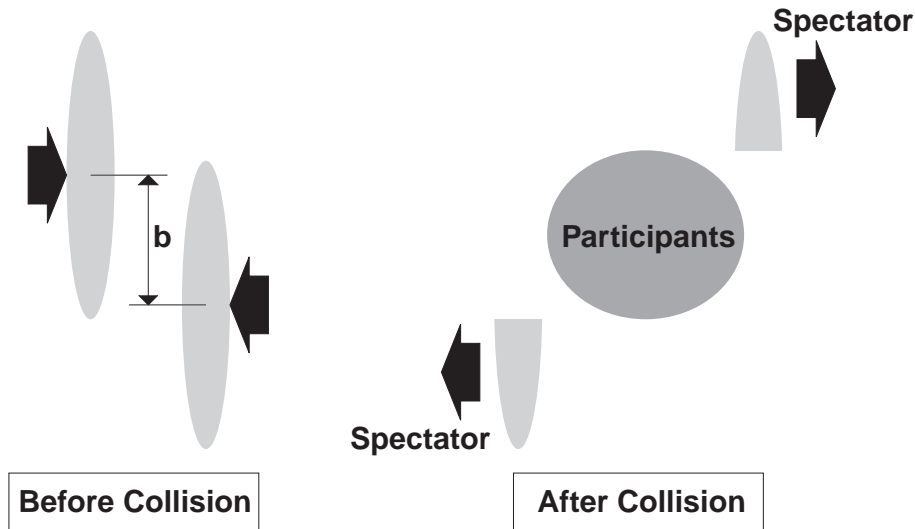
Figure 2.1: The sketch of the colliding nuclei before and after collision. They approach each other with impact parameter b before collision. After the collision, the system consists of two components: participants and spectators.

2.1.2   The Glauber Model

The Glauber Model describes the heavy ion collisions based on the Participant-Spectator Model, the nuclear density distribution, the geometry of the colliding the nucleus and the interaction between constituent nucleons [12, 136]. This model provides the estimation of total inelastic cross section of collisions of nucleus A and nucleus B, starting from nucleon-nucleon inelastic cross section σ_{NN}. From the Glauber Model, the number of nucleon-nucleon collisions occurred inside the participant region (N_{coll}) and the number of participants (N_{part}) in a collision with impact parameter b are also obtained. This picture of collisions is useful to study the scaling properties of particle production in heavy ion collisions. The coherent interaction of each nucleus scales N_{part}, where the momentum transfer, Q^2, is small. They are called soft process. On the other hand, N_{coll} scale is applicable when Q^2 is large and interaction can be considered as the incoherent sum of nucleon-nucleons binary collision. They are called hard process.

The nucleons in each colliding nucleus are distributed according to the Woods-Saxon distribution.

$$\rho(r) = \rho_0 \cdot \frac{1}{1 + \exp(\frac{r-R}{a})}, \tag{2.1}$$
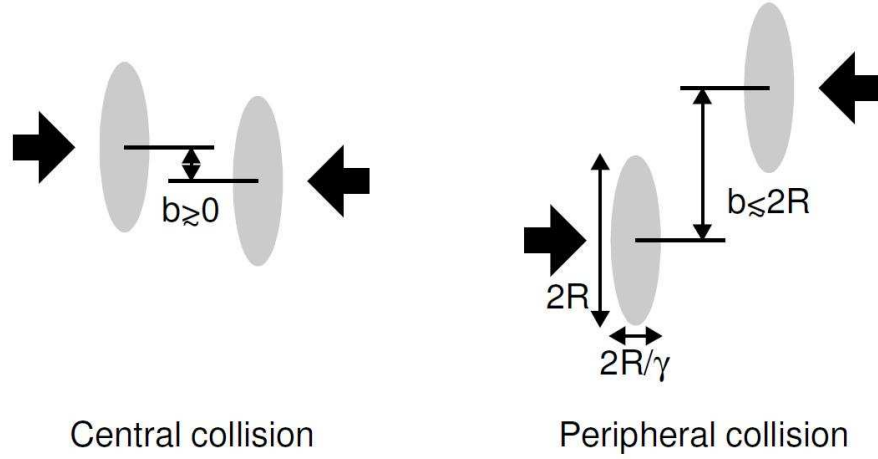
Figure 2.2: A cartoon of central (left) and peripheral (right) collisions.

where ρ_0 stands for the normal nuclear density, R is the radius, and a is diffuseness parameter. In case of Au nucleus, $R \simeq 6.64$ fm and a $\simeq 0.53$ fm. The probability for occurrence of nucleon-nucleon collision between the nucleus A and B along z-axis at an impact parameter b is expressed in the integral form.

$$T(b)\sigma_{NN} = \int \rho_A^z(b_A)db_A\rho_B^z(b_B)db_Bt(b - b_A + b_B)\sigma_{NN}, \tag{2.2}$$

where $\rho_A^z(b_A)$ and $\rho_B^z(b_B)$ are the z-integrated densities of nucleus A and B, $t(b)db$ is the probability for having a nucleon-nucleon collisions within the transverse element db when A and B collide with an impact parameter b. Up to A×B collisions can be occurred. The probability having n nucleon-nucleon collisions can be written using the binomial relation.

$$P(n, b) = \left(\begin{array}{c} AB \\ n \end{array} \right) (1 - s)^n(s)^{AB-n}, \tag{2.3}$$

where $s = 1 - T(b)\sigma_{NN}$. The probability for having at least one nucleon-nucleon collision in the collision of nucleus A and B at impact parameter b is

$$\frac{d\sigma_{AB}}{db} = \sum_{n=1}^{AB} P(n, b) = \sum_{n=0}^{AB} P(n, b) - P(0, b) = 1 - s^{AB}. \tag{2.4}$$

The total inelastic cross section σ_{AB} can be written as

$$\sigma_{AB} = 2\pi \int bdb(1 - s^{AB}). \tag{2.5}$$

The average number of inelastic nucleon-nucleon collisions N_{coll} at the impact parameter b is expressed as follows.

$$N_{coll}(b) =< n(b) >= \sum_{n=1}^{AB} np(n, b) = ABT(b)\sigma_{NN}. \tag{2.6}$$

The results of Glauber calculation are summarized at Appendix D.

2.1.3 Space Time Evolution of the Matter
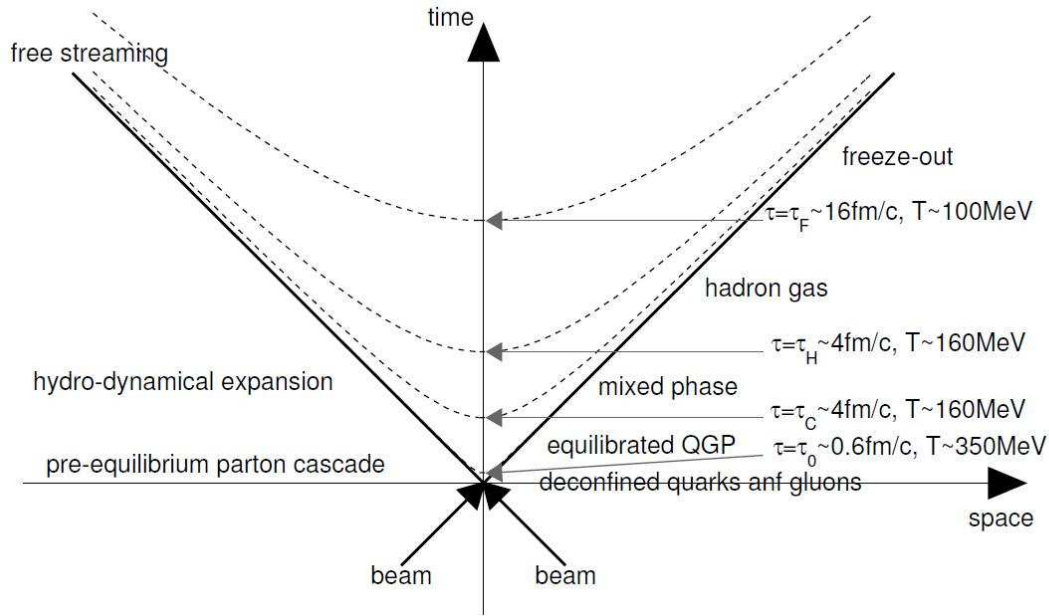
Figure 2.3: A space-time picture of a nucleus-nucleus collision. The times and temperatures Mixed phase would exist only if the transition is first order.

The matter created in heavy ion collisions undergoes space-time evolution. The evolution of the matter can be described based on the Bjorken's space-time scenario [13]. In the cylindrically symmetric collision at center of mass frame, the longitudinal proper time, τ, is expressed as:

$$\tau = \sqrt{t^2 - z^2}. \tag{2.7}$$

The evolution of the system is characterized with proper time τ. Figure 2.3 shows the diagram of the space-time evolution, which is according to the picture established by Bjorken [13]. It is assumed that the space-time evolution depends on only the proper time in the high-energy limit. The space-time evolution can be separated into 4 region as shown in Fig. 2.3

- pre-equilibrium ($\sim \tau_0$)
  A huge amount of energy is released in a tiny colliding volume. Free partons, mainly gluons, are produced by a collision between the two nuclei. The system is initially not in thermal equilibrium. The subsequent multiple parton scattering brings the matter to local equilibrium.

- Deconfined state (QGP) in thermal equilibrium ($\tau_0 \sim \tau_C$)
  If the deposited energy is large enough and exceeds the critical energy density, the QGP will be formed at τ_0. The matter created at RHIC is expected to expand and cool down according to hydrodynamics.

- Mixed phase ($\tau_C \sim \tau_H$)
  When the matter reaches the critical temperature T_c between QGP and ordinary hadronic matter, QGP begins to hadronize and the matter becomes the mixed phase consisting of the quarks, gluons and hadrons. This state would exist only if the transitions is first order.

- Hadron gas ($\tau_H \sim \tau_F$)
  The system finishes hadronization and produced hadrons keep interacting with each other until the temperature drops to the kinematical freeze-out temperature (τ_F). Hadrons cease to interact and move away after T_F.

What we really want to know is the information of QGP, while what we can observe is the integrated information from 0 to τ_F. Therefore, the understanding of each stage via various measurements is important in heavy ion collisions.

2.1.4 Initial Energy Density

Bjorken has provided a way to estimate the energy density in a collision system based on the experimental observables: the multiplicity of particles and the transverse energy [13]. We take $\mathscr{A}$ as a transverse overlapping area in the collision of the two nuclei and Δz as a longitudinal length of overlapping region. Then the colliding volume is expressed as $\mathscr{A}\Delta z$. Taking ΔN as a number of particles in this volume, following relation is derived.

$$\frac{\Delta N}{\mathscr{A}\Delta z} = \frac{1}{\mathscr{A}}\frac{dN}{dy}\frac{dy}{dz} = \frac{1}{\mathscr{A}}\frac{dN}{dy}\frac{1}{\tau_0 \cosh y}, \tag{2.8}$$

The energy of a particle with a rapidity y is $m_T \cosh y$, with $m_T = \sqrt{m_0^2 + p_T^2}$. Therefore, the initial energy density is expressed as,

$$\epsilon_0 = m_T \cosh y \frac{\Delta N}{\mathscr{A}\Delta z}. \tag{2.9}$$

Making use of Eq. 2.8 and Eq. 2.9, the energy density ϵ_0 at mid-rapidity region is expressed as,

$$\epsilon_0 = \frac{m_T}{\tau_0 \mathscr{A}}\frac{dN}{dy}\bigg|_{y=0}, \tag{2.10}$$

At RHIC, the energy density reaches to $\sim$5.5 GeV/fm^3 in Au+Au collisions [126].

2.2   Experimental Results at RHIC

Experiments at the Relativistic Heavy-Ion Collider (RHIC) have indeed provided convincing evidence that a thermalized medium is produced in heavy ion collisions at $\sqrt{s_{NN}} = 200$ GeV. In this section, a brief summary of the important observations and pertinent interpretations which is relevant to the motivation of this thesis is presented [14, 15, 16, 17]. At RHIC, many hadron p_{T} spectra and its azimuthal angle dependence with respect to reaction plane have been measured. Two major findings at RHIC may be classified by their p_{T} regime.

- Azimuthal Anisotropy ($p_{\mathrm{T}} < 5\mathrm{GeV}/c$)

- Jet Quenching ($p_{\mathrm{T}} > 5\mathrm{GeV}/c$)

2.2.1   Initial Nuclear Effect

There are known normal nuclear effects (initial state effect) which modify the yield and p_{T} distribution of produced particles. When one wants to extract the information of the matter created with heavy ion collisions, these nuclear effects should be taken into account.

Cronin Effect

Incident partons suffer multiple scatterings while passing through the nucleus (A) before the hard collision. Partons from the projectile nucleus collide with various target nucleons exchanging a transverse momentum in each collision. As a result, the p_{T} distribution of partons becomes wider compared to that in p + p collisions and is known as the Cronin effect [18]. The p_{T} distribution in p+A collisions is parameterized as

$$E\frac{d^3\sigma}{dp^3}(p_{\mathrm{T}}, A) = E\frac{d^3\sigma}{dp^3}(p_{\mathrm{T}}, p) \times A^{\alpha(p_{\mathrm{T}})}. \tag{2.11}$$

$\alpha(p_{\mathrm{T}})$ becomes greater than 1 for the p_{T} region of $p_{\mathrm{T}} >\sim 1$ GeV$/c$ in $\sqrt{s} = 200$ GeV collisions.

Nuclear (Anti-)Shadowing

It was found by the EMC group in μ+Fe scattering that parton distribution in free protons is modified when partons are bound in the nucleus [19]. Modification of parton distribution affects the yield of the particles. For momentum fractions $x < 0.1$ and $0.3 < x < 0.7$ (called as EMC region), a depletion is observed in the nuclear parton distributions. Momentum fractions at mid-rapidity can be expressed as the low x, or shadowing region and the larger x, or EMC region, is bridged by an enhancement known as anti-shadowing for $0.1 < x < 0.3$. Figure 2.4 shows the ratio of the parton structure functions ($F_2^A(x, Q^2)/F_2^D(x, Q^2)$) for different nuclei [20].

2.2.2   Jet Quenching

Particles with high p_{T} ($p_{\mathrm{T}} > 5\mathrm{GeV}/c$) are producted from hard processes in the initial collisions. The produced high-energy partons in the initial collision subsequently fragment into a spray
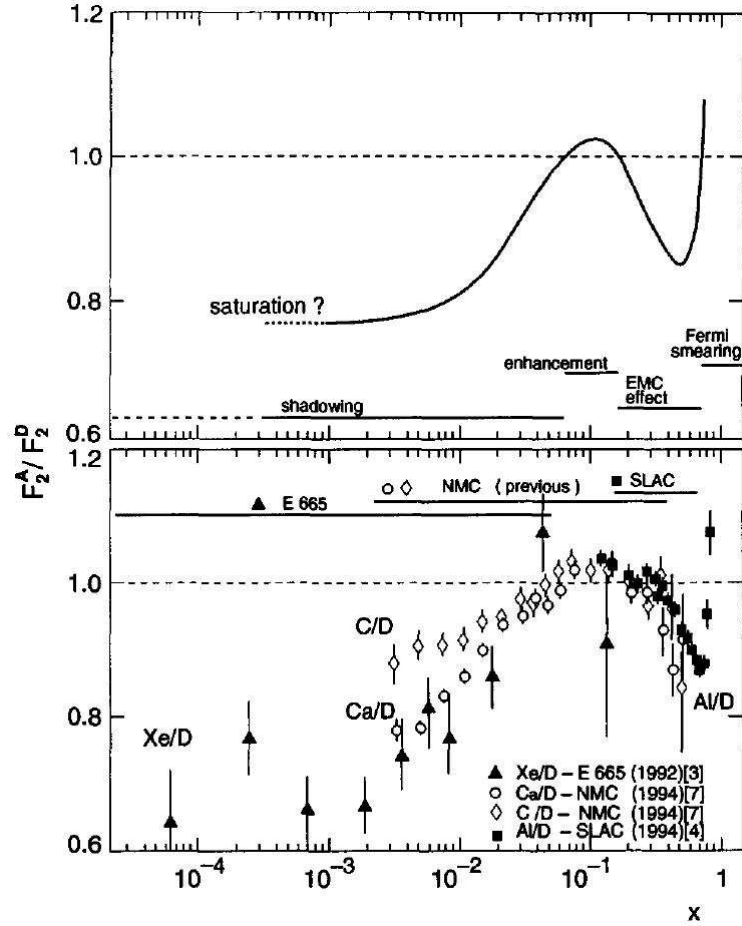
Figure 2.4: Top:A phenomenological curve of the ratio of the parton structure. Bottom:the ratio of the parton structure functions $(F_2^A(x, Q^2)/F_2^D(x, Q^2))$ for different nuclei [20].

of hadrons, called jet. Figure 2.5 illustrates interactions in $p + p$ and heavy ion collisions. The effect of the medium on these hard collision probes can be studied by comparing the yield of hard collision probes in heavy ion collisions to that in $p + p$ collisions.

Back-to-back jets are observed in high energy collisions of elementary particles, but are difficult to identify in the high-multiplicity environment in a heavy ion collision. However, a jet typically contains a leading particle which carries most of the momentum of the parent parton. Therefore, the modification of high p_{T} spectra in heavy-ion collisions essentially provides the information of the matter which high energy parton propagates through. It has been predicted that the yields of high p_{T} particles are suppressed compared with the binary scaled yield in p+p collisions at RHIC due to the energy loss of partons, which called jet quenching [21, 22].

(a) A hard $p + p$ interaction.　　　　(b) A hard interaction in a heavy-ion collision.
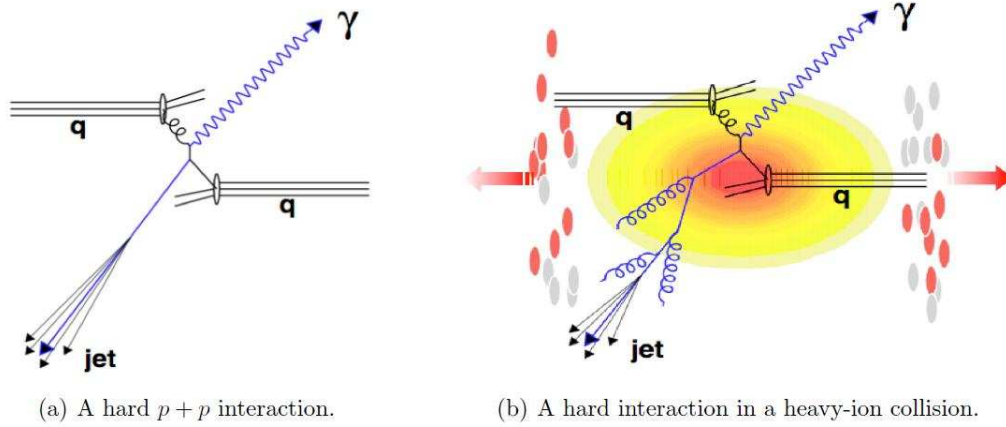
Figure 2.5: Illustration of interactions in $p + p$ and heavy ion collisions. Particles produced in heavy ion collisions will pass through the medium before being detected.

Experimental Result of Jet Quenching

The observed 'jet quenching' at RHIC is nicely demonstrated by the two particle azimuthal angular correlations. Since the high p_T particles are produced as back-to-back jets, peaks around $\Delta\phi \sim 0$ (near side) and $\Delta\phi \sim \pi$ (away side) are expected, where $\Delta\phi$ is the azimuthal angle between the leading particle and the associated particle. Figure 2.6 shows the two particles azimuthal angular correlations ($\Delta\phi$) for inclusive charged hadrons in p+ p, d+Au and Au+Au 200 GeV collisions [23]. One of the two particles is the trigger particle ($4 < p_T < 6$ GeV/c) and the other is the associated particle ($2 < p_T < p_T^{trig}$ GeV/c). Clear peaks around at $\Delta\phi \sim 0$ could be seen in p+ p, d+Au and Au+Au which is expected from the high p_T particles production. On the other hand, the away side peak at $\Delta\phi \sim \pi$ is vanished in Au+Au collisions, while $\Delta\phi \sim \pi$ peaks exist in p+ p and d+Au collisions. Absence to the peak at $\Delta\phi \sim \pi$ in Au+Au collisions indicates the suppression of the away side yields due to the final state interactions with the medium created in Au+Au collisions.

Nuclear modification factor (R_{AA}) is a good observable to quantify the magnitude of the yield suppression. R_{AA} is the ratio of the yield in heavy ion collisions over the binary scaled (N_{coll}) yield in $p + p$ collisions and is defined as bellows.

$$R_{AA}(p_T) \equiv \frac{dN_{AA}/dp_T}{N_{coll}dN_{pp}/dp_T}. \tag{2.12}$$

Thus, $R_{AA} = 1$ indicates there is no modification of the leading hadron spectrum in the heavy-ion collision.

Figure 2.7 shows R_{dAu} in minimum bias d+Au collisions, which mean any cut for the impact parameter is not applied, for π^0 and R_{AA} for π^0 in most central Au+Au collisions [124]. The data clearly indicates that the π^0 yield at high p_T is strongly suppressed in Au+Au collisions, while there is no suppression of high p_T particles in d+Au collisions. The data suggests that the suppression of high p_T hadrons in Au+Au is from not an initial nuclear effect but the effect of the produced dense medium. Figure 2.8 shows R_{AA} for π^0, η and direct γ in most central
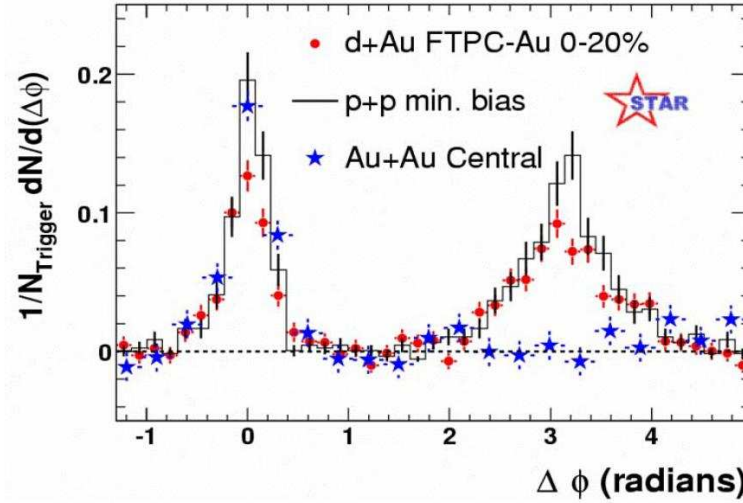
Figure 2.6: Comparison of two-particle azimuthal angular correlations of charged particles for central Au + Au, central d + Au and p+ p collisions, where $N_{Trigger}$ is the number of high p_T particles.

Au+Au collisions [109]. The data indicates that π^0 and η have a similar suppression pattern, while direct γ is not suppressed. This fact can be understood that light quarks lose a large fraction of their energy and direct γ does not lose their energy in the medium, since γ does not have color charge. Absence to the modification of γ yield also indicates the initial state effect is not large.
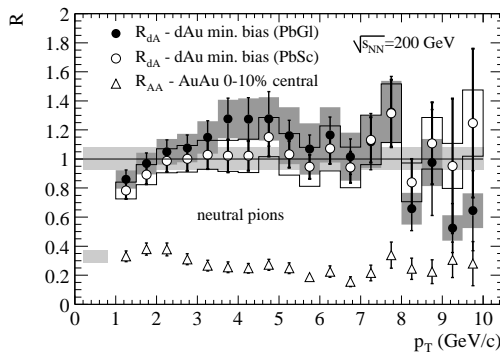
Figure 2.7: R_{dAu} in minimum bias d+Au collisions for π^0 and R_{AA} for π^0 in most central Au+Au collisions.
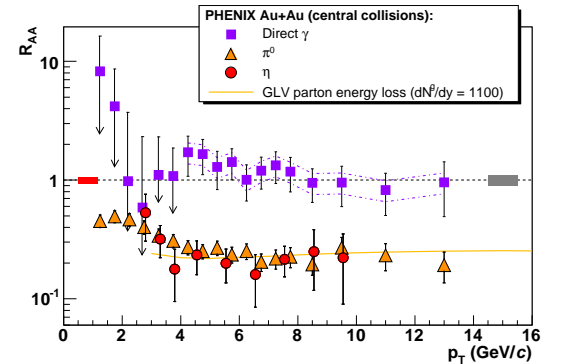
Figure 2.8: R_{AA} for π^0, η and direct γ in most central Au+Au collisions.

Theoretical Interpretation for Jet Quenching

For fast partons going through QGP, the most important microscopic process for their energy loss is radiative gluon bremsstrahlung radiation induced by the static gluon fields with a particular (e.g. plasma) screening configuration, similar to QED. The two effects complicate the

theoretical treatment of the energy loss. The one is the Landau Pomerancuk-Migdal (LPM) effect, which destructively interferes to the bremsstrahlung process. The similar process is also found at QED. The LPM effect occurs when the characteristic formation length ($1/\Delta p$) of the emitted gluon becomes large compensable to its mean free path in the medium [24]. The other is space time evolution of the matter. Since the energy loss obviously depends on the energy density of the medium, the space time dependence of the energy density should be taken into account for realistic calculations.

Two theoretical approaches are discussed here. One is PQM model which is quantified with the average squared transverse momentum transferred from the medium to the parton per mean free path ($\hat{q}$). The PQM model is based on BDMPS model [25, 26]. BDMPS is a perturbative calculation explicitly including only coherent radiative energy loss for the parton via gluon bremsstrahlung. In BDMPS models, the mean of energy loss for the parton ($< \Delta E >$) is expressed in terms of $\hat{q}$ in the limit of large parton initial energy (E) as following.

$$< \Delta E > \propto \alpha_s \hat{q} L^2, \tag{2.13}$$

where L is the in-medium path length of the parton. The PQM model incorporates a realistic transverse collision geometry, though with a static medium. The PQM model does not include initial state multiple scattering or modified nuclear parton distribution functions.

The other is a more realistic approach, GLV model, which is quantified with the gluon density (dN^g/dy) [27, 28]. The GLV model employs an operator product formalism in which probability amplitude for gluon emissions is calculated. An analytic expression is derived for the single gluon emission spectrum to all orders in opacity (the ratio of the length traversed to mean free path), assuming an infrared cutoff is given by the plasma frequency. A realistic transverse collision geometry and Bjorken expansion of the medium are taken into account in the GLV model. In GLV models, the fraction of energy loss for the parton ($< \Delta E > /E$) is expressed in terms of dN^g/dy in the limit of large parton energy (E) as following.

$$\frac{\Delta E}{E} \propto \alpha_s^3 \frac{dN^g}{dy} \frac{L}{E} \ln \frac{2E}{\mu^2 L}, \tag{2.14}$$

where μ the Debye screening scale in the plasma. The calculation also incorporates the Cronin effect and the nuclear shadowing.

Figure 2.9 shows R_{AA} for π^0 in 0-5% central Au+Au collisions and predictions from PQM [26] and GLV models [28] with various values of free parameter (left panels), and R_{AA} at $p_T = 20$ GeV/c predicted from PQM and GLV models (right panels). The property of the created medium can be determined via the comparison with the predicted R_{AA} between measured R_{AA}. The results are as follows [122].

$$PQM : \quad \hat{q} \;\; = \;\; 13.2^{+2.1}_{-3.2} GeV^2/fm \tag{2.15}$$

$$GLV : \quad \frac{dN^g}{dy} \;\; = \;\; 1400^{+270}_{-150}. \tag{2.16}$$

These values indicate a large medium density is achieved.
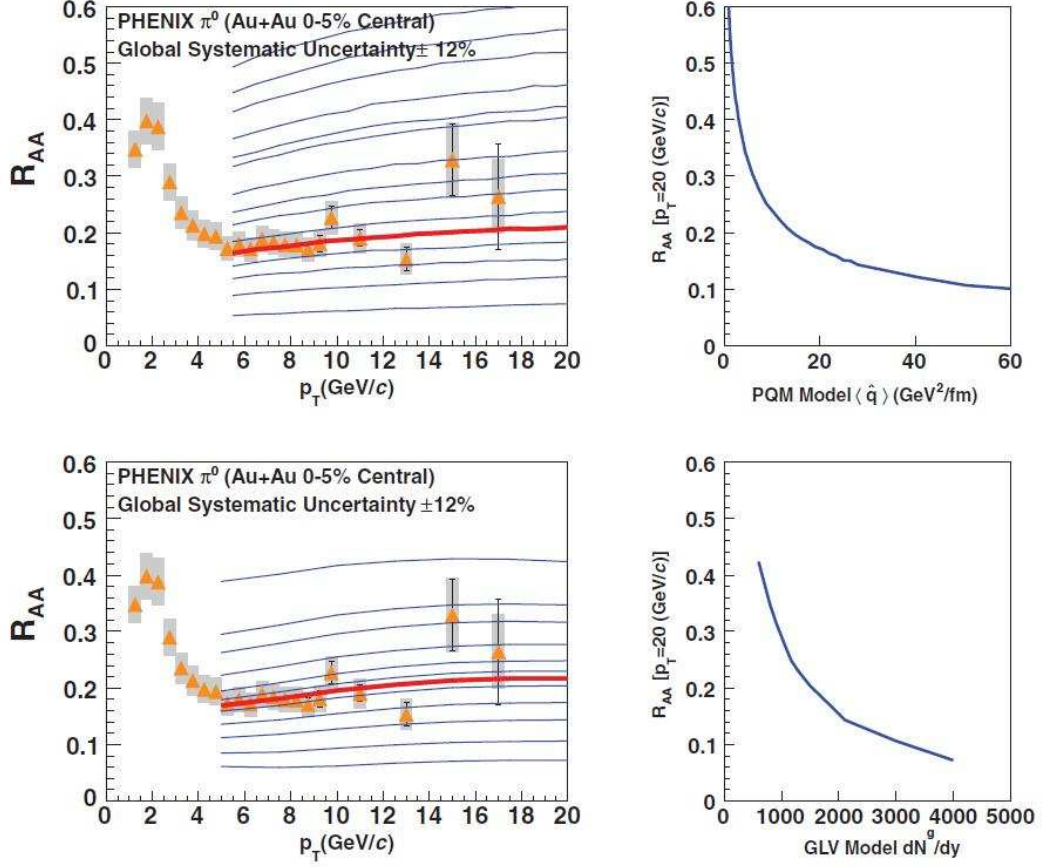
Figure 2.9: Left panels: R_{AA} for π^0 in 0-5% central Au+Au collisions and predictions from PQM [26] and GLV models [28] with various free parameters. Right panels: R_{AA} at $p_T = 20$ GeV/c predicted from PQM and GLV models.

2.2.3 Azimuthal Anisotropy

The distribution of the particle yield in the azimuthal space provides information about collective motion of the partons in the medium created in heavy ion collisions. In the non-central collisions, the spatial shape of initial medium created by the collisions is an almond like shape as shown in Figure 2.10. In Fig 2.10, x-axis is the direction of the impact parameter and z-axis is the direction of the beam axis. In the hydrodynamical framework, since the pressure gradient in x-z plane, which is the driving force of the collective flow, is larger than y direction in the initial stage of the collisions, the particles produced by collisions are expected to be emitted more to the x-z plane than to y direction. A large anisotropy can be generated only if the thermalization of the medium is rapid enough. In this way, the magnitude of collective flow (and its p_T dependence) is, in principle, a quantitative index of the thermalization time, τ_0.
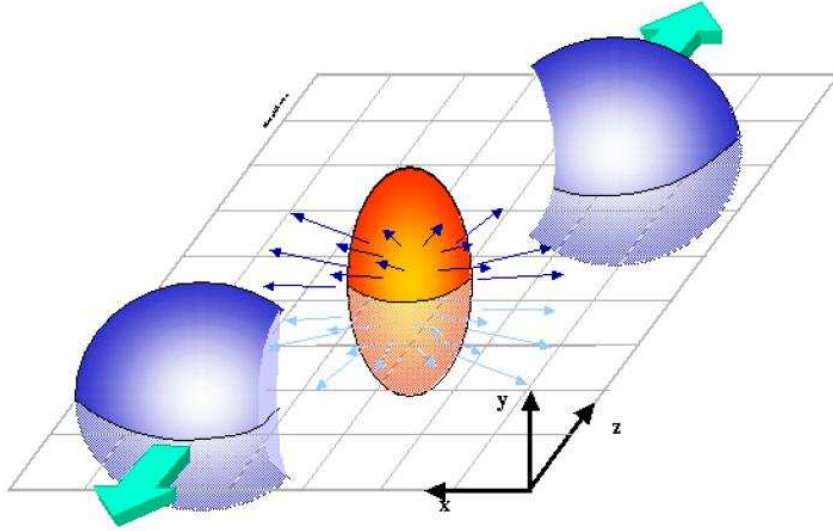
Figure 2.10: An illustration of non-central Au-Au collisions. The plane defined as the direction of the impact parameter (x) and direction of the beam axis (z) is called 'reaction plane'.

Experimental Result of Azimuthal Anisotropy

Experimentally, the magnitude of azimuthal anisotropy has been quantified using Fourier expansion of the azimuthal distribution of emitted particles. The particle distribution is expanded according to Fourier expansion (at mid rapidity, the system is mirror symmetric in the x-y plane and odd Fourier components vanish.)

$$\frac{d^2N}{d\mathbf{p}_T^2} \propto \frac{d^2N}{dp_T^2}[1 + 2v_2(p_T)\cos(2\phi) + ...], \tag{2.17}$$

where ϕ is the azimuthal angle of particles with respect to the reaction plane. Especially the second harmonic coefficient of the Fourier expansion of the azimuthal distribution is called as elliptic flow. $v_2(p_T)$ is defined as the magnitude of the elliptic flow. Left panel of Figure 2.11 shows the $v_2(p_T)$ of identified hadrons in minimum bias Au+Au collisions with hydrodynamical model calculations [30, 31, 32]. Large $v_2(p_T)$ has been observed in Au+Au collisions at RHIC. Applications of relativistic hydrodynamics have shown that the experimentally measured $v_2(p_T)$ for various hadrons is well described when a thermalization time of τ_0=0.5-1 fm and a small viscosity of the matter ($\eta/s \sim 0$) are assumed. Therefore, rapid thermalization and a small viscosity of the matter are suggested from the measurement of $v_2(p_T)$. The disagreement of hydrodynamic model with the data above 2 GeV/c indicates hydrodynamic model is only valid for low p_T particles as is expected, since another process, for example jet fragmentation, becomes dominant at high p_T region.

The other remarkable feature of the elliptic flow is a constituent-quark number scaling of $v_2^h(p_T)$, as determined by the number (n) of constituent quarks in each hadron (h). $v_2^q(p_T)$

which can be interpreted as v_2 of quarks is defined as

$$v_2^q(p_T/n) \equiv \frac{1}{n} v_2^h(p_T). \tag{2.18}$$

$v_2^q(p_T/n)$ of identified hadrons is shown at middle panel in Fig. 2.11. It is found that $v_2^q(p_T/n)$ of identified hadrons has the almost same shape. Empirically, the better scaling is found when use transverse kinetic energy (KE_T), which is defined as $\sqrt{p_T^2 + (M^h)^2} - (M^h)$, is used instead of p_T. $v_2^q(KE_T/n)$ of identified hadrons is shown at right panel in Figure 2.11.

Quark coalescence model is motivated by this observation and the measurement of baryon to meson ratios [127]. Successful description by the quark coalescence model implies a large thermalized source of quarks and anti-quarks. Then it may be a strong evidence for a QGP formation at RHIC, since the quark coalescence model is assumed that hadrons are produced from coalescence thermalized quark source in this model.
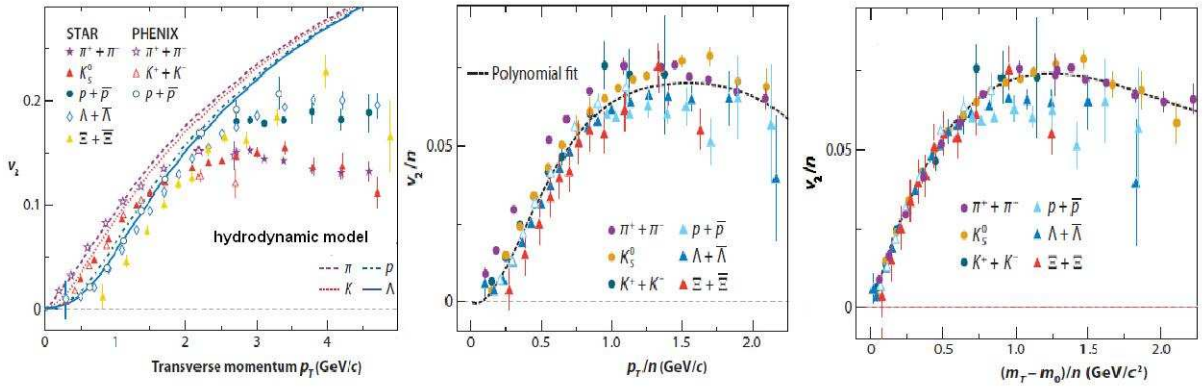
Figure 2.11: Left: $v_2(p_T)$ of identified hadrons in minimum bias Au+Au collisions hydrodynamic model calculations [30, 31, 32]. Middle: $v_2^q(p_T/n)$ of identified hadrons. Right: $v_2^q(KE_T/n)$ of identified hadrons.

Quark Coalescence Model

Quark coalescence (recombination) model is one of the models for hadron production in heavy ion collisions [29]. In this model, hadrons are produced by valence quarks in the thermal medium when they are close together in the phase space. The basic equation in the coalescence model for the formation of meson and baryon from quarks can be written as

$$\frac{d^3 N_M}{d^3 \mathbf{p}_M} = g_M \int \prod_{i=1}^{2} \left[d^3 \mathbf{x}_i d^3 \mathbf{p}_i f_i(\mathbf{x}_i, \mathbf{p}_i) \right] \times f_M(\mathbf{x}_1, \mathbf{x}_2 : \mathbf{p}_1, \mathbf{p}_2) \delta^3(\mathbf{p}_M - \mathbf{p}_1 - \mathbf{p}_2) \tag{2.19}$$

$$\frac{d^3 N_B}{d^3 \mathbf{p}_B} = g_B \int \prod_{i=1}^{3} \left[d^3 \mathbf{x}_i d^3 \mathbf{p}_i f_i(\mathbf{x}_i, \mathbf{p}_i) \right] \times f_B(\mathbf{x}_1, \mathbf{x}_2, \mathbf{x}_3 : \mathbf{p}_1, \mathbf{p}_2, \mathbf{p}_3) \delta^3(\mathbf{p}_B - \mathbf{p}_1 - \mathbf{p}_2 - \mathbf{p}_3). \tag{2.20}$$

The functions $f_i(\mathbf{x}_i, \mathbf{p}_i)$ is distribution functions of quarks and antiquarks in the phase space, and they are normalized to their numbers, $\int d^3\mathbf{x}_i d^3\mathbf{p}_i f_i(\mathbf{x}_i, \mathbf{p}_i) = N_i$. The factor $g_{M(B)}$ takes into account the probability of forming a colorless meson (baryon) from spin 1/2 colored quarks. $f_{M(B)}$ is Wigner function for forming meson (baryon) and depends on the overlap of the spatial and momentum distribution of its constituent quarks.

Let us consider elliptic flow in quark coalescence model at mid-rapidity ($|\mathbf{p}| \sim |\mathbf{p}_T|$). The momentum space distribution of quark (a) can be written in terms of the azimuthal angle ϕ.

$$f_a(\mathbf{p}_T) \sim \tilde{f}_a(p_T)(1 + 2v_2^a(p_T)\cos 2\phi). \tag{2.21}$$

The elliptic flow of mesons (v_2^M) becomes as bellow when the elliptic flow of mesons is small compared with unity ($v2 \ll 1$)

$$
\begin{aligned}
v_2^M(p_T) &= \frac{\int d\phi \cos 2\phi \, dN_M/d^2\mathbf{p}_T}{\int d\phi \, dN_M/d^2\mathbf{p}_T} \\
&\sim \int dp_{Ta} dp_{Tb} f_M [v_2^a(p_{Ta}) + v_2^b(p_{Tb})]\delta(p_T - p_{Ta} - p_{Tb})
\end{aligned}
\tag{2.22}
$$

When we take f_M to have a uniform distribution in momentum space as in Ref. [160], i.e. ,

$$f_M \propto \Theta(\Delta_p - |\mathbf{p}_a - \mathbf{p}_b|) \tag{2.23}$$

and the momentum window is very narrow ($\Delta_p \to 0$), Eq. 2.22 leads to the following expression.

$$v_2^M(p_T) = v_2^a(p_T/2) + v_2^b(p_T/2) \tag{2.24}$$

Therefore, when quarks have the same elliptic flow before hadronization, we arrive at a simple scaling law as follows.

$$v_2^M(p_T) = 2v_2^q(p_T/2) \tag{2.25}$$

We also obtain the following expression about the elliptic flow of baryons by the similar way.

$$v_3^M(p_T) = 3v_2^q(p_T/3) \tag{2.26}$$

Eq. 2.25 and Eq. 2.26 represent the constituent-quark number scaling which is found at RHIC.

AdS/CFT Correspondence

The observation of large azimuthal anisotropy at RHIC and the successful description of it by hydrodynamics with very small viscosity ($\eta/s \sim 0$) also have a great interest for super-string (brane) theorists, while it looks that there is little relation between the experiments at RHIC and super-string theory. The interest is motivated by so called, 'Anti-de Sitter space/Conformal Field Theory (AdS/CFT) Correspondence' which represents the equivalence between $N = 4$ supersymmetric Yang-Mills (SYM) gauge theory and the string theory on 5-dimensional anti-deSitter space [164]. Especially, the gauge theory at finite temperature in the strong coupling limit corresponds to the classical gravity theory for the black-hole on
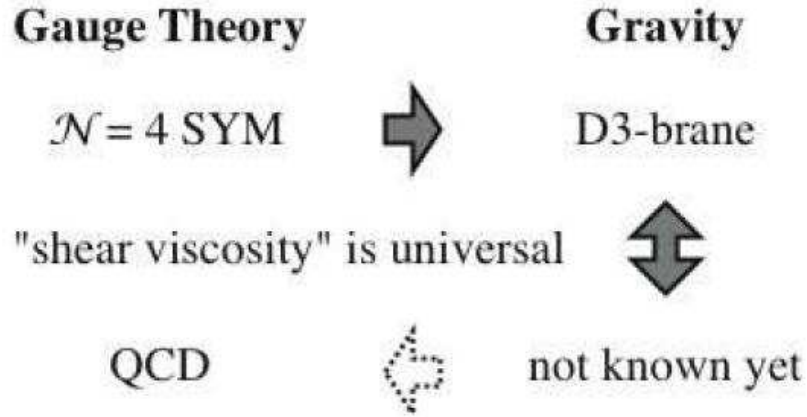
Figure 2.12: The black hole quantity corresponding to the 'viscosity' is universal, so probably the results for supersymmetric gauge theories are directly applicable to the real QCD.

5-dimensional anti-deSitter space. Since the calculation of the gauge theory in the strong coupling is difficult due to its non-perturbative nature, this correspondence has a possibility to be a useful method of the calculation of the the strong coupling gauge theory.

The most famous benefit of AdS/CFT correspondence is the result of the ratio of shear viscosity over the entropy density (η/s). η/s of the classical black-hole on 5-dimensional anti-deSitter space is determined as bellow [168].

$$\frac{\eta}{s} = \frac{1}{4\pi}. \tag{2.27}$$

This η/s is significantly small compared with various matters and the conjectured quantum lower bound. Based on the AdS/CFT correspondence, η/s of the gauge theory matter in the strong coupling limit becomes very small, $1/4\pi$. This claim can not be compared directly with the observation of small viscosity at RHIC, since QCD is not $N = 4$ supersymmetric Yang-Mills gauge theory. Black-hole which corresponds to QCD has been not found. However, it is known Eq. 2.27 is valid for various type of black-holes and rather general. Therefore, it is expected that Eq. 2.27 is 'universal value' of black-hole. When Eq. 2.27 is 'universal', η/s of the QCD matter in the strong coupling limit also becomes $1/4\pi$ which can be compared with the observation of small viscosity at RHIC. Figure 2.12 shows a conceptual view of above discussion.

In above way, AdS/CFT correspondence has a possibility to provide a useful method for the calculation of non-perturbative (strong coupling) QCD matter which is created at RHIC. In addition, the experiments at RHIC have a possibility to provide a first test of the super-string theory. It is worth to note that the QCD calculation using AdS/CFT correspondence still has several ambiguous points, for example, 'universal' assumption, AdS/CFT correspondence itself and the correction of finite coupling constant in QCD. Therefore, further study is necessary for AdS/CFT correspondence to be a reliable method for non-perturbative QCD.

2.3 Heavy Flavor

Heavy quarks (charm, bottom) are primarily produced in hard partonic scattering in nucleon-nucleon collisions, since the initial content of heavy flavor in nuclei is negligibly small. In addition, the energy scale for the production of heavy quarks $Q^2 \sim M_{c(b)}^2$ is significantly higher than λ_{QCD}. This gives us a coupling constant of the order of $\alpha_s \sim 0.3$, which is small enough to apply perturbative QCD calculation for the production of heavy quarks. Therefore, measurement of heavy quarks in $p + p$ collisions provides a good test of the perturbative QCD calculation.

Heavy quarks are also expected to be a special probe of the medium created in heavy ion collisions, since their mass is significantly larger than the typical temperature of the created medium (~ 200 MeV in Au+Au collisions at RHIC) and λ_{QCD}. The expectations for the heavy quark production in heavy ion collisions and the motion inside the medium are summarized as bellow.

- Heavy quarks are only produced in the initial stage in the heavy ion collision. Thus heavy quark spectra in $p + p$ collisions provide a well defined initial state, even for low-momentum heavy quarks. Then, generated heavy quarks propagate through the hot and dense medium created in heavy ion collisions. This feature makes the measurement of heavy quark a prime tool to extract properties of the medium.

- The magnitude of the suppression of heavy quarks yield at high p_{T} region is expected much smaller compared with that of light quarks due to their large mass. This expectation is based on the 'dead cone' effect [33]. The gluon radiation from heavy quarks, which is a dominant source of energy loss in the medium in the case of light quark, is hindered by the angular screening. That is, the soft gluon emission in the forward direction of a heavy quark is suppressed within the angle $\Theta = M_{c(b)}/E_{c(b)}$ due to the causality.

  Thermalization of heavy quarks is expected to be 'delayed' relative to light quarks by a factor of $M_{c(b)}/T$. The magnitude of the elliptic flow of heavy quarks is also expected much smaller to be compared with that of light quarks.

  In addition, the magnitude of the energy loss and the elliptic flow of bottom is expected to be smaller to be compared with that of charm due to the large difference of their masses.

Method of Measurement of Heavy Flavor at RHIC

Measurement of heavy flavor is carried out via electrons from semi-leptonic decay of heavy flavored hadron, so called 'single non-photonic electron' in this thesis. Figure 2.13 shows a conceptual view of measurement of heavy flavor at RHIC. The entire process from the production to measurement can be schematically represented as

$$p + p \quad (A + A) \overset{pQCD}{\longrightarrow} c(b) \overset{N.P.frag}{\longrightarrow} D(B) \overset{decay}{\longrightarrow} lepton \tag{2.28}$$

where N.P. frag stands for non-perturbative fragmentation process and lepton represents the final-state observable.

The advantage of the measurement of single electrons from heavy flavor at PHENIX is a good signal to noise ratio because of well controlled material budget, while we can not detect a
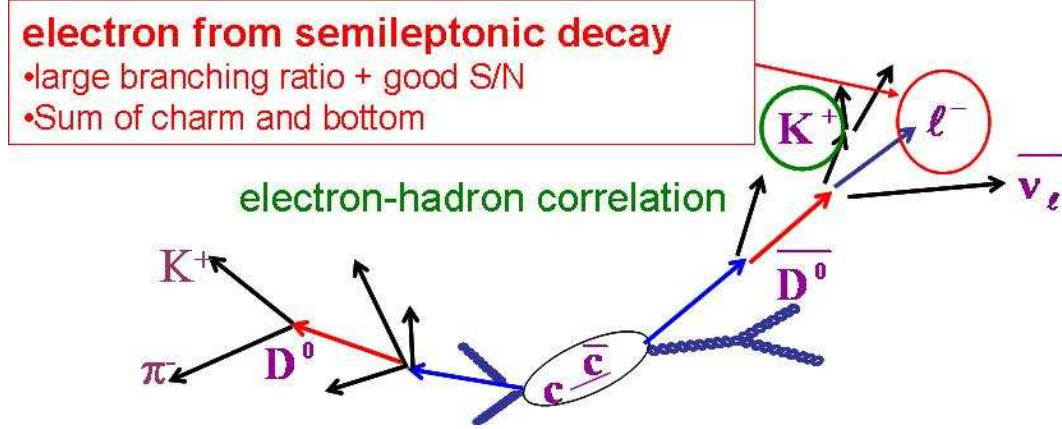
Figure 2.13: A conceptual view of measurement of heavy flavor at RHIC.

displaced vertexes of single non-photonic electrons. However, the observables are the mixture of single electrons from charm and bottom. The determination of the fraction of the contribution from bottom in the single non-photonic electrons is important to interpret the result of heavy flavor, since the behavior of bottom in the medium is expected to be quite different from that of charm due to the large difference of their mass.

A new analysis method is introduced in this thesis to measure the fraction of bottom in single non-photonic electrons. The correlation in unlike charge-sign electron-hadron pairs from weak decay of charmed hadrons is utilized, which is based on partial reconstruction of the $D/\bar{D} \to e^{\pm} K^{\mp} X$ decay as shown in Fig. 2.13. The new analysis method are described in Sec. 5.7.

In this section, the each step in Eq. 2.28 is briefly reviewed and the results of measurements of heavy quarks at RHIC are also described.

2.3.1 Heavy Flavor Production

The general perturbative calculation for the total cross section of quark pair production in the partonic level can be expressed by the following equation.

$$\sigma_{ij}(\tilde{s}, M_Q^2, \mu_R^2) = \frac{\alpha_s^2(\mu_R^2)}{M_Q^2} \sum_{k=0}^{\inf} (4\pi\alpha_s(\mu_R^2))^k \sum_{l=0}^{k} f_{ij}^{(k,l)}(\eta) \ln^l\left(\frac{\mu_R^2}{M_Q^2}\right), \qquad (2.29)$$

where μ_R^2 is called renormalization scale usually assumed to be $0.5 - 2 \times M_Q^2$ and $\tilde{s}$ is the partonic energy in center of mass frame. The dimensionless parameter $\eta = \tilde{s}/4M_Q^2 - 1$ reflects the phase space of the heavy quark pair production ($\sqrt{\tilde{s}}$ should be at least $2M_Q$ to create a quark-antiquark pair). i and j are the partonic indexes. $f_{ij}^{(k,l)}$ is a dimensionless scaling function representing the amplitude of a given partonic scattering diagram. k shows the order of the process diagram, $k = 0$ is called as Leading-Order (LO) and $k = 1$ is called as Next-Leading-Order (NLO). Figure 2.14 shows the Feynman diagram of LO and important NLO process. Using the parton distribution function in proton (PDF), we can write the total cross section

for heavy flavor production in term of $\sigma_{ij}(\tilde{s}, M_Q^2, \mu_R^2)$ in $p + p$ collisions as follows.

$$\sigma_{pp}(\tilde{s}, M_Q^2, \mu_R^2, \mu_F^2) = \sum_{i,j=q,\bar{q},g} \int_{\frac{4M_Q^2}{s}}^{1} d\tau \int_{\tau} 1\frac{dx_1}{x_1} f_i^p(x_1, \mu_F^2) f_j^p(\tau/x_1, \mu_F^2) \sigma_{ij}(\tau s, M_Q^2, \mu_R^2) \quad (2.30)$$

μ_F^2 a momentum transfer scale (factorization scale) of the PDF factorization and usually assumed to be $0.5 - 2 \times M_Q^2$. $f_i^p(x_1, \mu_F^2)$ is parton distribution function in term of a momentum fraction (x) and factorization scale. Eq. 2.30 have three free parameters, M_Q^2, μ_R^2 and μ_F^2. The uncertainty of the perturbative calculation is usually determined by varying these parameters.

2.3.2 Fragmentation

Colored heavy quarks pick up light quarks in order to create color singlet hadrons, which is called as fragmentation process. The differential cross section of heavy flavor hadrons $(\frac{d\sigma^H}{dp_T^H})$ can be written as follows using the factorization theorem.

$$\frac{d\sigma^H}{dp_T^H} = \int d\tilde{p}_T dz \frac{d\sigma_Q}{d\tilde{p}_T} D_Q^H(z)\delta(p_T^H - z\tilde{p}_T), \quad (2.31)$$

where $\tilde{p}_T$ is the transverse momentum of heavy quarks and p_T^H is the transverse momentum of heavy flavored hadrons. $\frac{d\sigma_Q}{d\tilde{p}_T}$ is the differential cross section of heavy quarks, and z is the momentum fraction of the quark carried by the hadron. $D_Q^H(z)$ is called as fragmentation function and determines the the probability of producing hadron with given momentum fraction (z).

The fragmentation function of heavy quarks should be much harder than that of a light hadron. In the limit of a very heavy quark, one expects that the fragmentation function for a heavy quark to go into any heavy hadron to be peaked near 1.

The fragmentation function can be split into a perturbative part and non-perturbative part. Non-perturbative effect in the calculation of the heavy quark fragmentation function is done in practice by convolving the perturbative result with a phenomenological non-perturbative form. There are various parameterizations for the non-perturbative part which have free parameters.

The free parameters in the non-perturbative parameterizations are determined by the experimental results in e^+e^- collisions based on 'universality of the fragmentation process' which is the assumption that the fragmentation function is independent of the hard-scattering process. In general, the parameters entering the non-perturbative forms do not have any absolute meaning, since these depend on the order of the perturbative calculation in the fragmentation function.

Figure 2.15(a) shows inclusive cross-section measurements of D^0, D^{*+} in CLEO and BELLE as a function of x_p which approximates the momentum fraction z [60, 64]. Figure 2.15(b) shows fragmentation a function for b quarks studied at LEP and SLD [65]. The most accurate approach to derive the fragmentation function is to use the Mellin transforms of the fragmentation function and obtain the momenta of this transform from the experimental data.

The treatment of the fragmentation process discussed above is expected to be valid in $p + p$ collisions. In the case of heavy ion collisions, the coalescence process becomes important in the fragmentation of heavy flavor.

2.3.3 Semi-Leptonic Decay

In decays of heavy flavored hadrons, semi-leptonic modes are generally accessible experimentally, because semi-leptonic branching ratios are large. Semi-leptonic decay is also more accessible theoretically than hadronic decays because of their relative simplicity which is a consequence of the fact that the effects of the strong interactions can be isolated. Therefore, they are the primary tool for the study of the CKM matrix and are well studied at CLEO, BELLE, BABAR and so on. Figure 2.16 shows an example of a Feynman diagram for the semi-leptonic decay. Top panel is simplified Feynman diagram and bottom panel is a slightly more realistic diagram which includes the contributions from complex interactions of gluons.

For processes where the momentum transfer is much less than the W boson mass, to a very good approximation, the amplitude for the semi-leptonic decay of a quark of type Q to one of type q ($Y_{Qq'} \rightarrow X_{qq'} l^+ \nu$) can be given by

$$M(Y_{Qq'} \rightarrow X_{qq'} l^+ \nu) = -i \frac{G_F}{\sqrt{2}} V_{qQ} L^\mu H_\mu. \tag{2.32}$$

Here, G_F is the Fermi constant of weak interaction and V_{qQ} is an element of the CKM matrix. L^μ is the leptonic current and H_μ is the hadronic current. In Eq. 2.32, only H_μ is difficult to calculate from first principles since it includes non-perturbative QCD effect as shown in Fig. 2.16. The hadronic current is usually parameterized with Lorentz invariant functions called 'form factors'. When one knows the form factors, the decay dynamics of semi-leptonic decays is determined according to Eq. 2.32. The form factors are functions of momentum transfer (q^2). In addition, the number of form factors and the parametrization form depend on the spin type of parent ($Y_{Qq'}$) and daughter ($X_{qq'}$) hadrons. As the simplest example, the hadronic current of pseudoscalar to pseudoscalar meson decays can be written as

$$H_\mu = F(q^2)(p + p')_\mu. \tag{2.33}$$

Here, p and p' are four momenta of the initial and final hadrons and $F(q^2)$ is form factor.

The form factors have been calculated by many theoretical models [68]. In this thesis, ISGW2 model is often used for the semi-leptonic decay of heavy flavored hadrons, which is based on quark model with the application of heavy quark symmetry [66, 67].

2.3.4 Fixed-Order plus Next-to-Leading-Log Calculation

Fixed-Order plus Next-to-Leading-Log (FONLL) calculation is the theory based on perturbative QCD calculation about heavy flavor production [77, 78, 79, 81]. FONLL can be compared directly with the experimental results, specially p_T distribution. The each process in Eq. 2.28 is implemented in FONLL as follows.

$$E \frac{d^3\sigma^l}{dp^3} = E^Q \frac{d^3\sigma^Q}{dp^3} \otimes D(Q \rightarrow H_Q) \otimes f(H_Q \rightarrow l), \tag{2.34}$$

where the symbol $\otimes$ denotes a generic convolution, the leptonic decay spectrum term $f(H_Q \rightarrow l)$ also implicitly accounts for the proper branching ratio and $D(Q \rightarrow H_Q)$ denotes fragmentation process.

The distribution of heavy quarks, $E d^3\sigma^Q/dp^3$ is evaluated at the Fixed-Order plus Next-to-Leading-Log (FONLL) level pQCD calculation, that is, FONLL includes the full fixed-order NLO result (FO) and re-summation perturbative terms proportional to $\alpha_s^n(\log^k(p_T/m))$ to all orders with next-to-leading logarithmic (NLL) accuracy (i.e. $k = n, n-1$), where m is mass of heavy quark. NLL terms take an important role to converge of the perturbative series for high p_T ($p_T > m$) region.

Heavy quark fragmentation is implemented within the FONLL formalism that merges the FO + NLL calculations. The NLL formalism is used to extract the non-perturbative fragmentation effects from the experimental data in e^+e^- collisions using Mellin transforms [83]. The decay of the D and B mesons into leptons is controlled by the experimentally measured decay spectra and branching ratios [61, 62].

Figure 2.17 shows the p_T distributions of B hadron measured in CDF with FONLL predictions in p+$\bar{\text{p}}$ collisions at $\sqrt{s} = 1960$ GeV [69, 70, 71, 79]. Figure 2.18 shows the differential cross sections of non-photonic electrons from heavy flavor measured in RHIC with FONLL predictions in $p + p$ collisions at $\sqrt{s} = 200$ GeV [77, 115, 119]. FONLL calculation provides a successful description for the experimental p_T distributions of heavy flavor. However, there is large theoretical uncertainty for the absolute value of cross section of heavy flavor at even FONLL. For example, FONLL predicts total cross section of charm, $\sigma_{c\bar{c}}$ to be $256^{+400}_{-146}\mu b$ and total cross section of bottom $\sigma_{b\bar{b}}$ to be $1.87^{+0.99}_{-0.67}\mu b$ in $p + p$ collisions at $\sqrt{s} = 200 GeV$.

2.3.5   Initial Nuclear Effect for Heavy Flavor

Initial nuclear modification of heavy flavor production is studied by the measurement of the electrons from heavy flavored hadrons in d+Au collisions at $\sqrt{s_{NN}} = 200$ GeV at PHENIX [128]. Figure 2.19 shows the nuclear modification factor of the electrons from heavy flavor in d+Au collisions (R_{dAu}) defined in Eq. 2.12. The measured R_{dAu} indicates the yield of the electrons from heavy flavor is slightly enhanced in d+Au collisions for the measured p_T range, while it is almost consistent with unity due to large uncertainty.

Figure 2.20 shows changes induced on charm (left) and bottom (right) cross-sections at mid-rapidity by the nuclear effects of the PDFs, calculated using the EKS 98 nuclear weight functions [129]. As shown in Fig. 2.20, charm production is not modified and bottom production is slightly enhanced (anti-shadowing) by the PDF modification. Therefore, the slight enhancement of the measured R_{dAu} could be interpreted as the cronin effect. In near future, the uncertainty of R_{dAu} will be significantly reduced and initial nuclear effect for heavy flavor production will be revealed precisely by the data of d+Au collisions at RHIC in Year 2008 RUN.

2.3.6   Medium Modification of Heavy Flavor

Medium modification of heavy quarks is studied by the measurement of the electrons from heavy flavored hadrons in Au+Au collisions at $\sqrt{s_{NN}} = 200$ GeV at PHENIX [114]. Figure 2.21 shows R_{AA} of the electrons from heavy flavor decays for two different p_T ranges as a function of the number of participant nucleons N_{part}. For the integration interval $p_T > 0.3$ GeV/c containing

more than half of the heavy flavor decay electrons, R_{AA} is consistent with unity for all N_{part} in accordance with the binary scaling of the total heavy-flavor yield. This fact supports the expectation that heavy flavor is only produced in the initial hard scattering. For the integration with $p_{\rm T} > 3.0$ GeV/c, the heavy flavor electron R_{AA} decreases systematically with N_{part}, while that is larger than R_{AA} of π^0 with $p_{\rm T} > 4.0$ GeV/c [130].

Figure 2.22 shows the measured R_{AA} and v_2^{HF} of the electrons from heavy flavor in 0-10% central (most central) and minimum bias collisions, and corresponding π^0 data at PHENIX [130, 131]. While at low $p_{\rm T}$ the suppression is smaller than that of π^0, R_{AA} of heavy flavor decay electrons approaches the same magnitude of π^0 for $p_{\rm T} > 4.0$ GeV/c. The observed large v_2^{HF} indicates that the charm relaxation time is comparable to the short time scale of QGP lifetime. Such behavior of heavy flavor is far from the early expectation. Therefore, the understanding of the behavior of heavy flavor is experimentally and theoretically challenging.
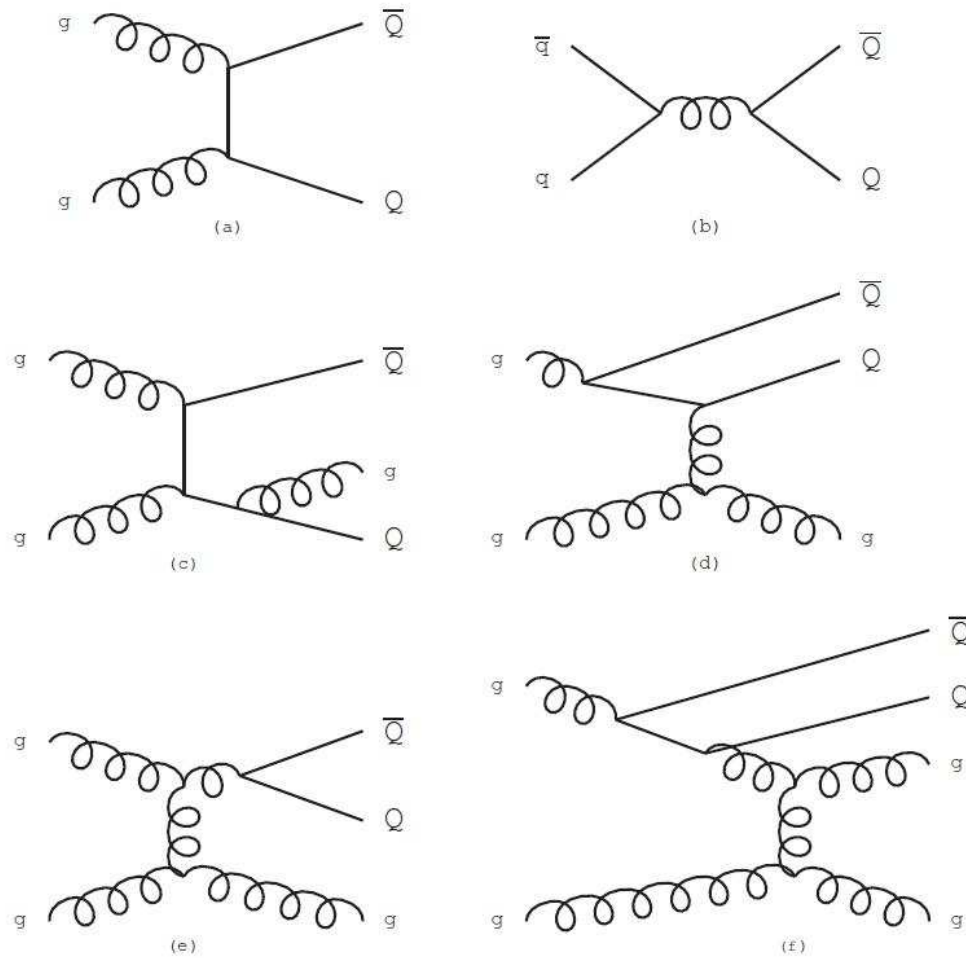
Figure 2.14: LO and most important NLO heavy quark production diagrams. LO - a) 'gluon fusion' b) 'quark-antiquark annihilation' NLO - c) Pair creation with gluon emission in output channel d) 'flavor excitation' e) 'gluon splitting' f) 'gluon splitting' but of 'flavor excitation' character.
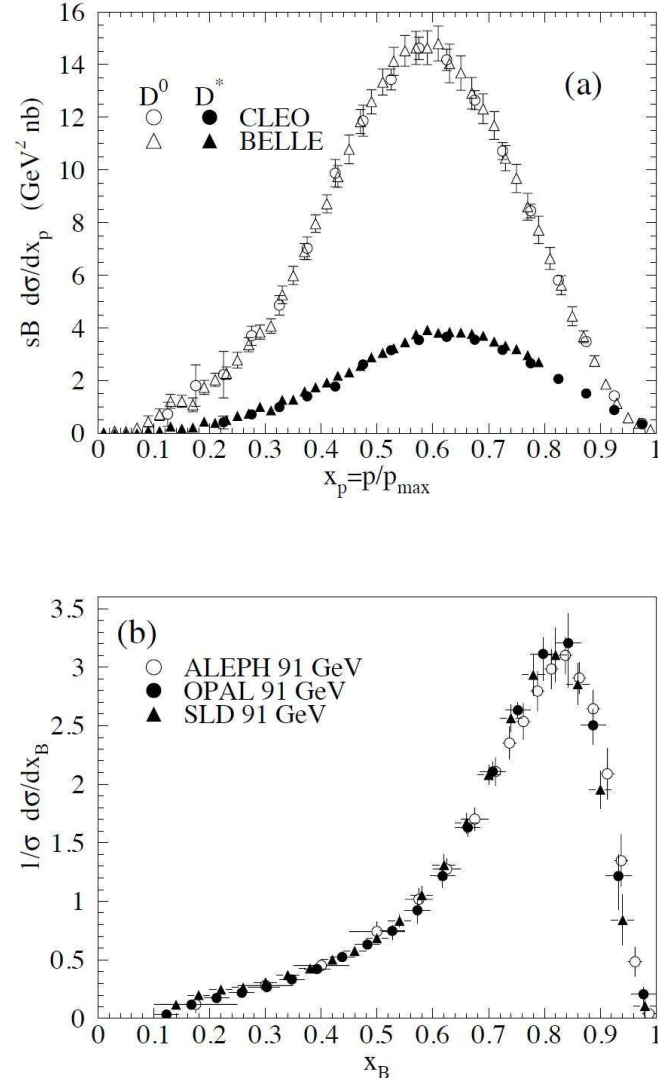
Figure 2.15: (a) Inclusive cross-section measurements of D^0, D^{*+} in CLEO and BELLE as a function of x_p which approximates the momentum fraction z [60, 64]. (b) Fragmentation function for b quarks studied at LEP and SLD [65].
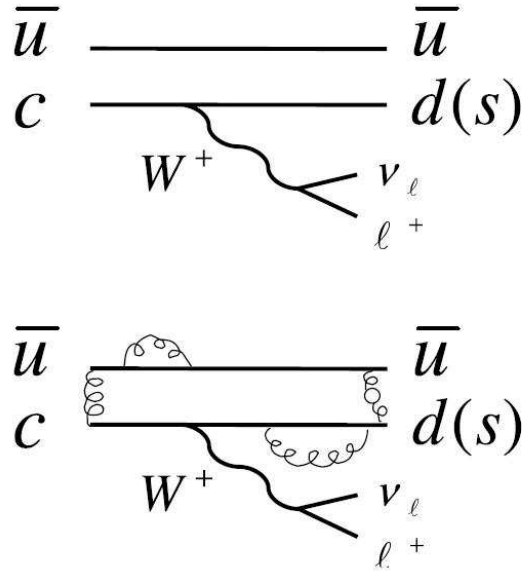
Figure 2.16: Top: Simplified feynman diagrams for $D^0 \rightarrow \pi^-(K^-)l^+\nu$. Bottom: A slightly more realistic diagram.
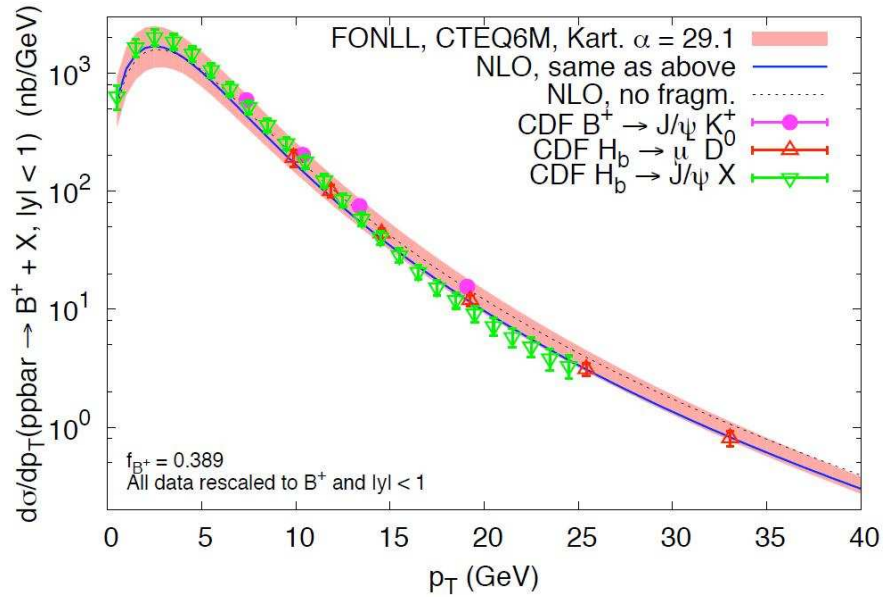
Figure 2.17: The p_{T} distributions B hadron measured in CDF with FONLL predictions in p+p̄ collisions at $\sqrt{s} = 1960 GeV$ [69, 70, 71, 79]
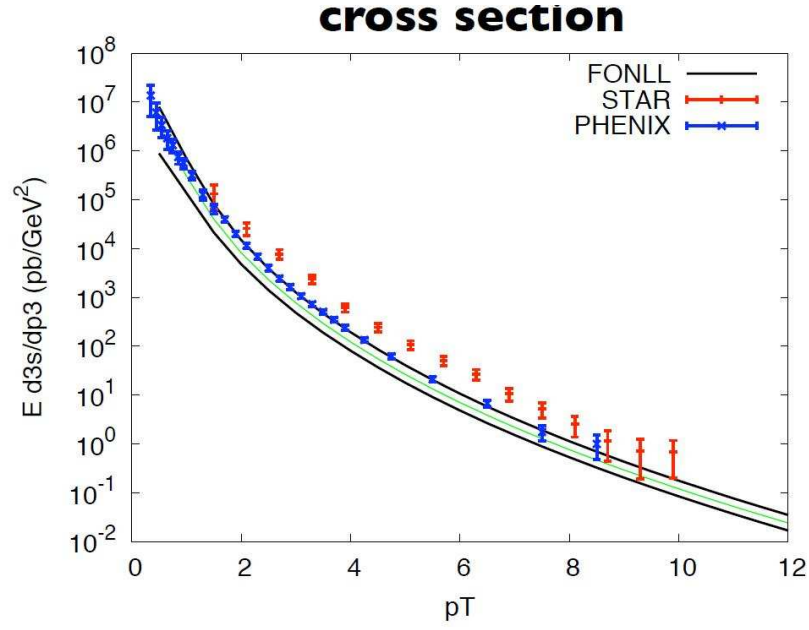
Figure 2.18: The differential cross sections of non-photonic electrons from heavy flavor measured in RHIC with FONLL predictions in $p+p$ collisions at $\sqrt{s} = 200 GeV$ [115, 119, 77]
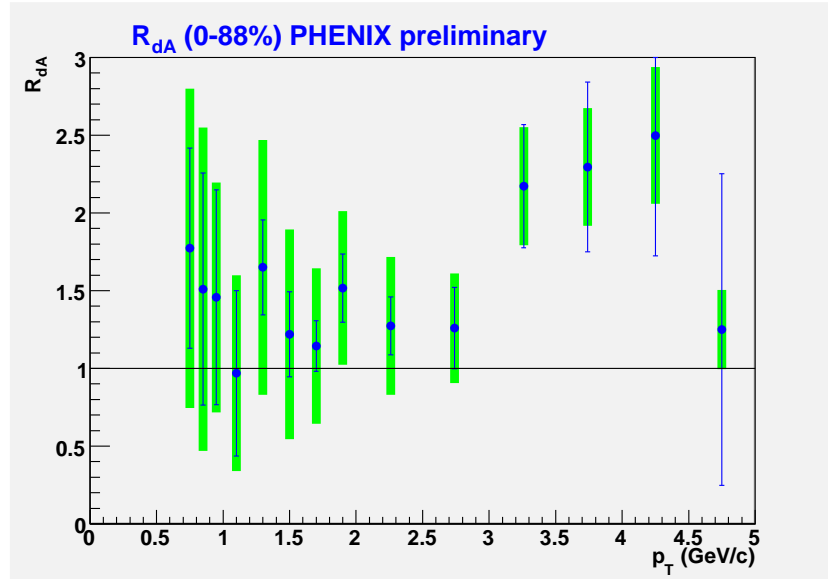
Figure 2.19: The nuclear modification factor of the electron from heavy flavor in d+Au collisions (R_{dAu})
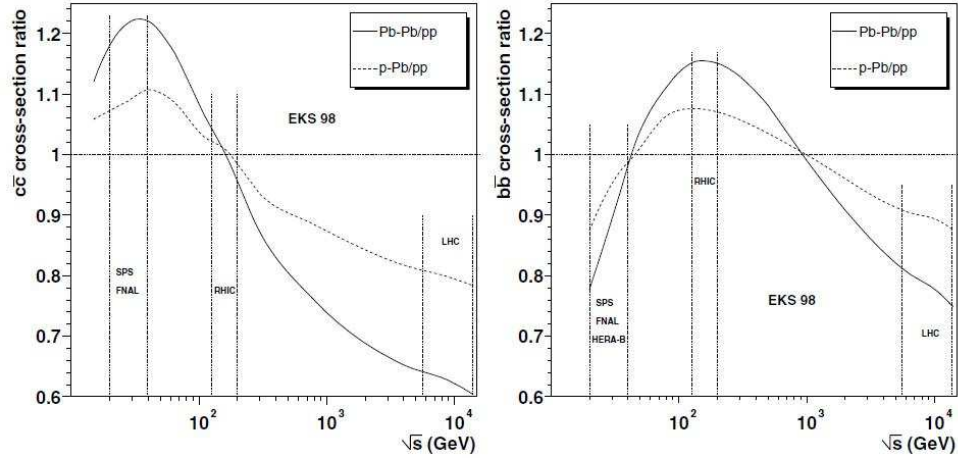
Figure 2.20: changes induced on charm (left) and bottom (right) cross-sections by the nuclear effects of the PDFs, calculated using the EKS 98 nuclear weight functions [129].
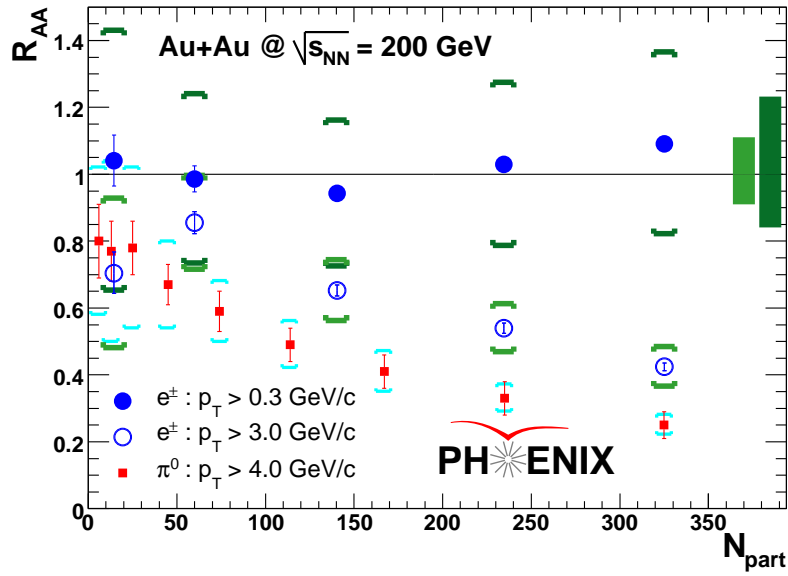
Figure 2.21: R_{AA} of heavy flavor electrons with p_T above 0.3 and 3 GeV/c and of π^0 with $p_\mathrm{T} > 4$ GeV/c as a function of N_{part}. The right (left) box at $R_{AA} = 1$ shows the relative uncertainty from the $p+p$ reference common to all points for $p_\mathrm{T} > 0.3(3)$ GeV/c
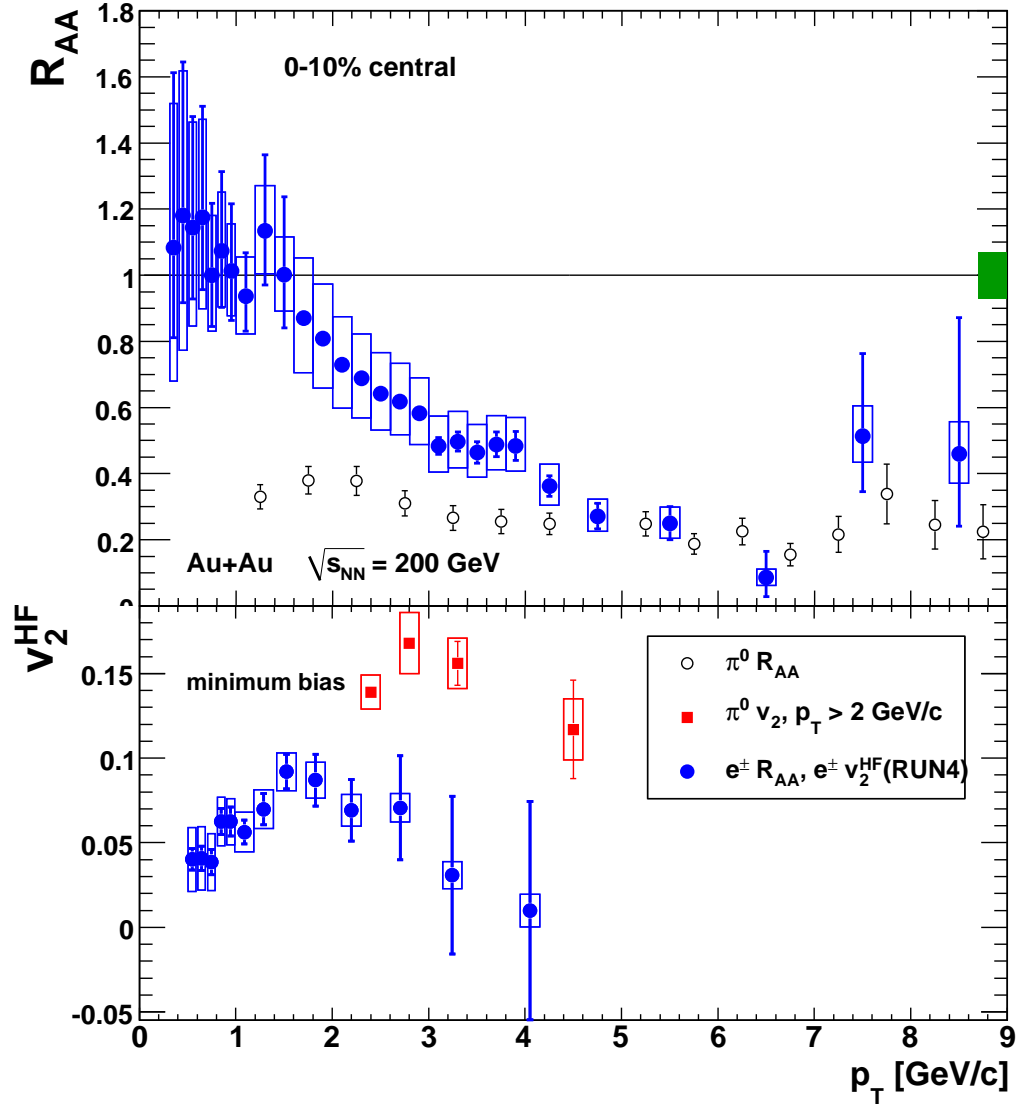
Figure 2.22: Top:R_{AA} of heavy flavor electrons in 0-10% central collisions compared with π^0 data and The box at $R_{AA} = 1$ shows the uncertainty in the number of binary collisions. Bottom: v_2^{HF} of heavy flavor electrons in minimum bias collisions compared with π^0.

Radiative Energy Loss

Figure 2.23 shows the comparison of the measured R_{AA} with DGLV and BDMPS models [34, 35]. DGLV model is based on GLV model. Radiative gluon emission and 'dead cone effect' is implemented as the source of energy loss in the medium in these models.

As already described, the single non-photonic electrons originate from charm and bottom whose behaviors in the medium should be different due to their large mass difference. The fraction of the contribution from bottom in all single non-photonic electrons from heavy flavor is calculated using perturbative QCD in Fig 2.23. The spectra of single non-photonic electrons from charm and bottom are merged according to the fraction, after the suppression pattern of the single electrons from charm and bottom is calculated separately. In Fig 2.23, the parameter in BDMPS $\hat{q}$ is 14 GeV^2/fm and that in DGLV dN^g/dy is 1000. These models with the chosen parameters provide a successful description of the measured R_{AA} of π^0 as shown in Sec. 2.2.2. The predicted R_{AA} of heavy flavor electrons are larger than that of π^0 due to 'dead cone' effect and larger than the measured R_{AA} of heavy flavor electrons. This fact indicates radiative gluon emission is not enough to describe the energy loss mechanism of heavy flavor in the medium.
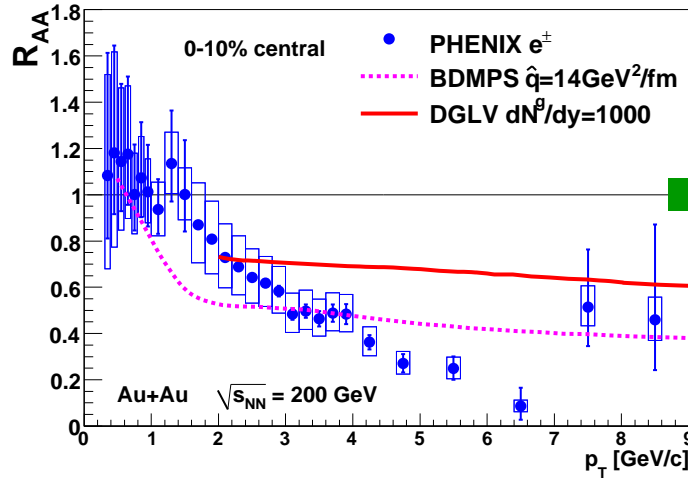
Figure 2.23: The comparison of the measured R_{AA} with DGLV and BDMPS models [34, 35].

Collisional Energy Loss

It has been pointed out that elastic scattering is an important source of energy loss of heavy flavor in the medium, while the effect of elastic scattering is negligible for the energy loss of light quark [37, 38]. It seems to be natural because most of produced heavy flavor are not ultra-relativistic. It may be worth noting here that for an electron traversing a hydrogen target, bremsstrahlung losses first exceed ionization losses when $\gamma\beta \sim 700$. Figure 2.24 shows the comparison of the energy loss from radiative emission and elastic scattering of charm and bottom [38]. The energy loss from elastic scattering is comparable to that from radiative

emission. Figure 2.25 shows the comparison of the measured R_{AA} with the extended DGLV including elastic scattering [36]. The parameter in the extended DGLV, dN^g/dy, is 1000. The extended DGLV still underpredicts the magnitude of the suppression of electrons from heavy flavor.
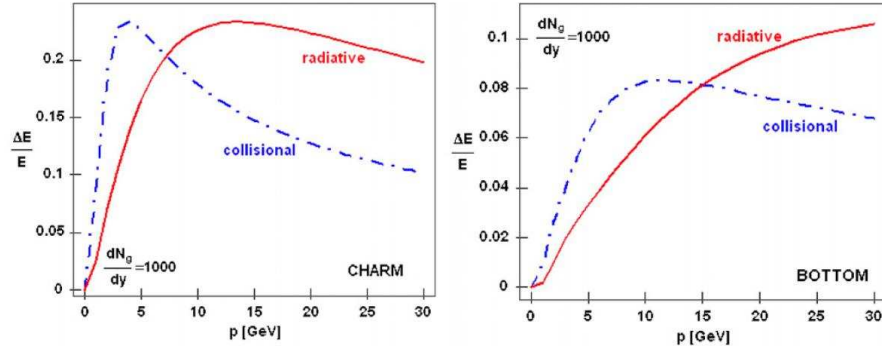
Figure 2.24: Comparison between collisional and medium-induced radiative fractional energy loss is shown as a function of momentum for charm and bottom quark jets [38].
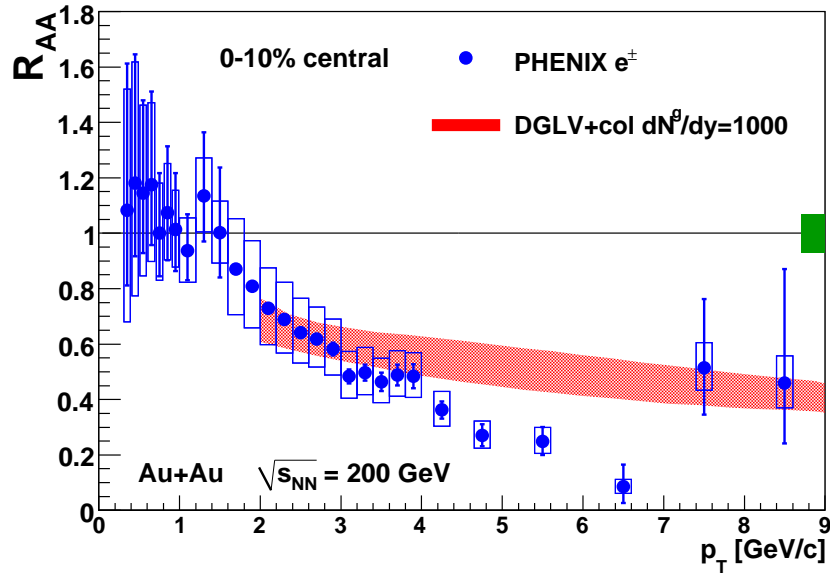
Figure 2.25: The comparison of the measured R_{AA} with the extended DGLV including elastic scattering [36].

Charm Alone Model

There is a simple and robust solution for the puzzle of the energy loss of heavy flavor. When we assume all single electrons are from charm quarks, the predicted R_{AA} agrees with the

experimental result because the suppression magnitude of bottom quark is expected to be much smaller than that of charm quarks. Figure 2.26 the comparison of the measured R_{AA} with the extended DGLV and BDMPS models when the contribution of bottom quark is neglected [35, 36]. In Fig 2.26, the parameter in BDMPS $\hat{q}$ is 14 GeV^2/fm and that in extended DGLV dN^g/dy is 1000.

Of course, this assumption is too extreme and may be incorrect. However, this model suggests that determination of the fraction of bottom in single non-photonic electrons is necessary to interpret the result of energy loss about heavy flavor and to extract the property of the medium from the result. The determination of the fraction of bottom in single non-photonic electrons is the most important subject in order to understand the behavior of heavy quarks in the hot and dense matter produced in Au+Au collisions at RHIC. It is the motivation of this thesis.
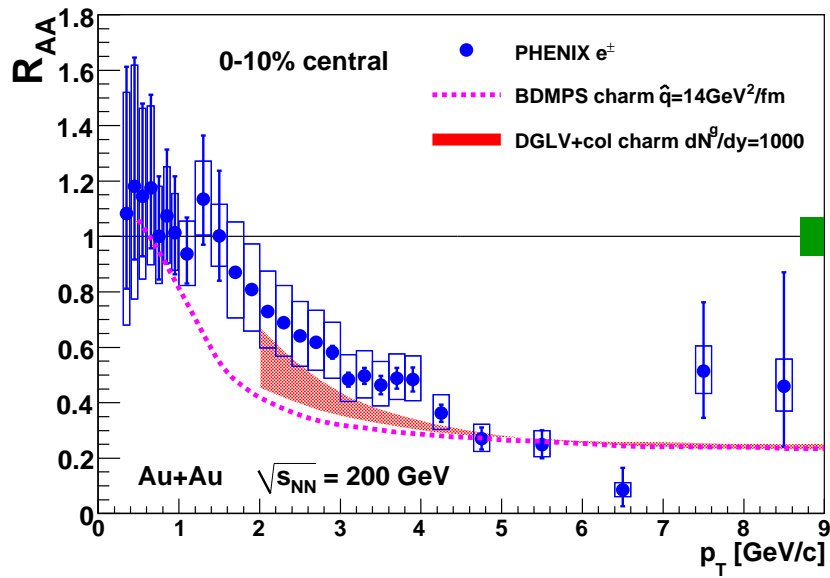
Figure 2.26: The comparison of the measured R_{AA} with the extended DGLV and BDMPS models when the contribution of bottom quark is neglected [35, 36].

Chapter 3

The Experimental Setup

The data analyzed in this thesis are $p + p$ collisions at $\sqrt{s} = 200$ GeV at the BNL Relativistic Heavy Ion Collider and are collected with the PHENIX detector using its two central arm spectrometers. Each spectrometer covers $\mid \eta \mid < 0.35$ in pseudorapidity and $\Delta\phi = \pi/2$ in azimuth in a nearly back-to-back configuration. The capability of charged particle tracking and electron identification is necessary to measure single electrons and a correlation in electron-hadron pairs. The arms include drift chambers (DC) and pad chambers (PC1,2,3) for charged particle tracking, a ring imaging Čerenkov detector (RICH) for electron identification, and an electromagnetic calorimeter (EMCal) for electron identification and triggering (ERTLL1). Beam-beam counters (BBCs), positioned at pseudorapidity $3.1 < \mid \eta \mid < 3.9$, measure the position of the collision vertex along the beam (z_{vtx}) and provide the interaction trigger (BBCLL1). In this chapter, the accelerator complex at BNL and the details of PHENIX detectors are presented.

3.1 Accelerator Complex at BNL

The Relativistic Heavy Ion Collider (RHIC) is a colliding-type accelerator at BNL to study the extreme hot and dense matter. The RHIC started its operation in 2000 [87]. Figure 3.1 shows the layout of the RHIC accelerator complex. The accelerator complex consists of Tandem Van de Graaff facility, Linear Accelerator (LINAC) facility, Booster Accelerator, Alternating Gradient Synchrotron (AGS), and Relativistic Heavy Ion Collider (RHIC). RHIC can accelerate form protons (p) to gold (Au)ions at the maximum center of mass energy of 500 GeV in $p + p$ collisions and 200 GeV per nucleon pair in Au+Au collisions.

Tandem Van de Graaff Facility

The heavy ion beam is supplied by the Tandem Van de Graaff facility. The facility consists of two 15 MeV electro-static accelerators (MP-7 and MP-8), each of which is about 24 meters long and aligned end-to-end.

A pulsed sputter ion source is used as an injector of Tandem Van de Graaff and provides a 500 μs long pulse of Au$^-$ with the peak intensity of 290 μA. Then the gold beam are accelerated from ground to +14 MV potential. They pass through a stripping foil in the high voltage terminal in the middle of Tandem. The partially stripped ions are accelerated back to ground
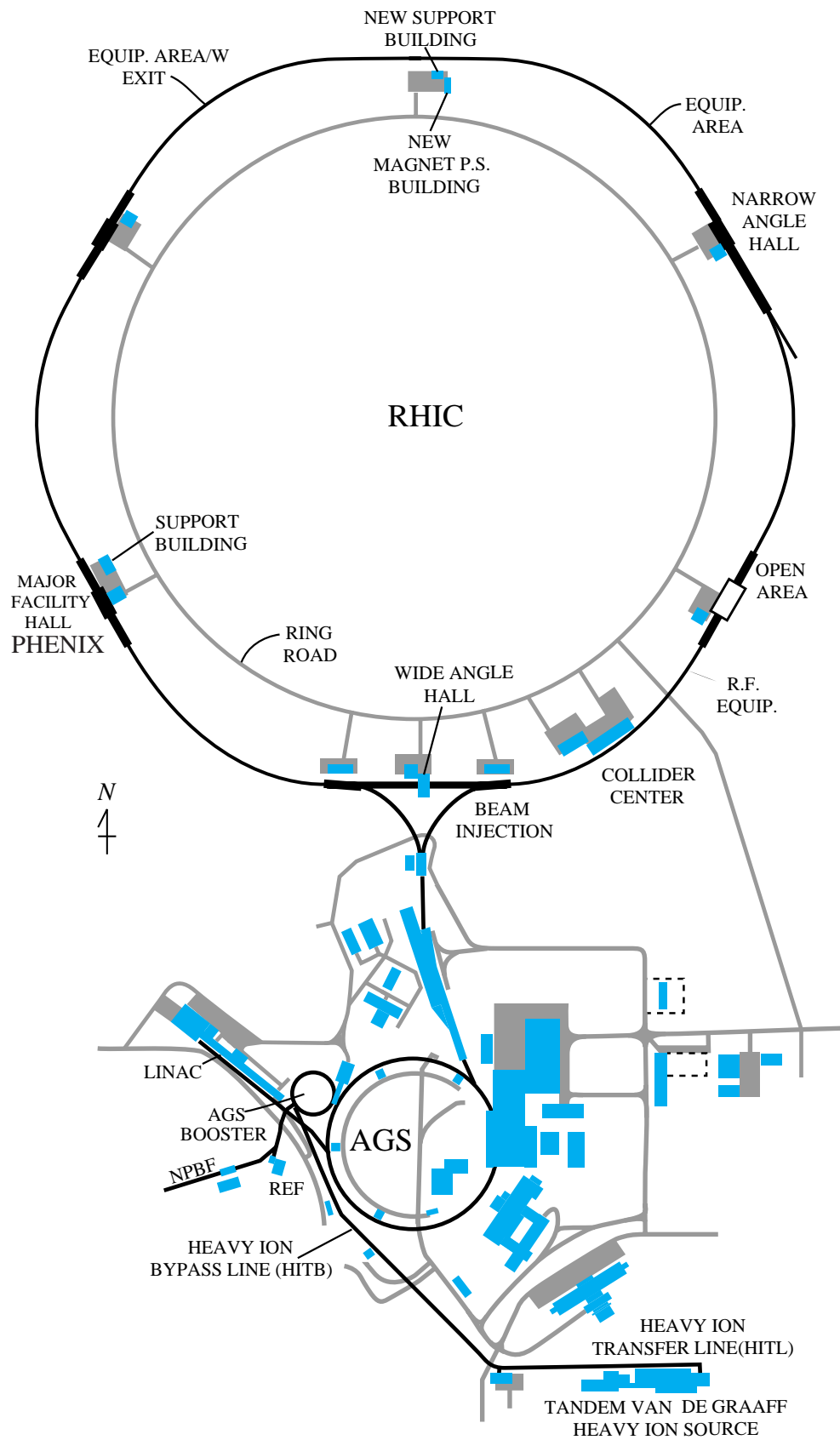
Figure 3.1: Accelerator Complex at Brookhaven National Laboratory.

potential and are selected charge state of Au^{12+}. When Au ions are accelerated, another carbon foil at the exit of Tandem is used to strip electrons and to make higher charged ion, Au^{32+}.

Linear Accelerator (LINAC) Facility

The polarized (70–80 %) or un-polarized proton beam is supplied by Linear Accelerator (LINAC) facility, which consists of Optically Pumped Polarized H^- Ion Sources (OPPIS), a radio-frequency quadrupole (RFQ) pre-injector, and nine radio-frequency cavities. The LINAC is capable to produce up to 35 mA proton beam at the energy of 200 MeV. The beam intensity is 15×10^{11} proton/pulse at the ion source and 6×10^{11} at the end of LINAC. The beam is injected into the Booster Accelerator for further acceleration.

Booster Accelerator

The Booster Accelerator facility accepts the beam from Tandem Van de Graaff facility, or the beam from LINAC. It is used as a pre-accelerator. The machine circumference is 200 m. In case of gold beam, the booster has the capability to accelerate the beam to the energy of 72 MeV/nucleon and strip the beam to +77 charge state.

Alternating Gradient Synchrotron (AGS)

The Alternating Gradient Synchrotron (AGS) accepts the beam from Booster and is served as an injector for the RHIC. The AGS has the circumference of 800 m.

The AGS employed the concept of alternating gradient focusing, in which the field gradients of the accelerator's 240 magnets are successively alternated inward and outward, permitting particles to be propelled and focused in both the horizontal and vertical plane at the same time.

In the AGS, the gold beam is stripped to +79 charge state and is accelerated to an energy of 10 GeV/nucleon. The maximum energy of polarized proton beam is 24.3 GeV. The beam is delivered to RHIC via AGS to RHIC Line (ATRL).

3.1.1   Relativistic Heavy Ion Collider (RHIC)

There are two rings in RHIC, each of which has circumference of 3.83 km. They are called Blue Ring (circulating clockwise) and Yellow Ring (circulating counter-clockwise). Rings are kept to be the vacuum of 5×10^{-11} Torr. Each ring has 192 superconducting dipole magnets with the magnet field of 3.46 T. Also, 12 common dipole magnets, 492 quadrupole magnets and 852 trim or corrector magnets are used. For $p + p$ collisions, 2 superconducting Helical Siberian Snakes were installed in each ring to avoid the depolarization during the acceleration of the polarized protons [89].

The RHIC accepts the heavy ion or proton beams from AGS and store them. The designed maximum energy is $\sqrt{s_{NN}} = 200$ GeV for Au+Au and $\sqrt{s} = 500$ GeV for $p + p$, respectively. The designed maximum luminosity is $2 \times 10^{26} \text{cm}^{-2}\text{sec}^{-1}$ for gold beam and $2 \times 10^{32} \text{cm}^{-2}\text{sec}^{-1}$ for proton beam. Each bunch has the length of 5 ns. In $p+p$ run, the polarization of ~ 60 % was achieved at Year 2006/2007. Table. 3.1 summarize the major parameters achieved in Year-2005 and Year-2006 Run in $p + p$ collisions.

The RHIC collides two beams head-on using DX dipole magnet at six interaction regions. Four of the interaction regions are equipped with the experiments: PHENIX, STAR, BRAHMS, and PHOBOS.

Table 3.1: The parameters of RHIC accelerator in Year-2005 and Year-2006 $p + p$ RUN.

parameter	Year-2005	Year-2006
beam energy (GeV)	100	100
revolution frequency (kHz)	78	
number of bunches	106	111
number of particles/bunch (10^{11})	0.9	1.35
emittance ($\beta^* = 1$)(mm mrad)	28	18
peak luminosity (10^{30} cm^{-2}s^{-1})	10	35
average luminosity (10^{30} cm^{-2}s^{-1})	6	20

3.2 PHENIX Experiment

The PHENIX experiment is one of the large-scale experiments at RHIC [84, 85, 86]. The PHENIX is designed to measure a wide variety of physics observables of QGP formation as possible.

3.2.1 PHENIX Global Coordinate System

The PHENIX global coordinate system defines the geometrical center of the interaction point as the origin (0,0,0). Figure 3.4 shows the definition of global coordinate system used in the PHENIX experiment. Taking the beam-line as a z-axis (North is positive z direction), the direction to west arm is defined as x-axis, and upward is defined as y-axis. The azimuthal angle ϕ is measured counter-clockwise relative to the positive x direction, and the negative x direction is $\phi = 180$ degrees. The polar angle θ is defined as the angle relative to z-axis. Using the polar angle θ, the pseudo-rapidity variable is expressed as:

$$\eta = -\ln \tan(\frac{\theta}{2}). \tag{3.1}$$

3.2.2 Detector Overview

Figure 3.2 illustrates the experimental layout of PHENIX detectors in RUN Year-2005 and Year-2006. Both beam view (top) and side view (bottom) are shown. The PHENIX consists of trigger counters, a central magnet, two muon magnets, two central arms, and two muon arms. The acceptance coverage, and the function of the detector subsystems are briefly summarized in Table 3.2. The details about detectors are presented in the following sections. The pseudo-rapidity coverage of PHENIX Central Arm and Muon Arm are $\mid \eta \mid < 0.35$ and $1.2 < \mid \eta \mid < 2.4$, respectively. Around the interaction point, the beryllium beam pipe is used and its diameter and thickness are 76mm and 1mm, respectively. Figure 3.3 shows the acceptance of both central arm and muon arm in the pseudo rapidity - ϕ angle plane. The measurement of electron is performed by using the central arm.
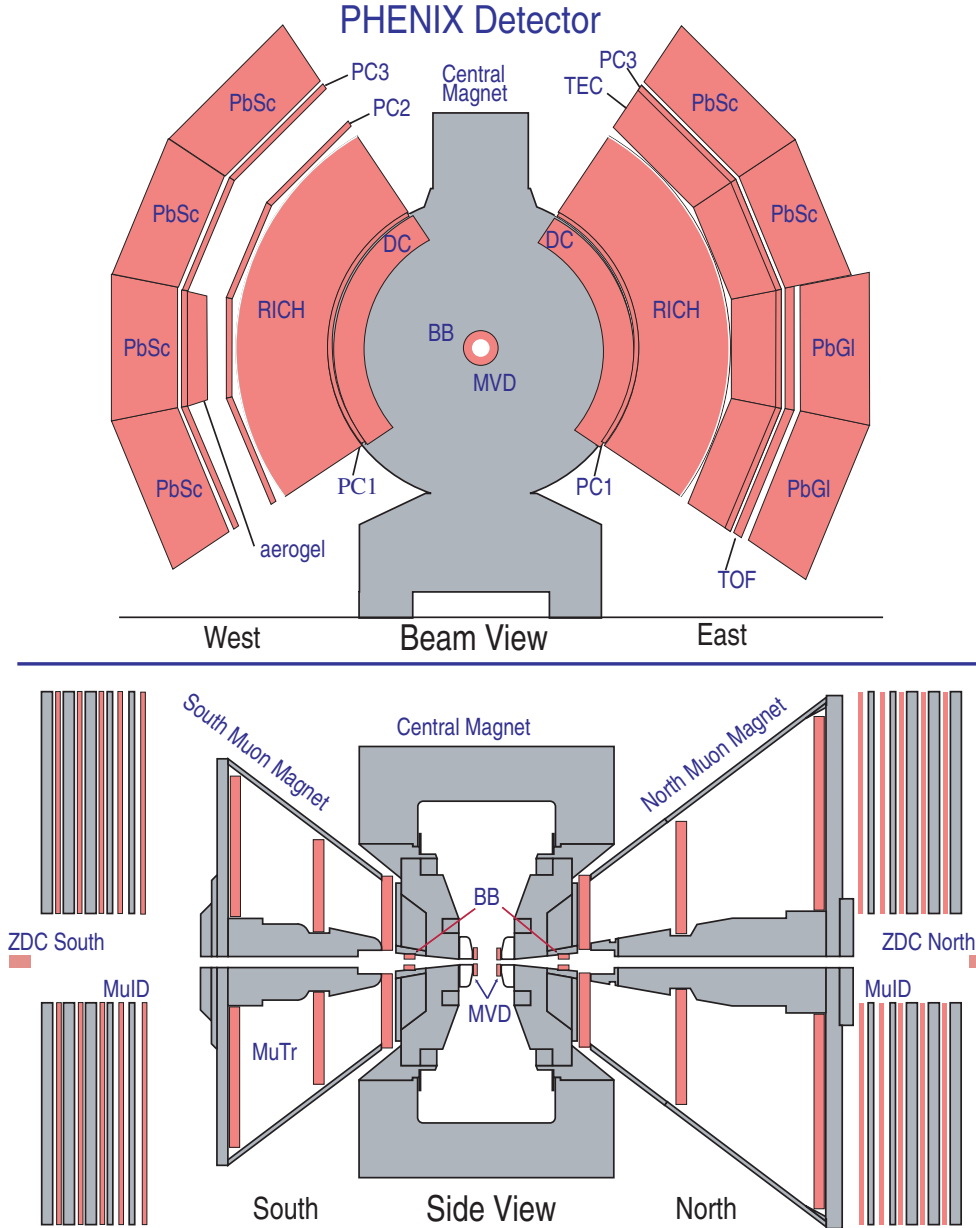
Figure 3.2: Experimental Layout of PHENIX Detector in Year-2005 and 2006 Run. TOP) Beam view : Inner detectors, two Central Arms, and Central Magnet are shown. BOTTOM)Side view : Inner detectors, two Muon Arms, Central Magnet, and Muon Magnets are shown.
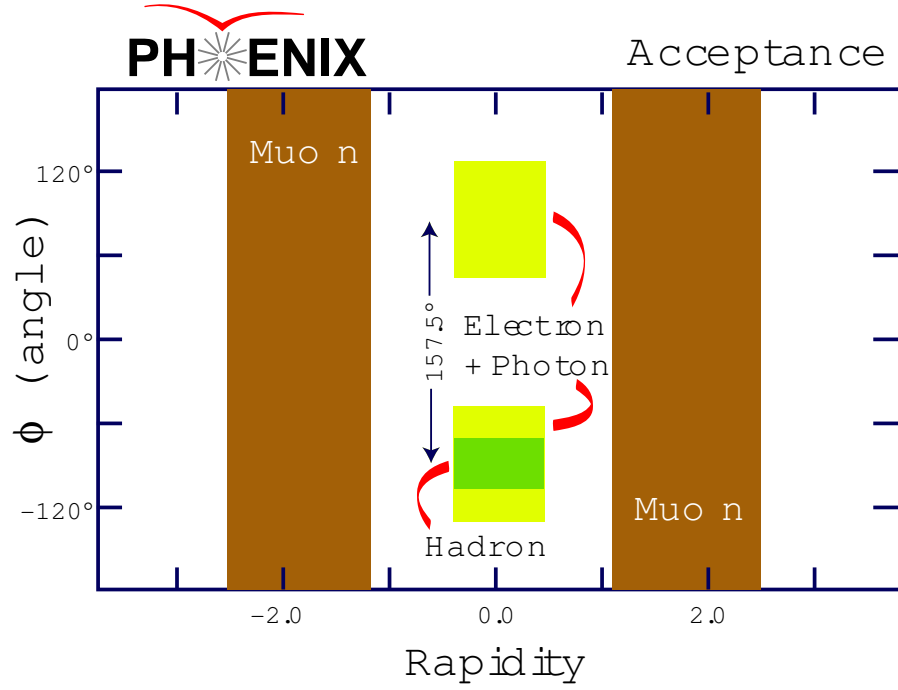
Figure 3.3: The PHENIX acceptance in terms of rapidity and ϕ angle.

Table 3.2: Summary of the PHENIX Detector Subsystems.

Element	$\Delta\eta$	$\Delta\phi$	Purpose and Special Feature
Central Magnet (CM)	± 0.5	360º	Up to 1.0 T·m.
Muon Magnet (MM)	± 1.1-2.5	360º	0.72 T·m for $\eta=\pm 2$, 0.36 T·m for $\eta=\pm 1.3$.
BBC	$\pm(3.0$-3.9)	360º	Start timing, fast vertex.
Drift chambers (DC)	± 0.35	90º × 2	Good momentum and mass resolution, $\Delta p/p = 1.0\%$ at $p = 1 GeV/c$.
Pad Chamber (PC)	± 0.35	90º × 2	Pattern recognition, tracking for non-bend direction.
TEC	± 0.35	90º × 2	Pattern recognition, dE/dx.
RICH	± 0.35	90º × 2	Electron identification.
TOF	± 0.35	30º	Good hadron identification, $\sigma < 100 ps$.
PbSc	± 0.35	90º × 1.5	Photon detection.
PbGl	± 0.35	45º	Photon detection.
Muon chambers (μT)	± 1.2-2.4	360º	Tracking for muons.
Muon identifier (μID)	± 1.2-2.4	360º	Concrete absorbers and chambers for μ/hadron separation.
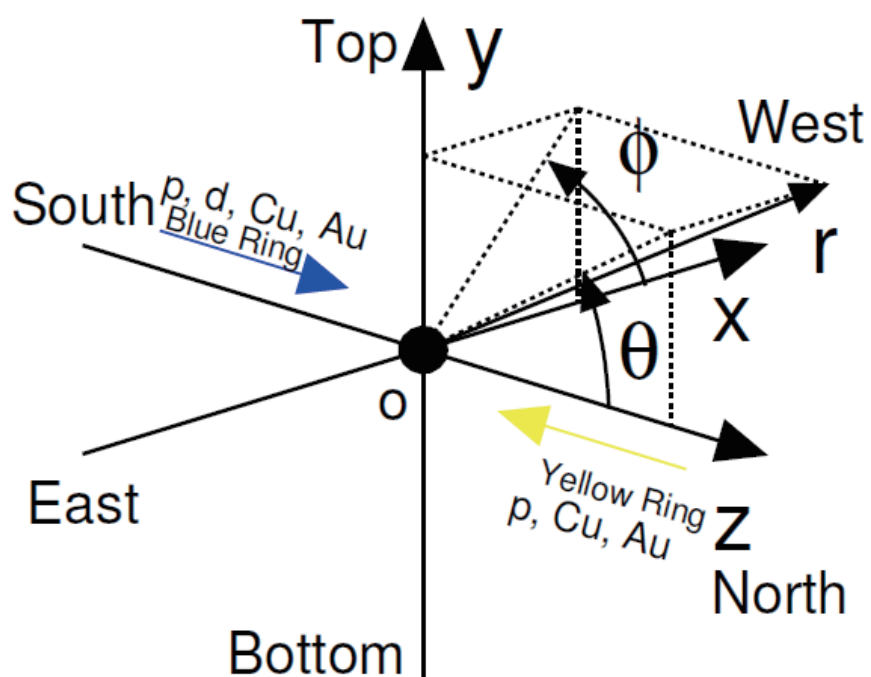
Figure 3.4: Definition of global coordinate system used in the PHENIX

3.3 The Trigger Counters

The PHENIX trigger system consists of Beam-Beam Counters (BBC) and Zero-Degree Calorimeters (ZDC). The ZDC is the common trigger device among four RHIC experiments. The details about BBC and ZDC are presented in this section.

3.3.1 Beam-Beam Counters (BBC)

The Beam-Beam Counters (BBC) provide the measurement of collision point and start signal for time of flight measurement [88].

There are two arrays of BBC in PHENIX along the beam line. They are quartz Cherenkov detectors which locate at 144 cm from the interaction point and surround the beam axis with the 10 cm of inner diameter and 30 cm of outer diameter. The pseudo-rapidity coverage is $\eta = \pm(3.0 - 3.9)$. Each counter consists of 64 one-inch diameter mesh-dynode (15 step) Photo Multiplier Tubes (PMT:Hamamatsu R6178) equipped with 3 cm quartz on the head of PMT as a Cherenkov radiator. Figure 3.5 shows the pictures of the (a) single BBC, (b) a BBC array, and (c) BBC location.

The BBC detects the particles such as $\pi^{+/-}$ from collisions. The start signal for timing measurement (T_0) and the beam-beam collision point along beam axis (z-vertex) are provided by using the average arriving time of particles between North (T_1) and South BBC array (T_2) and their difference. They are calculated as:

$$T_0 = \frac{(T_1 + T_2)}{2} - \frac{|z_{bbc}|}{c} + t_{offset}, \tag{3.2}$$

$$z-\text{vertex} = \frac{c(T_1 - T_2)}{2}, \tag{3.3}$$

where z_{bbc} is the BBC position of 144 cm, c is the velocity of light, and t_{offset} is the time offset intrinsically introduced by devices.

Figure 3.6 (a) shows the distribution of timing deviation of a typical BBC element from the BBC average time. Figure 3.6 (b) shows the distribution of time resolution over all BBC elements. The time resolution of a single BBC element was 52±4 ps (rms) and the z-vertex resolution was ∼0.5 cm under the experimental condition.

3.3.2 Zero-Degree Calorimeters (ZDC)

The Zero-Degree Calorimeters (ZDC) is a hadron calorimeter designed to detect the forward neutrons and measure their total energy [90, 91]. The ZDC's have the angular acceptance of $|\theta| < 2$ mrad. There are two ZDC's in PHENIX.

They are sampling type hadron calorimeters which positioned at 18 m from the interaction point and sit just behind the DX dipole magnet as shown in Fig. 3.7. The DX dipole magnets serve to bend the incoming beams to the colliding region and outgoing beams to the collider beam line [92]. Because of the magnetic bending by DX dipole magnet, only the neutrons can reach to ZDC.
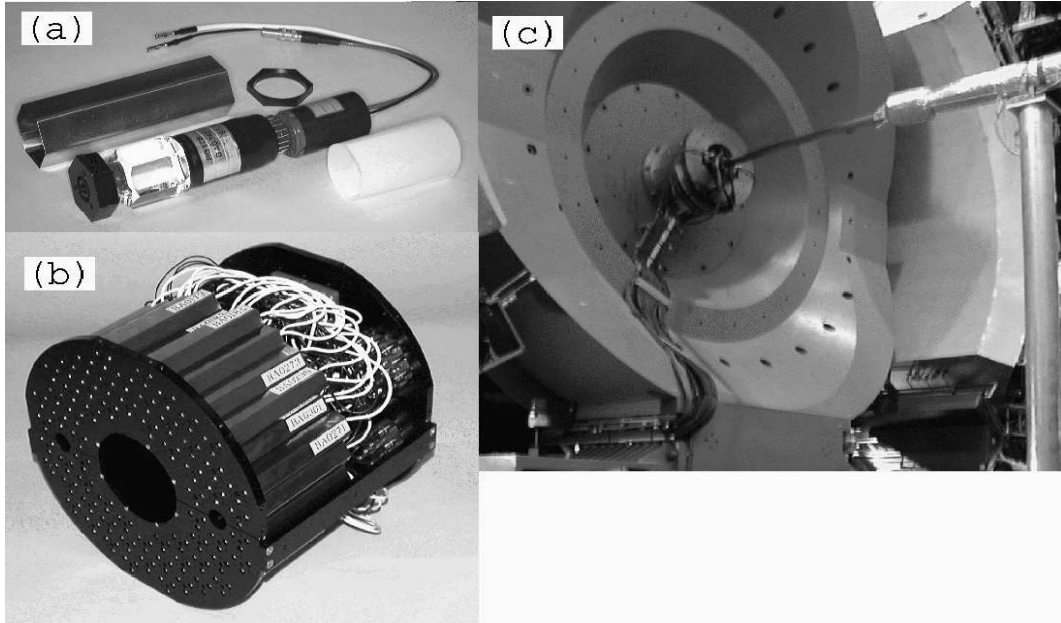
Figure 3.5: (a) Single BBC. (b) A BBC array comprising 64 BBC elements. (c) The BBC is shown mounted around beam pipe and just behind the Central Magnet.
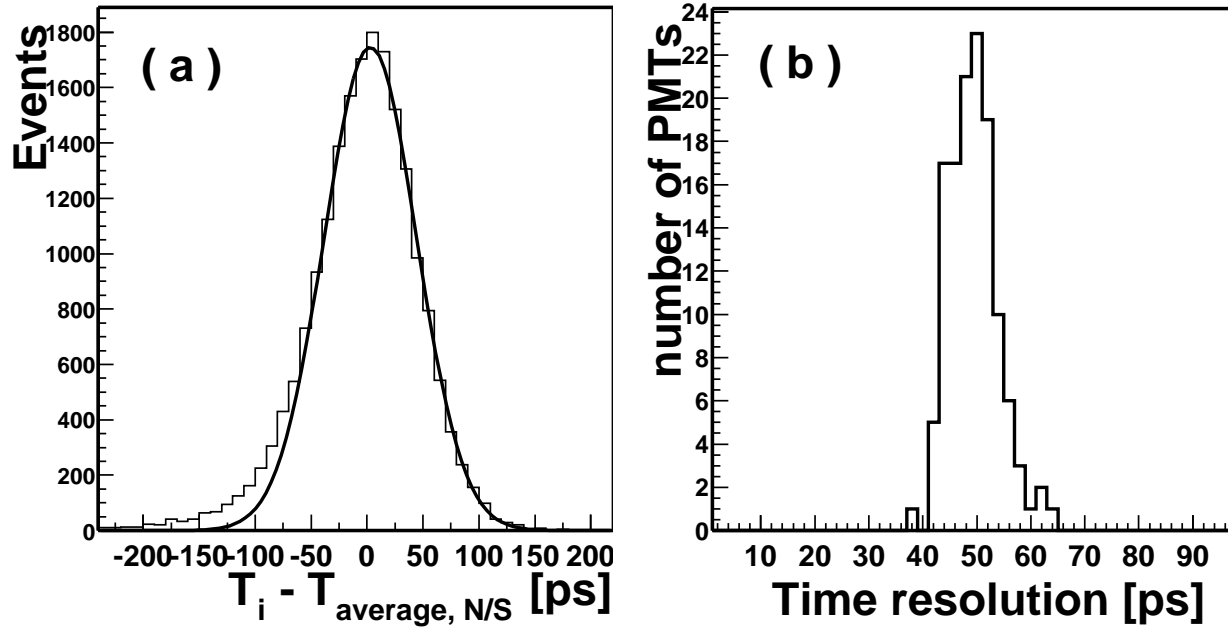
Figure 3.6: (a) The distribution of timing deviation for a typical BBC element from averaged hit timing of all BBC element. (b) The profile of the timing resolution for each BBC element.

Figure 3.7: The ZDC location. A)Top view and B)beam view of ZDC location. Charged fragments are bended by Dipole Magnets towards the outside of the acceptance of ZDC.

Each ZDC consists of 27 layers of tungsten absorbers and fibers which are connected to a PMT (Hamamatsu R329-2). Taking the correlation between North and South provides the background rejection due to single-beam interaction with the residual gas in the beam pipe. The energy resolution of ZDC was obtained to be $\delta E/E \simeq 218/\sqrt{E(\mathrm{GeV})}$ % from the test beam results.

3.4 The Central Magnet

The PHENIX Central Magnet (CM) provides the axial field of $\int B \cdot dl = 0.78$ T·m at $\theta = 90$ degrees. It is used to determine the momentum of charged particles using magnetic bending. The CM is energized by two, inner and outer, pairs of concentric coils, which can be operated separately, with the same polarities or opposite polarities. In RUN Year-2005 and Year-2006, the same polarity operation was chosen. The operation is called as CM++ or CM- - according to the polarity of the magnetic field. The magnetic field produced by the magnets is shown in Figure 3.8. The pole faces of the magnet are positioned at ± 45 cm in z direction covering the rapidity range of ± 0.35. The CM pole tips also serve as the hadron absorbers for the muon spectrometers.

Figure 3.8: The field lines of the central magnet and muon magnets shown on a vertical cutaway drawing of the PHENIX magnets. The beams travel along the $r = 0$-axis in this figure and collide at $r = z = 0$. Arrows indicate the field direction

3.5 The Central Arms

The PHENIX central arms are designed to detect charged particles and photons. The central arm consists of tracking devices, particle identification devices, and calorimetry devices. In this section, the details about central arm devices are reviewed.

3.5.1 Drift Chambers (DC)

The Drift Chambers (DC) are used to measure the charged particle trajectories in $r - \phi$ plane and to provide the high resolution momentum determination. The requirements for DC are (1) single wire resolution better than 150 μm in r-ϕ, (2) single wire two track separation better than 1.5 mm, (3) single track efficiency greater than 99 %, and (4) spatial resolution in z-direction better than 2 mm.

The DC system consists of two independent gas volumes located in the west and east arms, respectively. DC's are filled with the gas mixture of 50 % Argon and 50 % Ethane. The DC's are placed between 2.02 and 2.46 m in radial distance from the interaction point for both West and East arm. They occupy 180 cm in z-direction and 90 degrees per arm in azimuth.

Figure 3.9 (a) shows the construction of a cylindrical titanium frame of a DC. Each DC consists of 20 sectors, each of which covers 4.5 degrees in azimuth. In each sector, there are six types of wire modules stacked radially. They are called X1, U1, V1, X2, U2, V2. The sketch of a sector and the layout of wire position are shown in Figure 3.9 (b).

The X1 and X2 wires run in parallel to the beam axis in order to perform the track measurements in $r - \phi$ plane. They are followed by two sets of small angle U, V wire planes. U1, V1, U2, and V2 wires have stereo angle of about 6 degrees relative to the X wires in order to measure the z-coordinate of the track. The X wire modules contain 12 sense (anode) planes and 4 cathode planes. Both U and V wire modules contain 4 sense (anode) planes and 4 cathode planes. They form the cells with a 2 $\sim$ 2.5 cm drift space in ϕ direction. In this scheme, 40 drift cells are located at different radii in the DC frame.

The DC system contains roughly 6,500 anode wires. Each wires are separated into two halves by the Kapton support at $z = 0$, and the signals are independently extracted. Thus, the number of total readout channel is 13,000. The anode wires are separated by Potential (P) wires and surrounded by Gate (G) and Back (B) wires. The P wires form a strong electric field and separate sensitive regions of individual anode wires. The G wires limit the track sample length to roughly 3 mm and terminate the unwanted drift line. The B wire has a rather low potential and terminates most of the drift lines from side.

With a 50-50 mixture of argon-ethane gas, the stable drift velocity plateau at 53 mm/μs is achieved for the field gradation from 800 V cm up to 1.4 kV cm. Therefore, the maximum drift time in a cell is approximately 470 ns.

3.5.2 Pad Chambers (PC)

The Pad Chambers (PC) is used to determine the space points which are used for momentum determination in the z direction(p_z). The PC's are the multi-wire proportional chambers with cathode readout that form three separate layers (PC1, PC2, PC3) in the central arm. PC1
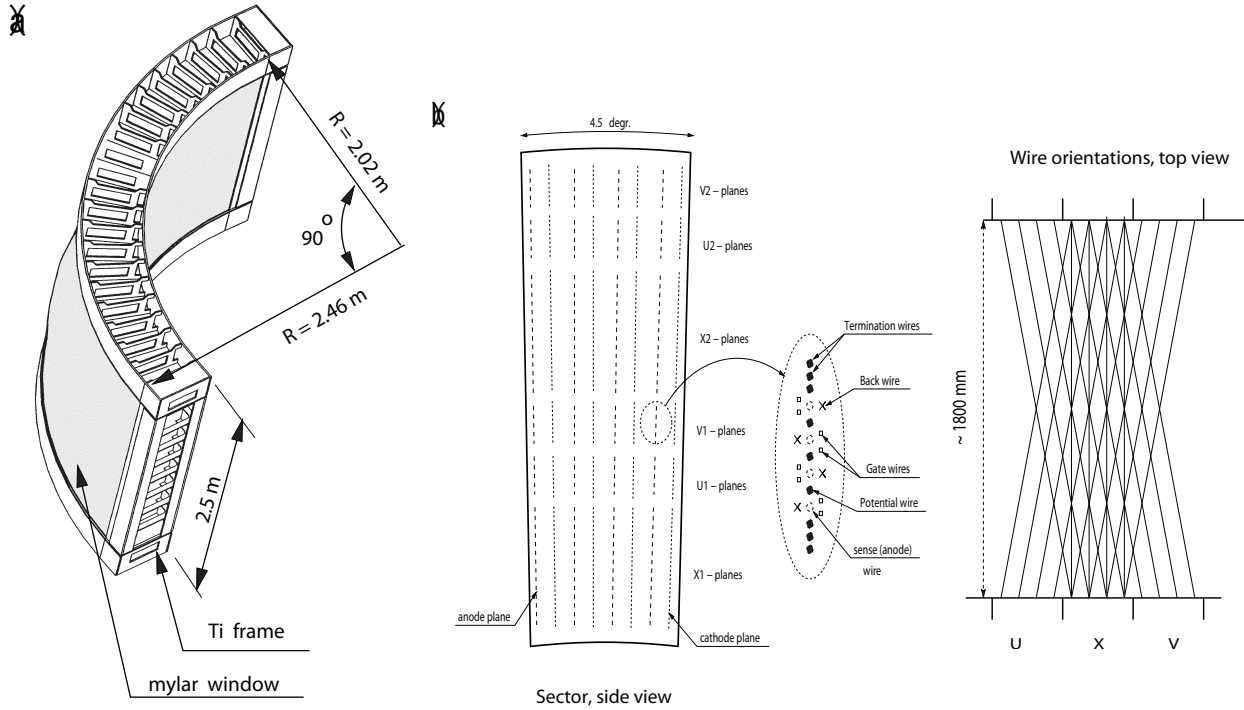
Figure 3.9: (a) The construction of a DC frame. (b)The layout of wire position within one sector of DC.

layer is innermost chamber located between DC and RICH, occupying 2.47 m through 2.52 m in radial distance from the interaction point, PC2 layer is placed behind RICH occupying 4.15 m through 4.21 m, and PC3 is located in front of EMCal occupying 4.91 m through 4.98 m. PC1 is essential for determination of the three dimensional momentum by by providing the z coordinate at the exit of the DC. The combination of DC and PC1 information provides the direction vector through RICH. PC2 and PC3 are needed to resolve ambiguities in outer detectors where about 30 % of the particle striking the EMCal are produced by either secondary interactions and the particle decays outside the aperture of DC and PC1.

Each detector consists of a cathode panel, single plane of anode and field wires. Figure 3.10 shows the vertical cut through of a PC. Each panel is fabricated as an FR4-honeycomb-FR4 sandwich. The wires are lying in a gas volume between two cathode planes. The gas was chosen to be the mixture of 50 % Argon and 50 % Ethane at atmospheric pressure. One cathode is finely segmented into an array of pixels as shown in Fig. 3.11. The position resolution was measured to be ±1.7 mm for PC1 along the wire (z-direction).

3.5.3   Ring Imaging Cherenkov detectors (RICH)

The Ring Imaging Cherenkov detectors (RICH) are the primary devices for the electron identification in PHENIX [93]. They are threshold gas type Cherenkov detector and provides e/π separation below the pion Cherenkov threshold, which is set at 4.85 GeV/c . Figure 3.12 shows
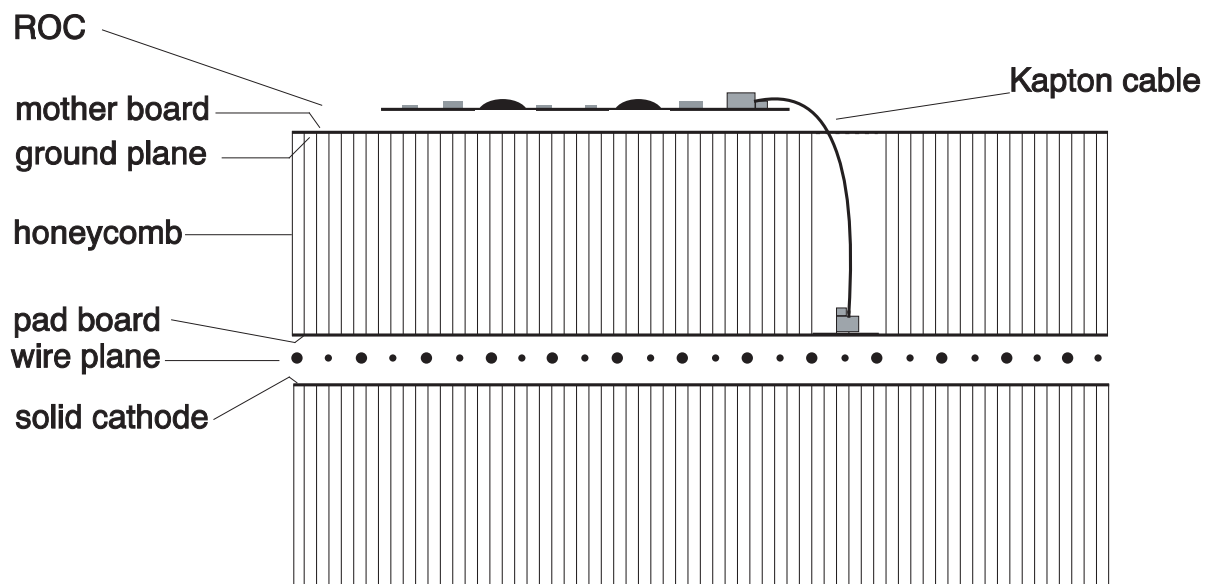
Figure 3.10: The vertical cut through a PC.
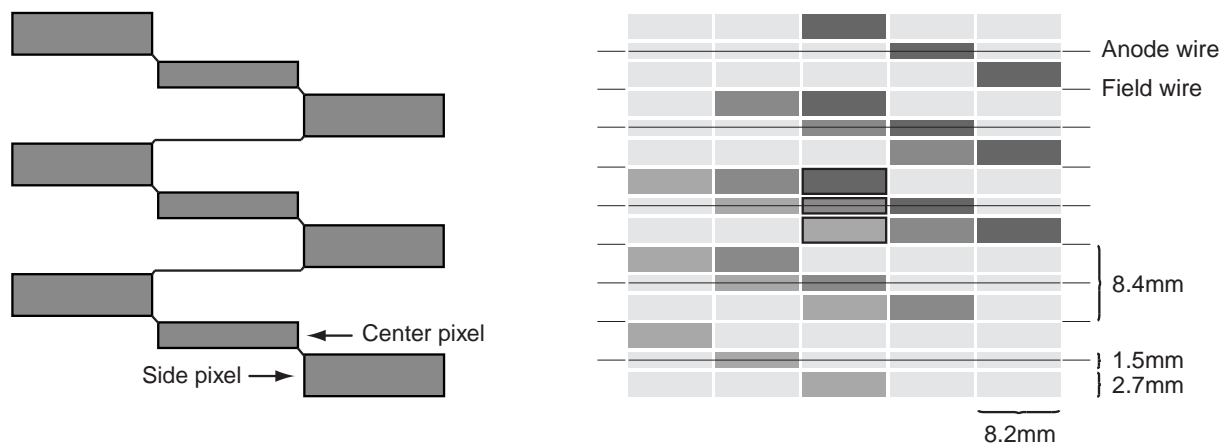
Figure 3.11: The pad and pixel geometry(left). A cell defined by three pixels is at the center of the right picture

the cut-away view of a RICH detector. The RICH is placed between 2.5 m and 4.1 m in radial distance from the interaction point for both West and East arm. They cover the 70 to 110 degrees in polar angle, and 90 degrees per arm in azimuth. Figure 3.13 shows a schematic view of the RICH. In the RICH gas vessel, charged particles moving faster than the speed of light in the gas emit Cherenkov photons. The emitted photons are reflected and focused by the spherical mirror on the plane of phototube array. Radiator gas filled in the RICH is CO_2 gas at 1 atm. RICH have the pion rejection power at the order of 10^4 for single track. In high multiplicityenvironment, there are the source of miss identification such as ring sharing.

Each gas vessel is fabricated from aluminum, and has a volume of about 40 m^3. The entrance and exit windows are made of aluminized Kapton with 125 μm thick.

In each gas vessel, two arrays of 24 aluminum-evaporated mirror panels are mounted on the graphite-epoxy mirror support. The arrays are located symmetrically about $z = 0$. The shape of each mirror is a section of a sphere of radius 4.0 m, whose center is located at $|z| = 2.0$ m.

The Cherenkov photons emitted by the charged particles are reflected by the mirrors, and detected by two arrays of 1280 Hamamatsu H3171S UV photomultiplier tubes which are placed behind the Central Magnet in order to avoid the direct hit of the particles [95].

The PMT has a bi-alkaline photocahode and a linear-focussed 10 stage dynode. It is equipped with 2 inch ϕ Winston cones and magnetic shields that allow the operation under the magnetic field of 100 G. In total, RICH have 5120 PMT's (2 (arm) $\times$ 2 (side) $\times$ 16 (θ) $\times$ 80 (ϕ)). The angular segmentation is approximately 1° $\times$ 1° in θ and ϕ.

The quantum efficiency is about 20 % (5 %) at the wavelength of 300 nm (200 nm). The typical dark current is 10 nA. The typical operation voltage of PMT is 1.4 kV $\sim$ 1.8 kV and the gain is $\sim 10^7$.

The RICH Frond-End Electronics (FEE) processes the signal from 5120 PMT's in total at each bunch crossing (9.4MHz) and transmits digitized data to the PHENIX data acquisition system on the trigger signal supplied by the PHENIX global trigger system ($\sim$25 kHz)[96]. The acceptable charge range is from 0 to 10 photoelectrons, which corresponds to the input charge from 0 to 160 pC preceded by the preamplifier. Charge resolution is $\sim$1/10 photoelectron and timing resolution is $\sim$ 240 ps. Both of the charge and timing outputs are stored in Analog Memory Unit (AMU) clocked at the RHIC bunch crossing frequency. The analog data stored in the AUM are digitized only after the receipt of an acceptance from the PHENIX global trigger system.

3.5.4   Electro-Magnetic Calorimeters (EMCal)

The primary role of the Electro-Magnetic Calorimeters (EMCal) is to provide a measurements of energy and hit position of both photons and electrons [97, 98].

Two kinds of EMCal are installed in PHENIX as shown in Figure 3.2. One is lead-scintillator calorimeter (PbSc) and the other is lead-glass calorimeter (PbGl). Each arm ($\Delta\phi = 90$°) is divided into four sectors in azimuth. The PbGl's occupy the lower two sectors of East Arm and the PbSc occupy other six sectors. The EMCal surface is placed at 510 cm (PbSc) and 550 cm (PbGl) in radial distance from the interaction point.
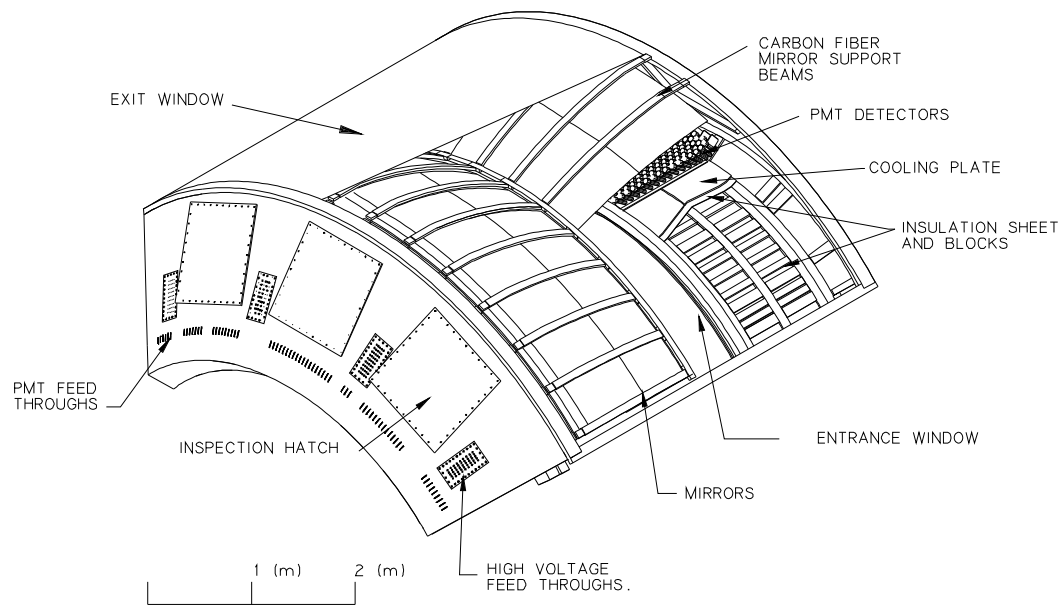
Figure 3.12: The cut-away view of RICH detector.
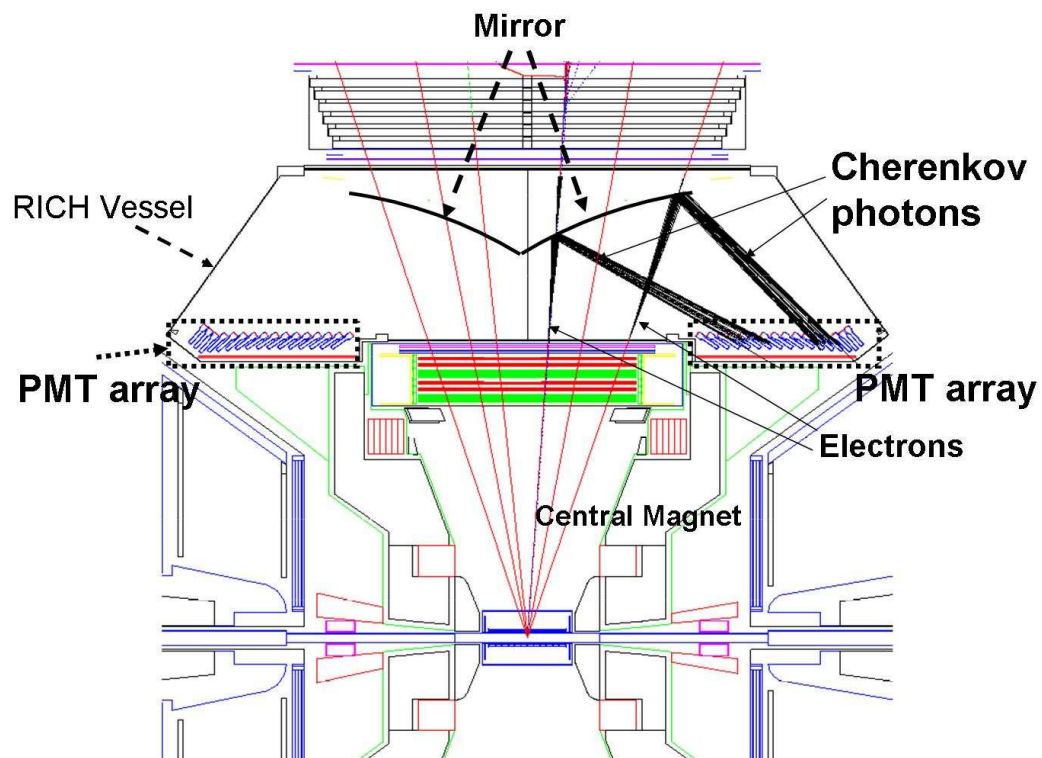
Figure 3.13: A schematic view of the RICH detector

Lead-scintillator calorimeter (PbSc)

The PbSc is a shashlik type sampling calorimeter made of alternating tiles of lead and scintillator. It consists of 15552 individual towers (5.2 cm × 5.2 cm × 37.5 cm). Total radiation length of PbSc is 18.2 X_0 and Moliere radius is ∼ 6 cm. Each tower contains 66 sampling cells: 1.5 mm of lead and 4 mm of injection molded scintillator, ganged together by penetrating optical fibers doped with wave length shifter for light collection. Lights are read out by 30 mmϕ PMT's (FEU115, MELS, Russia) which are implemented at the back of the towers. Figure 3.14 shows a PbSc calorimeter module which is assembled from four towers. The energy resolutions were evaluated as follows from the tests using electron beams:

$$\delta E/E \;=\; 8.1~\%/\sqrt{E(\text{GeV})} + 2.1~\% \quad (\text{PbSc}), \tag{3.4}$$
$$\tag{3.5}$$

The measured position resolution of PbSc depends on both energy E (in the unit of GeV) and impact angle θ ($\theta = 0$ means orthogonal impact). It is expressed as:

$$\sigma_x(E, \theta) \;=\; \sigma_0(E) + \Delta \times \sin\theta, \tag{3.6}$$
$$\sigma_0(E) \;=\; 1.55~\text{mm} + \frac{5.7~\text{mm}}{\sqrt{E(\text{GeV})}}, \tag{3.7}$$

where, σ_0 is the position resolution for orthogonal incidence and Δ is given by the radiation length of ∼ 20 mm.

Lead-glass calorimeter (PbGl)

The PbGl is a Cherenkov calorimeter with 1.648 of index of refraction. It consists of 9216 individual towers (4 cm × 4 cm × 40 cm), which were previously used in WA98 experiment at CERN. Total radiation length of PbGl is 14.4 X_0 and Moliere radius is ∼ 4 cm. Each PbGl sector comprises 192 super-modules (SM) in an array of 16 (wide) by 12 (high). Figure 3.15 shows a PbGl super-module which consists of 24 lead-glass towers in an array of 6 (wide) by 4 (high). At the back of the towers, PMT's (FEU84) are implemented for readout.

The energy resolutions of PbGl were also evaluated as follows from the tests using electron beams:

$$\delta E/E \;=\; 6.0~\%/\sqrt{E(\text{GeV})} + 0.8~\% \quad (\text{PbGl}). \tag{3.8}$$

The measured position resolution of PbGl was:

$$\sigma_x(E) = 0.2~\text{mm} + \frac{8.4~\text{mm}}{\sqrt{E(\text{GeV})}}. \tag{3.9}$$
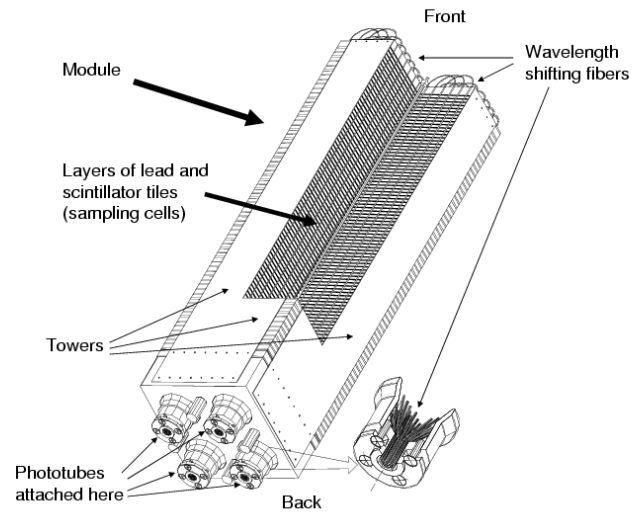
Figure 3.14: Cut-away view of a PbSc module showing a stack of scintillator and lead plates, wavelength shifting fiber.
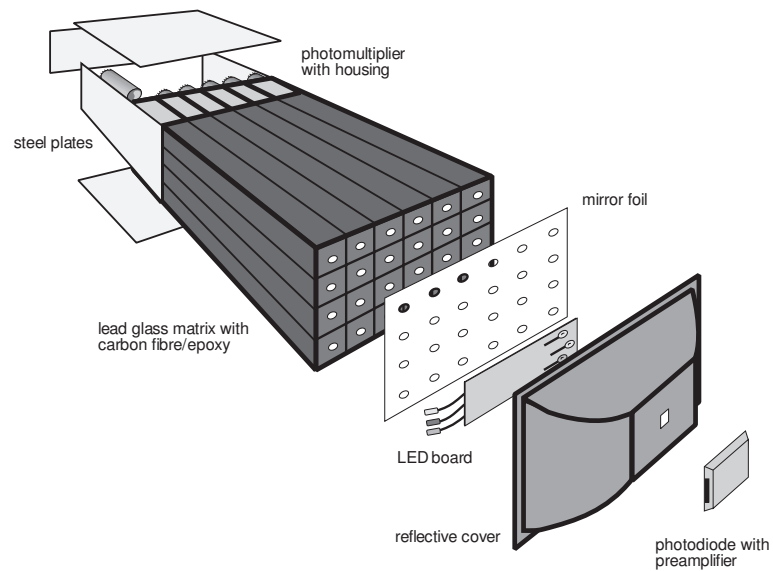
Figure 3.15: A PbGl super-module

3.5.5 Time of Flight Counter (TOF)

The Time of Flight Counter (TOF) provides the measurements of the flight time of the particles. It is a primary particle identification device for charged hadrons and achieves the π/K separation up to 2.4 GeV/c and K/p separation up to 4 GeV/c .

The TOF consists of 10 TOF panels. They are mounted on the east central arm at 510 cm in radial distance from the interaction point, covering the whole η range of the central arm 30 degrees in azimuth. Figure 3.16 shows the sketch of a single TOF panel. A TOF panel consists of 96 segments, each of which is equipped with a plastic scintillator slat and two 19 mmϕ PMT's (Hamamatsu R3478S) at both ends of the slat. The PMT has a bi-alkaline photocathode and a 8 stage linear-focused dynode. The magnetic shielding is provided by μ-metal with an inner diameter of 23 mm. The slat is oriented along the r-ϕ direction and provides the information of time and longitudinal position.
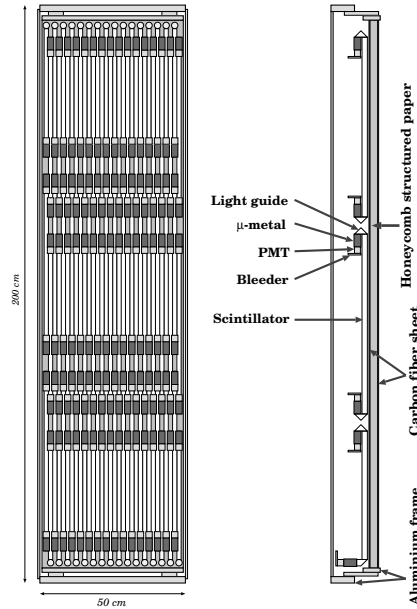
Figure 3.16: The components of single TOF panel.

3.5.6 Aerogel Cherenkov Counters (ACC)

The Aerogel Cherenkov Counters (ACC) is used to identify charged K at high momentum region. A cell of the aerogel Cherenkov counters consists of $22(z) \times 11(\phi) \times 12(r)$ cm^3 aerogel with refractive index of ~ 1.01, an integration cube and two 3-inch phototubes. The aerogel Cherenkov counter covers the region of $22.5°(\phi) \times 0.7(\eta)$.

3.5.7 Time Expansion Chambers (TEC)

The Time Expansion Chambers (TEC) is a transition radiation detector and gives information of charged particle tracking and electron identification by dE/dx and transition radiation. One

TEC sector has an active area of $3.1 - 3.5 m(z) \times 1.7 - 1.9 m(\phi)$ and consists of 6 individual chambers. Each chamber is buled in two layers: one is window support and radiator foils and the other is the active elements of the wire chamber. The chamber is filled with a Xe/CO_2 gas mixture. The TEC covers the region of $90°(\phi) \times 0.7(\eta)$.
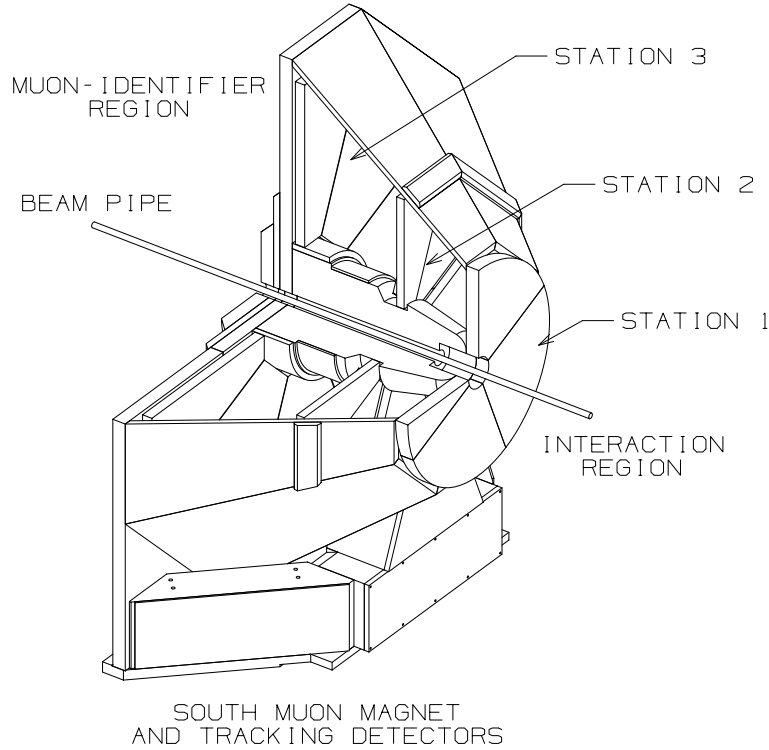
Figure 3.17: The cut-away view of the Muon magnet and the Muon Tracker.

3.6   The Muon Arm

3.6.1   Muon Magnet

The Muon Magnet provides the radial magnetic field. In Figure 3.17, the cut-away view of the Muon Magnet is shown as well as the Muon Tracker which is described in the next section. The central iron "piston" defines the minimum polar angle of spectrometer. The rest of iron yoke consists of an eight-sided "lamp shade", which defines the maximum polar angle. The resulting radial magnetic field has an integral that is roughly proportional to the polar angle.

3.6.2   Muon Tracker (MuTr)

Muon Tracker (MuTr) provides the measurement of the muon track. Figure 3.17 shows the schematic diagram of the MuTr. The MuTr consists of three stations of cathode strip chambers, each of which is the shape of octant built with a 3.175 mm half gap, 5 mm cathode strip and with alternate strips readout. The honeycomb construction is used for station 1 and 3, and thin foil construction is used for station 2 in order to produce a cathode pattern.

Figure 3.18: A picture of the converters.

3.6.3 Muon Identifier (MuID)

Muon Identifier (MuID) is the primary device for muon identification. MuID consists of five layers of chambers interleaved with steel absorbers.

In oder to set the punch-through probability for pions of up to 4 GeV/c to be 3 % or less, a total steel depth of 90 cm, corresponding to 5.4 hadronic interaction length, is required. Subtracting the thickness of the muon magnet backplate, a total depth of 60 cm of steel is required in MuID itself. A muon at the vertex must have a energy of at least 1.9 GeV to reach MuID, and 2.7 GeV to penetrate through MuID .

3.7 Photon Converter

The converter was installed around beam pipe at a part of physics run. The aim of the installation of the converter is to determine the amount of the electrons from γ conversion. Figure 3.18 shows a picture of the converters.

The converter is a thick brass sheet which material budget is well known. The composition of the brass converter is Cu (70 %), Zu (29.88 %), Fe (0.05 %) and Pb (0.07 %). The ideal mass density is 8.5 [g/cm^3]. The tube shape with 3.85 (3.94) [cm] inner (outer) radius, 60.96 [cm] height and 0.0254 [cm] thickness is placed at PHENIX center along with beam axis. The density of the converter was checked by measurement of the area and the weight of a piece of the converter that was installed. The determined area density is 0.215313[g/cm^2]. Thus, the density of the converter is 8.4769 [g/cm^3] because the thickness is 0,0254[cm].

3.8   Trigger

The Level-1 trigger (LVL1) have been designed to ensure a significant fraction of the physics events of interest are recorded, due to the limited speed of PHENIX data acquisition system. The LVL1 trigger is a pipelined and dead timeless system. The triggers consist of two type: One is the Local Level-1 (LL1) system and the other is the Global Level-1 (GL1) system. LL1 system communicates directly with the detectors such as BBC, EMCal and RICH. The input data from these detectors is processed by the following LL1 algorithms to produce a set of reduced input data for each RHIC beam crossing. In this section, BBC LL1 trigger (BBCLL1) and EMCal-RICH LL1 trigger (ERTLL1) are presented in this section. These triggers are designed to select the physics events of interest in this thesis.

3.8.1   BBC LL1 trigger (BBCLL1)

The main trigger for events in PHENIX relies on a coincidence between the two BBC modules. The timing information of BBC is used to determine the position of the collision point. BBC LL1 trigger (BBCLL1) in an event trigger, which requires the event to occur within the nominal interaction region ($| z | < 37.5$ cm). The BBCLL1 is defined as our minimum bias trigger condition for the data in $p + p$ collisions.

3.8.2   EMCal-RICH LL1 trigger (ERTLL1)

EMCal-RICH LL1 trigger (ERTLL1) is used as the electron and high energy photon events. For the photon triggers, on the EMCal information is used. Acceptance coverage of each of the EMCal and RICH is divided into 16 trigger segments. Each segment consists of 9(PbSc)/16(PbGl, RICH) trigger tiles. Each trigger tile consists of 144 EMCal towers (20 RICH phototubes). EMCal has two different methods, 2X2 tower sum and 4×4 tower sum, to sum the energy of towers. The energy threshold value of EMCal for the hit dentition can be changed. If there is a hit tile defined by 4×4 sum (2×2 sum) in the EMCal part, ERTLL1 4×4 (ERTLL1 2x2) is issued. There are 3 versions of this trigger, which differ only in the threshold energy. 4×4a, 4×4b, and 4×4c, as they are named, require respectively a 2.1, 2.8 and 1.4 GeV energy deposit in a 4×4 tower block made up of 4 neighboring basic tiles. These triggers are photon triggers which provide enough rejection power to record all triggered events.

   If there are an EMCal hit tile defined by 2×2 sum and an associated RICH hit tile, an electron trigger, ERTLL1 E is issued. Association of EMCal and RICH tiles is performed using the look-up table in the ERTLL1 module. The GL1 receives and combines the LL1 data to make a trigger decision. The GL1 also manages busy signals.

3.9   The Data Acquisition System

The PHENIX data acquisition system processes the signals from each detector, produces the trigger decision, and stores the triggered data. The typical data logging rate of PHENIX was ∼1 kHz for Au+Au collisions and ∼5 kHz for $p + p$ collisions. The zero-suppressed event sizes
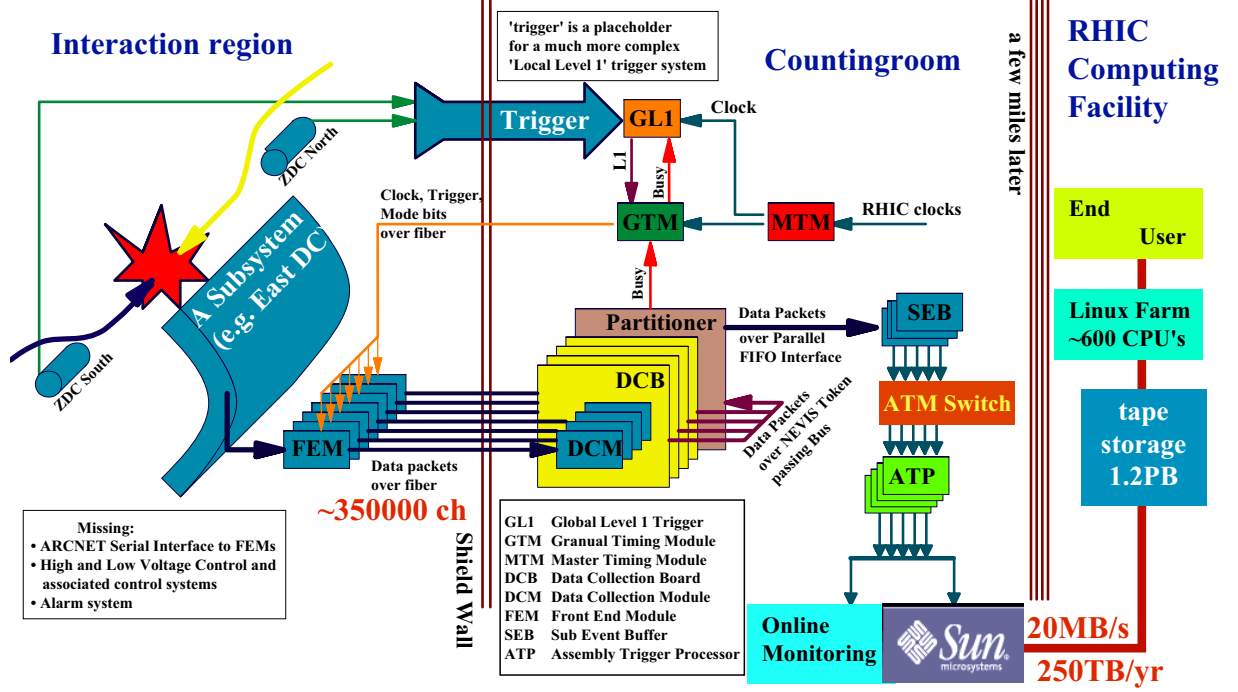
Figure 3.19: Schematic diagram of the data acquisition flow.

are 160 kbytes for Au+Au and 40 kbytes for $p+p$, respectively. The block diagram of the data acquisition flow is shown in Fig. 3.19.

The data acquisition system employs the concept of granule and partition. A granule is smallest unit, which consists of individual timing control and data collection for each detector. The partition is the combination of granules, that share busy signals and accept signals. This configuration makes it possible to run the data acquisition in desired combination of detectors.

Overall control of the data acquisition is provided by the Master Timing Module (MTM), the Granule Timing Module (GTM), and the Global Level-1 Trigger System (GL1). The MTM receives 9.4 MHz RHIC clock and deliver it to GTM and GL1. The MTM also receives LVL1 accept signal. The GTM deliver the clock, the control commands (Mode Bits), event accept signal to each detector's FEM. The GTM is capable of a fine delay tuning of the clock in ~50 ps step, in order to compensate the timing difference among FEM's. The GL1 produces the first Level-1 (LVL1) trigger decision, combining LVL1 signal from detector components.

The FEM of each detector is designed to convert the analog response of the detectors into the digitized signal. The LVL1 trigger signals are simultaneously generated. The generation of global decision, whether event should be taken or not, takes ~30 B.C. While the GL1 system is making decision, the event data is stored in AMU. After receiving the accept signal, each FEM starts to digitize the data.

The data collection from each FEM is performed by Data Collection Modules (DCM) via G-LINK. The DCM's have the capability to receive 100 Gbytes of uncompressed event data

per second at the highest trigger rate. The DCM's provide data buffering, zero suppression, error checking, and data formatting. The DCM send the compressed data to PHENIX Event Builder (EvB).

The EvB is the system which consists of 32 Sub Event Buffers (SEB), Asynchronous Transfer Mode (ATM) switch, and 28 Assembly Trigger Processors (ATP). The SEB's are the front end of EvB and communicate with each granule. The SEB's transfer the data from granules to ATP via ATM, where event assemble is performed. The combined data is once stored to the disk and used for online monitoring and for generation of trigger decision by the second level (LVL2) software trigger.

The data storage is finally provided by HPSS-based tape storage robot system with maximum transfer rate of 20 Mbytes/s. Combining the buffering to local disk, the maximum data logging rate become ∼60 Mbytes/s.

Chapter 4

Run Conditions

4.1   Overview

The recorded data by the PHENIX is summarized at Table 4.1. The analysis in this thesis has been performed using the $p+p$ data sample obtained during the RHIC in Year-2005 run (RUN5) and Year-2006 run (RUN6) period. The beam and trigger conditions are described briefly in this chapter.

Table 4.1: The recorded data summary at the PHENIX

	Year	Species	$\sqrt{s}(GEV)$	recorded luminosity
RUN1	2000	Au-Au	130	$1\mu b^{-1}$
RUN2	2001-02	Au-Au	200	$24\ \mu b^{-1}$
		p-p	200	$0.15\ pb^{-1}$
RUN3	2002-03	d-Au	200	$2.74\ nb^{-1}$
		p-p	200	$0.35\ pb^{-1}$
RUN4	2003-04	Au-Au	200	$241\ \mu b^{-1}$
		Au-Au	62.4	$9\ \mu b^{-1}$
RUN5	2005	Cu-Cu	200	$3\ nb^{-1}$
		Cu-Cu	62.4	$0.19\ nb^{-1}$
		Cu-Cu	22.4	$2.7\ \mu b^{-1}$
		p-p	200	$3.8\ pb^{-1}$
RUN6	2006	p-p	200	$10.7\ pb^{-1}$
		p-p	62.4	$0.1\ pb^{-1}$
RUN7	2007	Au-Au	200	$813\ \mu b^{-1}$

4.2   Collisions in $p + p$ at $\sqrt{s}$=200GeV in 2005 and 2006

During the polarized proton run period in the RHIC RUN5 (April 16, 2005- June 24,2005) and the RHIC RUN6 (March 4, 2006-June 5, 2006), p + p collisions at $\sqrt{s}$ =200 GeV were

collected with the PHENIX detector. The mode of 111 bunch was used and there were 1.3×10^{11}
protons in each bunch. The peak luminosity was 3.5×10^{31} cm^{-2} s^{-1}. The delivered integrated
luminosities of p + p collisions in RUN5 and RUN6 are shown as a function of date in Figure 4.1
and Figure 4.2, respectively. The recorded integrated luminosities are 3.8 pb^{-1} (RUN5) and
10.7 pb^{-1} (RUN6).

The data for the analysis was taken with the 'Minimum Bias (MB)' trigger and the 'ERT'
trigger. The 'ERT' trigger consists of ERT electron and ERT photon trigger. The trigger logic
of the MB, ERT electron and ERT photon triggers for the $p + p$ collisions are defined as:

$$\text{Minimum} \quad \text{Bias} \quad \equiv \quad \text{BBCLL1}(> 0\text{tubes}), \tag{4.1}$$

$$\text{ERT} \quad \text{electron} \quad \equiv \quad \text{ERTLL1\_E} \cap \text{BBCLL1}(> 0\text{tubes}), \tag{4.2}$$

$$\text{ERT} \quad \text{photon} \quad \equiv \quad \text{ERTLL1\_4x4i} \cap \text{BBCLL1}(> 0\text{tubes}), (i = a, b, c) \tag{4.3}$$

where BBCLL1($>$ 0 tubes) means that at least one hit is required in each BBC and the vertex
position obtained by BBCLL1 online in z direction, zBBCLL1, is required to be less than 37.5
cm. ERTLL1_E denotes the coincidence of a EMCal hit with energy deposit above the ERTLL1
2x2 threshold and a RICH hit of ≥ 3 photoelectrons. ERTLL1_4x4i denotes the EMCal trigger
with 4x4 tower sum. 4x4a, 4x4b and 4x4c mean different energy thresholds. The threshold
values of these ERTLL1 4x4 triggers are 2.1 GeV (4x4a), 2.8 GeV (4x4b) and 1.4 (4x4c) during
RUN5 and RUN6 p + p 200 GeV periods. The threshold value of ERTLL1 2x2 trigger is shown
in Table 4.2.

Table 4.2: RUN summary of the RUN5 and RUN6 $p + p$ 200GeV periods

RUN	polarization	RUN number	Magnet polarity	ERT 2x2 threshold	Converter
RUN5	longitudinal	166030-171594	CM- -	0.4GeV	Without
RUN5	longitudinal	171595-172080	CM- -	0.4GeV	With
RUN5	longitudinal	172081-179846	CM- -	0.4GeV	Without
RUN6	transverse	188216-197795	CM++	0.4GeV	Without
RUN6	longitudinal	198061-199767	CM++	0.4GeV	Without
RUN6	longitudinal	200240-204639	CM++	0.6GeV	Without
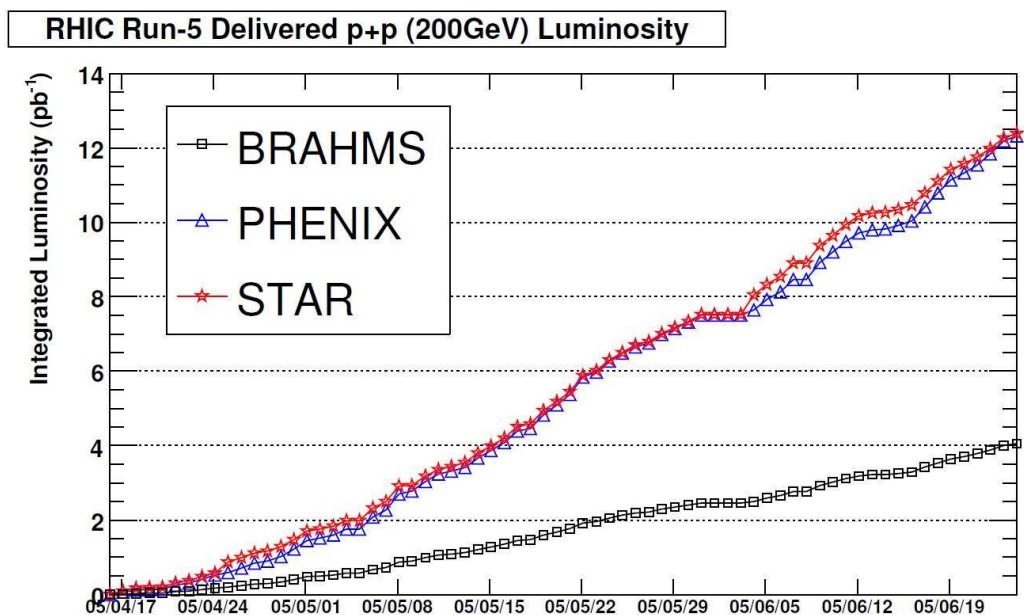
Figure 4.1: The delivered integrated luminosities of p + p collisions in RUN5 as a function of date
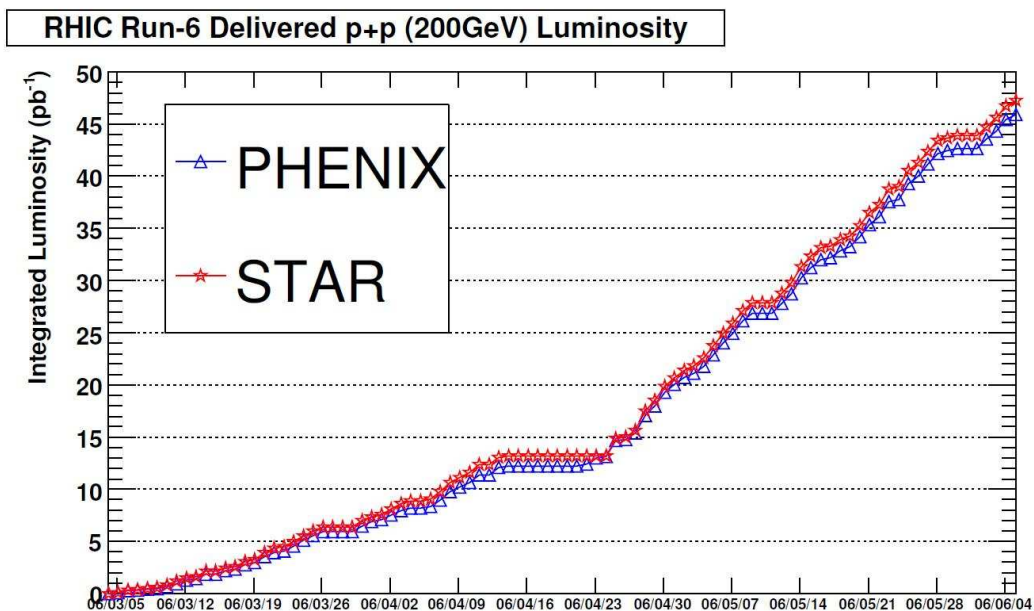
Figure 4.2: The delivered integrated luminosities of p + p collisions in RUN6 as a function of date

Chapter 5

Data Analysis

This chapter describes the data analysis to extract the electron samples from semi-leptonic decay of charm and bottom, so called as 'single non-photonic electron', in $p + p$ collisions at $\sqrt{s} = 200$ GeV. The data taken with the 'Minimum Bias' trigger (MB data) and the data taken with the 'ERT' trigger (ERT data) is used to the analysis. Specially, the data taken with 4x4c ERT photon trigger (PH data) in ERT trigger is used to determine the total yield of the electrons from semi-leptonic decay of heavy flavor.

The analysis procedure is following.

1. Inclusive electron spectrum is measured in RUN5 and RUN6 data. (Sec. 5.1 - Sec. 5.5)

2. The spectrum of single electrons from heavy flavor is measured by subtraction of background electrons. The contribution of background electrons is evaluated by 'converter method' and 'cocktail method'. (Sec. 5.6)

3. The fraction of bottom contribution in single electrons is determined by using the correlation in electron-hadron pairs. (Sec. 5.7 - Sec. 5.10)

The formalization of invariant yield is described in Sec. 5.1. Sec. 5.2 describes reconstruction and momentum determination of charged particles by using DC and PC. Sec. 5.3 describes the method of electron identification by using EMCal and RICH. Selection of runs used for this analysis is described in Sec. 5.4. In Sec. 5.5, reconstruction efficiency of electrons and PH trigger efficiency are determined. Then inclusive electron spectrum is measured in RUN5 and RUN6 data.

The spectrum of single electrons from heavy flavor is determined by 'converter method' and 'cocktail method' in RUN5 and RUN6 data in Sec. 5.6.

Sec. 5.7 describes a new analysis method to determine the fraction of bottom contribution in single electrons. The method uses the correlation in electron-hadron pairs in real data and simulation. The correlation in electron-hadron pairs in real data is studied in Sec. 5.8 and that in simulation is studied in Sec. 5.9. In Sec. 5.10, the correlations in real data and simulation are compared to obtain the fraction of bottom.

5.1 Invariant Yield

The invariant yield in Lorentz invariant form can be written as,

$$E\frac{d^3\sigma}{dp^3} = \frac{d^3\sigma}{p_T dy dp_T d\phi} = \frac{d^2\sigma}{2\pi p_T dp_T dy},$$ (5.1)

where p is the momentum of the particle, y is the rapidity, $p_T = \sqrt{p_x^2 + p_y^2}$ is the transverse momentum, and ϕ is azimuthal angle.

The goal of this analysis is to obtain the invariant yield $d\sigma/dy$, differential cross section $d^2\sigma/dydp_T$ of the electrons from semi-leptonic decay of charm and bottom at mid-rapidity. Using the number of measured electrons, $d^2\sigma/dydp_T$ of the electrons can be extracted experimentally as follows.

$$\frac{1}{2\pi p_T}\frac{d^2\sigma}{dydp_T} = \frac{1}{2\pi p_T}\frac{N_e(p_T)}{\int Ldt\epsilon(p_T)\epsilon_{bias}\Delta p_T\Delta y},$$ (5.2)

where

- $N_e(p_T)$ is the number of reconstructed electrons in a p_T bin

- ϵ_{bias} is BBC trigger bias

- $\epsilon(p_T)$ is the overall efficiency including acceptance, reconstruction efficiency and trigger efficiency

- Δy is the rapidity bin width and is set to $\Delta y = 1$

- Δp_T is the p_T bin width

- $\int Ldt$ is the integrated luminosity.

5.1.1 Integrated Luminosity

The integrated luminosity can be expressed using the number of minimum bias (MB) triggered events (N_{MB}).

$$\int Ldt = \frac{N_{MB}}{\sigma_{p+p}\epsilon_{BBC}^{p+p}},$$ (5.3)

where σ_{p+p} is the cross section of inelastic $p+p$ collisions at $\sqrt{s} = 200$GeV, and ϵ_{BBC}^{p+p} the BBC trigger (MB trigger) efficiency. The MB trigger cross section in $p+p$ collisions, which is defined as $\sigma_{p+p}\epsilon_{BBC}^{p+p}$, has been determined to be 21.8± 2.1 mb, by using a van der Merr scan measurement in RUN2 [101]. The MB trigger cross section in RUN5 and RUN6 is determined to be the 23.0± 2.2 mb by making correction of BBC efficiency to take into account the change of BBC mask [99, 100].

The equivalent number of sampled minimum bias events in the data taken with 4x4c ERT photon trigger (PH data), N_{MB}^{sample} instead of N_{MB} is used to obtain the integrated luminosity of PH data set. The *scale_down_factor* of 4x4c photon (PH) trigger, which represents the fraction of recorded MB events in triggered PH events, is determined and recorded at each run. N_{MB}^{sample} is determined as *scale_down_factor* $\times N_{MB}$.

5.1.2   BBC Trigger Bias

BBC trigger bias, ϵ_{bias} is PHENIX-specific term referring to the probability that the BBC counter makes MB trigger for an event containing specific particle of interest due to the acceptance of the BBCs. It is obvious that events with a hard parton scattering have higher probability of making BBC MB trigger because the track multiplicity in the BBC is higher for these events. This means that of all events that contain a hard scattering process, The apparent cross section of events which contain hard scattering will be higher than the BBC trigger cross section, $\sigma_{p+p}\epsilon_{BBC}^{p+p}$. The fact that the trigger cross section depends upon the physics process is what we term 'bias'.

ϵ_{bias} is determined to be 0.79±0.02 as the p_{T} independent fraction for hard scattering process, from the yield ratio of high p_{T} π^0 with and without the BBC trigger [101]. This measured value of the constant BBC trigger bias is in good agreement with PYTHIA calculations of the BBC efficiency for hard pQCD partonic scattering processes.

5.2   Reconstruction of Track and Momentum

5.2.1   Variables for Particle Trajectory Measurements
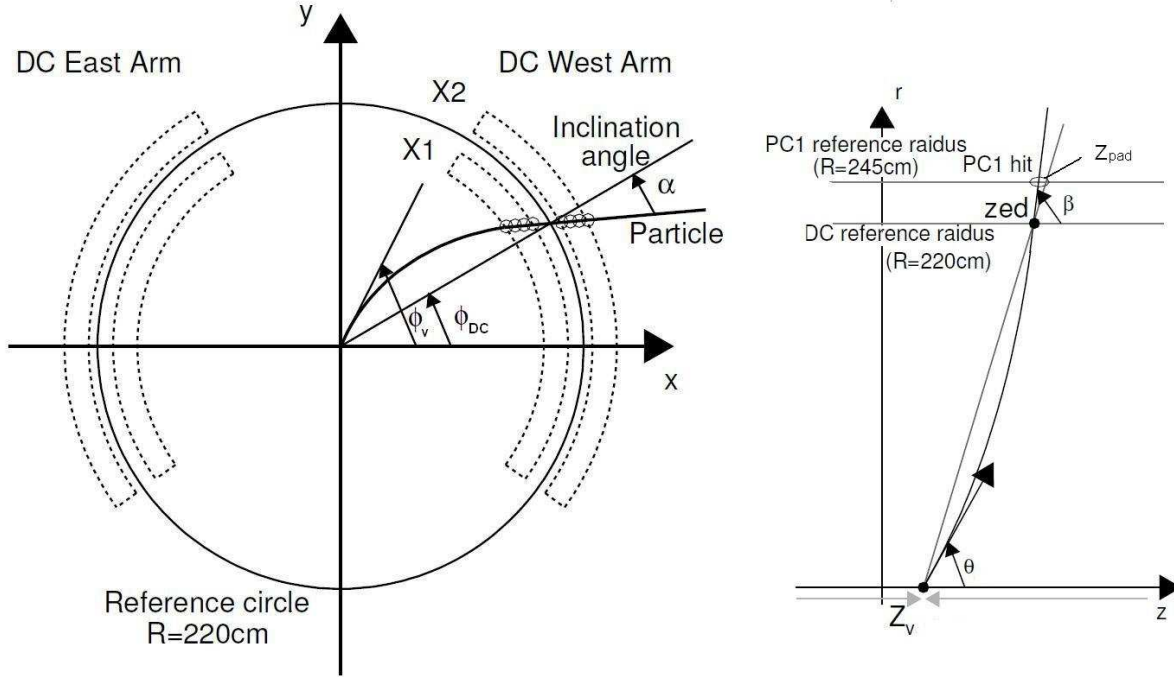
Figure 5.1: A particle trajectory and the parameters used in the track reconstruction are shown in Left: beam view and RIGHT:side view of PHENIX central

The detailed explanation about the track reconstruction technique in PHENIX can be found in published papers [102, 103]. The essential parts are explained in this section.

Figure 5.1 shows a particle trajectory in PHENIX up to PC1 and the definition of parameters, which are introduced in order to describe the charged particle trajectory traveling through the axial magnetic field. The variables are summarized as follows:

- Measured variables

  - α : The angle between the projection of trajectory in the $x - y$ plane and the radial direction, at the intersection point of the trajectory with the circle of reference radius $R_{DC} =$ 2.2 m..

  - β : Considering the plane which includes the z-axis and z_{pad}, β is defined as the angle between the projection of trajectory onto that plane and the z-axis.

  - z_{pad} : The intersection point of the trajectory with PC1 surface radius $R_{PC1} =$ 2.45 m, .

  - ϕ_{DC} : The ϕ-angle of intersection point of particle trajectory with the circle of radius with R_{DC}.

- Variables to be reconstructed

  - θ_v : The angle between the initial direction of the particle trajectory and z-axis.

  - ϕ_v : The initial azimuthal angle of the particle trajectory.

  - p_{T} : The transverse momentum.

5.2.2 Track and Momentum Reconstruction Technique
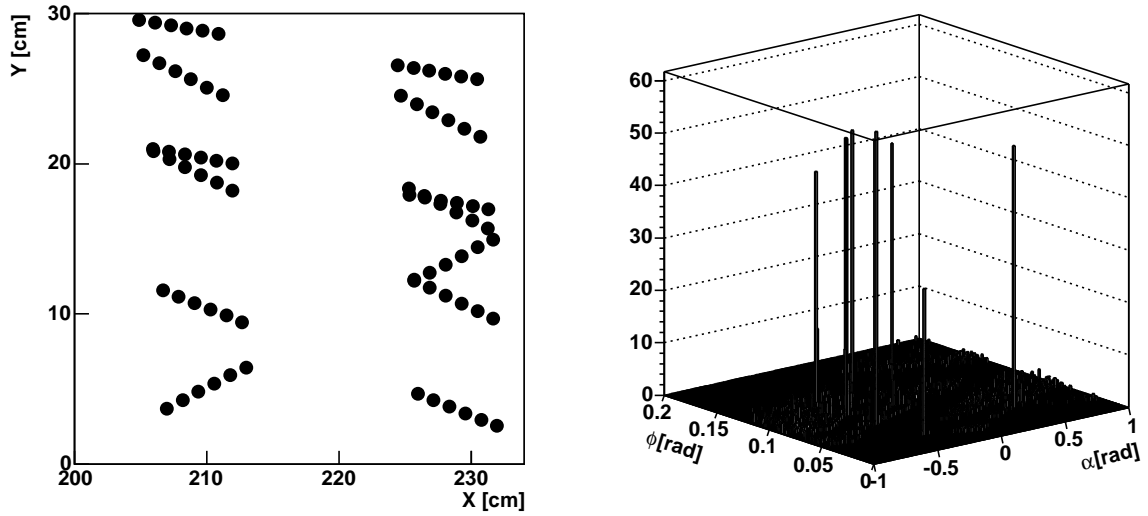
Figure 5.2: The Hough transformation of the DC hits in the x-y plane to the feature space of α and ϕ. The left panel shows simulated hits for a small physical region of the drift chamber. The right panel shows the Hough transform feature space for this region. Tracks appear as peaks in this plot.

The intersection of particle trajectory with various detector planes is uniquely determined by three variables: θ_v, ϕ_v, and p_{T}. They are reconstructed from the measured variables: α, β, z_{pad}, ϕ_{DC} and vertex information. The collision vertex is assumed to be (0,0) in x-y plane in PHENIX and z position of the vertex is determined by the timing information of BBC as described at Sec. 3.3.1. Hough Transform technique is used for the track reconstruction. The Hough Transform is a general algorithm for finding straight lines. It is popular in image processing. Figure 5.2 shows a simple example of Hough Transform in a part of the DC hits. In case of PHENIX, track reconstruction started from finding the hits in X1 and X2 wires.

1. Project the drift chamber hits onto $x - y$ $(r - \phi)$ plane at $z = 0$.

2. Perform the Hough Transform using all possible X1-X2 hit combinations taking α and ϕ_{DC} as the parameters in Hough Space. For example if there are 6 hits in X1-wires and 6 hits in X2-wires, total 36 combination are taken.

3. Associate X-wire hits with the reconstructed track.

4. Perform a Hough Transform of the UV-wires and associate the resulting UV hits with the reconstructed track in order to obtain the z information.

5. Associate PC1 hit.

The α measured in the drift chamber is closely related to the field integral along the track trajectory. The transverse momentum, $p_T(\text{GeV}/c)$ and the α-angle (mrad) have the following approximate relation:

$$p_T \sim \frac{K}{\alpha},\tag{5.4}$$

where $K \sim 0.10$ [rad GeV/c] is the effective field integral, expressed as :

$$K = \frac{e}{R} \int lBdl.\tag{5.5}$$

Here, e is the elementary charge in the hybrid unit (e=0.2998 GeV/c T^{-1}m^{-1}) and R is the DC reference radius.

However, due to the small non-uniformity of the focusing magnetic field along the flight path of charged particles, an accurate analytical expression for the momentum of the particles is not possible. Therefore, the non-linear grid interpolation technique is used [104]. A four-dimensional field integral grid is constructed within the entire radial extent of the central arm for momentum determination based on drift chamber hits. The parameters of the field integral are momentum p, polar angle at the vertex, θ_v, z-vertex, and radial distance r at which the filed integral $f(p, r, \theta_v, z)$ is calculated. The field integral grid is generated by explicitly swimming particles through the magnetic field map from survey measurement and numerically integrating to obtain for $f(p, r, \theta_v, z)$ each grid point. An iterative procedure is used to determine the momentum for reconstructed tracks, using Eq. 5.4 as an initial guess. The initial estimate of θ_v is given by the z-vertex and DC hit position.

Each reconstructed track is associated with hit information of outer detectors (PC2,PC3, EMCal and RICH). In the association with the outer detectors, the residual magnetic field is not taken into account and the track is assumed to be a straight line.

The momentum resolution depends on (1) the intrinsic angular resolution of the DC and (2) the multiple scattering of a charged particle as it travels up to DC due to the intervening material. As a result, the momentum resolution is about 1% for tracks with p_T=1 GeV/c and the reconstruction efficiency is above 99% for a single track.

5.2.3 Track Quality

The quality of a reconstructed charged track is defined using hit information of X and UV wires in the DC and the associated PC1 hit. This information is implemented in the data of reconstructed tracks as the 6-bit variable, quality, for each track. Table 5.1 is the definition of quality. The best case is quality = 63 and the second best case is quality = 31, where the PC1 hit is ambiguous, but the UV hit is unique.

Table 5.1: The bit definition of quality variable.

bit		decimal	description
LSB	0	1	X1 hits used
	1	2	X2 hits used
	2	4	UV hits found
	3	8	Unique UV. (No hit sharing)
	4	16	PC1 hits found
MSB	5	32	Unique PC1 (No hit sharing).

5.2.4 Analysis Variables

The information of the reconstructed track and the associated hits of the detectors are recorded in so called nano Summary Data Tape (nDST) in PHENIX. Parameters which characterize events, such as the collision vertex and centrality, are also recorded in the nDST. In this thesis, the variables in the nDST are written in Sans serif font. For example, there are the total momentum mom, initial polar angle the0 and initial azimuthal angle phi0 etc. The z position of the collision point measured at BBC counter is defined as bbcz. The variables about track reconstruction which are used in this thesis are summarized at Table 5.2

Table 5.2: The track variables used in the analysis.

Variable	Description
bbcz	The z position of the collision point measured at BBC counter.
mom	Total momentum of the reconstructed track.
phi0	This is the initial ϕ direction of the track at the vertex.
the0	This is the initial θ direction of the track at the vertex.
alpha	The angle between the track in the DC $x - y$ plane and the radial direction.
beta	θ angle of the track vector as it passes through the DC reference radius.
quality	The quality of the Drift Chamber Tracks.
phi	ϕ coordinate at which the track crosses the DC reference radius.
zed	z coordinate at which the track crosses the DC reference radius.
pc1phi	ϕ coordinate of the measured hit in PC1.
pc1z	z coordinate of the measured hit in PC1.
pc3phi	ϕ coordinate of the measured hit in PC3.
pc3z	z coordinate of the measured hit in PC3.
emcphi	ϕ coordinate of the measured hit in EMCal.
emcz	z coordinate of the measured hit in EMCal.
pemcphi	ϕ coordinate of the reconstructed track projection at EMCal surface.
pemcz	z coordinate of the reconstructed track projection at EMCal surface.

5.3   Electron Identification

Electron identification is performed for the reconstructed particles by RICH and EMCal and is described in this section.

5.3.1   Summary of Variables

The electron identification (eID) is performed by combining the information from tracking, RICH, and EMCal. The variables used in the analysis are summarized in Table 5.3. The details are explained in succeeding sections.

Table 5.3: The eID variables used in the analysis.

Variable	Description
RICH	
n0	The number of fired phototubes in the nominal ring area (3.8[cm]<r< 8.0[cm])
n1	The number of fired phototubes in the larger ring (r< 11.0[cm])
npe0	The number of photo electrons detected in nominal ring radius
disp	Displacement between the projection point on the RICH phototube plane and the centroid of the associated fired phototubes
chi2	Ring shape calculated from hit PMT's in the nominal ring radiusZ
EMCAL	
ecore	The shower energy detected at EMCal(summed up 3×3 towers)(GeV)
emcsdphi_e	The difference between the track projection and the EMCal cluster position in the ϕ direction at EMCal surface normalized by σ
emcsdz_e	The difference between the track projection and the EMCal cluster position in the z direction at EMCal surface normalized by σ
prob	The probability for a shower being a EM shower from the shower shape in EMCal

5.3.2   Electron Identification with RICH

RICH Calibration

Gain calibration is performed for each phototube by fitting the raw ADC spectrum. Gaussian functions are used to fit the pedestal peak and the one photo-electron peak, and those peak positions ($ADC_{pedestal}$ and $ADC_{1p.e.}$) are obtained. Using these values, the number of photo-electrons ($N_{p.e.}$) of the phototube is calculated from its ADC value (ADC) as follows:

$$N_{p.e.} = \frac{ADC - ADC_{pedestal}}{ADC_{1p.e.} - ADC_{pedestal}}. \tag{5.6}$$

Figure 5.3 shows the distribution of the number of photo-electrons in each phototube. The simultaneous Gaussian fit to the peaks gives the one photo-electron peak position of 1.034 ± 0.003 and the width of 0.259 ± 0.003, respectively. The hit phototube in RICH is defined to have greater than 0.2 photo-electron.
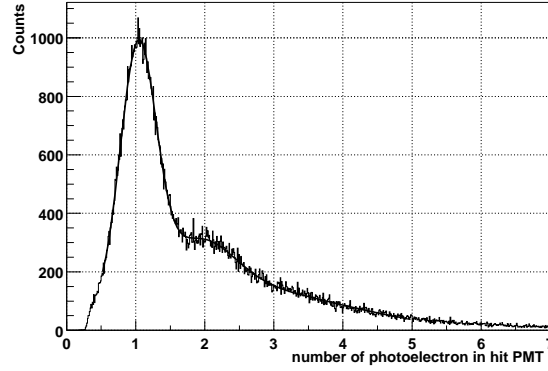
Figure 5.3: The distribution of the number of photo-electrons in each hit phototube.

Track - RICH Ring Association : n0, npe0, disp

After the track reconstruction with DC and PC1 (DC-PC1 track), the tracks are associated with the PC2, PC3 and EMCal. The hit positions of the outer detectors or projection points of the DC-PC1 track if any associated hit is not found are used for the association with RICH. The tracks are projected with respect to the RICH mirror and the reflected tracks are projected onto the RICH phototube plane. Then, fired phototubes around the projection points of the reflected tracks are associated with the tracks.

Figure 5.4 shows a part of the phototube array surface with the definition of the variables which characterizes the association between a track and hit phototubes in RICH. A reconstructed track projection vector which is reflected by the mirror, track projection position at the phototube array surface (R_0), hit phototube's 1–5, and hit phototube position vector (R_i) are shown.

The distances between the center of hit phototube R_i and the track projection vector is calculated as r_{cor}^i (r_{cor}^1 and r_{cor}^3 in Fig. 5.4, for example). Figure 5.5 shows the r_{cor} distribution for the charged tracks for (a) simulation and (b) real data. The $\langle r_{cor} \rangle$ of 5.9 cm is ideal ring radius. The shaded area shows the r_{cor} range of 5.9 ± 2.5 cm corresponding ±1σ region.

The number of the fired phototubes with the association of the track, n0, n1 is defined as follows.

$$\text{n0} \equiv \text{number of fired phototube in } 3.4 < r_{cor} < 8.4\text{cm,} \quad (5.7)$$

$$\text{n1} \equiv \text{number of fired phototube in } r_{cor} < 11.0\text{cm.} \quad (5.8)$$

The variable which represents the association between track and the number of photo-electrons
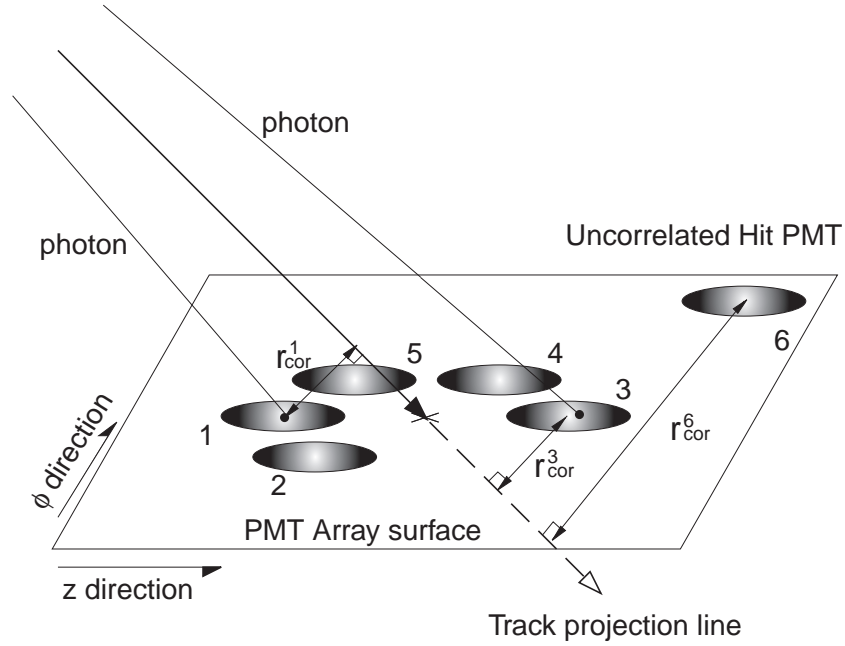
Figure 5.4: The schematic description of the definition of variable which characterize the RICH ring. The track projection vector and five hit phototube are shown as an example. The distance between the center of hit phototube 1, 3 and the track projection vector are represented as r_{cor}^1 and r_{cor}^3, respectively.
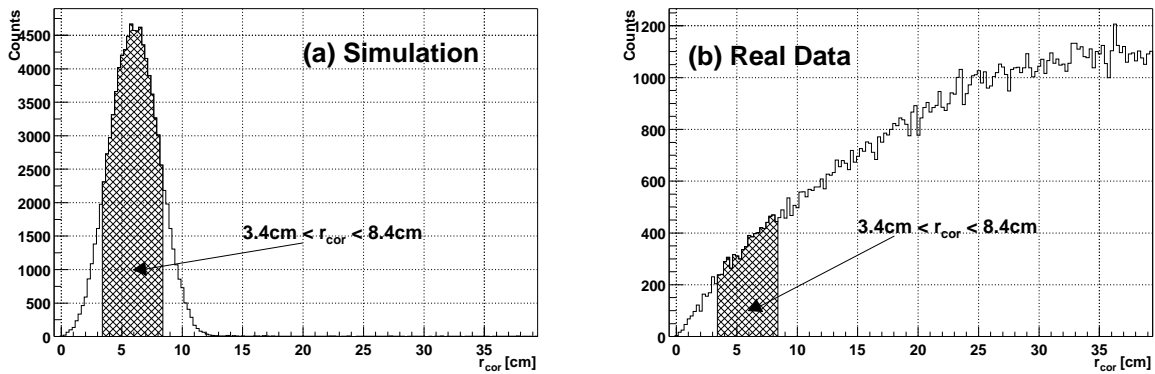
Figure 5.5: The r_{cor} distribution for (a) single electron simulation and (b) real data. The shaded area shows the r_{cor} region from 3.4 cm to 8.4 cm. Since r_{cor} is calculated for all hit phototube, there is large random association in real data.

in an associated RICH ring, npe0 is defined as

$$\text{npe0} \equiv \sum_{3.4 \text{ cm} < r_i < 8.4 \text{ cm}} N_{p.e}(i), \tag{5.9}$$

where $N_{p.e}(i)$ is the number of photo-electron in the hit phototube denoted as i.

The position of ring center, R_{center}, is derived as the weighted average of hit phototube position R_i, where the weights are taken to be $N_{p.e}(i)$

$$R_{center} \equiv \frac{\sum_i N_{p.e}(i) \times R_i}{\text{npe0}}. \tag{5.10}$$

The distance between the RICH ring center, R_{center}, and the reconstructed track projection line is defined as disp.

RICH Ring Shape : chi2/npe0

The variable which represents the ring shape is chi2/npe0. It is the weighted average of the deviation of the hit phototube position from the ideal ring radius, r_0. The weight is taken to be the number of photo-electrons in each phototube. The definition of chi2/npe0 is

$$\text{chi2/npe0} \equiv \frac{\sum_{3.4 \text{ cm} < r_i < 8.4 \text{ cm}} (r_i - r_0)^2 \times N_{p.e}(i)}{\text{npe0}}, \tag{5.11}$$

where r_i represents the distance between phototube hit position and track projection point in the plane perpendicular to the track projection line, and $r_0 = 5.9$ cm represents the mean ring radius $\langle r_{cor} \rangle$ as shown in Fig. 5.5.

5.3.3 Electron Identification with EMCal

EMCal measures the energy and hit position of electrons and photons. EMCal consists of eight sectors, W0-W3 (in the west arm, from bottom to top) and E0-E3 (in the east arm, from bottom to top). The sectors E0 and E1 are PbGl and the rest are PbSc. Energy calibration of each EMCal tower is performed using the π^0 peak mass reconstructed from two photons.

Track - EMCal Hit Position Association : emcsdphi_e, emcsdz_e

The distance between the reconstructed track projection point at the surface of the EMCal and the hit position (shower center) of EMCal is parametrized by emcdphi variable in ϕ direction, emcdz variable in z-direction.

$$\text{emcdz} = \text{emcz} - \text{pemcz}, \tag{5.12}$$
$$\text{emcdphi} = \text{emcphi} - \text{pemcphi}, \tag{5.13}$$

where pemcz and pemcphi are the projected z and ϕ position of the reconstructed track at EMC surface, emcz and emcphi is the z and ϕ position of EMC hit. emcdz and emcdphi are normalized by $\sigma_{\text{emcdz}}(p)$ and $\sigma_{\text{emcdphi}}(p)$, which are the typical momentum dependent width of

emcdphi and emcdz values. Figure. 5.6 shows $\sigma_{\mathsf{emcphi}}(p)$ (Left) and $\sigma_{\mathsf{emcz}}(p)$ (Right) as a function of momentum. The normalized variables, emcsdphi_e, emcsdz_e are determined as bellow.

$$\mathsf{emcsdz\_e} \;\; = \;\; \frac{\mathsf{emcdz} - <\mathsf{emcdz}>}{\sigma_{\mathsf{emcsdz}}(p)}, \tag{5.14}$$

$$\mathsf{emcsdphi\_e} \;\; = \;\; \frac{\mathsf{emcdphi} - <\mathsf{emcdphi}>}{\sigma_{\mathsf{emcsdphi}}(p)}, \tag{5.15}$$

emcsdz_e and emcsdphi_e depend on the total momentum, the momentum direction and the electric charge of electrons/positrons and the sector and position of EMCal due to the residual field. These variables are calibrated to the standard normal distribution with a mean of 0 and a σ of 1 for convenience of the analysis.
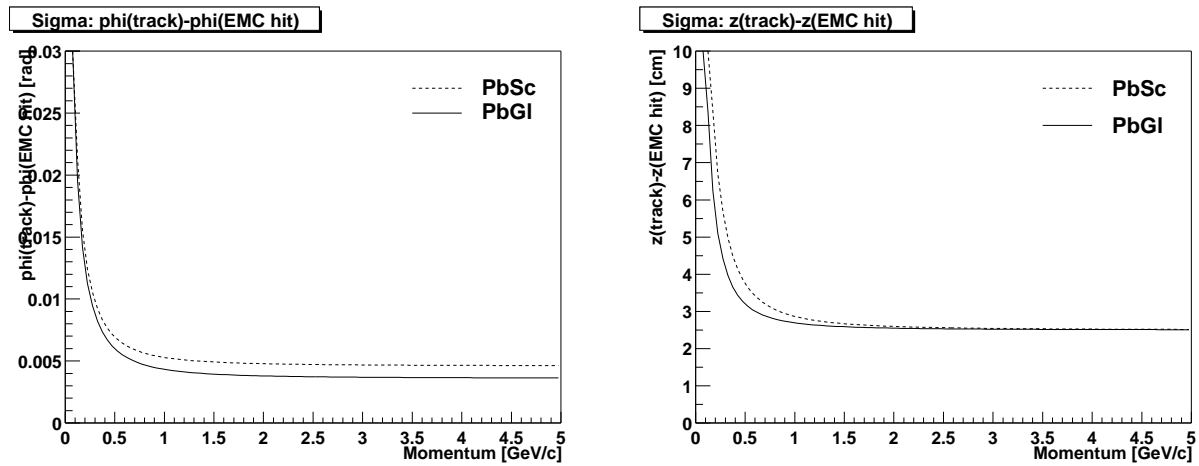
Figure 5.6: Left : The momentum dependence of σ_ϕ. Right : The momentum dependence of σ_z. The dashed line and solid line correspond to the 1 σ value of PbSc and PbGl, respectively.

Energy - Momentum Matching : ecore/mom

Since the electron deposits all of its energy in EMCal and the mass is small compared to its momentum, the ratio of the momentum, mom to the shower energy detected at EMCal, ecore is around one in case of the electron track. In the analysis, the ratio ecore/mom is used to select electron candidate.

Probability for Shower Shape Matching: prob

To reduce charged hadron background in the electron candidates, the shower shape information at the EMCal is used. This hadron rejection comes from the χ^2 variable,

$$\chi^2 = \sum_i \frac{E_i - E_i'}{\sigma_i^2}, \tag{5.16}$$

where E_i is the energy measured at tower number (i) of EMCal, E_i' is the predicted energy for an electromagnetic particle of total energy $\sum E_i$, and σ_i is the standard deviation for E_i'. Both E_i' and σ_i are obtained from the electron test beam data. prob is defined as the probability for a shower being an EM shower, which is obtained by mapping χ^2 to the probability.

5.3.4 Used Cut for the Electron Reconstruction

The following cuts are used to select the electron candidate.

- **Event Cut**: $-25 <$ bbcz < 25 (cm)

- **Track Quality**: quality>15 (PC1 hit is required)

- **RICH Hit**: n0$>= 2$

- **RICH Associate**: disp< 6

- **RICH Shape**: npe0/chi2< 25

- **EMCal E/p**:
  1.4$>$ecore/mom> 0.65 ($p_T < 0.7$ GeV/c)
  1.4$>$ecore/mom> 0.7 ($0.7 < p_T < 1$ GeV/c)
  1.4$>$ecore/mom> 0.75 ($1 < p_T < 2$ GeV/c)
  1.4$>$ecore/mom> 0.8 ($2 < p_T$ GeV/c)

- **EMCal Associate**: |emcsdphi_e|<4\& |emcsdz_e|<4

- **EMCal Shower Shape**: prob> 0.01

These cuts are called as 'standard eID cut' in this thesis. Hadron contamination in the selected electron samples with standard eID cut is bellow 1% level for $p_T < 5$ GeV/c, as described at Sec. 5.5.3.

Since pion emits Cerenkov light for $p_T >4.85$ GeV/c, the pion rejection power of RICH is reduced significantly. Therefore, 'tight electron cut' is applied to identify high p_T (>5.0 GeV/c) electrons. 'Tight electron cut' is defined as follows.

- **Event Cut**: $-25 <$ bbcz < 25 (cm)

- **Track Quality**: quality>15 (pc1 hit was requite)

- **RICH Hit**: n0$>= 2$\&\& n1$>= 5$

- **RICH Associate**: disp< 6

- **RICH Shape**: npe0/chi2< 25

- **EMCal E/p**: 1.4$>$ecore/mom> 0.8

- **EMCal Associate**: |emcsdphi_e|<4&|emcsdz_e|<4

- **EMCal Shower Shape**: prob> 0.1

5.3.5   Detector Response

The variables used for the track reconstruction and the electron identification are studied in the real data and the simulation.

PISA Simulation

Detector simulation is performed PISA, using the GEANT3 simulator of the PHENIX detector [105]. The PISA simulation is important in this analysis, since some of the correction factors are obtained from PISA simulation. To study the detector response with the PISA simulation, a single particle simulation for a sample of electrons is performed with the PISA simulation. CM- - magnetic field is used as the RUN5 configuration and CM++ magnetic field is used as the RUN6 configuration. Kinematic conditions of the generated single electron, which are determined to have wider region than analyzed region, are as follows.

- Transverse momentum: $0. < p_T < 12.0$ GeV/c (flat)

- Rapidity: $|y|< 0.5$ (flat)

- Azimuthal angle: $0 < \phi < 2\pi$ (flat)

- vertex z: $|\text{vertex } z| < 40$ cm

Distributions of each variable in simulation which characterizes detector response are weighted according to the input p_T, so that the distribution of the input p_T have a realistic p_T distribution of electrons.

Comparison Between Real Data and Simulation

The distributions of the variables for the electron identification in the PISA simulation are compared to those of the real data. The applied cuts for the comparison of each variable are summarized at Table 5.4. Electron sample with $0.5< p_T <5$ GeV/c is selected for this comparison. Electron sample for the comparison is selected by the the 'standard eID' without the cut for the compared variable. n1>= 1 and 0.8<ecore/mom< 1.4 cut is used instead of n0 cut for the n0 comparison.

Figure 5.7, 5.8 and 5.9 show the distributions of RICH variables, n0, disp and chi2/npe0 at each RICH sector, respectively. In addition, Figure 5.10, 5.11 and 5.12 show the distributions of EMCal variables at each sector, emcsdphi_e, emcsdz_e and prob, respectively. Figure 5.13 and 5.14 show mean and sigma values of ecore/mom distributions as a function of electron p_T. In Fig. 5.7-5.14, black squares show the results from the real data in RUN5 and red circles show these from the PISA simulation with RUN5 tuning parameters and CM- - field. The distribution

Table 5.4: The eID cut used for the comparison of the variables.

Used cut	Compared variable					
	n0	disp	npe0/chi2	emcsdphi(z)_e	ecore/mom	prob
n0>= 2	×(n1>= 1)	○	○	○	○	○
disp< 6	○	×	○	○	○	○
npe0/chi2< 25	○	○	×	○	○	○
|emcsdphi(z)_e|<4	○	○	○	×	○	○
ecore/mom cut ○	○	○	○	×	○	
prob> 0.01	○	○	○	○	○	×

in simulation is normalized by the number of entries at each sector. The distributions of the simulation and these of the real data match well. The difference of the efficiency of the cut for the each variable between the real data and the simulation is less than 1%, as described in Sec.5.5.5. The comparison between real data and simulation in RUN6 is described in Sec.B.1
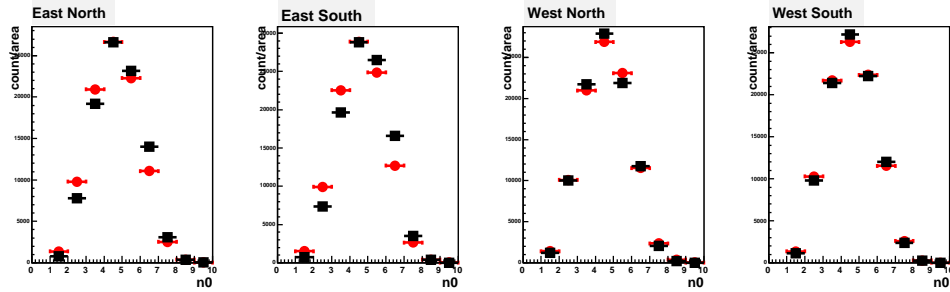
Figure 5.7: The distribution of n0 with the standard eID cut without n0 cut and the $0.5< p_{\mathrm{T}} <5$ GeV/c cut in the real data (square) and simulation (circle).

Acceptance Evaluation for eID

Detector area with low efficiency, dead or noisy is removed from the data analysis by fiducial cut. The same fiducial cut is also applied for the simulation to make the geometrical acceptance of the simulation identical as that of the real data, so that the reconstruction efficiency is evaluated from the simulation. The distributions of phi, zed of the simulation are compared with these of the real data for the electron samples selected by the standard eID and a transverse momentum with $0.5< p_{\mathrm{T}} <5$ GeV/c. Figure 5.15 shows the distributions of phi at North (top panel) and South (bottom panel)sector, and Figure 5.16 shows the distributions of zed at East (top panel) and West (bottom panel) sector. In Fig. 5.15 and 5.16, black squares show the real data in RUN5 and red circles show the PISA simulation with RUN5 tuning parameters and CM- - field. The distributions of simulation are normalized by number of entries in the reference regions, where are little low efficiency, dead or noisy area. In Fig 5.15 and 5.16, the used reference
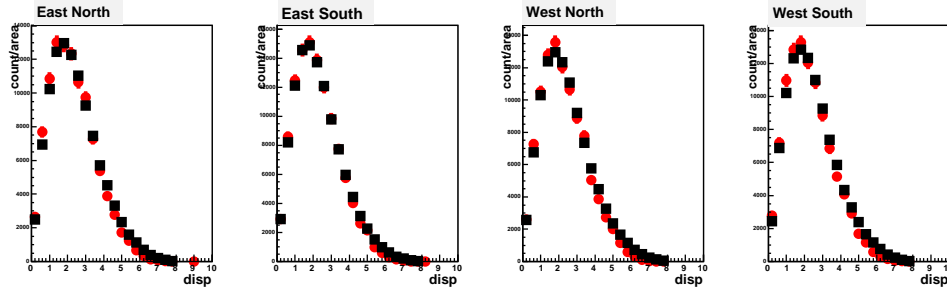
Figure 5.8: The distribution of disp with the standard eID cut without disp cut and the 0.5< p_T <5 GeV/c cut in the real data (square) and simulation (circle).
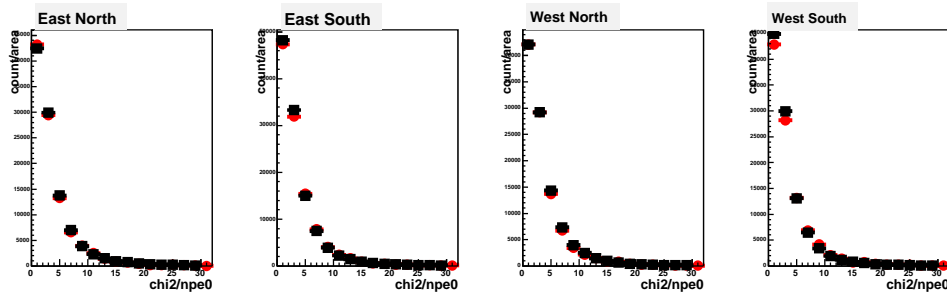
Figure 5.9: The distribution of chi2/npe0 with the standard eID cut without chi2/npe0 cut and the 0.5< p_T <5 GeV/c cut in the real data (square) and simulation (circle).

region to normalize is region 1. The ratio of the number of entries in the simulation over that in the real data except for the reference region used for the normalization is calculated for each reference region. The same procedure is done for the real data in RUN6 and the simulation with RUN6 tuning parameters and CM++ field. The distribution of phi, zed in RUN6 is described at Sec. B.2 The results of the ratios in RUN5 and RUN6 are summarized at Table 5.5. The geometrical acceptance of the PISA simulation agrees with the real data within 3%.

Table 5.5: The ratio of the number of entries at the simulation over that at real data

reference region	the simulation/real (RUN5)	the simulation/real (RUN6)
region 1	0.98	1.01
region 2	0.97	0.97
region 3	0.98	1.01
region 4	0.99	0.98
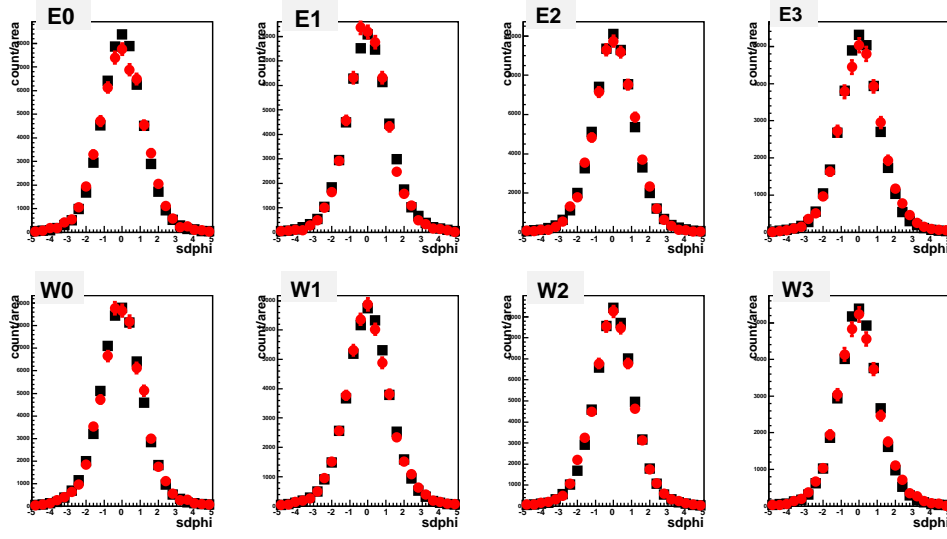
Figure 5.10: The distribution of emcsdphi_e with the standard eID cut without emcsdphi(z)_e cut and the $0.5< p_\mathrm{T} <5$ GeV/c cut in the real data (square) and simulation (circle).
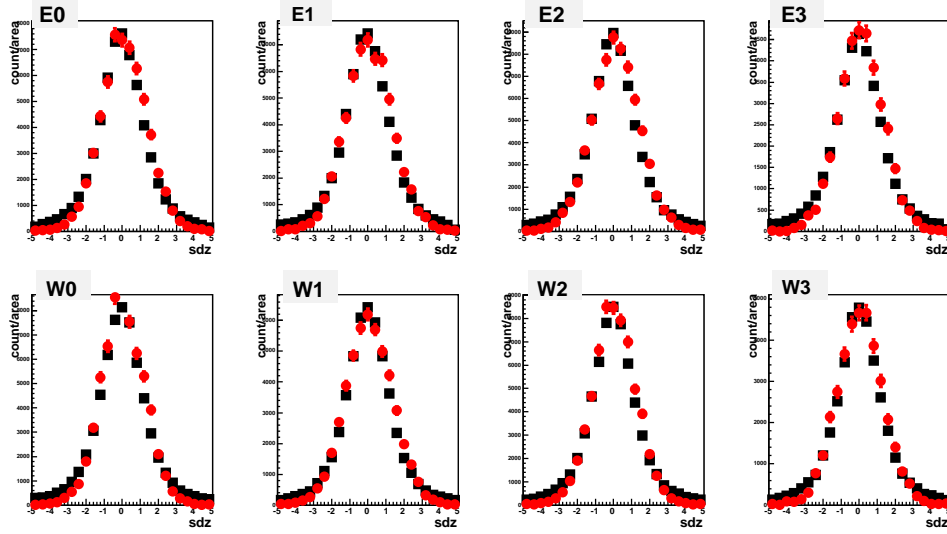
Figure 5.11: The distribution of emcsdz_e with the standard eID cut without emcsdphi(z)_e cut and the $0.5< p_\mathrm{T} <5$ GeV/c cut in the real data (square) and simulation (circle).
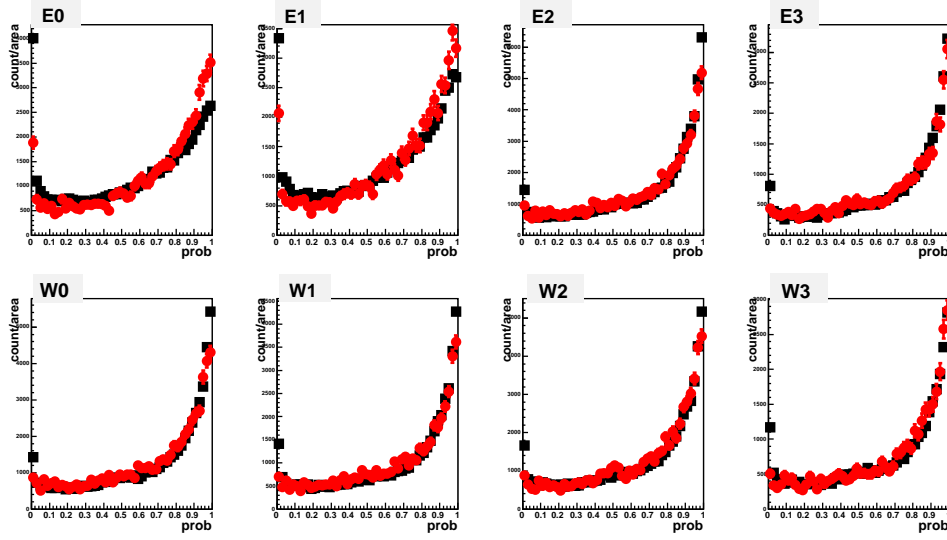
Figure 5.12: The distribution of prob with the standard eID cut without prob cut and the $0.5 < p_T < 5$ GeV/c cut in the real data (square) and simulation (circle).
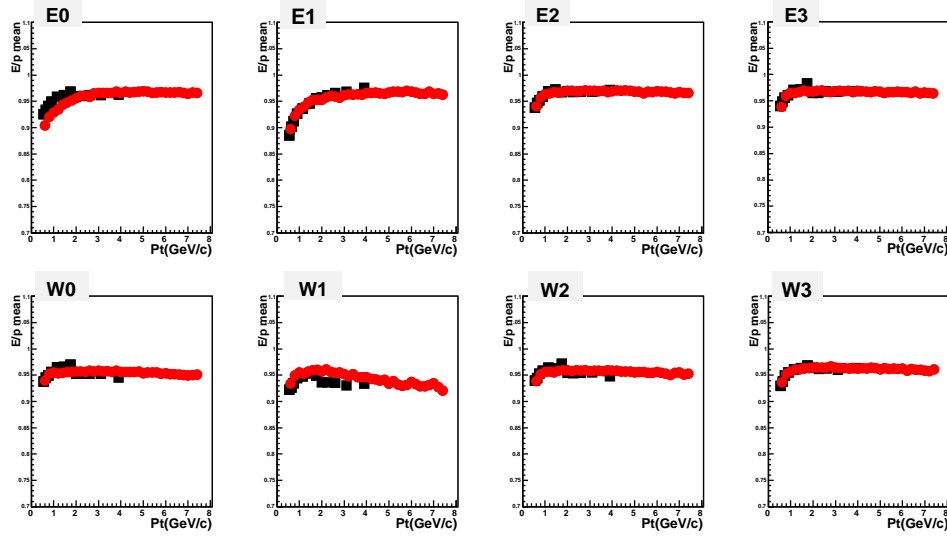
Figure 5.13: The mean value of ecore/mom distribution with the standard eID cut as a fiction of electron p_T in the real data (square) and simulation (circle).
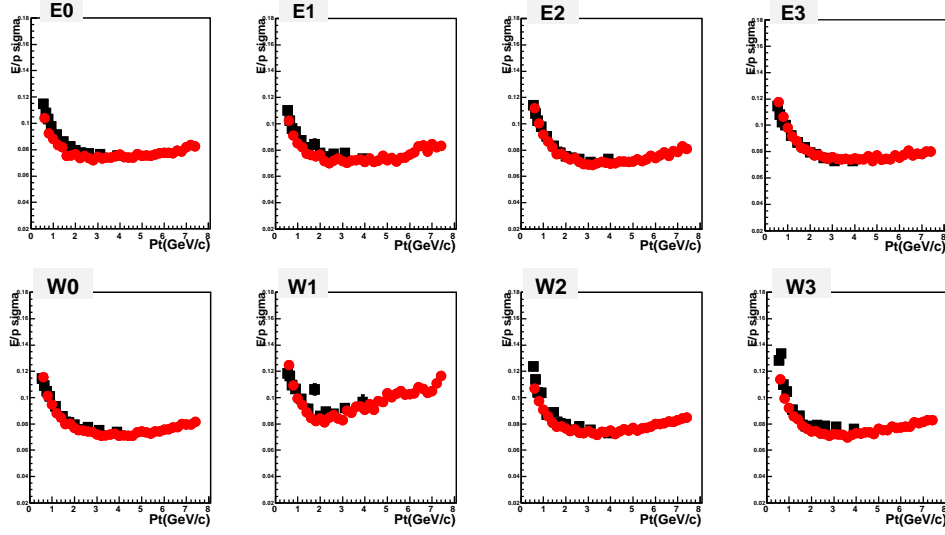
Figure 5.14: The sigma value of ecore/mom distribution with the standard eID cut as a fiction of electron p_T in the real data (square) and simulation (circle).
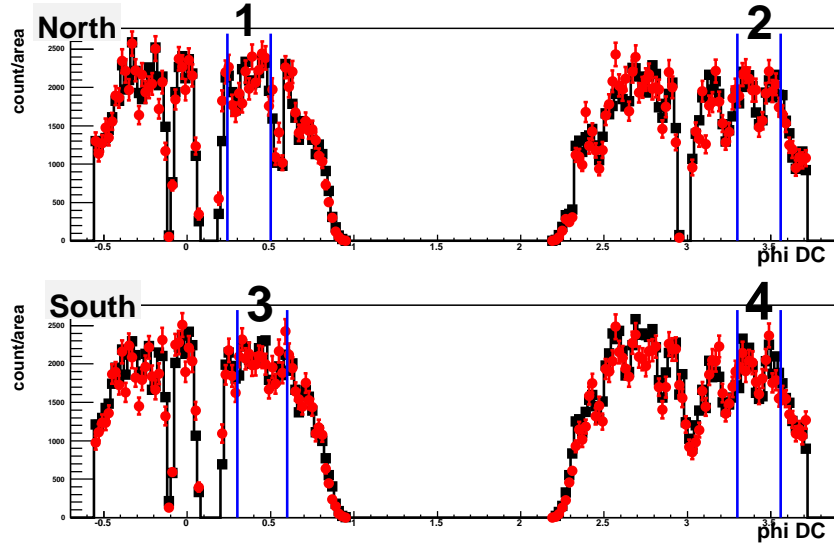
Figure 5.15: The distribution of phi with the standard eID cut and the $0.5 < p_T < 5$ GeV/c cut in the real data in RUN5 (square) and simulation (circle).
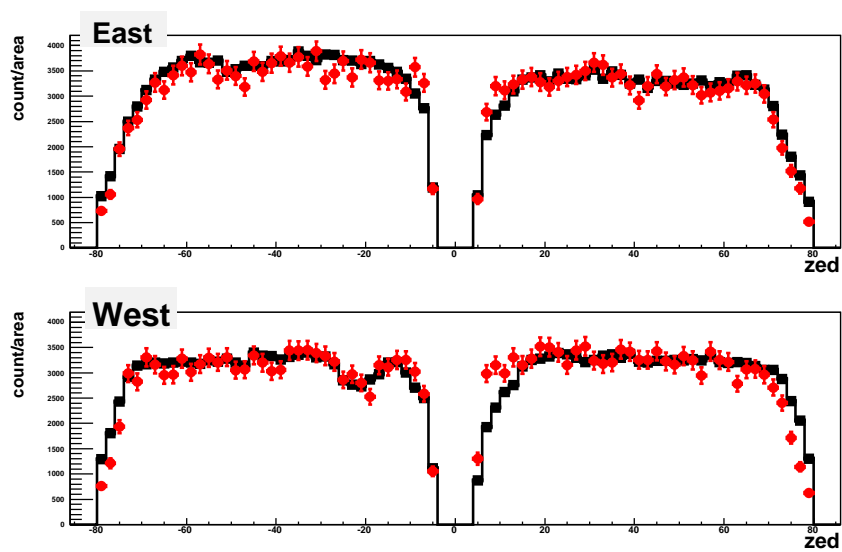
Figure 5.16: The distribution of zed with the standard eID cut and the $0.5 < p_\mathrm{T} < 5$ GeV/c cut in the real data in RUN5 (square) and simulation (circle).

5.4 Run Selection

Table 5.6: Summary of run group

RUN group	RUN Number
RUN5	
G5A	166030-171594 & 172081-176573
C	171595-172080
G5B	176574-178936
G5L	178936-179846
RUN6	
G6	188216-202500
G6HBD	202500-204639

Electron yield and hadron yield per event are checked for each run taken during RUN5 and RUN6, which tells the stability of the track reconstruction and the electron identification performance as a function of time period. Furthermore, some runs, which have low electron yield due to inefficient detector response, are removed in the analysis.

Physics runs in RUN5 and RUN6 are divided into several run groups according to detector and trigger configuration as listed at Table 5.6. The PH trigger mask (4x4c) is changed after RUN176574 in RUN5. As a result, the 4x4c trigger efficiency in G5A and G5B is slightly different. Electron yield in the G5L group is reduced, since two of RICH data packets are disabled during this period. The G5L group is not used for this analysis. The photon converter is installed in the C group.

A new detector, Hadron Blind Detector (HBD) is installed at the front of East DC in the G6HBD group for the performance test of the HBD. The G6HBD group is not used for this analysis, since the amount of the electrons from γ conversion increases due to the material budget of the HBD. The fiducial cut and offline mask for the 4x4c trigger are applied so that the detector and trigger configuration become identical during the G6 group.

The good runs in the G5A, G5B, G6 and C groups are selected as follows.

- Select the good runs according to the hadron yield ($0.4 < p_T < 5$ GeV/c) in each run in MB trigger data

- Select the good runs according to the electron yield ($0.5 < p_T < 5$ GeV/c) in each run in MB trigger data

- Select the good runs according to the electron yield ($1.6 < p_T < 5$ GeV/c) in each run in PH trigger data

The procedure to select good runs according to the hadron yield is as follows. The hadron is selected by the quality> 15, n0< 0 cut and with $0.4 < p_T < 5$ GeV/c.

1. Mean of $N_{ch}(run)$ in each good run ($< N_{ch} >$) and RMS of $N_{ch}(run)$ in good runs (σ) are obtained.

2. calculate the following ratio,

$$\frac{\mid N_{ch}(run) - < N_{ch} > \mid}{\sigma}. \tag{5.17}$$

3. Remove runs which the ratio is above 2.5 from good runs.

The above procedure is continued, until no run is removed by the procedure.

The procedure to select good runs according to the electron yield is as follows. The electron is selected by the standard eID cut and with 0.5 (1.6)$< p_T <$5 GeV/c for MB (PH) data.

1. Mean of $N_{ele}(run)$ in each good run ($< N_{ele} >$) and statistical errors of $N_{ele}(run)$ in good runs ($\sigma(run)$) are obtained.

2. calculate the following ratio,

$$\frac{\mid N_{ele}(run) - < N_{ele} > \mid}{\sigma(run)}. \tag{5.18}$$

3. Remove runs with the ratio is larger than 3 from good runs.

The above procedure is also continued, until no run is removed by the procedure.

As a result, 596 runs out of 722 runs in the G5A and G5B group are selected in RUN5 and 501 runs out of 643 runs in the G6 group are selected in RUN6. 51 runs out of 58 runs in the C group in RUN5 are selected as good runs for the converter analysis. As an example, Figure 5.17 and Figure 5.18 show the electron yield in 0.5-5.0 GeV/c per MB event as a function of run number in RUN5 and RUN6, respectively. Black circles show the selected good runs and blue squares show runs rejected for this analysis.

5.5   Inclusive Electron Spectrum

Invariant yield of inclusive electron is obtained using Eq. 5.2 and this procedure is described in this section. In Eq 5.2, $\epsilon(p_T)$, which is the overall efficiency including acceptance, reconstruction efficiency and trigger efficiency, can be written as follows in MB and PH data.

$$\epsilon(p_T) = A \times \epsilon_{eff}(p_T) \quad \text{(MBdata)}, \tag{5.19}$$
$$\epsilon(p_T) = A \times \epsilon_{eff}(p_T) \times \epsilon_{trig}(p_T) \quad \text{(PHdata)}, \tag{5.20}$$

where $A \times \epsilon_{eff}(p_T)$ is the acceptance times the reconstruction efficiency for electrons and $\epsilon_{trig}(p_T)$ is the 4x4c (PH) trigger efficiency.
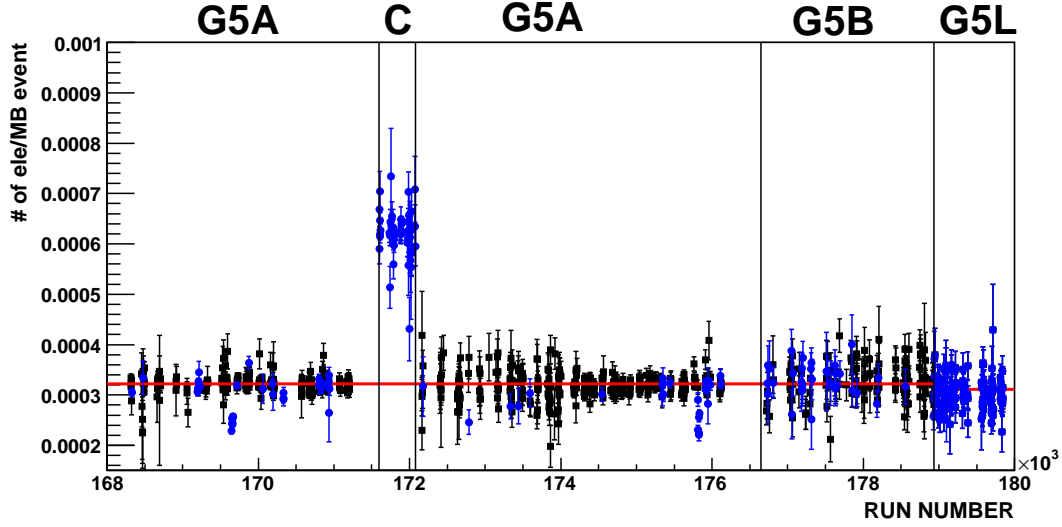
Figure 5.17: Electron yield in 0.5-5.0 GeV/c per MB event in RUN5 as a function of run number. Black circles show good runs and blue squares show bad runs.

5.5.1 Reconstruction Efficiency for Electron

Reconstruction Efficiency with Standard eID Cut

$A \times \epsilon_{eff}(p_T)$ with the standard eID cut is determined by the PISA simulation. The simulation sample described in Sec. 5.3.5 is used. $A \times \epsilon_{eff}(p_T)$ is determined as bellow.

$$A \times \epsilon_{eff}(p_T) = \frac{\text{output} \quad \text{with} \quad \text{standard} \quad \text{eID} \quad \text{cut}(p_T)}{\text{input}(p_T) \times w(p_T)}, \tag{5.21}$$

where $w(p_T)$ is the weighting factor which is used so that the input distribution of p_T in the simulation have the realistic form for inclusive electrons. Figure 5.19 shows the result of the geometrical acceptance times electron reconstruction efficiency as a function of electron p_T in RUN5. Figure 5.20 also shows the result of the geometrical acceptance times electron reconstruction efficiency in RUN6. Red points show electron efficiency and blue points show positron. Black points show efficiency of electron and positron. Green line is a fit function of efficiency of electron and positron. Fit function is

$$p_0 + \frac{p_1}{p_T} + \frac{p_2}{p_T^2} + p_3 \times p_T + p_4 \times p_T^2. \tag{5.22}$$

The fit function is used as the efficiency curve of electron and positron.

Reconstruction Efficiency with Tight eID

In p_T above 4.85 GeV/c, pions start emitting Cerenkov light in CO2 gas in the RICH detector. Since rejection power of RICH is reduced, the tight eID cut, as is defined at Sec 5.3.4 is applied above 5 GeV/c.
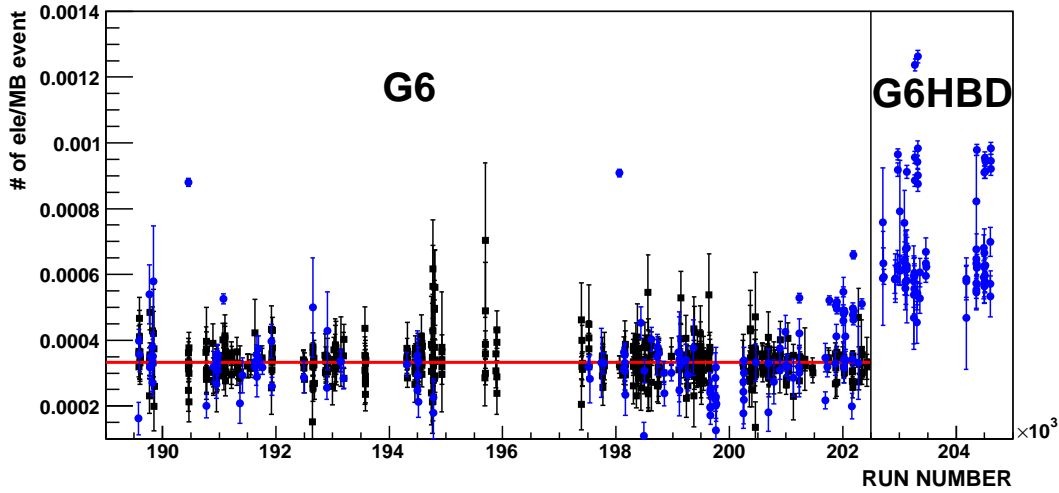
Figure 5.18: Electron yield in 0.5-5.0 GeV/c per MB event in RUN6 as a function of run number. Black circles show good runs and blue squares show bad runs.

The tight eID cut requires n1>4 and prob>0.1 in addition to the standard eID cut. Efficiency of tight eID cut is calculated as bellow.

$$\epsilon_{tight}(0.8 < \mathsf{ecore}/\mathsf{mom} < 1.4) = \epsilon_{standard}(0.8 < \mathsf{ecore}/\mathsf{mom} < 1.4) \times R_{tight}, \qquad (5.23)$$

where R_{tight} is the efficiency corresponding to the additional cuts in the tight eID cut (prob>0.1 and n1>4). R_{tight} is determined from the ratio of the number of electron in 0.8<ecore/mom<1.4 with the tight eID cut over that with the standard eID cut in the real data. Figure 5.21 and Figure 5.22 show the ratios as a function of electron p_T in RUN5 and RUN6, respectively. These figures indicate the ratio is independent of the p_T in 2.0< p_T < 5.0 GeV/c and then it drops. The constant behavior below 5.0 GeV/c is due to independence of n1 and prob cut on electron p_T. The drop is due to large hadron contamination in electron with standard eID cut. Therefore, R_{tight} itself is expected to be independent of p_T even above 5.0 GeV/c. In Fig.5.21 and Fig.5.22, black line is a constant value fit to the ratios in 2.0< p_T < 5 GeV/c. The fitted values are used as relative efficiency. The values are 0.587±0.003 and 0.599±0.002 for RUN5 and RUN6, respectively.

5.5.2   Trigger Efficiency

Figure 5.23 and 5.24 show raw spectra of electrons with the standard eID cut in RUN5 MB and RUN6 MB data, respectively. In Fig. 5.23 and 5.24, blue circles show all electron in MB data and red squares show 4x4c fired electrons. 4x4c trigger efficiency is determined as a ratio of PH fired electrons over measured electrons in MB data. Figure 5.25 and 5.26 shows the determined efficiency of PH trigger in RUN5 and RUN6.
The solid curves in Fig. 5.25 and Fig. 5.26 are the fitted functions with the following parame-
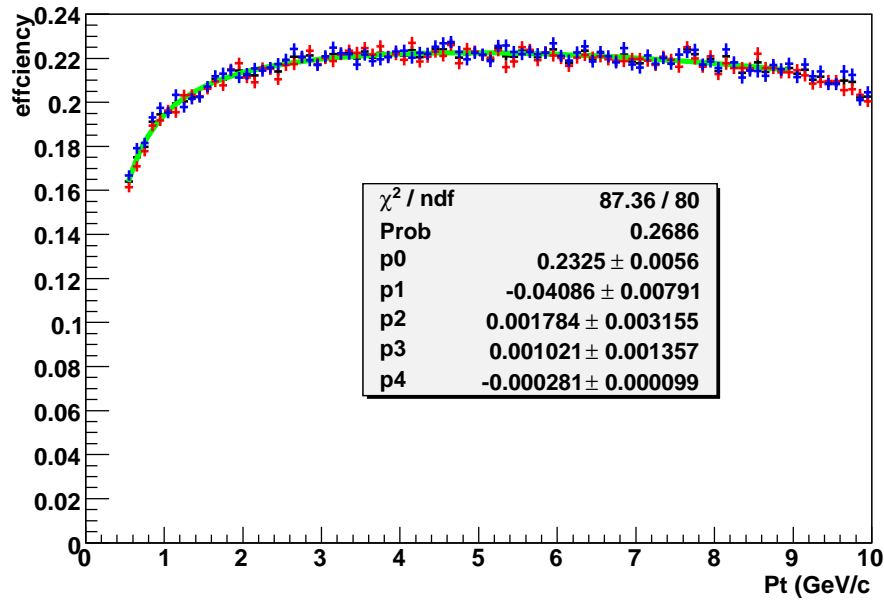
Figure 5.19: Electron efficiency as a function of electron p_T. Red points are electron efficiency and blue points are positron in RUN5. Black points are efficiency of electron and positron. Green line is a fit function of efficiency of electron and positron.

terization:

$$\frac{p_0}{1 + p_3} \times (p_3 + \tanh(p_1 \times (p_T - p_2))). \tag{5.24}$$

These fitted functions are used for the efficiency of PH trigger in RUN5 and RUN6.

5.5.3 Hadron Contamination

Hadron contamination in the electrons selected with the standard eID cut using estimated via ecore/mom distribution. The distribution of ecore/mom has a peak around one in the case of the electron peak, while the hadron track has a small ecore/mom value.

Hadron Contamination below 5GeV/c

The idea is to use prob cut is to enrich the hadron contamination. The prob> 0.01 cut has about 50% hadron efficiency for $p_T > 1$ GeV/c and 99% efficiency to electrons. Therefore, the hadron contamination is increased by a factor of 100 if we reverse the prob cut (prob< 0.01). Then we can look at the ecore/mom distribution to see much enhanced hadron contamination.

The procedure we used is the following:

Two ecore/mom distributions of inclusive charged particles are prepared as the distributions of hadrons. (H_a) is the ecore/mom distribution of hadrons with prob< 0.01 (rejected sample) and (H_b) is the ecore/mom distribution of hadrons with prob> 0.01 (accepted sample).

We also make ecore/mom distribution of electron candidate with the reverse cut (prob< 0.01)
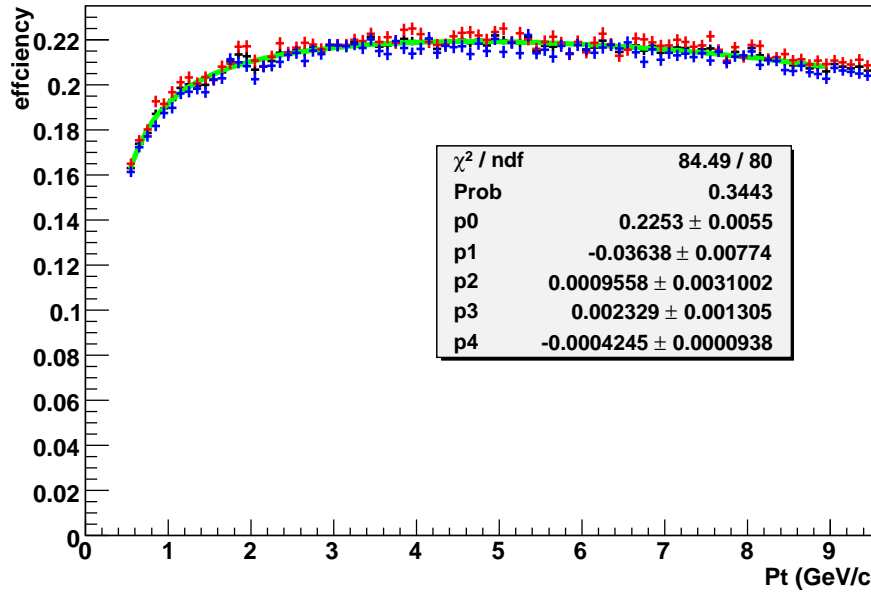
Figure 5.20: Electron efficiency as a function of electron p_T. Red points are electron efficiency and blue points are positron in RUN6. Black points are efficiency of electron and positron. Green line is a fit function of efficiency of electron and positron.

and with normal cut (prob> 0.01). The former (E_a) contains large hadron contamination, and the latter (E_b) is the normal electron candidate sample. For both samples, the standard eID cuts except the prob cut is applied. The distribution of rejected hadron sample (H_a) is scaled by a factor of f_h and the distribution of the accepted electron candidate (E_b) by a factor of f_e corresponding to the efficiency of the prob cut, so that sum of these two distribution reproduces the ecore/mom distribution of the rejected electron sample (E_a).

$$E_a \sim f_e \times E_b + f_h \times H_a, \tag{5.25}$$

When $f_e \times E_b + f_h \times H_a$ is roughly consistent with E_a, the $f_e \times E_b$ term corresponds to the real electron component in E_a, and the $f_h \times H_a$ term is the hadron component in E_a. Since $f_h \times H_a$ presents the hadron contamination in the rejected electron sample, the hadron contamination in accepted electron sample should be presented as the distribution $f_h \times H_b$ by using the fixed normalization factor f_h . In this way, the hadron contamination in the accepted electron sample can be determined as $(f_h \times H_b)/E_b$

Figure 5.27 shows the comparison of the ecore/mom distribution in RUN5 MB data produced by this procedure. The four panels in the figure correspond to four different p_T bins. In each panel, the green histogram is the ecore/mom distribution of the rejected hadron (H_a), the black histogram is the distribution of the accepted electron sample (E_b) scaled by a factor of $f_e = 0.02$. The blue histogram is the sum of the two. The red histogram is the distribution of rejected electrons (E_a) and the magenta histogram is the distribution of accepted hadrons (H_b), which represents hadron contamination in the selected electrons with standard eID cut. The same
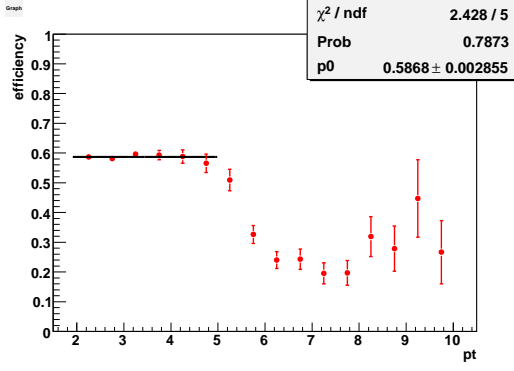
Figure 5.21: The ratios the number of electron in 0.8<ecore/mom<1.4 with tight eID cut over that with standard eID cut as a function of electron p_T in RUN5.
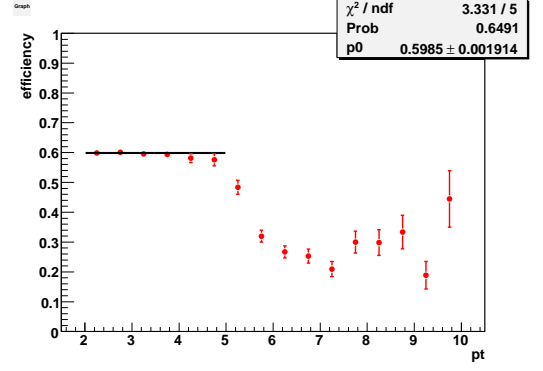
Figure 5.22: The ratios the number of electron in 0.8<ecore/mom<1.4 with tight eID cut over that with standard eID cut as a function of electron p_T in RUN6.
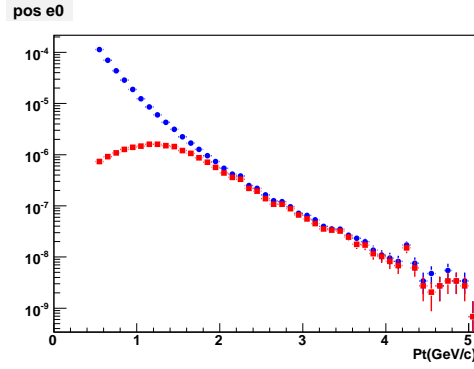
Figure 5.23: Raw spectra of electrons in RUN5 MB data. Blue circles show all electrons in MB data and red squares show 4X4c fired electrons.
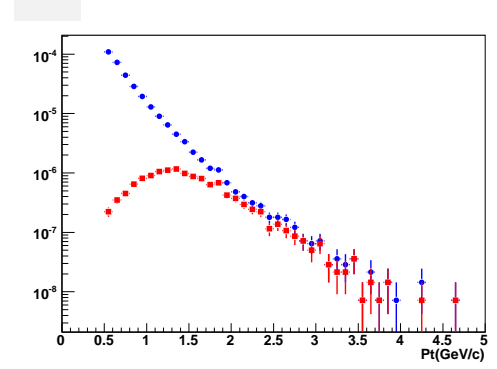
Figure 5.24: Raw spectra of electrons in RUN6 MB data. Blue points show all electrons in RUN6 MB data and red squares show 4X4c fired electrons.

rescaling factor f_h is used for all panels. The sum of the two distribution roughly reproduces the rejected electron distribution as described in Eq. 5.25.

The same comparison is done for ERT data to study the hadron contamination in the electrons with $2.0 < p_T < 5.0$ GeV/c. The results of the estimation of hadron contamination in MB and ERT data are summarized at Table 5.7.

Hadron contamination is less than 1% for 0.7 GeV/c <electron p_T < 4.5 GeV/c. In 4.5-5.0 GeV/c range, hadron contamination becomes about 2%, since pions start emitting Cerenkov light in CO2 gas in RICH detector above 4.85 GeV/c.

Hadron Contamination above 5GeV/c

Hadron background is estimated by similar 'reverse prob method'. Hadron background is not negligible above p_T >5.0 GeV/c, even when the tight eID is applied.
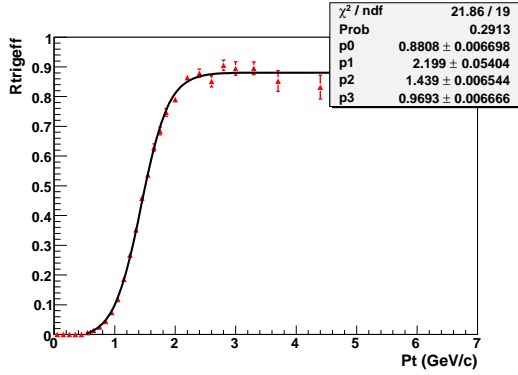
Figure 5.25: Trigger efficiency of 4x4c trigger in RUN5.
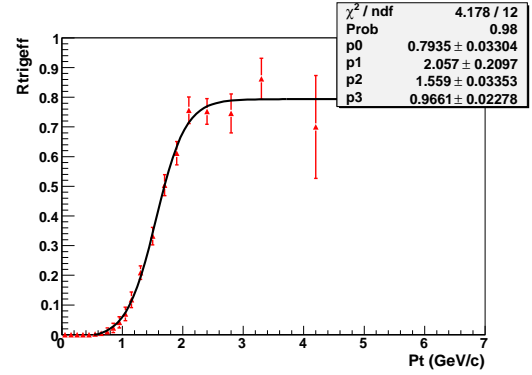
Figure 5.26: Trigger efficiency of 4x4c trigger in RUN6.

Table 5.7: Estimated hadron contamination

electron p_{T} range	hadron contamination(RUN5)	hadron contamination(RUN6)
0.5-0.7 GeV/c	0.0123	0.0147
0.7-1.0 GeV/c	0.0074	0.0089
1.0-2.0 GeV/c	0.0042	0.0052
2.0-2.5 GeV/c	0.0045	0.0044
2.5-3.0 GeV/c	0.0036	0.0039
3.0-3.5 GeV/c	0.0033	0.0039
3.5-4.0 GeV/c	0.0035	0.0039
4.0-4.5 GeV/c	0.0057	0.0061
4.5-5.0 GeV/c	0.0155	0.0201

R_{tight} shown at Fig. 5.21 drops into about half for electron p_{T} >5.0 GeV/c. This represents hadron contamination with the standard eID cut becomes $\sim$50% above p_{T} >5.0 GeV/c. Therefore, when we apply the reverse prob cut (prob< 0.01), the selected particles are hadrons with $\sim$99% purity since the reverse prob cut increases the hadron contamination by a factor of 100. We use the ecore/mom distributions of the particles which is selected by the standard eID cut and the reverse prob cut to estimate hadron background in electron samples.

Figure 5.28 shows the ecore/mom distribution of electrons with tight eID cut and estimated that of hadron as described above from RUN5 data. Black points show the distribution of electron and blue points show estimated that of hadron. The estimated distribution of hadron is normalized by number of entries in 0.6<ecore/mom<0.75.
Blue lines are exponential fit to the ecore/mom distribution of hadron. Red lines are gauss + exponential fit to the distribution of electrons in the condition that exponential parts are fixed at blue lines.

Signals are counted as number of entries in 0.8<ecore/mom<1.4. Hadron background is estimated from fit functions. The fitting error is counted into the statistical error of the signals. The results for RUN5 and RUN6 are summarized in Table 5.8.
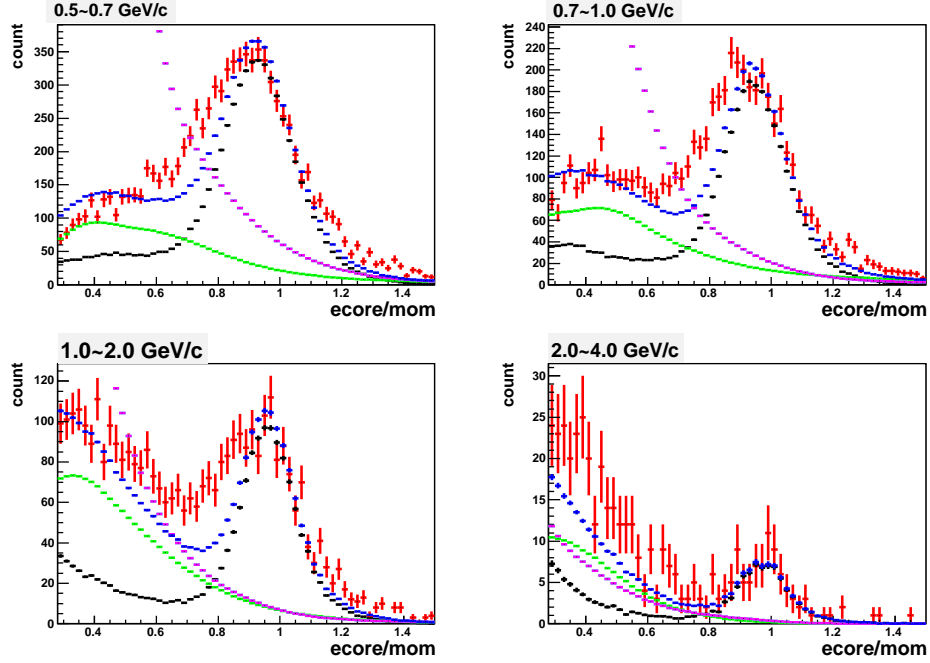
Figure 5.27: The distributions of ecore/mom in RUN5 MB data were used to study hadron contamination in $0.5 < p_{\mathrm{T}} < 4.0$ GeV/c

Table 5.8: Estimated hadron background

electron p_{T} range	hadron background(RUN5)	hadron background(RUN6)
5.0-6.0 GeV/c	0.033	0.038
6.0-7.0 GeV/c	0.051	0.066
7.0-8.0 GeV/c	0.137	0.146
8.0-9.0 GeV/c	0.259	0.156
9.0-10.0 GeV/c	0.257	0.250

5.5.4 Invariant Cross Section of Inclusive Electron

The overall efficiency, $\epsilon(p_{\mathrm{T}})$ can be determined from the obtained electron reconstruction efficiency and trigger efficiency. Therefore, we are ready to determine invariant cross section of inclusive electron according to Eq 5.2

Figure 5.29 and 5.30 show invariant cross sections of inclusive electrons for MB and PH triggered events in RUN5 and RUN6, respectively. Blue circles show the spectrum of electrons in MB data and red squares show that of electrons in PH data with the standard eID cut. Green triangles show electrons for PH data with tight eID cut. These cross sections of inclusive electron are consistent with each other among three cases.
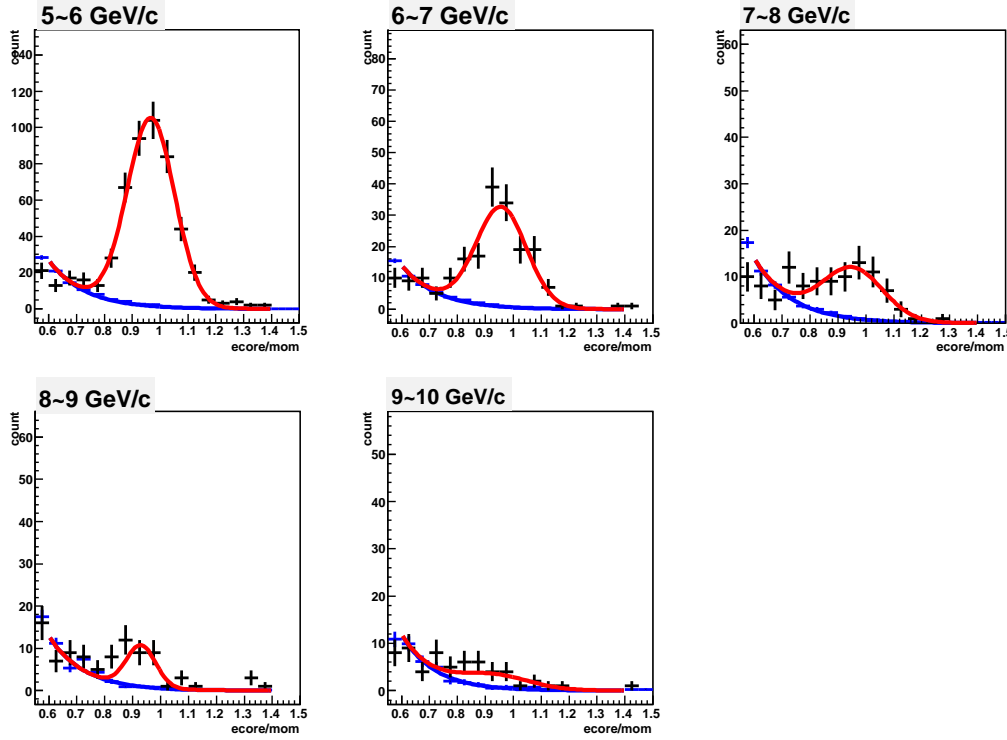
Figure 5.28: The ecore/mom distribution of electrons with tight eID cut and estimated that of hadron as described above in RUN5. Black points show the distribution of electron and blue points show estimated that of hadron.

5.5.5 Systematic Errors

Geometrical Acceptance

Since the simulation reproduces the real data about the phi distribution within 3% as shown at Sec. 5.3.5, 3% systematic error is assinged for geometical acceptance for RUN5 and RUN6.

eID Parameters

Systematic error for eID parameters is determined by the comparison of the efficiency of each eID parameter between the real data and the PISA simulation.

Efficiency of each eID parameter in the simulation is determined from the distribution of the parameter with other cuts being applied. For example, efficiency of n0 cut in the simulation is determined as follows.

$$\frac{\int_2 N(n0)dn0}{\int_0 N(n0)dn0}, \tag{5.26}$$

where N is the distribution of n0 with the standard cut except n0 being applied

The efficiency of each cut for eID parameter in the real data is determined by tagging the electrons from conversion and dalitz decay. The reconstructed invariant mass distribution of e^+ e^- pair has the peaks at the low mass region as shown in Figure 5.31. It is a useful tool to tag
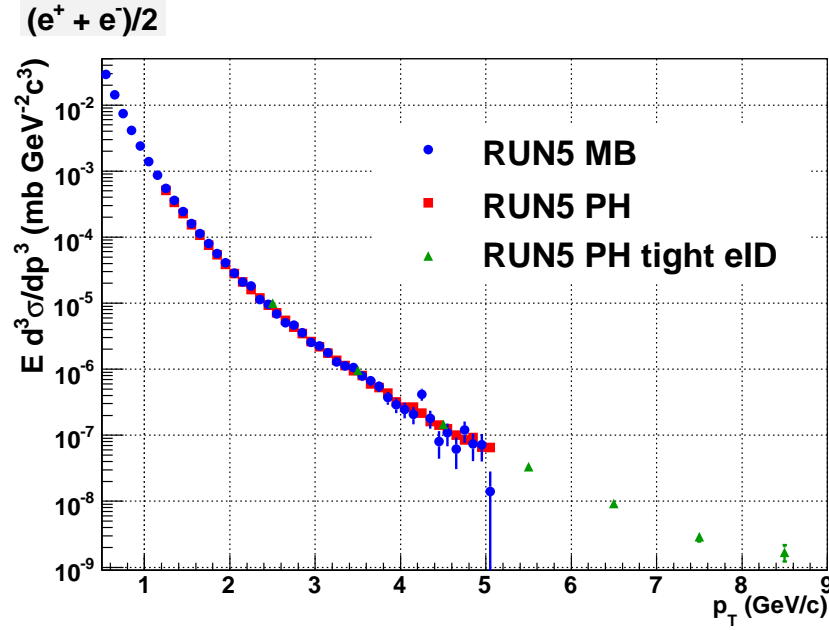
Figure 5.29: Invariant cross section of inclusive electrons in RUN5 MB and PH triggered events. Blue circles show electrons in MB events and red squares show electrons in PH triggered events with standard eID cut. Green triangles show electrons in PH triggered events with tight eID cut.

pure electrons. The sources of the peaks are π^0 Dalitz decay ($\pi^0 \to e^+e^-\gamma$) and γ conversion at the beam pipe. Since the track reconstruction algorithm assumes that all tracks come from the collision vertex, the electron pairs produced at the point with $R > 0$ are reconstructed to have incorrect momentum. This is schematically shown in Fig. 5.32. As a result, each of the conversion pairs acquires the fake p_T and the invariant mass is approximately proportional to $\int Bdl$. Therefore, the reconstructed mass of conversion electron pairs is determined by the location of the conversion sources. The peak position of the pairs from γ conversion at the beam pipe is around 20 MeV/c^2.

Using these clearly tagged pairs of electrons, the efficiency of each eID cut in the real data could be evaluated. One electron is selected by the standard eID cut and the other electron is selected by the standard eID cut except the cut for the parameter whose efficiency will be evaluated. Figure 5.33 shows the invariant mass distribution of e^+e^- in RUN5 PH fired events. Black points show the mass distribution when both electrons are selected by the standard eID cut and red points show that when one electron is selected by the standard eID cut and the other is selected the cut without n0 (RICH fire (n1>1) is required)
Efficiency of n0 cut in real data is determined as follows.

$$\frac{\int_0^{0.04} N(mass)dmass \ (n0 > 1)}{\int_0^{0.04} N(mass)dmass}, \tag{5.27}$$

where, N is the distribution of the invariant mass.
The efficiencies of other parameters are also determined in the same way. The results are
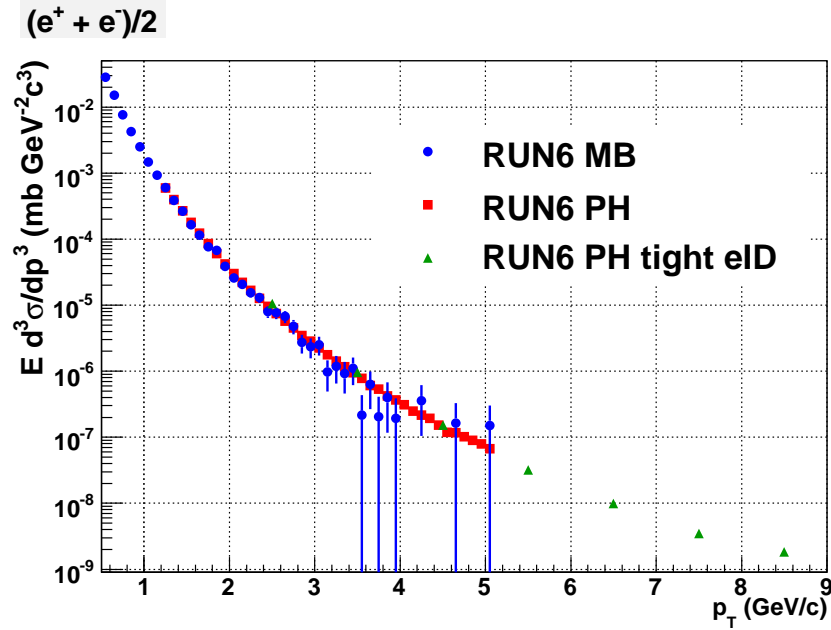
Figure 5.30: Invariant cross section of inclusive electrons in RUN6 MB and PH triggered events. Blue circles show electrons in MB events and red squares show electrons in PH triggered events with standard eID cut. Green triangles show electrons in PH triggered events with tight eID cut.

summarized in Table 5.9. The efficiencies in the simulation agrees well with these in real data.

Systematic error of 1% is assigned for RICH paramenters from Table 5.9, since the efficiencies of RICH parameter are expected not to depend on electron p_T. Systematic error of 2% is assigned for EMC parameters to be conservative, since the efficiencies of EMCal parameters may have small p_T dependence.

Trigger Efficiency

The systematic error of the PH trigger efficiency is evaluated based on the error of the fit in Fig 5.25 and 5.26. We assign the systematic error of the PH trigger efficiency in RUN5 as 3% $\oplus$ 5% $\times \frac{1}{\epsilon_{trig}-1}$ and 4% $\oplus$ 10% $\times \frac{1}{\epsilon_{trig}-1}$.

Tight eID Efficiency

The relative efficiency (R_{tight}) is independent of p_T in 2< p_T <5 GeV/c as shown in Fig. 5.21 and 5.22. The efficiency of the tighter RICH cut(n1>4) is ∼ 70% and this part should be p_T independent. The efficiency of the prob cut is approximately 90%. The 10% loss due to the prob may have some small p_T dependence. We assign 20% of the 10% loss as possible p_T dependence of the prob cut, which is enough conservative compared with the result in PISA simulation. Therefore, the systematic error for the relative efficiency (R_{tight}) for high p_T extension is 10%× 20% = 2%.
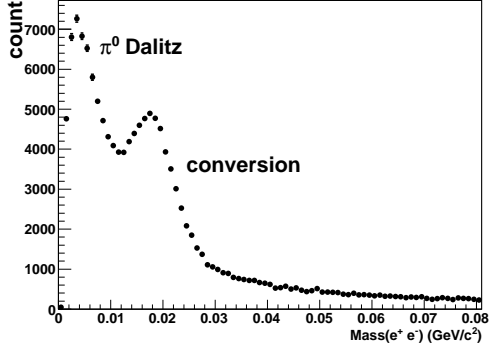
Figure 5.31: The invariant e^+e^- mass peak in data sample.
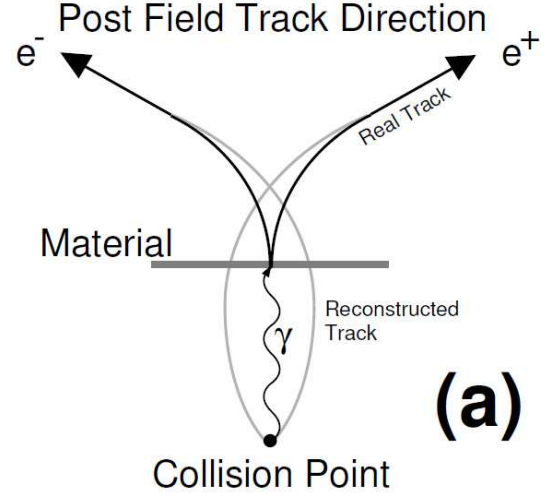
Figure 5.32: The production of conversion electrons.
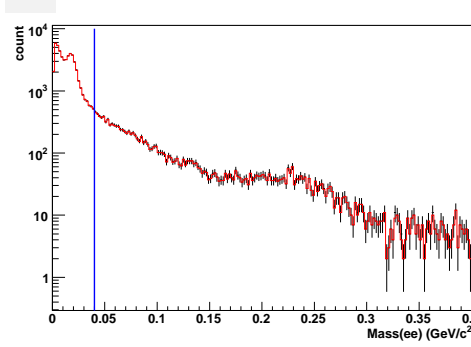
Figure 5.33: e^+e^- mass distribution in RUN5 PH fired events. Black points show the mass distribution when both electrons are applied all cuts and red points show the one when one electron is applied all cuts and the other is applied all cuts except n0 cut.

5.5.6 Absolute Normalization

Systematic error for absolute normalization is described in Sec. 5.1.1 and 5.1.2.

- We use $\sigma_{BBC} = 23.0 \pm 2.2$ mb. Thus, systematic error is 9.6%

- We use $\epsilon_{bias} = 0.79 \pm 0.02$. Thus, systematic error is 2.5%

The systematic error for the absolute normalization is assigned to 9.9% from the quadratic sum of the two components.

Table 5.9: The efficiency of eID parameter at real data and the simulation

eID parameter	real (RUN5)	simulation (RUN5)	real (RUN6)	simulation (RUN6)
RICH				
n0	99.4%	98.5%	99.3%	98.5 %
disp	99.0%	99.3%	99.2%	99.3 %
chi^2	99.7%	99.4%	99.6%	99.4 %
EMC				
e/p	97.7%	97.6%	96.1%	97.1 %
prob	98.8%	98.7%	98.4%	98.7 %
$\delta\phi_{EMC}$	99.3%	99.5%	99.1%	99.4 %
δz_{EMC}	99.3%	99.5%	99.4%	99.5 %

5.6 Single Electron From Heavy Flavor

The inclusive electron spectrum consists of three components:

1. 'non-photonic' electrons from semi-leptonic decay of heavy-flavor (single non-photonic electron). This component is what we want to measure.

2. 'photonic' background from Dalitz decays of light neutral mesons and external photon conversions (mainly in the beam pipe).

3. 'non-photonic' background from $K \to e\pi\nu$ (K_{e3}), dielectron decays of vector mesons and quarkonium (J/ψ and Υ) and Drell-Yan process.

The photonic background (2) is much larger than the non-photonic background except at highest p_T (>5GeV/c). The signal of electrons from heavy-flavor decays is small compared to the background at low p_T ($S/N < 0.2$ for $p_T < 0.5$ GeV/c) but rises with increasing p_T ($S/N > 1$ for $p_T > 2$ GeV/c).

In order to extract the heavy-flavor signal, the background has to be subtracted from the inclusive electron spectrum. 'cocktail method' and 'converter method' are used in this analysis to subtract the electron background [114, 115, 117, 118].

5.6.1 Cocktail Method

One technique to accomplish this task is the so-called 'cocktail subtraction' method. A cocktail of electron spectra from all background sources is calculated using a Monte Carlo event generator of hadron decays and then subtracted from the inclusive electron spectra [108]. This technique relies on the fact that the p_T distributions of the relevant background sources are known well enough. It turns out that the PHENIX measurements of the relevant electron sources are precise enough to allow for cocktail calculations that constrain the background within a systematic uncertainty better than 15 % for all p_T [118]. This uncertainty is in the same order with the signal to background ratio at the lowest p_T and, therefore, it is not sufficiently small to extract the heavy-flavor signal via the cocktail subtraction over the full p_T range. The cocktail method is useful at high p_T, *e.g.* for $p_T > 2$ GeV/c, where signal to background ratio is large and the cocktail input is known with small systematic uncertainties as discussed in the following.

Neutral Pions

The most important background source is the π^0. π^0 decays contribute to the photonic background in two ways. First, the Dalitz decay of π^0 ($\pi^0 \to e^+e^-\gamma$) is a primary source of electrons from the collision vertex and, second, the conversion of photons from the decay $\pi^0 \to \gamma\gamma$ in material in the PHENIX central arm aperture (mainly the beam pipe) gives a source of electrons originating not from the original collision vertex. The contribution from photon conversions is small compared to the contribution from Dalitz decays, since material budget in the PHENIX central arms is well controlled.

The p_T distribution of π^0 is obtained via simultaneous fit to $\pi^{\pm}$ (low p_T) and π^0 (high p_T) spectra at PHENIX [106, 107]. This approach is only valid under the assumption that the invariant π^0 spectrum and the averaged charged pion spectrum $(\pi^+ + \pi^-)/2$ are the same. This assumption is justified with a few % presicion at PHENIX, while at low p_T, *i.e.* for $p_T < 1$ GeV/c, the decay of η mesons into three π^0 creates a tiny charge asymmetry.

χ^2 / ndf	22.78 / 34
c	398.6 ± 72.49
p0	0.6832 ± 0.02124
a	0.3458 ± 0.03399
b	0.09714 ± 0.02125
n	8.204 ± 0.05338
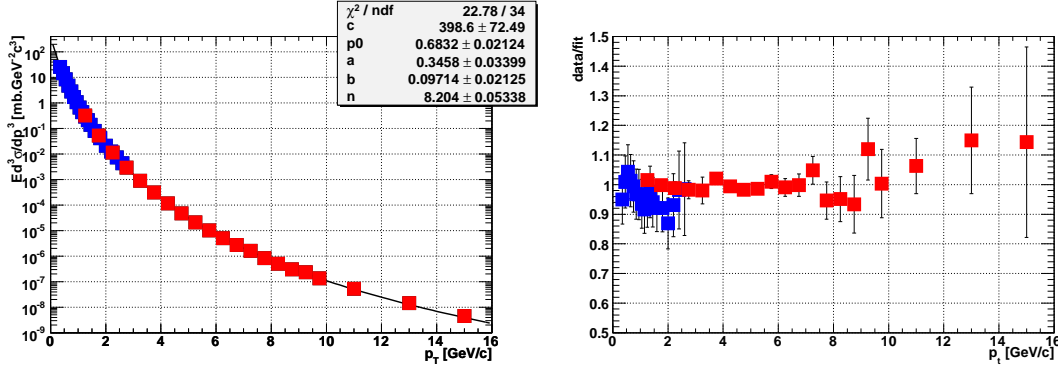
Figure 5.34: Invariant differential cross section of (blue symbols at low p_T) and π^0s (red symbols) together with a fit according to $\pi^{\pm}$ Eq. 5.28 (left panel). Ratio of the data to the fit (right panel).

Figure. 5.34 shows the comparison of the neutral and charged averaged invariant differential cross sections of pions in $p + p$ collisions at $\sqrt{s} = 200$ GeV in comparison with a simultaneous fit to the data with a modified Hagedorn parameterization:

$$E\frac{d^3\sigma}{d^3p} = \frac{c}{(exp(-ap_T - bp_T^2) + p_T/p_0)^n}. \tag{5.28}$$

Both an absolute comparison as well as the ratio of the data to the fit are shown to demonstrate the good quality of the parameterization.

Other Light Mesons

Other light mesons contributing to the electron cocktail are the η, ρ, ω, η', and ϕ mesons. The η meson has the largest contribution among these mesons.

For the cocktail calculation, the shape of the invariant p_T distributions, and the relative yield to the π^0 yield are required as input parameter. The p_T spectra are derived from the pion spectrum assuming the m_T scaling, *i.e.* the same modified Hagedorn parameterizations are used (Eq. 5.28), only p_T is replaced by $\sqrt{p_T^2 + m_{meson}^2 - m_{\pi^0}^2}$.

Since this approach of m_T scaling ensures that at high p_T the spectral shapes of all meson distributions are the same, the normalization of the meson spectra relative to the pion spectrum can be given by the ratios meson-to-pion at high p_T (5 GeV/c is used). The following values are used.

- $\eta/\pi^0 = 0.48 \pm 0.03$ [109]

- $\rho/\pi^0 = 1.00 \pm 0.30$ [110]

- $\omega/\pi^0 = 0.90 \pm 0.06$ [111]

- $\eta'/\pi^0 = 0.25 \pm 0.075$ [110]

- $\phi/\pi^0 = 0.40 \pm 0.12$ [110]

The resulting η/π^0 ratio agrees within experimental uncertainties for $p_T > 2$ GeV/c with the corresponding PHENIX data for $p + p$ collisions [109].

K_{e3} Decay

The contribution from the K_{e3} decay of kaons in flight is evaluated via the PISA simulation to take into account the effect of the exact analysis cuts (specially ecore/mom cut). The measured yield of electrons originating not from the collisions vertex depends on the analysis cut. The input kaon spectrum is parameterized based on the measured charged kaon spectrum in $p + p$ collisions at PHENIX [112]. The contribution from kaon decays is only relevant (*i.e.* larger than 5 %) for electrons with $p_T < 1$ GeV/c. The contribution becomes negligible for electrons with $p_T > 2$ GeV/c.

Photon Conversions

The contribution from γ conversions depends almost entirely on the material present in the detector aperture. Apart from the beam pipe, which is made of Beryllium and contributes less than 0.3 % of a radiation length to the material budget, Helium bags constitute the only material between the beam pipe and the tracking and electron identification detectors in RUN5 setup. As is verified by the PISA simulation of π^0 decays, the ratio of electrons from the conversion of photons from $\pi^0 \to \gamma\gamma$ decays to electrons from π^0 Dalitz decays is 0.403 with a systematic uncertainty of about 10 %, independent of p_T in the relevant range. For heavier mesons, this ratio is rescaled in the cocktail to properly account for the fact that the branching ratio of the Dalitz decay relative to the $\gamma\gamma$ decay increases slightly with increasing parent meson mass.

The material budget between the beam pipe and the tracking detector in RUN6 setup increase slightly, since there are not Helium bags at RUN6 to install HBD. The effect is also estimated by the PISA simulation. It is found that the ratio of the electrons from air conversion due to the absence of He bag to the electrons from π^0 Dalitz decays is 7±1%.

It is crucial to note that the contribution from photon conversion to the background electron spectra is less than half of the contribution from direct Dalitz decays. For a reliable measurement of single non-photonic electrons, this is essential.

Direct Photon

Contributions to the background electrons from direct radiation have two process. First, real photons produced in initial hard scattering processes, *i.e.* direct photons convert to electron pairs in material in the PHENIX detector as photons from light neutral meson decays. Second,
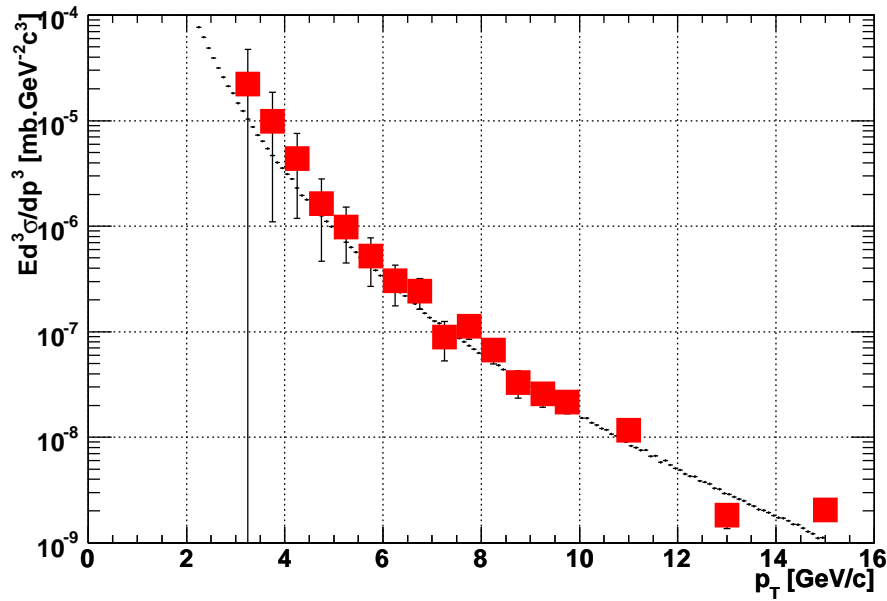
Figure 5.35: Measured direct photon spectrum (large symbols shown in red) compared with the cocktail parameterization (histogram indicated by small 'datapoints') for $p + p$ collisions.

every source of real photons also presents a source of virtual photons. In the case of the π^0 these two sources are the the $\gamma\gamma$ decay of π^0 and the corresponding Dalitz decays, which is also called an internal conversion. Similarly, direct real photon production is accompanied by direct virtual photon production, *i.e.* the emission of e^+e^- pairs.

The measured real direct photon spectrum is parameterized. The corresponding conversion electron spectrum of these is added to the electron cocktail. Figure 5.35 shows the measured direct photon spectrum with the cocktail parameterization [113].

The ratio of virtual direct photons to real direct photons depends on p_T because the phase space for dielectron emission increases with increasing p_T [133]. The very same effect is seen in the Dalitz decays of light neutral mesons, *i.e.* the Dalitz decay branching ratio relative to the two photon decay branching ratio is larger for the η meson than for the π^0. Consequently, the ratio of virtual and real direct photon emission increases with p_T or, to be more precise, a logarithmic dependence. Such dependence is implemented for internal conversion of virtual photons based on the theory [133].

Quarkonium and Drell-Yan

The contribution from di-electron decay of J/ψ and Υ becomes significant above ~ 2 GeV/c due to their large mass, while the contribution is negligible at low p_T. The p_T spectrum of J/ψ is measured up to 9 GeV/c via di-electron decay at mid-rapidity in $p + p$ collisions at PHENIX [123]. The p_T spectrum of J/ψ is fitted with a power-law function and m_T scaling. The average shape of these two function is used for the cocktail calculations. The deviation for

each function is taken into account as systematic error.

Unlike the case of J/ψ, there is not a measured p_T spectrum of Υ at mid-rapidity in $p+p$ collisions at $\sqrt{s} = 200$ GeV. Therefore, p_T spectrum of Υ is taken from NLO pQCD calculation [137]. The total cross section at mid-rapidity $(d\sigma/dy \mid_{y=0})$ in NLO pQCD is 6.89×10^{-6} mb. This value is compatible with the measured cross section at PHENIX and STAR and it is found the contribution of Υ is not significant [138, 139].

LO pQCD calculation is used for the estimation of the contribution of Drell-Yan process. The result from LO pQCD calculation is scaled by a factor of 1.5 to take into account the higher order effect. The contribution of Drell-Yan process becomes important as electron p_T increases. However, the contribution from Drell-Yan process is found not to be significant for the measured p_T range (up to 9GeV/c) compared to other background sources.

Implemented Cocktail in RUN5 and RUN6

Figure 5.36 and 5.37 show the invariant cross section for background electrons calculated by cocktail method in the $p+p$ collisions in RUN5 and RUN6, respectively.

Systematic Errors

Systematic errors are estimated for all cocktail ingredients, propagated to the corresponding electron spectra, and then added in quadrature to determine the total cocktail systematic error.

The following systematic errors are evaluated and listed up as follows.

- pion spectra: To evaluate this uncertainty the full cocktail calculation is repeated in $\pm 1\sigma$ uncertainty bands for the pion input, propagating the uncertainty in the pion spectra to the electron cocktail. With systematic uncertainty of 10 % almost independent on p_T, the pion input represents the largest contributor to the electron cocktail uncertainty up to ~ 5 GeV/c.

- light mesons: Since the contributions from all other mesons are much smaller than the contribution from η decay only η is of practical relevance. The systematic uncertainties are calculated from particle ratios listed above. This contribution is small compared to the uncertainty in the pion spectra and it depends on p_T only slightly.

- conversion material: The contribution from photon conversions obviously depends on the material present in the aperture. An analysis of fully reconstructed dielectrons from photon conversions suggests that this uncertainty is not larger than 10 %. Therefore, 10% systermatic error is assigned.

- K_{e3} decay: This contribution is estimated via the PISA simulation. Given the limited statistics of this calculation a 50 % systematic error is assigned, which is only relevant at low p_T, *i.e.* below 1 GeV/c.

- direct radiation: This contribution is directly propagated from the systematic error quoted for the direct photon measurement. It is relevant only at high p_T.

- quarkonium and Drell-Yan: The contribution from J/ψ di-electron decay among dominant in these contributions and becomes significant above 2 GeV/c. The p_T distribution of J/ψ is well measured at PHENIX [123] and 10% systematic error is assinged for the abusolute value for J/ψ contribution. In addition, the differece from two fit function (power-law and m_T scaling) is taken into accout as systematic error. 40% systematic error is assinged for the contribution from Υ based on the comparison of the total cross section between NLO pQCD and the result from PHENIX and STAR. The uncertainty of the contribution from Drell-Yan process is unclear. Therefore, 100% systematic error is assined for the contribution from Drell-Yan process to be conservative.

Figure 5.38 shows individual contributions to the cocktail systematic error and the resulting total systematic error. A fit of the total systematic error is shown in Fig. 5.38 , where the fitting function is parameterized as follows:

$$SE[\%] = p_0 \times \exp(p_1 \times p_\mathrm{T}) + p_2 + p_3 \times p_\mathrm{T} + p_4 \times p_\mathrm{T}^2 + p_5 \times p_\mathrm{T}^3. \qquad (5.29)$$
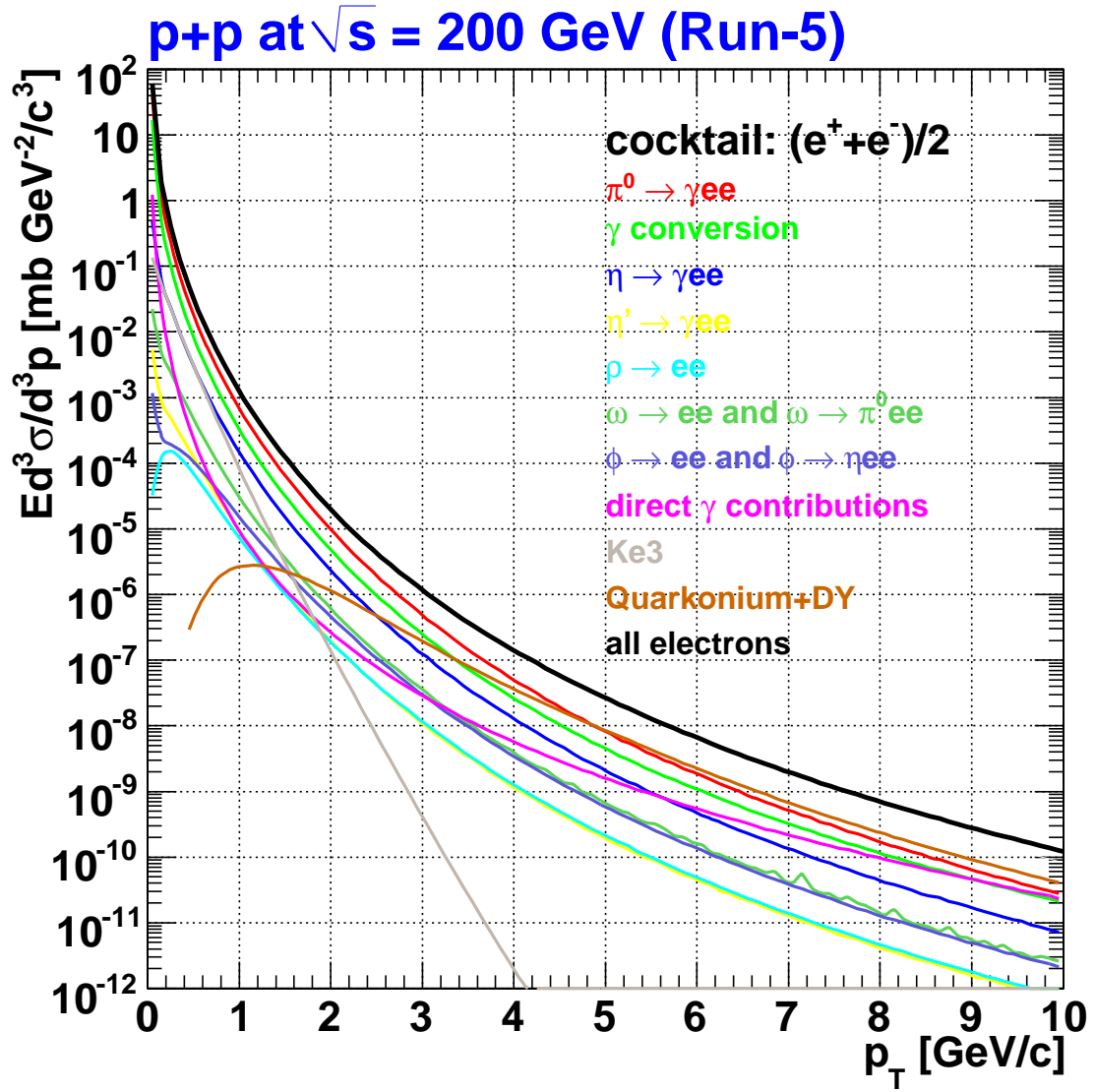
Figure 5.36: Invariant cross section of electrons from all sources considered in the RUN5 $p + p$ cocktail
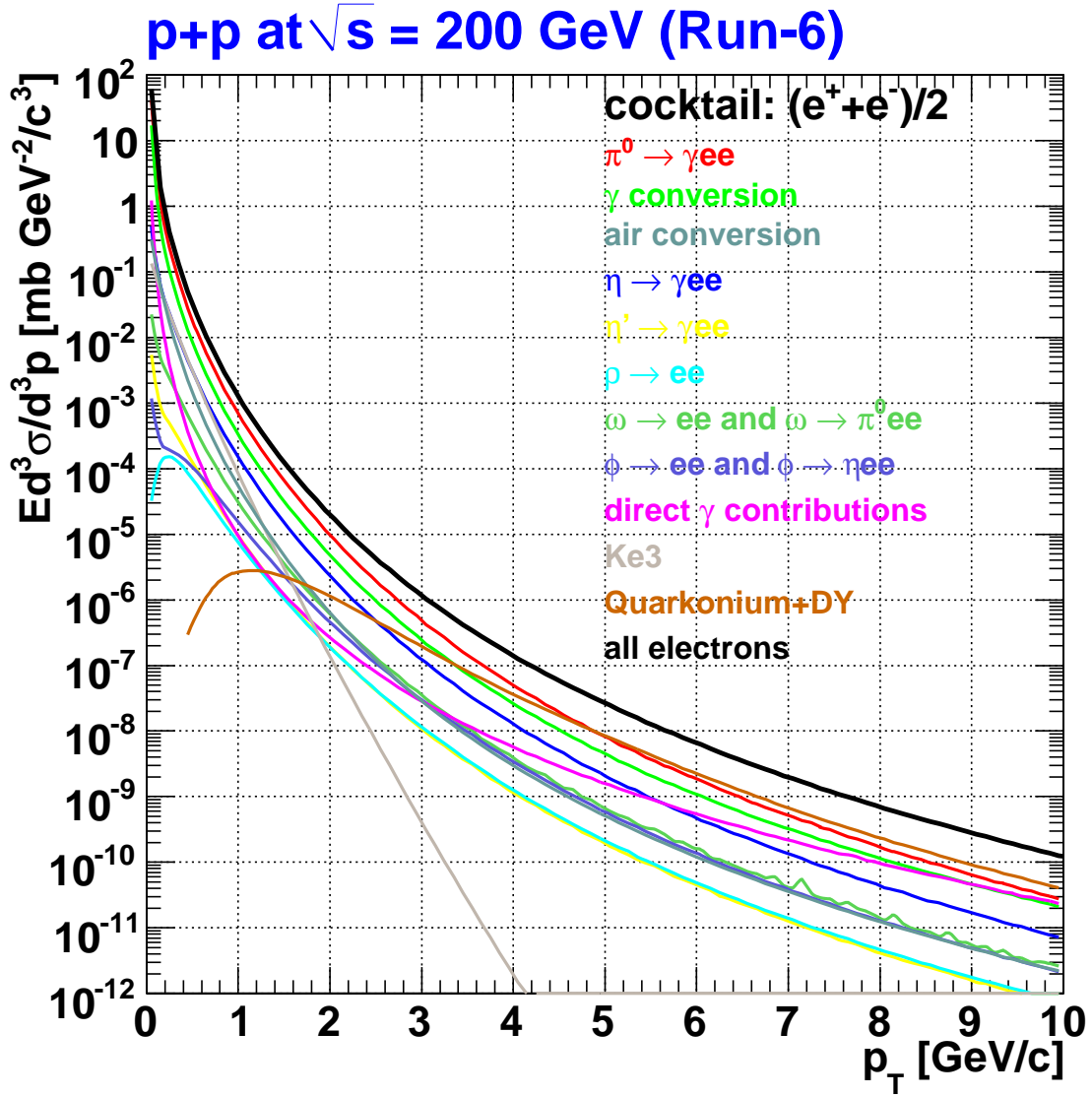
Figure 5.37: Invariant cross section of electrons from all sources considered in the RUN6 $p + p$ cocktail
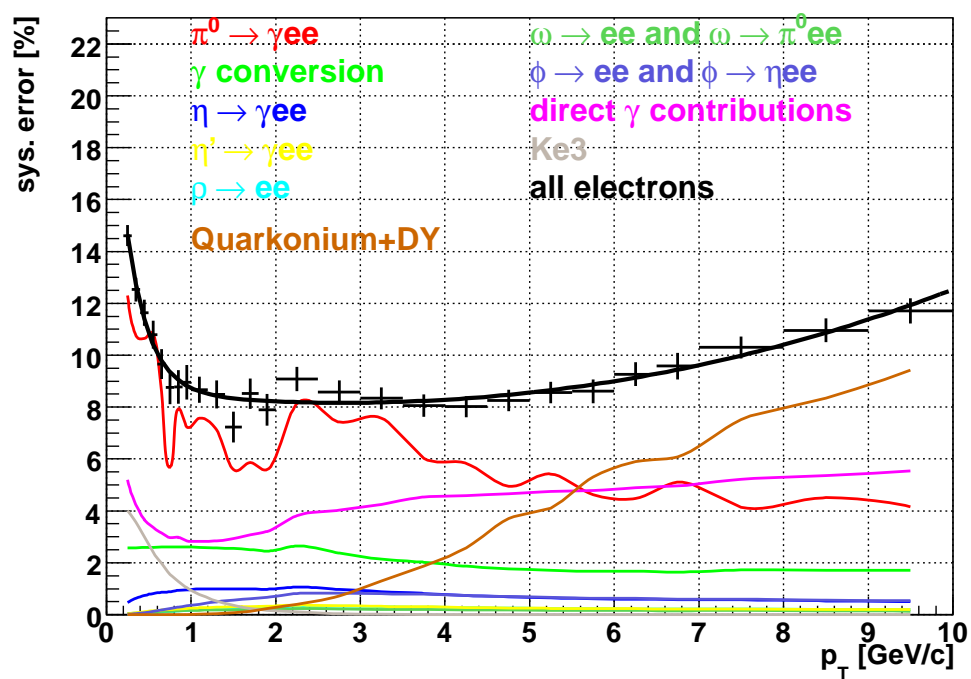
Figure 5.38: Individual contributions to the cocktail systematic error. The total error is depicted by the data points which are shown together with a fit.

5.6.2   Converter Method

The 'converter subtraction' method is used, which directly measures the photonic background and, thus, allows to extend the heavy-flavor measurement to the low p_T with good precision. Photonic and non-photonic electrons are obtained by measuring the difference of inclusive electron yields with and without a photon converter with precise and well known thickness: a brass sheet of 1.680 % radiation length (X_0).

The C run group in RUN5 is the physics run with the converter. The G5A run group in RUN5 is used to compare with the electron yield with that in C run group. Figure 5.39 shows the corresponding inclusive electron spectra. In Fig. 5.39, open symbols show the spectra in the converter run and closed symbols show the spectra in the non-converter run. Red squares show the results in the PH data set and blue circles show the results in the MB data set.
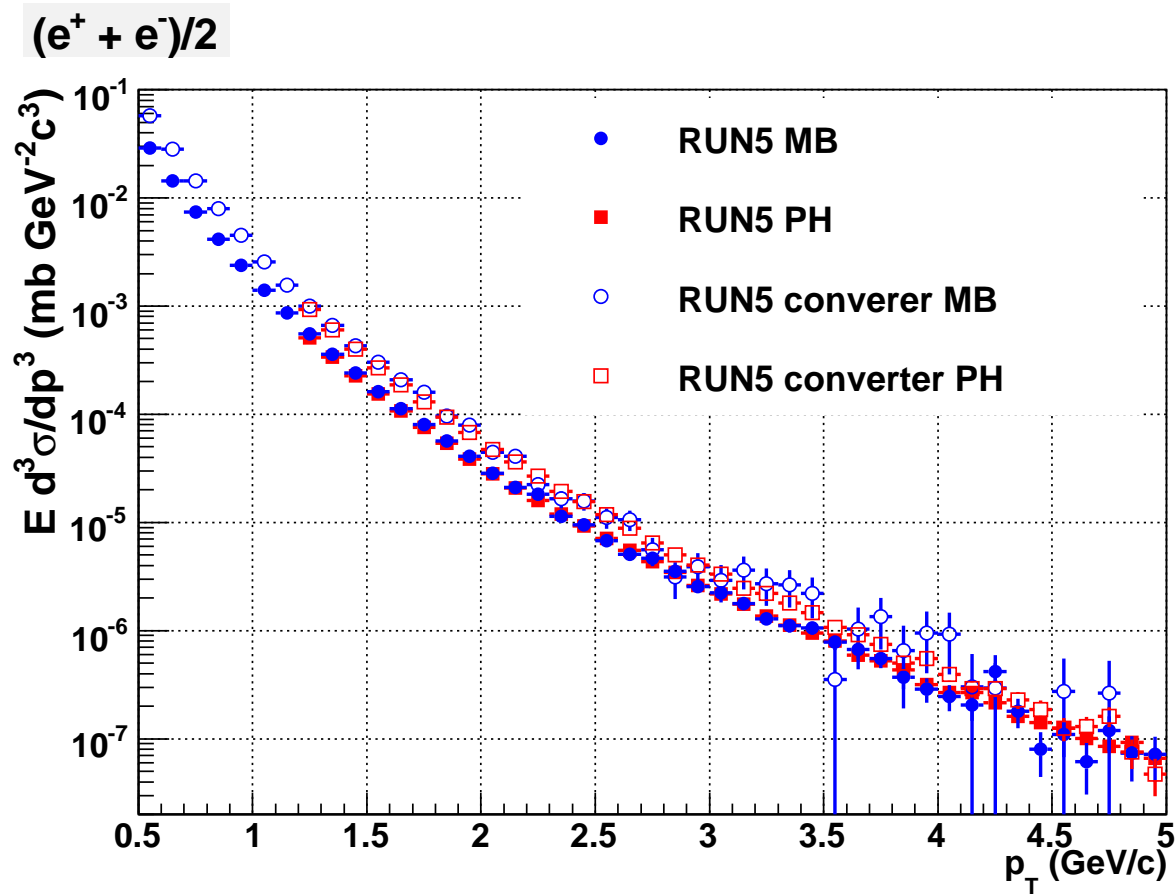
Figure 5.39: Invariant yields of inclusive electrons in coveter and non-converter runs. Open symbols show the spectra in the converter run and closed symbols show the spectra in the non-converter run. Red squares show the results in PH data set and blue circles show the results in MB data set.

Method to Subtract Photonic Electrons

Raw yields in coveter and non-converter runs can be expressed as the following relations:

$$N_e^{\text{Conv}-\text{out}} = N_e^\gamma + N_e^{\text{Non}-\gamma}, \tag{5.30}$$
$$N_e^{\text{Conv}-\text{in}} = R_\gamma N_e^\gamma + (1-\epsilon)N_e^{\text{Non}-\gamma}. \tag{5.31}$$

Here, $N_e^{\text{Conv}-\text{in}}$ ($N_e^{\text{Conv}-\text{out}}$) is the measured electron raw yield with (without) the converter. N_e^γ ($N_e^{\text{Non}-\gamma}$) is the photonic (non-photonic) electron yields. ϵ represents the blocking factor of the converter which is a small loss of $N_e^{\text{Non}-\gamma}$ due to the converter. R_γ is the multiplication factor of the photonic electron due to the existence of the converter. Then, N_e^γ and $N_e^{\text{Non}-\gamma}$ are determined as follows.

$$N_e^\gamma = \frac{N_e^{\text{Conv}-\text{in}} - N_e^{\text{Conv}-\text{out}}}{R_\gamma - 1 + \epsilon}, , \tag{5.32}$$

$$N_e^{Non-\gamma} = \frac{R_\gamma N_e^{\text{Conv}-\text{out}} - N_e^{\text{Conv}-\text{in}}}{R_\gamma - 1 + \epsilon}. \tag{5.33}$$

Non-photonic electrons still include a small background which needs to be subtracted to obtain the electrons from semi-leptonic decay of heavy flavor. These are K_{e3} electrons ($E\frac{d^3\sigma^{K_{e3}}}{dp^3}$), $\rho \to e^+e^-$ ($E\frac{d^3\sigma^{\rho\to e^+e^-}}{dp^3}$) ,$\omega \to e^+e^-$ ($E\frac{d^3\sigma^{\omega\to e^+e^-}}{dp^3}$), $J/\psi,\Upsilon \to e^+e^-$ ($E\frac{d^3\sigma^{J/\psi\ \Upsilon\to e^+e^-}}{dp^3}$) and Drell-Yan process. The spectrum of the electrons from semi-leptonic decay of heavy flavor (single non-photonic electrons) is determined as follows.

$$
\begin{aligned}
E\frac{d^3\sigma^{HQ}}{dp^3} &= E\frac{d^3\sigma^{non-\gamma}}{dp^3} - E\frac{d^3\sigma^{K_{e3}}}{dp^3} - E\frac{d^3\sigma^{\rho\to e^+e^-}}{dp^3} - E\frac{d^3\sigma^{\omega\to e^+e^-}}{dp^3} \\
&\quad - E\frac{d^3\sigma^{J/\psi,\Upsilon\to e^+e^-}}{dp^3} - E\frac{d^3\sigma^{DY}}{dp^3}.
\end{aligned}
\tag{5.34}
$$

The yield of K_{e3} electrons, $\rho \to e^+e^-$, $\omega \to e^+e^-$, $J/\psi\ \Upsilon \to e^+e^-$ and Drell-Yan process are determined at the cocktail calculation. Obtained $E\frac{d^3\sigma^{HQ}}{dp^3}$ still have little background, di-electron decay of light mesons. Such background is negligible.

R_γ and the Blocking Factor

The blocking factor is determined to be $2.1\% \pm 1\%$ from the comparision of the conversion peak at the beam pipe between the simulation and real data [114, 118].

R_γ is the crucial parameter in the converter subtraction method. The source of photonic electron is a mixture of mesons (π^0, η, η', ω, and ϕ) decaying into real or virtual photons with their different p_T slopes. However, the photonic electron contributions from π^0 decays occupies almost of all photonic electrons and determine R_γ.

To calculate R_γ, it is necessary to know exactly the amount of material amounts near the interaction point. Table 5.10 shows the list of each material thickness. The converter sheet is rolled just around beam pipe in converter runs. Conversion probability (P^{Conv}) in Tab. 5.10 is calculated for the case of electrons emitted from photon with $p_\text{T} = 1.0$ GeV/c [43]. The

Table 5.10: Radiation length (L) of each material near the interaction point. Conversion probability (P^{Conv}) is calculated for the case of electrons emitted from photon with $p_{\text{T}} = 1.0$ GeV/c [43].

Material	L (X_0 [g/cm^2])	P^{Conv}
Beam pipe (Be)	0.288 %	0.201 %
Air ($r < 30$ cm)	0.099 %	0.069 %
Total	0.387 %	0.270 %
Converter (brass)	1.680 %	1.226 %

equivalent conversion probability of a virtual photon in π^0 Dalitz decay (P^{Dalitz}) is 0.598% [43]. R_γ can be estimated with these values for the photon with $p_{\text{T}} = 1.0$ GeV/c.

$$R_\gamma = \frac{P^{\text{Conv}} + P^{\text{Dalitz}} \text{ (with converter)}}{P^{\text{Conv}} + P^{\text{Dalitz}} \text{ (without converter)}} \sim 2.41. \tag{5.35}$$

To obtain more realistic R_γ for considering geometrical effects and p_{T} dependence of the conversion provability, the PISA simulations for photon conversions from π^0 are performed with (without) the converter. We use the spectra of the light mesons which are used cocktail calculation. The R_γ for π^0 ($R_\gamma^{\pi^0}$) is determined from the the simulation as bellow.

$$R_\gamma^{\pi^0} = 2.37 + 0.07 \tanh(0.6 p_{\text{T}}). \tag{5.36}$$

The η meson is the second dominant source of the photonic electrons. Since η mass is larger than π^0 mass, the phase space of η Dalitz decay is slightly than π^0. The relative branching ratio (Dalitz decay)/(two γ decay) is 1.2% for π^0 and 1.5 % for η [46]. This difference makes R_γ^η smaller than $R_\gamma^{\pi^0}$. R_γ for η (R_γ^η) is determined as bellow.

$$
\begin{aligned}
R_\gamma^\eta &= \frac{P_{\text{bp}} + P_{\text{air}} + P_{\text{Dalitz}}^\eta + P_{\text{conv}}}{P_{\text{bp}} + P_{\text{air}} + P_{\text{Dalitz}}^\eta} \\
&\sim 1 + (R_\gamma^{\pi^0} - 1) \times \frac{0.87\%}{1.1\%}.
\end{aligned} \tag{5.37}
$$

Contributions from other mesons which undergo Dalitz decay (η', ρ, ω, and ϕ) are small (6 % at $p_{\text{T}} = 3$ GeV/c, and smaller at lower p_{T}). The particle ratios used in the cocktail calculation are used to calculate total R_γ. The uncertainties in the particle ratios are included in the systematic uncertainties of R_γ.

In this method, it is essential that the amount of material is accurately modeled in the simulation. We compare the yield of identified photon conversion pairs in the data and in the simulation, and conclude that the simulation reproduces R_γ within $\pm 2.7\%$. Figure. 5.40 and 5.41 show R_γ as a solid curve, which is compared with the ratio of inclusive electron yield with/without photon converter (R_{CN})

R_{CN}

R_{CN} is defined as the ratio of inclusive electron yield with/without photon converter. Figure. 5.40 and 5.41 show R_{CN} measured in RUN5 MB and PH data, respectively.
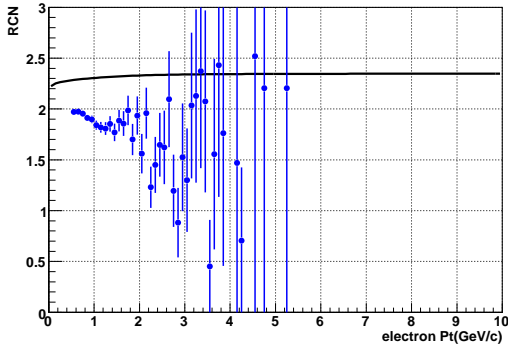
Figure 5.40: The ratios of the electron yield in the converter run over the non-converter run (R_{CN}) as a function of electron p_T in RUN5 MB data. The black line is $R_\gamma(p_T)$
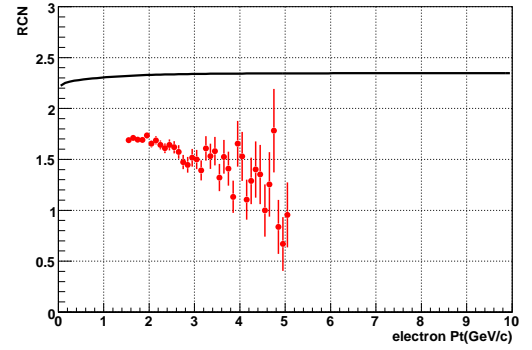
Figure 5.41: The ratios of the electron yield in the converter run over the non-converter run (R_{CN}) as a function of electron p_T in RUN5 PH data. The black line is $R_\gamma(p_T)$

If there are no non-photonic contribution , then $R_{CN} = R_\gamma$. Figure 5.40 and 5.41 show that R_{CN} gradually decreases with increasing p_{Te}, while R_γ slightly increases with p_T. The difference between R_{CN} and R_γ proves the existence of non-photonic electrons. The systematic error of R_{CN} is originated from the instability of the efficiency of electron reconstruction during the C run group and the G5A run group. We assign 1% systematic error for R_{CN}.

Converter Method for RUN6

Since there are no converter run during RUN6, we use R_{CN} measured in RUN5 for RUN6 converter analysis. Statistics is improved in RUN6 and this is the great advance in RUN6 data analysis. However, the statistical error of non-photonic electron yield in the converter method is not improved in RUN6, since the statistics in the converter method is determined by the RUN5 converter run. Thus, we obtain only photonic electron spectrum to compare with cocktail. The comparison with photonic electrons in the cocktail between the measured photonic electrons is used to determine the normalization factor of cocktail. The difference of the photonic electron between RUN5 and RUN6 due to the absence of the Helium bags is taken into account as follows.

$$E\frac{d^3\sigma^\gamma}{dp^3} = \left(E\frac{d^3\sigma^{incl}}{dp^3} - E\frac{d^3\sigma^{air}}{dp^3}\right) \times \frac{R_{CN}(RUN5)-1+\epsilon}{R_\gamma(p_T)-1+\epsilon}, \tag{5.38}$$

$$E\frac{d^3\sigma^{non-\gamma}}{dp^3} = \left(E\frac{d^3\sigma^{incl}}{dp^3} - E\frac{d^3\sigma^{air}}{dp^3}\right) \times \frac{R_\gamma(p_T)-R_{CN}(RUN5)}{R_\gamma(p_T)-1+\epsilon}. \tag{5.39}$$

Here,

- $E\frac{d^3\sigma^{incl}}{dp^3}$ is the spectrum of inclusive electrons in RUN6.

- $E\frac{d^3\sigma^{air}}{dp^3}$ is the spectrum of electrons from air conversion, which is determined by the cocktail calculation without He bag.

- $R_{CN}(RUN5)$ is the R_{CN} which is measured in RUN5.

Systematic Errors

The systematic error of converter analysis is determined as follows. The details of each systematic error are already described.

- $R_\gamma(p_T)$: The systematic error of $R_\gamma(p_T)$ is assigned 0.062.

- R_{CN}: 1% systematic error is assinged to R_{CN}.

- ϵ: 0.01 is assigned as systematic error.

The systematic error is defined as the quadratic sum of the deviation from the above change of each parameters.

5.6.3   Comparison of the Results from Two Methods

The spectra of photonic and non-photonic electrons are obtained from the two methods, cocktail method and converter method. The results from these methods should be consistent with each other. This comparison can be used to reduce the uncertainty of the cocktail. The spectrum shape of the cocktail is determined by the spectrum shape of the parent mesons, dominated by π^0. At high p_T, the acceptance curve for parent mesons becomes almost constant in p_T. The shape and slope of the spectrum is well determined, while it is more difficult to determine the absolute normalization of the data. Therefore in the cocktail calculation, the shape of the spectrum can well be determined. It is useful to tune the absolute normalization of the cocktail from the comparison between the measure photonic electrons and the cocktail at high p_T.

Photonic Electrons

The photonic electrons are obtained according to Eq. 5.32 and Eq. 5.38. The spectra of the measured photonic electrons are compared with the photonic component in the cocktail. Figure 5.42 and 5.43 show the ratio of measured/cocktail photonic electron spectra in RUN5 and RUN6, respectively. In Fig. 5.42 and 5.43, blue circles show the ratios in MB data and red squares show the ratios in PH data. Systematic error of the cocktail is also shown as the dotted line in these figures. The spectra of the cocktail are consistent with those of the measure photonic electrons within the systematic error of the cocktail.

Normalization of Cocktail

We tune the absolute normalization of the photonic component in the cocktail from the comparison with the measured photonic electrons and the photonic electrons in the cocktail. The shape and slope of the meson spectra, which is used as the input of cocktail, is determined with the best precision for high p_T at PHENIX.

The ratios of measured/cocktail photonic electron spectra above 1.7 GeV/c are fitted with a constant, which is expected behavior. The fitted lines are shown as striate lines in Fig. 5.42 and
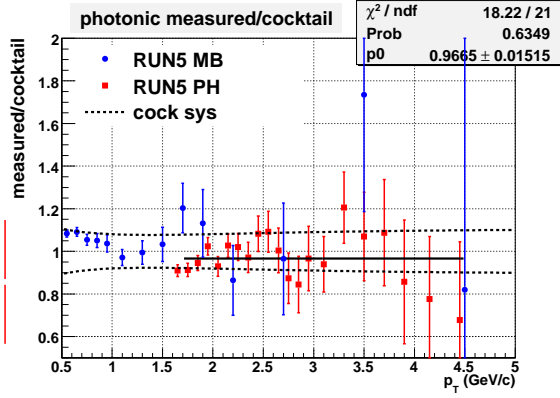
Figure 5.42: The ratio of measured/cocktail photonic electron spectra in RUN5. Blue circles show the ratios at MB data and red squares show the ratios in PH data. Dotted line show systematic error of the cocktail.
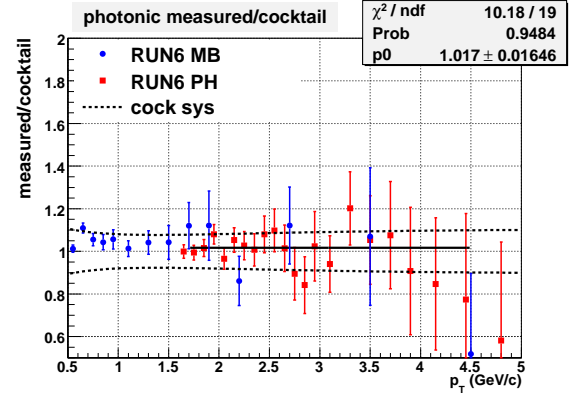
Figure 5.43: The ratio of measured/cocktail photonic electron spectra in RUN6. Blue circles show the ratios at MB data and red squares show the ratios in PH data. Dotted line show systematic error of the cocktail.

Fig. 5.43. The fitted values are 0.97±0.02 and 1.017 ± 0.02 in RUN5 and RUN6, respectively. We calculate the re-normalization factor of the cocktail as 0.992± 0.025 for RUN5 and RUN6, since the normalization factor should be common within RUN5 and RUN6.

After the rescaling, systematic error of the photonic component in the cocktail is determined as follows.

$$SE_R^{photo}(p_T) = \sqrt{(SE^{photo}(p_T) - SE^{photo}(1.9GeV/c))^2 + (\frac{0.025}{0.992})^2}, \qquad (5.40)$$

where $SE^{photo}(p_T)$ is the systematic error of the photonic component before the normalization and $SE_R^{photo}(p_T)$ is the systematic error of the photonic component after the normalization. Since the normalization point is 1.9GeV/c, the deviation from 1.9GeV/c is taken into account as the systematic error. Total systematic error is defined as the quadratic sum of $SE_R^{photo}(p_T)$ and the systematic error of non-photonic background that is dominated by J/ψ. Figure 5.44 show the systematic error of the cocktail. Black line shows the systematic error of the photonic component in the cocktail before the normalization. Red line shows the systematic error of the photonic component after the normalization. Orange line shows the systematic error of non-photonic background and blue line shows the calculated total systematic error.

5.6.4 Results

The spectra of the single non-photonic electron are determined via two independent method, cocktail method and converter method in RUN5 and RUN6. Converter method could determine the spectrum of the single non-photonic electrons at low p_T with good precision as already described. On the other hand, cocktail method provides better precision than converter method towards high p_T, *e.g.* for $p_T \sim 1.5$ GeV/c, since the converter method starts to suffer from a lack of statistical precision and the cocktail input is known with small systematic uncertainties at high p_T. Therefore, we use cocktail method at high p_T and converter method at low p_T.
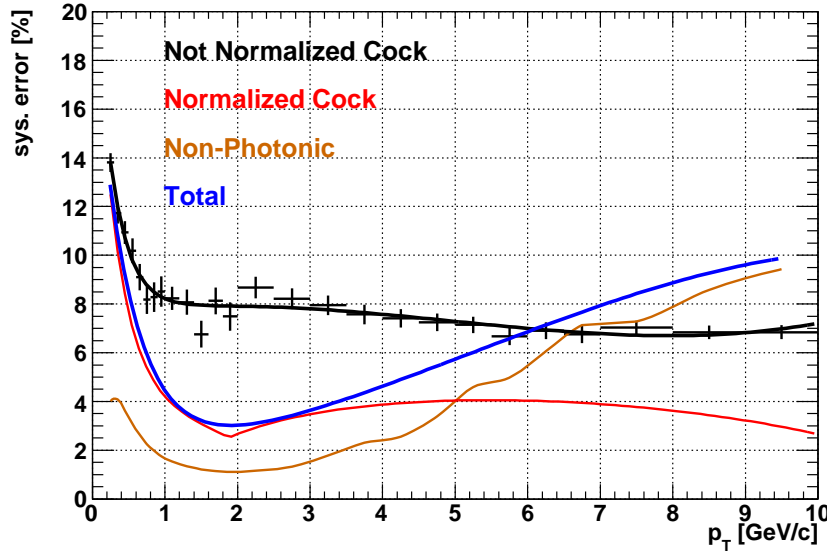
Figure 5.44: The systematic error of the cocktail. Black line show the total systematic error of the cocktail before the normalization of the cocktail.Red line shows the systematic error after the normalization.

RUN5 and RUN6 Results

Figure 5.45 and 5.46 show the obtained invariant cross section of the single non-photonic electrons with systematic errors in RUN 5 and RUN6, respectively. 9.9% systematic error for the abusolute normalization is **NOT** included in Fig.5.45 and 5.46. Circle points show the result from converter method and triangle points show the result from cocktail method. Open symbols show the result from MB data and closed symbols show the result from PH data. Closed squares show the result from PH data with tight eID cut.

Combined Result

The result from converter method in RUN5 is used for low p_T and the combined result in RUN5 and RUN6 from cocktail method is used for high p_T. Since the precision of the converter analysis is determined by the statistics at the converter runs in RUN5, we use only the result from converter method at RUN5 MB data for low p_T. When the results from RUN5 and RUN6 with cocktail method are combined, the results from PH data are used to improve the statistics for high p_T. BLUE (Best Linear Unbiased Estimate) method is applied to combine the results of RUN5 and RUN6 [134, 135], since a part of systematic errors of RUN5 and RUN6 are correlated. Error sources are summarized at Table 5.11. Error sources are divided into three types in this thesis as follows according to the nature of the error.

- **TYPE A** Point-to-point errors.

- **TYPE B** momentum-correlated errors.

- **TYPE C** Absolute normalization errors.

The averages and errors were determined according to BLUE as bellow.

$$< r > \; = \; \frac{r_{run5}(\sigma_{run6}^2 - \rho\sigma_{run5}\sigma_{run6}) + r_{run6}(\sigma_{run5}^2 - \rho\sigma_{run5}\sigma_{run6})}{\sigma_{run5}^2 + \sigma_{run6}^2 - 2\rho\sigma_{run5}\sigma_{run6}}, \tag{5.41}$$

$$\sigma \; = \; \sqrt{\frac{\sigma_{run5}^2\sigma_{run6}^2(1 - \rho^2)}{\sigma_{run5}^2 + \sigma_{run6}^2 - 2\rho\sigma_{run5}\sigma_{run6}}}. \tag{5.42}$$

Here, r_{runi} and σ_{runi} are respectively the average of the yield of the single non-photonic electrons and total error in RUNi (i=5 or 6). ρ is the correlation coefficient between RUN5 and RUN6. ρ is defined as

$$\rho = \frac{\sum_\alpha \rho^\alpha \sigma_{run5}^\alpha \sigma_{run6}^\alpha}{\sigma_{run5}\sigma_{run6}}, \tag{5.43}$$

where α is the type of error. α = A, B or C. Total errors were determined as below.

$$\sigma_{runi} = \sqrt{(\sigma_{runi}^{stat})^2 + (\sigma_{runi}^{sys})^2}. \tag{5.44}$$

Table 5.11: Summary of error source

error source	correlation run5/6 (Type)
statistics	0 % (A)
PISA geometries	0%(B)
eID cut	0%(B)
cocktail calculation	100%(B)
trigger efficiency	0% (B)

The combined results from cocktail method are shown in Figure 5.47 and 5.48. χ^2/ndf is 17.2/33 with the standard eID cuts from 1.7GeV/c to 5GeV/c and is 3.2/7 with the tight eID cut from 1.7GeV/c to 9GeV/c. The values indicate the results in RUN5 and RUN6 are consistent.

The spectrum of the single non-photonic electron is shown in Figure 5.49. FONLL calculation, which is Fixed-Order plus Next-to-Leading-Log perturbative QCD calculation [77], is also shown in Fig 5.49.
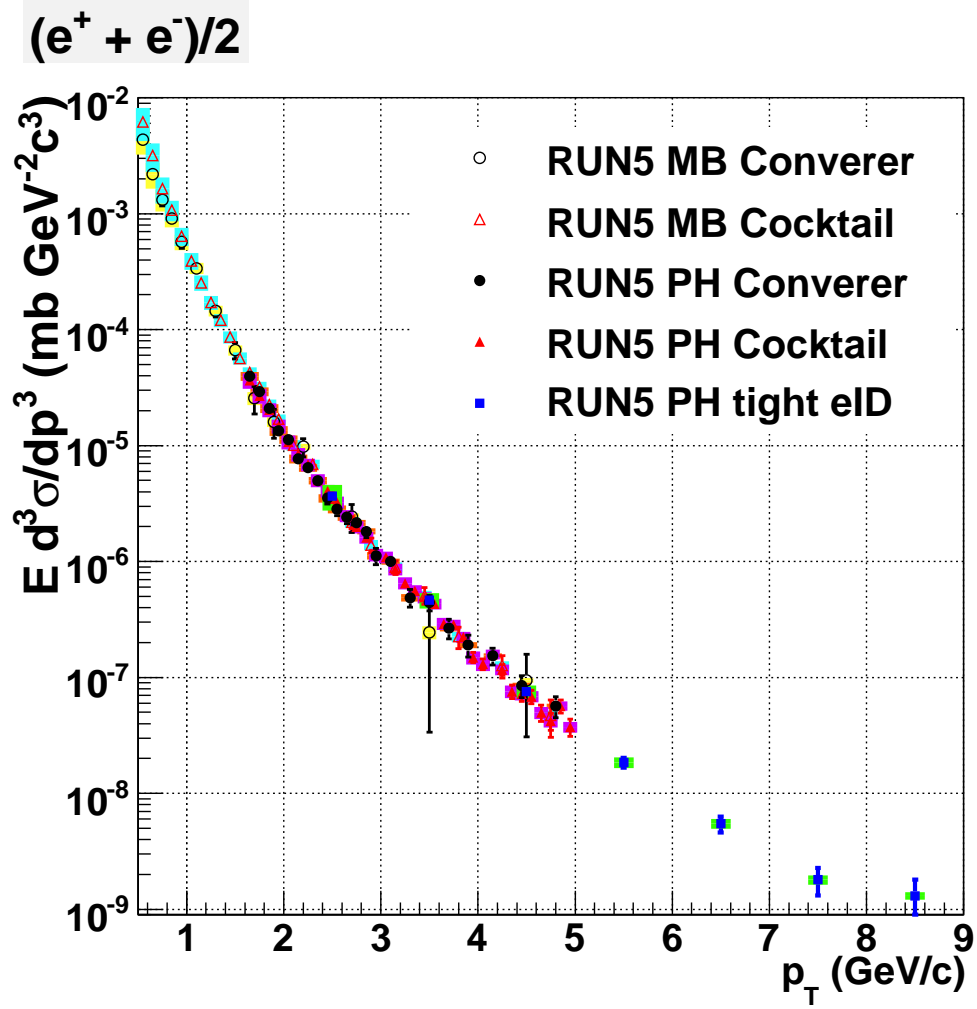
Figure 5.45: The invariant cross section of electrons from heavy flavor decay in RUN5 MB and PH data. Circle points show the result from converter method and triangle points show the result from cocktail method. Open symbols show the result at MB data and closed symbols show the result at PH data. Closed squares show the result at PH data with tight eID cut.
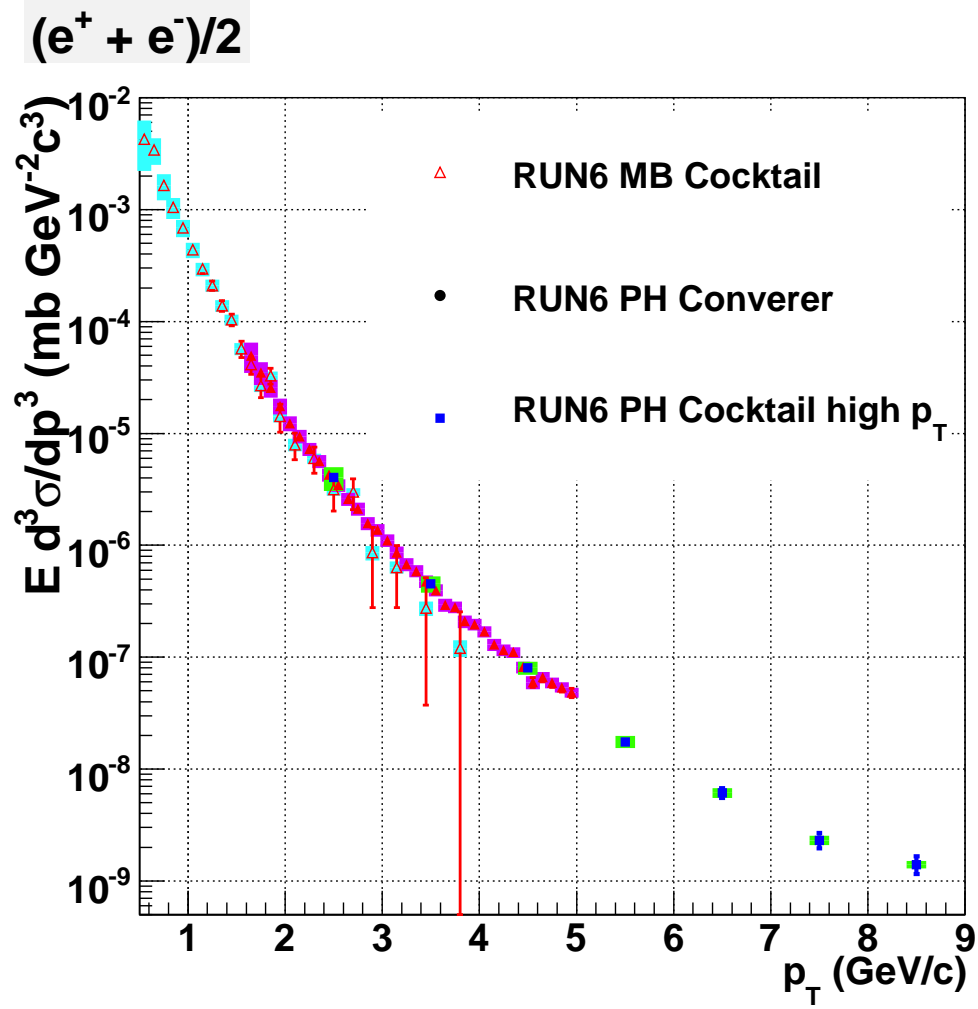
Figure 5.46: The invariant cross section of electrons from heavy flavor decay in RUN6 MB and PH data. Circle points show the result from converter method and triangle points show the result from cocktail method. Open symbols show the result at MB data and closed symbols show the result at PH data. Closed squares show the result at PH data with tight eID cut.
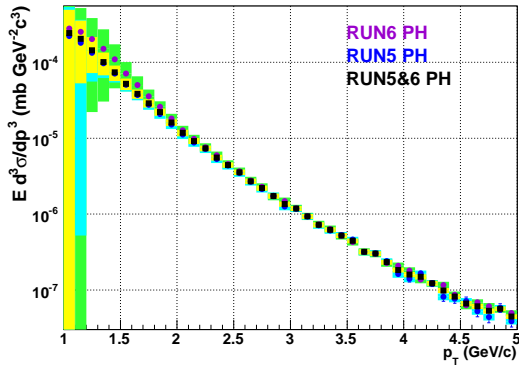
Figure 5.47: The invariant cross section of electrons from heavy flavor decay in RUN6 PH data. Red points show the results from cocktail method and black points show the result at high p_T extension.
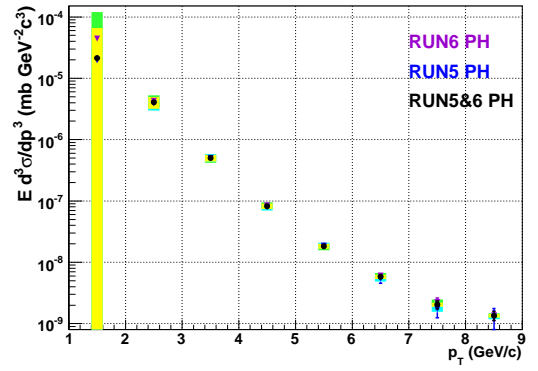
Figure 5.48: The invariant cross section of electrons from heavy flavor decay in RUN6 PH data. Red points show the results from cocktail method and black points show the result at high p_T extension.
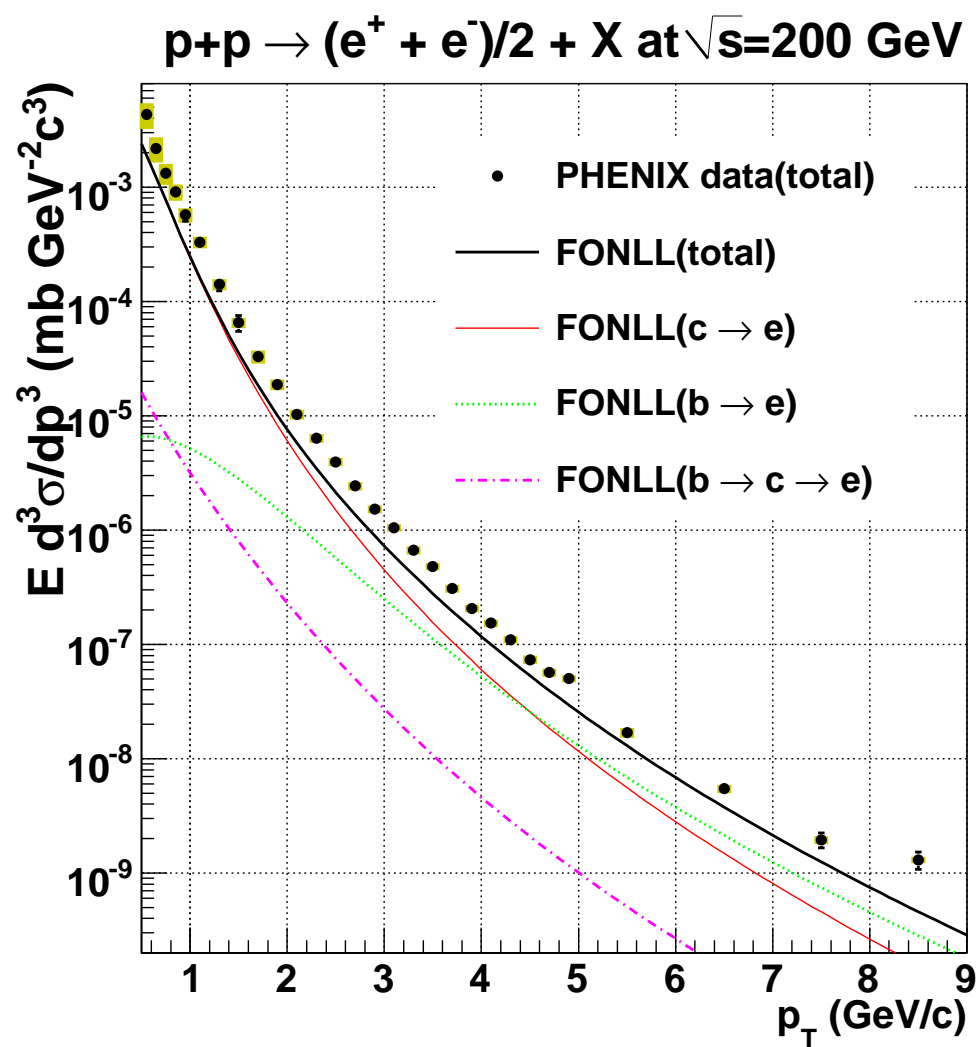
Figure 5.49: The spectrum of the single non-photonic electrons in RUN5 and RUN6 with FONLL calculation [77].

5.7   Overview of Extraction of $(b \to e)/(c \to e + b \to e)$

The spectrum of the electron from semi-leptonic decay of charm and bottom is obtained in the previous analysis. The fraction of the single electrons from bottom in single non-photonic electrons $((b \to e)/(c \to e + b \to e))$ is crucial parameter to understand the behavior of the heavy quarks in the hot and dense matter. In this section, the method to extract the fraction utilizing the correlation of the single non-photonic electrons and the associated hadrons is described. ERT triggered data in RUN5 and RUN6 is used in the correlation analysis.

5.7.1   Extraction Method

The extraction of $(b \to e)/(c \to e+b \to e)$ by utilizing the correlation of the single non-photonic electrons and the associated hadrons is based on partial reconstruction of $D^0 \to e^+ K^- \nu_e$ decay. Unlike charge sign pairs of trigger electrons for $2.0 < p_T < 7.0$ GeV/c and associated hadrons for $0.4 < p_T < 5.0$ GeV/c are reconstructed as partial reconstruction of $D^0 \to e^+ K^- \nu_e$ decay. Since most of charged kaons do not reach the hadron identification detector (TOF and EMCal) due to their short life time, the reconstruction efficiency of identified charged kaon is rather small. Therefore, kaon identification is not performed in the analysis and inclusive hadrons are assigned to be kaons. As a result, this analysis is NO Particle IDentified (NO PID) partial reconstruction of D^0.

Determination of the background is crucial for this analysis, since the signal to background ratio is not good ($\sim 1/10$). There are two main sources in the background. The one is the combinatorial background from electrons and hadrons, where the selected trigger electron is not from semi-leptonic decay of heavy flavor. The other is the combinatorial background, where the trigger electron is the single non-photonic electron and the associated hadron is not from heavy flavor decay. The best way to subtract these backgrounds is to use like sign charge pairs of electrons and hadrons. This subtraction method is essential in this analysis. Since electron hadron pairs with opposite charge signs are produced only by weak decay, the background subtraction using like sign pairs cancel out the combinatorial background completely for the contribution of the trigger electron from $e^+ e^-$ pair creation. The electrons from $e^+ e^-$ pair creation are most in all background of the trigger electrons. Moreover, most of the associated hadrons not from heavy flavor decay are from jet fragmentation. The background subtraction using like sign pair cancel out most of contribution from the combination of the single non-photonic electrons and the hadrons from jet fragmentation, since jet is basically charge independent.

Figure 5.50 shows a conceptual view of invariant mass distributions of unlike sign pairs and like sign pairs. N_{tag} is defined as the number of unlike sign electron-hadron pair entries (N_{unlike}) minus number of like sign electron-hadron pair entries (N_{like}). As already described, extracted signals N_{tag} are interpreted as the electron-hadron pairs mostly from heavy flavor decays, which are reconstructed partially such as $D/\bar{D} \to e^{\pm} K^{\mp} X$ decay. N_{tag} contains inclusive signals from other heavy flavored hadons (D^+,B^+,B^0 etc) and the remaining contribution from the associated hadron which is not from heavy flavor decay. These effect are evaluated by using the Monte-Carlo event generators.

The analysis procedure is as follows.
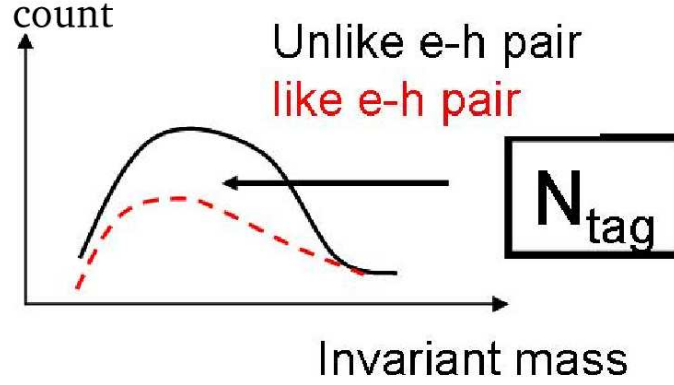
Figure 5.50: A conceptual view of invariant mass distributions of unlike sign pairs and like sign pairs.

Tagging efficiency (ϵ_{data}), which is a similar variable as a conditional probability of the detection of an associated hadron in PHENIX detector when the electron from semi-leptonic decay of heavy flavored hadron is detected, is defined as below.

$$\epsilon_{data} \equiv \frac{N_{tag}}{N_{e(HF)}} = \frac{N_{c \to tag} + N_{b \to tag}}{N_{c \to e} + N_{b \to e}}, \tag{5.45}$$

where $N_{e(HF)}$ is the number of electrons from semi-leptonic decay of heavy flavor. $N_{c(b) \to e}$ is the number of electrons from semi-leptonic decay of charmed (bottomed) hadrons. $N_{c(b) \to tag}$ is the number of reconstructed signals (N_{tag}) for charm (bottom) production. Since N_{tag} include the contribution only from the single electrons from heavy flavor, ϵ_{data} could be written by only charm and bottom terms. ϵ_{data} is determined from real data analysis. The analysis detail to obtain ϵ_{data} is written at Sec. 5.8.

As a next step, tagging efficiency in the case of charm production ϵ_c and tagging efficiency in the case of bottom production ϵ_b are defined as bellow.

$$\epsilon_c \equiv \frac{N_{c \to tag}}{N_{c \to e}}, \qquad \epsilon_b \equiv \frac{N_{b \to tag}}{N_{b \to e}}. \tag{5.46}$$

$\epsilon_{c(b)}$ is determined from the Monte-Carlo event generators. Since the extracted signal N_{tag} is dominated by decay products of heavy flavored hadrons, tagging efficiency is determined by decay kinematics in the first order. Therefore, we can determine $\epsilon_{c(b)}$ with good precision using the simulation. The analysis detail to obtain $\epsilon_{c(b)}$ is written at Sec. 5.9.

Then, the fraction of bottom contribution to the electrons from heavy flavor is determined as,

$$\frac{N_{b \to e}}{N_{c \to e} + N_{b \to e}} = \frac{\epsilon_c - \epsilon_{data}}{\epsilon_c - \epsilon_b}, \tag{5.47}$$

5.7.2   Electrons from $e^+ e^-$ Creation

The contribution of the trigger electrons from $e^+ e^-$ creation must be canceled out in the subtraction of like sign electron-hadron pairs. This is the most important issue in this analysis. This

fact is confirmed by PYTHIA event generator [49, 50]. Figure 5.51 shows invariant mass distributions of unlike sign electron-hadron pairs (black) and like sign electron-hadron pairs (red) in $| y | < 0.4$, where the trigger electron is from e^+e^- creation in PYTHIA events. Subtracted invariant mass distribution of electron-hadron pairs is shown in the right panels. Tagging effi-
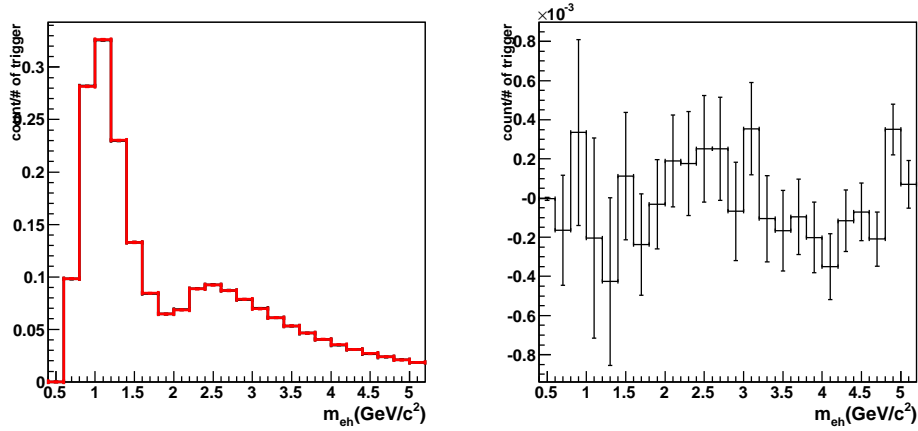
Figure 5.51: The invariant mass distribution of electron-hadron pairs in $| y | < 0.4$, when the trigger electron is photonic electron. In left panels, black lines are unlike charge sign pairs and red lines are like charge sign pairs. Subtracted invariant mass distribution of electron-hadron pairs was shown in the right panels.

ciency for the electrons from e^+e^- creation, ϵ_{photo} is -0.00051$\pm$ 0.00097 in $| y | < 0.4$. This result confirms the issue that the contribution of the electrons from e^+e^- creation is canceled out completely.

5.8 Correlation Analysis at Real Data

In this section, tagging efficiency in the real data analysis, ϵ_{data}, is obtained. ERT triggered data in RUN5 and RUN6 is used in this correlation analysis.

5.8.1 Used Cut for the Correlation Analysis

The following cuts are used to select the trigger electrons and the associated hadrons in real data and the simulation.

- **Event Cut**:$-25 < $ bbcz $ < 25$ (cm)

- **Electron Cut**: The standard electron cut is applied for the tracks with $2 < p_\mathrm{T} < 5$ GeV/c and the tight electron cut is applied above 5 GeV/c. The details of this cut are described in Sec. 5.3.4
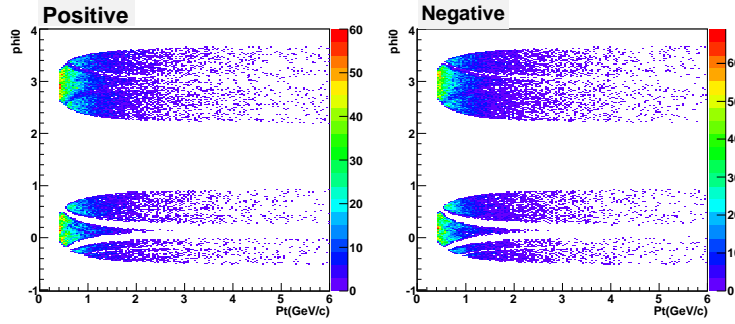
Figure 5.52: Phase spaces of positive charged hadron with the geometrical cut in RUN5.

- **Hadron Cut**: `quality`> 15 and `n0`<0 (RICH veto) cut is applied to select hadron for the charged particles with $0.4 < p_T < 5.0$ GeV/c. The selected hadron tracks are analyzed with the kaon hypothesis, that is, the selected particles have kaon mass.

- **Acceptance Filter**: Since the acceptance (phase space) for positive charged particles and negative charged particles is different due to the detector geometry of PHENIX, the effect of the difference in the phase space needs to be corrected for the subtraction of the like charge sign pairs. The fiducial cut is applied to make the phase space of negative and positive charged tracks identical as the correction for the phase space effect. Figure 5.52 shows the phase spaces of associated negative charged particle and positive charged particle with the geometrical cut.

- **Electron Pair Cut**: RICH veto cut (`n0`<0) used in hadron cut does not reject electron contamination in the selected hadrons completely due to dead area and limited acceptance of RICH. Since about a half of the measured electrons above 2 GeV/c is produced via the $e^+ e^-$ pair creation, there are strong charge correlation of electron pairs in the events where the trigger electron is found. It is found that the effect of such electron contamination in the hadron tracks is not negligible. The electron contamination is rejected using M_{ee}, which is the invariant mass between identified trigger electrons and the associated tracks where their mass is assigned to be electron mass (0.511MeV). Most of the electron pairs are produced from π^0 Dalitz decay and γ conversion at the beam pipe. They could be identified via the reconstructed invariant mass distribution of $e^+ e^-$ pair as the peaks at the low mass region. Figure 5.53 shows the M_{ee} distribution of unlike and like pairs of the selected electron and hadron in RUN6. In Fig 5.53, black points show unlike charge sign pairs and red points show like charge sign pairs. The clear peak is shown at the low mass region and $M_{ee} > 0.08$GeV is required for the rejection of these electron pairs.

5.8.2 Calculation of ϵ_{data}

Tagging efficiency in the real data, ϵ_{data} is calculated with the trigger electron for $2.0 < p_T < 7.0$ GeV/c.
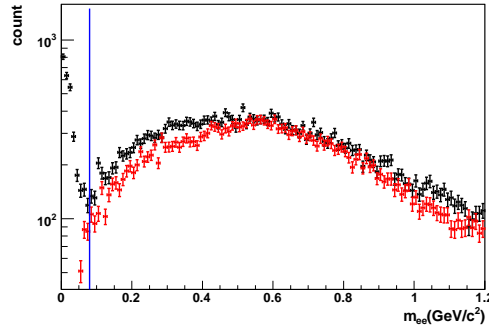
Figure 5.53: M_{ee} distribution of unlike sign and like sign pairs of the selected electron and hadron in RUN6. Black points show unlike charge sign pairs and red points show like charge sign pairs.

Count of N_{tag}

M_{eh} is defined as the invariant mass of particle pairs when the trigger particle is assumed to be electron and the associated particle is assumed to be kaon. Figure 5.54 and Figure 5.55 show invariant mass distributions (M_{eh}) of unlike and like sign pairs of the trigger electrons and the associated hadrons at each electron p_T range in RUN5 and RUN6, respectively. In Fig .5.54 and 5.55, black lines are unlike charge sign pairs and red lines are like charge sign pairs. Title in each panel shows the trigger electron p_T range. Clear excess of unlike sign pairs can be seen. The excess indicates the existence of the $D^0 \rightarrow e^+ K^- \nu_e$ signals. The distributions of like sign pairs are subtracted from the distributions of unlike sign pairs to utilize the effect of semi-leptonic decay of D and B hadrons.

Subtracted invariant mass distributions still include the contribution of the remaining electron pairs which have $M_{ee} > 0.08$ GeV. These remaining electron pairs must be estimated and subtracted to count signals. Identified electron pairs are used to estimate the amount of the remaining electron pairs. One of the electron pair is the trigger electron and the other is associated electron with $0.4 < p_T < 5.0$ GeV/c. The contribution of the remaining electron pairs is estimated by the normalized M_{eh} distribution of the identified electron pairs in M_{ee} >0.08 GeV. Normalization of the M_{eh} distribution of the identified electron pairs, where the associated electron is assigned as kaon mass, is determined by the number of entries in M_{ee} <0.08 GeV of the electron and hadron pairs (the number of entries in the peaks from π^0 Dalitz and beam pipe conversion). Figure 5.56 and 5.57 show the subtracted M_{eh} distributions of electron hadron pairs and the estimated M_{eh} distributions of the remaining electron pairs at each electron p_T range in RUN5 and RUN6, respectively. In Fig .5.56 and 5.57, black points show the subtracted M_{eh} distributions and red points show the estimated M_{eh} distributions of the remaining electron pairs.

The estimated M_{eh} distributions of the remaining electron pairs are subtracted from the M_{eh} distributions of electron hadron pairs. After this subtraction, the M_{eh} distributions are regarded as the extracted signals. Figure 5.58 and 5.59 show the extracted reconstruction signals in RUN5 and RUN6 respectively. In Fig .5.58 and 5.59, numbers of entries in $0.4 < M_{eh}$
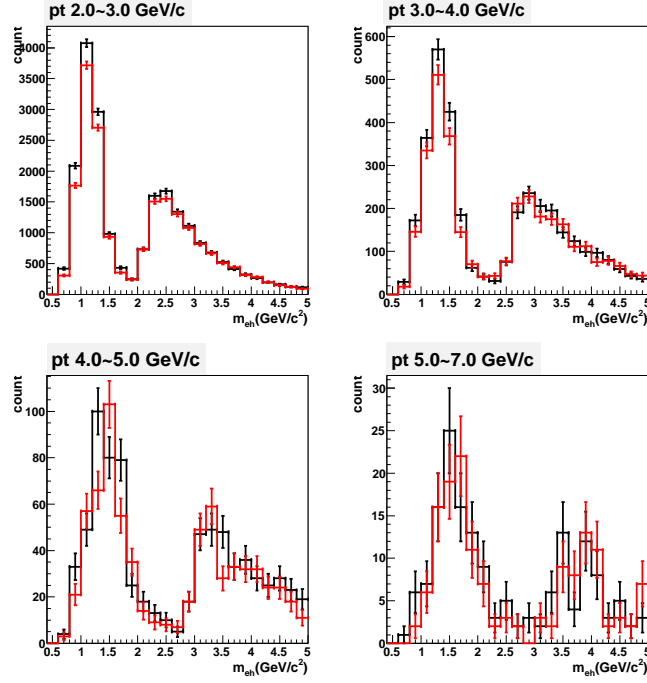
Figure 5.54: Invariant mass distribution from trigger electrons and associated hadrons in RUN5. Black lines are unlike charge sign pairs and red lines are like charge sign pairs.

< 1.9 GeV are counted as N_{tag}, since this analysis is partial reconstruction of D and it is not necessary to require tight mass cut around D region. The results of N_{tag} are summarized in Table 5.13 and Table 5.14.

Number of Electrons from Heavy Flavor

The number of single non-photonic electrons, $N_{e(HF)}$ in Eq. 5.45 is counted according to the following equation.

$$N_{e(HF)} = \int dp_{\mathrm{T}} N_e(p_{\mathrm{T}}) \times R_{HF}(p_{\mathrm{T}}), \tag{5.48}$$

where, $N_e(p_{\mathrm{T}})$ is the number of measured electrons and $R_{HF}(p_{\mathrm{T}})$ is the fraction of single non-photonic electrons in measured inclusive electrons as a function of electron p_{T}. $R_{HF}(p_{\mathrm{T}})$ is determined as the ratio of the spectrum of single non-photonic electrons obtained at Section5.6.4 over the sum of spectrum of single non-photonic electrons and the background electrons in the cocktail. Figure 5.60 and Figure 5.61 show the obtained $R_{HF}(p_{\mathrm{T}})$ in RUN5 and RUN6, respectively. The obtained $R_{HF}(p_{\mathrm{T}})$ is fitted, which is shown black line in Fig.5.60 and 5.61. The number of single non-photonic electrons is calculated from the fitted line.

5.8.3   Systematic Error of ϵ_{data}

The following factors are considered.

- The subtraction of like sign pairs
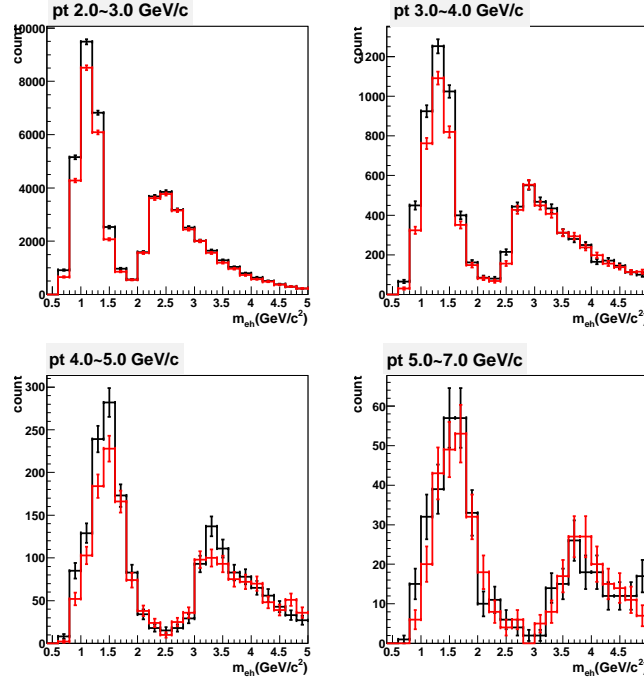
Figure 5.55: Invariant mass distribution from trigger electrons and associated hadrons in RUN6. Black lines are unlike charge sign pairs and red lines are like charge sign pairs.

- The subtraction of the remaining electron pairs

- The counting of single non-photonic electrons

- Other contributions to N_{tag} background

Subtraction of Like Sign Entries

Systematic error associated with the subtraction of like sign entries is determined based on the effect of the difference in the phase space with the acceptance filter described in Sec. 5.8.1. The effect of the difference in the phase space on the extracted signals (N_{tag}) is evaluated by using un-correlated electron hadron pairs. Event mixing method is used to create the pairs of un-correlated electrons and hadrons.

The M_{eh} distributions of the un-correlated like sign pairs are expected to be identical as these of the un-correlated unlike sign pairs, if the phase space of negative and positive charged tracks is identical. Therefore, the discrepancy between unity and the ratio of (unlike sign)/(like sign) M_{eh} distribution in mixing events is used for the estimation of the systematic error. Figure 5.62 shows the ratio of (unlike sign)/(like sign) M_{eh} distribution in mixing events in RUN5. The ratios of (unlike sign)/(like sign) M_{eh} distributions are fitted by a constant as shown at Fig. 5.62. Result of fit is summarized at Table 5.12.

When the fit result is consistent with unity within the fitting error, (error of the fit)$\times$(M_{eh} distribution of like sign pairs) is assigned as the systematic error for the subtraction of like
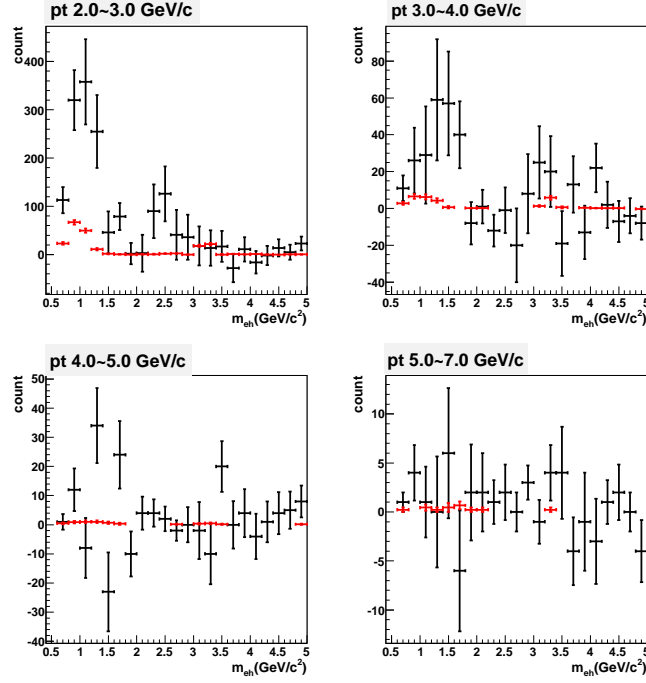
Figure 5.56: Subtracted M_{eh} distribution of electron-hadron pairs (black points) and estimated M_{eh} distributions of the remaining electron pairs (red points) in RUN5.

sign entries. When the fit result is not consistent with unity within fitting error, (the deviation of the fitted value from unity) $\times$(M_{eh} distribution) is assigned as the systematic error for the subtraction.

Table 5.12: Result of fit for (mixing unlike sign)/(mixing like sign) by constant

electron p_{T} range	mean(RUN5)	error(RUN5)	mean(RUN6)	error(RUN6)
2.0-3.0 GeV/c	0.9995	0.0005	1.0009	0.0002
3.0-4.0 GeV/c	1.006	0.001	1.002	0.0004
4.0-5.0 GeV/c	1.005	0.003	1.002	0.001
5.0-7.0 GeV/c	0.998	0.004	1.002	0.001

Subtraction of Remaining Electron Pairs

The systematic error for the subtraction of the remaining electron pairs is evaluated by the error of the normalization factors for the M_{ee} distribution of identified electron pairs. The error of the normalization factors is determined by the statistical uncertainty of the numbers of entries of identified electron pairs and electron hadron pairs in M_{ee} <0.08 GeV. The uncertainty of normalization is assigned as the systematic error for subtraction of the remaining electron pairs.
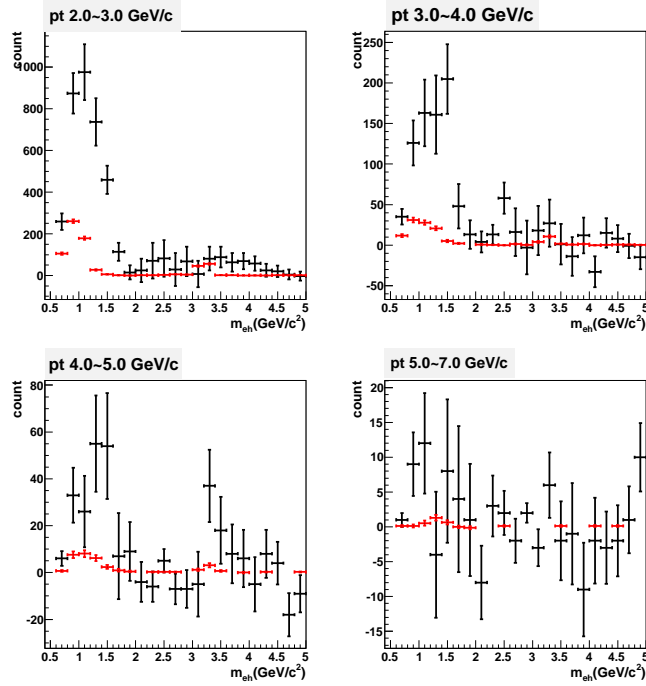
Figure 5.57: Subtracted M_{eh} distribution of electron-hadron pairs (black points) and estimated M_{eh} distributions of the remaining electron pairs (red points) in RUN6.

Count of Electrons from Heavy Flavor

This uncertainty is the largest source of the systematic error of N_{tag}. Systematic error for the number of electrons from heavy flavor is calculated based on the systematic error of spectra of electrons from heavy flavor decay. The systematic error of spectra are shown in Fig.5.60 and 5.61.

Other Contributions to N_{tag} Background

Following sources are possible to make correlation of electrons and hadrons.

- **K_{e3} decay**:
  Since $K_L \rightarrow e^{\pm}\pi^{\mp}$ is weak decay, the subtraction of like sign entries can not cancel out this contribution. Therefore, $K_L \rightarrow e^{\pm}\pi^{\mp}$ is possible to be background source of charge correlation of electrons and hadrons. This contribution is estimated by the PISA simulation which is used at the cocktail calculation. It is found the contribution of K_{e3} decay to N_{tag} is 0.5% level. Therefore, this contribution can be neglected.

- **Hadron-hadron correlation**:
  The charge correlation of hadron hadron pairs becomes the background source of charge correlation of electron and hadron pairs, since there is small hadron contamination in trigger electrons .
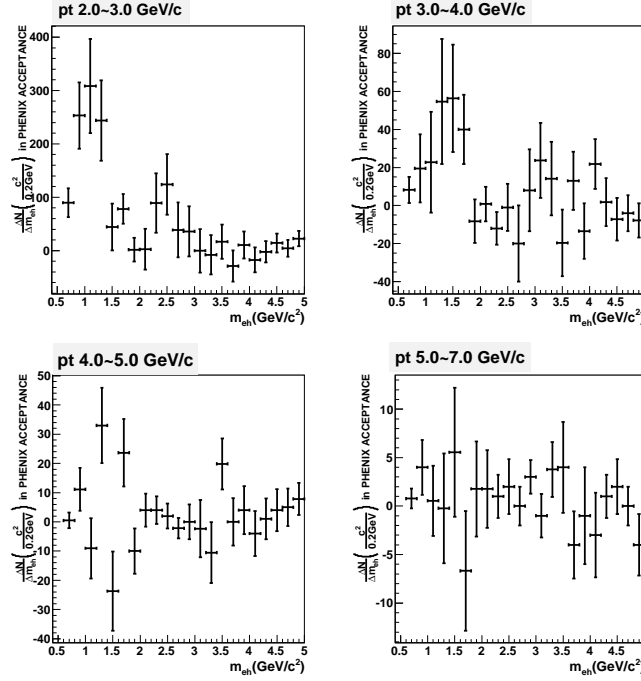
Figure 5.58: Subtracted invariant mass distribution of electron-hadron pairs after subtraction of estimated remaining electron pairs in RUN5.

The amount of hadron contamination in the trigger electrons is less than 0.5% at $2.0 < p_T < 5.0$ GeV/c, which is estimated in Sec. 5.5.3. The tagging efficiency of hadron hadron pairs correlation (ϵ_{had}) is determined from real data analysis. As a result, the contribution of hadron hadron correlation to N_{tag} is 0.5% level at $2.0 < p_T < 5.0$ GeV/c. This contribution can be also neglected at $2.0 < p_T < 5.0$ GeV/c.

Hadron background is not negligible at high p_T (>5.0 GeV/c) as estimated in Sec. 5.5.3, while tight eID cut is applied. The number of hadron contamination is calculated according to Table 5.7. The tagging efficiency of hadron hadron pairs (ϵ_{had}) at high p_T is also determined from real data analysis. The amount of hadron contamination is calculated from the estimated number of hadron contamination in the trigger electrons and the tagging efficiency of hadron hadron pairs. This contribution is subtracted from extracted signals (N_{tag}) at high p_T (>5.0 GeV/c) region. Tagging efficiency of hadrons depends on the distribution of hadron p_T . The p_T distribution of hadron with above cuts may differ from that of hadron background in electrons with tight eID cut. 50% systematic error is assiged for this subtraction.

5.8.4   Results of ϵ_{data}

ϵ_{data} is calculated from N_{tag} and the number of electrons from heavy flavor decay. ϵ_{data} and used values are summarized in Table 5.13 and 5.14.
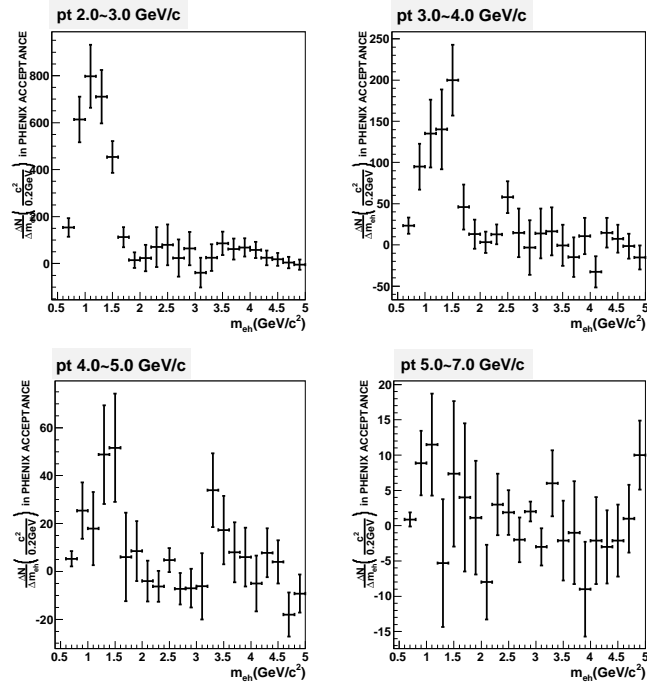
Figure 5.59: Subtracted invariant mass distribution of electron-hadron pairs after subtraction of estimated remaining electron pairs in RUN6.
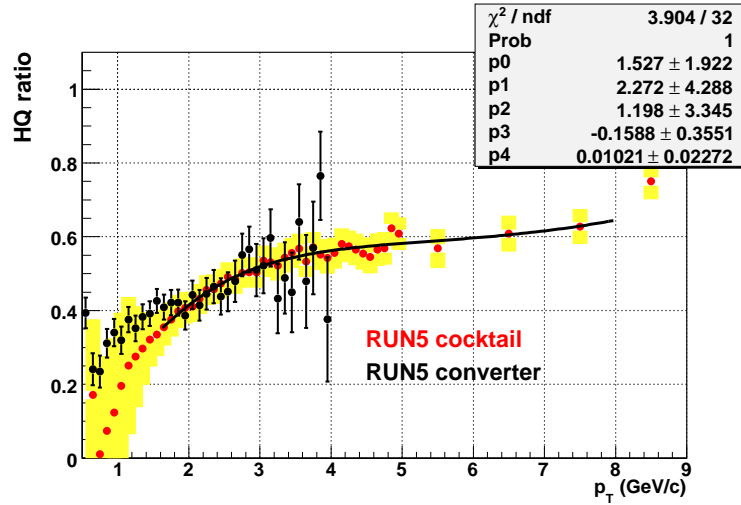
Figure 5.60: The fraction of electron from heavy flavor decay in inclusive electrons in RUN5 as a function of electron p_T.
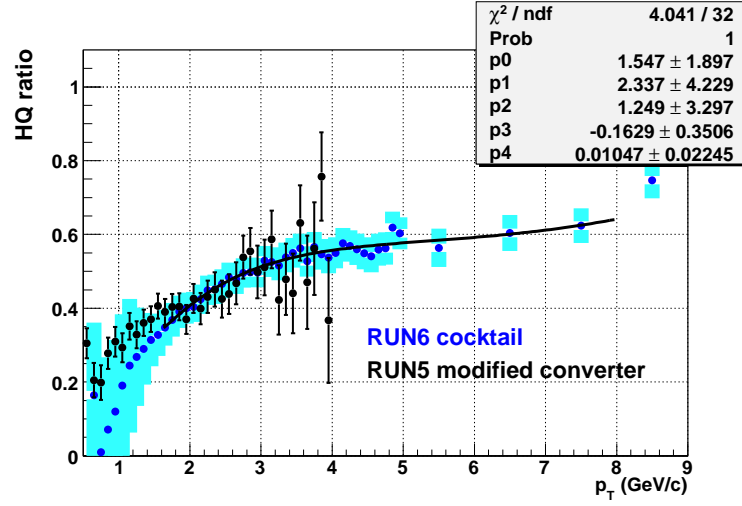
Figure 5.61: The fraction of electron from heavy flavor decay in inclusive electrons in RUN6 as a function of electron p_T.
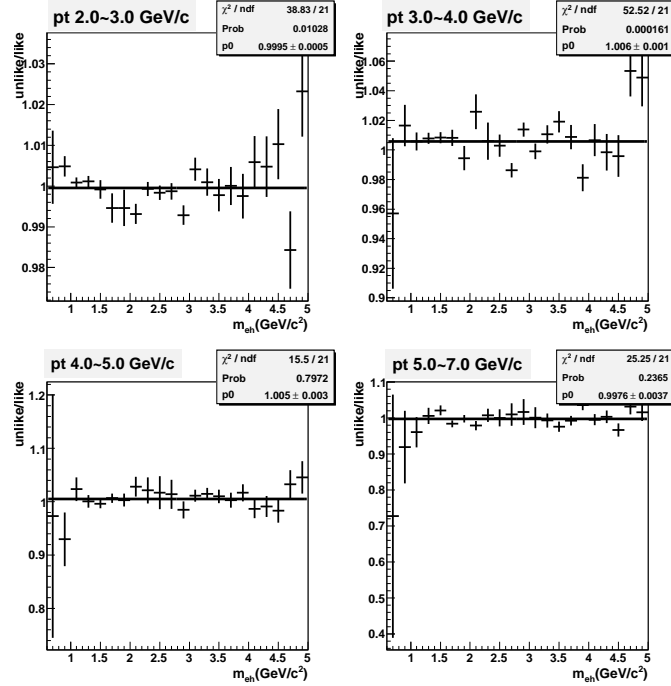
Figure 5.62: The ratio of (unlike sign)/(like sign) M_{eh} distribution in mixing events in RUN5.

Table 5.13: ϵ_{data} and used values at each electron p_T range(RUN5)

electron p_T 2.0-3.0 GeV/c	
number of unlike sign entries	11050.
number of like sign entries	9872.
number of (unlike -like)	$1178.0 \pm 144.6 \pm 5.0$
remaining e-e pair	$153.3 \pm 7.4 \pm 6.1$
N_{tag}	$1024.7 \pm 144.8 \pm 7.9$
number of heavy flavor electron	$31402.2 \pm 262.5 \pm 2783.$
ϵ_{data}	$0.0326 \pm 0.0046 \pm 0.0029$
electron p_T 3.0-4.0 GeV/c	
number of unlike sign entries	1770.
number of like sign entries	1548.
number of (unlike -like)	$222.0 \pm 57.6 \pm 9.3$
remaining e-e pair	$20.7 \pm 2.5 \pm 2.5$
N_{tag}	$201.3 \pm 57.7 \pm 9.6$
number of heavy flavor electron	$5310.1 \pm 99.4 \pm 402.5$
ϵ_{data}	$0.0379 \pm 0.0109 \pm 0.0034$
electron p_T 4.0-5.0 GeV/c	
number of unlike sign entries	353.
number of like sign entries	323.
number of (unlike -like)	$30.0 \pm 26.00 \pm 1.6$
remaining e-e pair	$4.5 \pm 0.9 \pm 1.2$
N_{tag}	$25.5 \pm 26.0 \pm 2.0$
number of heavy flavor electron	$1181.9 \pm 45.5 \pm 89.2$
ϵ_{data}	$0.0216 \pm 0.0220 \pm 0.0023$
electron p_T 5.0-7.0 GeV/c	
number of unlike sign entries	78.
number of like sign entries	71.
number of (unlike -like)	$7. \pm 12.2 \pm 0.3$
remaining e-e pair	$2.0 \pm 0.7 \pm 1.1$
number of background hadron	$17.8 \pm 3.7(\mathrm{sys})$
signal from hadron	$1.5 \pm 0.8(\mathrm{sys})$
N_{tag}	$3.5 \pm 12.2 \pm 1.4$
number of heavy flavor electron	$269.9 \pm 21.8 \pm 23.5$
ϵ_{data}	$0.0131 \pm 0.0457 \pm 0.0052$

Table 5.14: ϵ_{data} and used values at each electron p_T range(RUN6)

electron p_T 2.0-3.0 GeV/c	
number of unlike sign entries	26066.
number of like sign entries	22630.
number of (unlike -like)	3436. $\pm$220.7 $\pm$ 5.0
remaining e-e pair	578.4 $\pm$ 13.6 $\pm$ 15.5
N_{tag}	2857.6 $\pm$ 221.1 $\pm$ 16.1
number of heavy flavor electron	76408. $\pm$ 412.5 $\pm$ 6763.9
ϵ_{data}	0.0374 $\pm$ 0.0029 $\pm$ 0.0033
electron p_T 3.0-4.0 GeV/c	
number of unlike sign entries	4191.
number of like sign entries	3447.
number of (unlike -like)	744.0 $\pm$ 87.4 $\pm$ 7.0
remaining e-e pair	98.3 $\pm$ 5.5 $\pm$ 7.2
N_{tag}	645.7 $\pm$ 87.6 $\pm$ 7.2
number of heavy flavor electron	12897.0 $\pm$ 155.7 $\pm$ 977.4
ϵ_{data}	0.0501 $\pm$ 0.0068 $\pm$ 0.0039
electron p_T 4.0-5.0 GeV/c	
number of unlike sign entries	951.
number of like sign entries	774.
number of (unlike -like)	177.0 $\pm$ 41.5 $\pm$0.5
remaining e-e pair	26.2 $\pm$ 2.6 $\pm$ 4.5
N_{tag}	150.8 $\pm$ 41.9 $\pm$ 4.7
number of heavy flavor electron	2933.0 $\pm$ 72.0 $\pm$ 222.
ϵ_{data}	0.0514 $\pm$ 0.0142 $\pm$ 0.0042
electron p_T 5.0-7.0 GeV/c	
number of unlike sign entries	216.00
number of like sign entries	183.0
number of (unlike -like)	33.0 $\pm$ 20.0 $\pm$0.4
remaining e-e pair	2.7$\pm$ 0.7 $\pm$ 1.1
number of background hadron	51.5 $\pm$ 10(sys)
signal from hadron	4.5 $\pm$ 2.3(sys)
N_{tag}	25.8 $\pm$ 20.0 $\pm$ 2.6
number of heavy flavor electron	638.4 $\pm$ 33.6 $\pm$ 54.6
ϵ_{data}	0.0404 $\pm$ 0.0314 $\pm$ 0.0057

5.9   Simulation Study for Correlation Analysis

This section describes the evaluation of ϵ_c and ϵ_b. ϵ_c and ϵ_b are determined by using Monte-Carlo event generator as outlined in Sec. 5.7.1.

5.9.1   Simulation Overview

Figure 5.63 shows a conceptual view of the simulation study. The simulation is performed in three steps. First, $p + p$ collision at 200 GeV in the center of mass system is generated by PYTHIA event generator [49, 50]. As a next step, the decay of D and B hadrons in the generated event is simulated by using EvtGen event generator [51, 52, 53]. Therefore, the event which contains D and B hadrons is generated by the combination of PYTHIA and EvtGen. Finally, all stable particles in the generated event are put into the PISA simulation to evaluate the detector response.
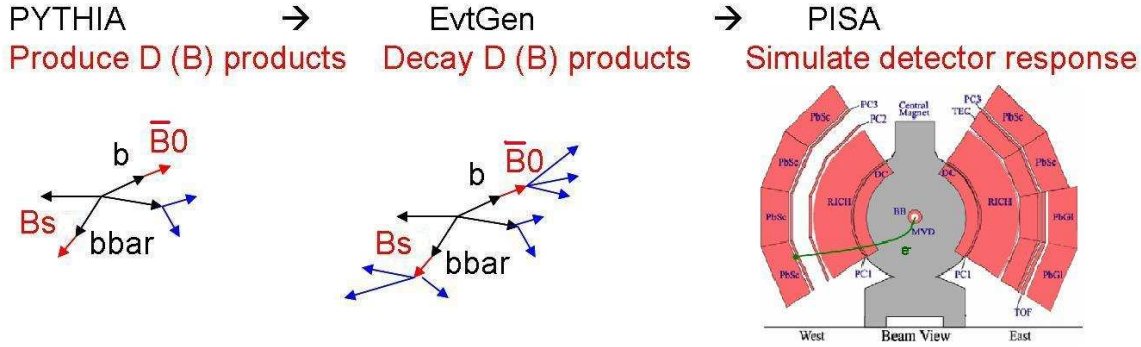
Figure 5.63: A conceptual view of the simulation study

PYTHIA Simulation

PYTHIA simulation (version 6.403) is used to generate $p + p$ collision at 200 GeV in the center of mass system. PYTHIA parameters are tuned to reproduce previous results of heavy flavor production measured by PHENIX [44, 115, 116, 118] and jet production measured by CDF [39, 40]. Since ϵ_c and ϵ_b contain inclusive signals from various heavy flavored hadons, the production ratios of D or B mesons and baryons (D^+/D^0,B^+/B^0 etc) are most important parameters to determine ϵ_c and ϵ_b. Therefore, the production ratios are also tuned according to the experimental results [45, 48, 54]. Tuning parameters of PYTHIA are summarized at Table 5.15. Tuning status of PYTHIA is described in Appendix. C

EvtGen Simulation

EvtGen (version alpha-00-14-05) is used to simulate the decay of D and B hadrons [52, 53]. EvtGen simulation provides a framework for implementation of the decay process of D and B

Table 5.15: PYTHIA tuning parameters

parameter name	value
charm mass	1.25 GeV
bottom mass	4.3 GeV
k_{T}	1.5 GeV/c
PDF	CTEQ5L
PARJ(13) (charm production)	0.55
PARJ(2) (charm production)	0.36
PARJ(2) (bottom production)	0.44
MSTP(82)	4
PARP(81)	1.9
PARP(82)	2.0
PARP(83)	0.5
PARP(84)	0.4
PARP(85)	0.9
PARP(86)	0.95
PARP(89)	1800
PARP(90)	0.25
PARP(67)	4.0

hadrons. EvtGen simulation is tuned to reproduce the results of heavy flavor decay at CLEO, BaBar and Belle [55, 56, 57, 58, 59, 63]. Semi-leptonic decay of D and B hadrons is main interest in this analysis. Most of semi-leptonic decay is simulated based on the ISGW2 model in EvtGen [66, 67]. For example, Figure 5.64 shows the electron energy spectrum of inclusive semi-leptonic decay of B meson ($B \rightarrow e\nu X$) in EvtGen simulation and that in CLEO data [55].

PISA Simulation

All stable particles in the generated event are put into the PISA simulation to evaluate the detector response. The PISA simulation is tuned for the RUN5 and RUN6 detector response as described in Sec. 5.3.4.

5.9.2 Calculation of ϵ_c and ϵ_b

ϵ_c and ϵ_b are determined via the simulation as outlined in the previous subsection. PYTHIA with MSEL of 4 and 5 are used to produce charm and bottom and to determine ϵ_c and ϵ_b, respectively. For the calculation of ϵ_c and ϵ_b, electron hadron pairs in the simulation are processed in a similar way to evaluate ϵ_{data} in the real data analysis. In the simulation, the
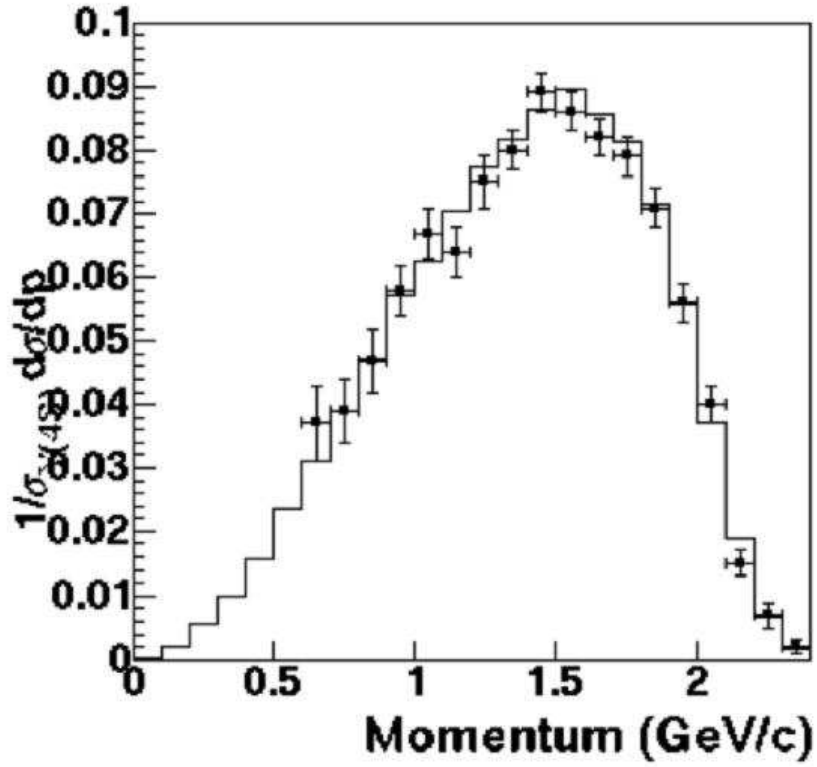
Figure 5.64: Electron energy spectrum at $B \to e\nu X$ of EvtGen and CLEO [55].

rejection of the estimated remaining electron pairs and the calculation of the number of single non-photonic electrons are not performed, since we can reject background for the trigger electron by looking the parent particle in the simulation. Only the subtraction of the M_{eh} distribution of like sign pairs is performed to extract signals from heavy flavor. As a next step, the M_{eh} distribution is normalized by the number of trigger electrons.

Figure 5.65 to 5.68 show the normalized reconstruction signals in charm and bottom production at each electron p_T range in RUN5 configuration. Red points show reconstruction signals in charm production and blue points show these in bottom production.

ϵ_c and ϵ_b at each electron p_T range are determined as the number of entries in $0.4 < M_{eh}$ < 1.9 GeV in Fig.5.65 to 5.68. Results of ϵ_c and ϵ_b are summarized in Table 5.16. ϵ_c increases as electron p_T increases by kinematic reason.

Table 5.16: Result of ϵ_c

electron p_{T} range	ϵ_c RUN5	ϵ_b RUN5	ϵ_c RUN6	ϵ_b RUN6
2.0-3.0 GeV/c	0.0378	0.0162	0.0371	0.156
3.0-4.0 GeV/c	0.0566	0.0160	0.0563	0.0168
4.0-5.0 GeV/c	0.0810	0.0210	0.0781	0.0198
5.0-7.0 GeV/c	0.0921	0.0275	0.0913	0.0270
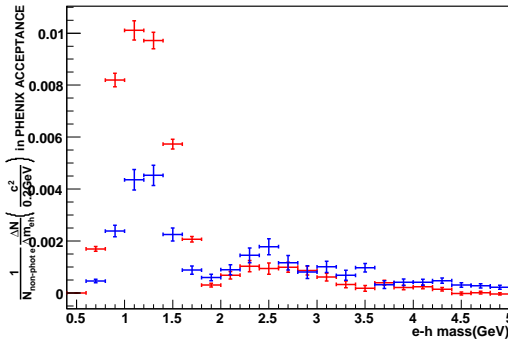
Figure 5.65: Subtracted and normalized invariant mass distributions of electron-hadron pairs in charm and bottom production. Red points show charm case and blue points show bottom case. p_{T} range of trigger electrons is 2.0-3.0 GeV/c.
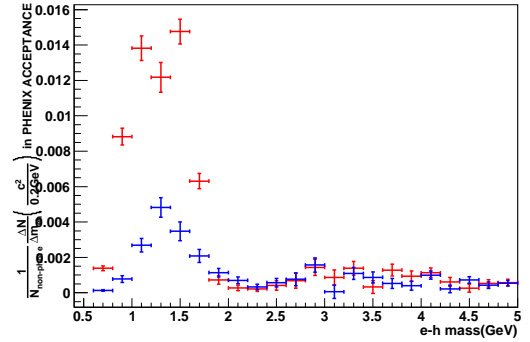
Figure 5.66: Subtracted and normalized invariant mass distributions of electron-hadron pairs in charm and bottom production. p_{T} range of trigger electrons is 3.0-4.0 GeV/c.
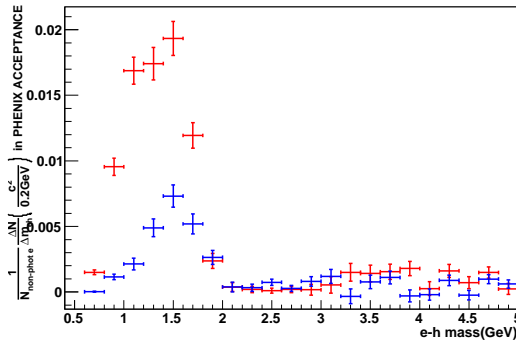
Figure 5.67: Subtracted and normalized invariant mass distributions of electron-hadron pairs in charm and bottom production. p_{T} range of trigger electrons is 4.0-5.0 GeV/c.
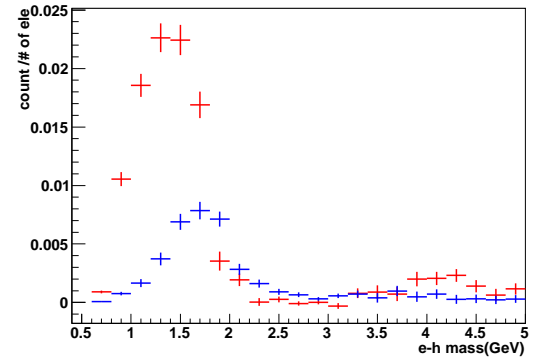
Figure 5.68: Subtracted and normalized invariant mass distributions of electron-hadron pairs in charm and bottom production. p_{T} range of trigger electrons is 5.0-7.0 GeV/c.

5.9.3 Systematic Errors for ϵ_c and ϵ_b

Systematic error for ϵ_c and ϵ_b can be categorized into two components. One is systematic error of the difference in reconstruction efficiency including geometrical acceptance between real data and PISA simulation. This component is common factor for ϵ_c and ϵ_b. The other is from the uncertainty of the event generator (PYTHIA and EvtGen). The uncertainty of ϵ_c and ϵ_b originated from the uncertainty of PYTHIA and EvtGen needs to be assigned as systematic error. These errors are estimated for ϵ_c and ϵ_b separately. The following factors are considered.

- Production ratios of charmed and bottomed hadrons

- Branching ratios of charmed and bottomed hadrons

- Momentum distribution of charmed and bottomed hadrons

- PYTHIA parameters

Geometrical Acceptance

3% systematic error is assigned for geometical acceptnace, as described in Sec. 5.3.5 for RUN5 and RUN6 configuration.

Production Ratios of Charmed and Bottomed Hadrons

Production ratios of D and B hadrons (D^+/D^0, D_s/D^0, B^+/B^0, B_s/B^0...) are one of the most important parameters to determine ϵ_c and ϵ_b. Although the production ratios in the generated events are tuned based on the experimental results as already described, the ratios have considerable uncertainty [45, 48, 54]. Therefore, the uncertainty of the production ratios should be considered as the systematic error source.

D^+/D^0, D_s/D^0 and Λ_c/D^0 ratios in PYTHIA are summarized in Table 5.17. The assigned uncertainties of D^+/D^0,D_s/D^0,Λ_c/D^0 based on experimental results are also listed in Table 5.17. B^+/B^0, B_s/B^0 and B baryons/B^0 ratios and uncertainty are summarized in Ta-

Table 5.17: D^+/D^0,D_s/D^0,Λ_c/D^0 ratios from other experiments   [45, 48, 54] and PYTHIA (default and tuned)

	PYTHIA (default)	CDF ($p+p$)	P.D.G (e^+e^-@$\sqrt{s} = 91$GeV)	PYTHIA (tuned)
D^+/D^0	0.3	0.45		0.45 ± 0.1
D_s/D^0	0.2	0.23	0.29	0.25 ± 0.1
Λ_c/D^0	0.1		0.17	0.1 ± 0.05

ble 5.18. B^+/B^0 is fixed to 1, since there are no reason to break isospin symmetry. B_s/B^0 and B baryons/B^0 ratios and their uncertainty are summarized in Table 5.18. Since there are little experimental results of B_s/B^0 and B baryons/B^0 ratios, 50% uncertainty is assigned for B_s/B^0 ratio and 75% uncertainty is assigned for B baryons/B^0 ratio.

Table 5.18: B^+/B^0,B_s/B^0,B baryons/B^0 ratios from other experiment [46] and PYTHIA (tuned)

	P.D.G $(e^+e^-@\sqrt{s} = 91\text{GeV})$	PYTHIA (tuned)
B^+/B^0	1	1
B_s/B^0	0.35	0.4± 0.2
B baryons/B^0	0.2	0.2 ± 0.15

The effect of the assigned uncertainty on the tagging efficiency is regarded as the systematic error of the tagging efficiency. For the study of this effect, details of ϵ_c and ϵ_b are evaluated for each decay channel at each trigger electron p_T range. For example, the results at the trigger electron with $2 < p_T < 3\,\text{GeV}/c$ are summarized in Table 5.19. For the results at other electron p_T are shown in Appendix. E.

The effect on the ϵ_c and ϵ_c are calculated by changing the production ratios of D and B hadrons according to the assigned uncertainties. The results are summarized in Table5.20 and 5.21.

Branching Ratio

Branching ratios in EvtGen simulation are implemented according to P.D.G and the results from CLEO, BarBar etc [52, 53]. However, branching ratios listed in P.D.G have uncertainty and there is small discrepancy in the branching ratios between P.D.G values and implemented values in EvtGen for some decay channels. For these decay channels, these discrepancy are taken as the uncertainty of the branching ratios for corresponding channel. The implemented and P.D.G values of branching ratios are summarized in Table 5.22. The assigned uncertainty of branching ratios are also summarized in Table 5.22.

We calculate the effect of the uncertainty of the branching ratios on the ϵ_c and ϵ_c by the similar way used to estimate the systematic errors of the production ratio. That is, the effect on the ϵ_c and ϵ_c are calculated when the branching ratios of D and B hadrons are changed according to the assigned uncertainty. The results are summarized in Table 5.22 and assigned as a systematic error for the branching ratio.

$b \rightarrow c \rightarrow e$ Process

There is discrepancy in the production ratios of D hadrons which originates from inclusive $b \rightarrow c$ process between P.D.G and EvtGen, which is the known problem of EvtGen. The production ratios of D hadrons in inclusive $b \rightarrow c$ process in P.D.G and EvtGen are summarized at Table 5.23. As a result, D^+/D^0 in B decay are 0.30 and 0.41 in P.D.G value and EvtGen, respectively. The effect of this discrepancy in $b \rightarrow c \rightarrow e$ needs to be considered as systematic error of tagging efficiency of ϵ_b. The difference in D^+/D^0 in B decay makes $\sim 4\%$ effect on the tagging efficiency in $c \rightarrow e$ process, which is estimated in the same way to estimate the uncertainty from the production ratio. The 4% effect of the tagging efficiecy in $c \rightarrow e$ process

changes the tagging efficiency of bottom production via $b \to c \to e$ process, which is evaluated from Table 5.19. It is found that such effect is less than 2%.

Momentum Distribution of Charmed and Bottomed Hadrons
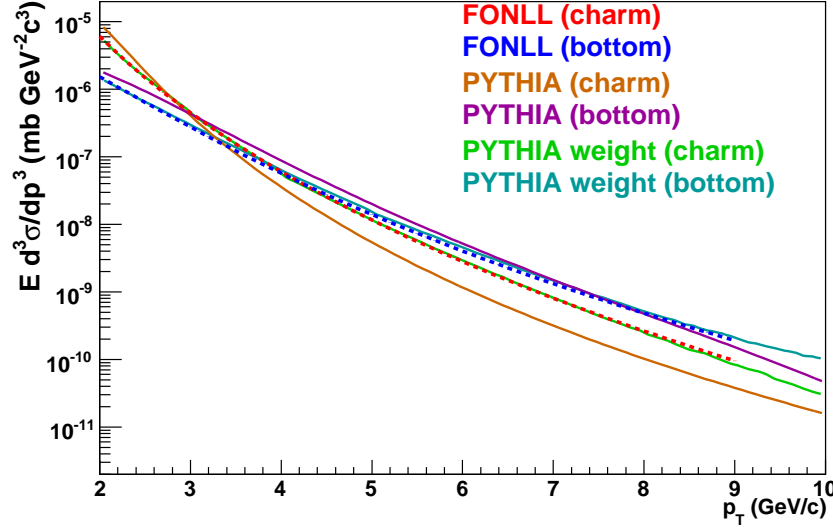
Figure 5.69: The spectra of the single electrons from charm and bottom at PYTHIA and FONLL [77]. Dark orange line and magenta line show the spectra from charm and bottom at PYTHIA. Green line and cyan line show the spectra of the electrons from charm and bottom at PYTHIA with weighting factor. Red line and blue lines show the spectra from charm and bottom at FONLL.

D and B hadrons in the PYTHIA simulation have the uncertainty in their momentum distribution. Tagging efficiency as a function of trigger electron p_T depends on the momentum distributions of parent D and B hadrons. Therefore, the systematic error for the momentum distribution of the parent particles should be estimated.

The shape of the p_T spectra of the electrons from charm and bottom reflects the momentum distribution of the parent particles. The difference of the momentum distribution of the parent particles between PYTHIA and the experimental results can be estimated by comparing the shape of electron p_T spectra obtained by PYTHIA and real data. Figure 5.69 shows the p_T spectra of the electrons from charm (Dark Orange) and bottom (Magenta) at PYTHIA. The spectra of the electrons from PYTHIA are compared with the spectra from FONLL [81], where the shape of the spectra from FONLL almost agrees with the experimental results including PHENIX [77, 78, 79]. Weighting factor, $w(p_T)$, is defined as follows.

$$w(p_T) = FONLL(p_T)/PYTHIA(p_T). \tag{5.49}$$

This weighting factor is used to correct the difference of the momentum distribution. In Fig 5.69, green line and cyan line show the spectra of the electrons from charm and bottom produced

at PYTHIA with weighting factor. The difference of ϵ_c and ϵ_b between with and without the weighting reflects the correction of the momentum distribution. As a result, about 1.5% systematic error is assinged for ϵ_c and about 2% systematic error is assigned for ϵ_b

PYTHIA Uncertainty

N_{tag} includes the remaining contribution from the associated hadron which is not from heavy flavor decay (jet fragmentation). Such effect has the dependence of the PYTHIA parameters and this dependence should be included into the systematic error. Study is done to estimate the amount of the contribution from the associated hadron which is from jet fragmentation.

ϵ_c and ϵ_b are calculated in the two cases for all stable particles and only decay daughters of D and B hadrons in generated events. Figure 5.70 shows a conceptual view of this procedure. In Fig.5.70, blue particles are decay daughters of D and B hadrons and green particles are from jet fragmentation simulated with PYTHIA. The contribution of jet fragmentation generated by PYTHIA can be estimated by comparison between the above two cases (with and without hadron from jet fragmentation). It is found that the contribution of jet fragmentation to ϵ_c and ϵ_b is less than 15%. Therefore, the effect of uncertainty of jet fragmentation on the tagging efficiency is expected to be small. For a example, if the uncertainty of the contribution of jet fragmentation in PYTHIA is 20%, the uncertainty of ϵ_c and ϵ_b becomes $15\% \times 20\% = 3\%$.

More precisely, the uncertainty from the PYTHIA dependence on the contribution of jet fragmentation is estimated by looking at the measured yield of associated hadrons as a function of azimuthal angle between the trigger non-photonic electrons and the associated hadron (correlation function) in charm and bottom production. Since the contribution of jet fragmentation is not canceled out for the inclusive multiplicity, the inclusive multiplicity is a good observable to study the PYTHIA dependence of the jet fragmentation. The multiplicity in RUN5 is obtained in Appendix. C. Some parameter sets, which are expected to affect the contribution of jet fragmentation, are prepared to estimate the effect of PYTHIA uncertainty on the ϵ_c and ϵ_b as follows.

- default PYTHIA (1)

- PARP(90) 0.25→0.16 (2)

- P.D.F CTEQ5L→GRV94L (3)

- charm mass 1.2→1.4GeV/c^2, bottom mass 4.3→4.5GeV/c^2 (4)

Figure 5.71 shows the inclusive multiplicity as a function of azimuthal angle between the trigger single non-photonic electrons and the associated hadron. Black points show the result in RUN5 data obtained at Appendix. C and various lines show the results from PYTHIA with the parameter sets. Since (1) and (2) parameter sets are NOT consistent with real data, the deviation of ϵ_c and ϵ_b with the (1) and (2) parameter sets from tuned PYTHIA gives enough conservative systematic error. We assign 6% systematic error as PYTHIA uncertainty, since the deviations are 5% for ϵ_c and ϵ_b.
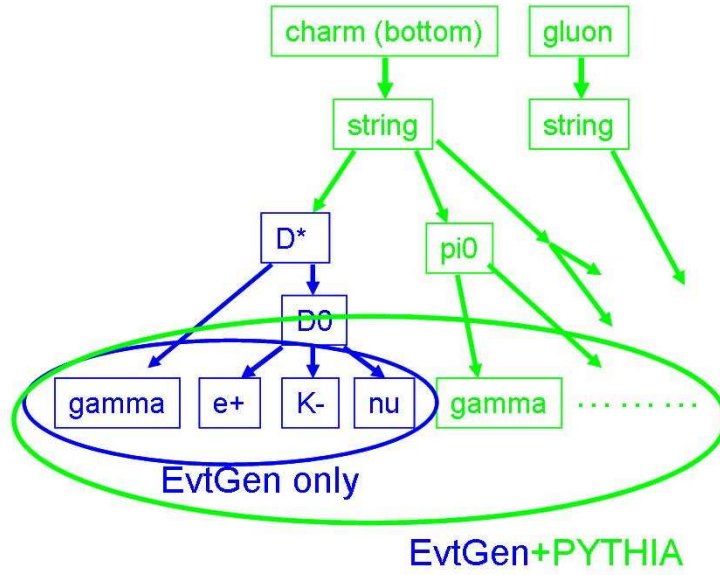
Figure 5.70: Conceptual view of the procedure to estimate contribution of jet fragmentation simulated by PYTHIA. Blue particles are D mesons ans baryons simulated by EvtGen and green particles are jet fragmentation simulated by PYTHIA.

Summary of Systematic Error for PYTHIA and EvtGen

Systematic error of ϵ_c and ϵ_b are summarized in Table 5.24.

5.10 ϵ_{data}, ϵ_c and ϵ_b

ϵ_{data}, ϵ_c and ϵ_b are obtained in Sec. 5.8 and 5.9. The location of effective bin center of electron p_T at each p_T range is determined as weighted mean of electron p_T at each p_T range. Since the bin center of $\epsilon_{c(b)}(p_T)$ is different from the bin center of $\epsilon_{data}(p_T)$, it is necessary to correct to $\epsilon_{c(b)}(p_T)$ the value at the same p_T as used in ϵ_{data}. This is done as follows.

$$\epsilon_{c(b)}(p_T^{real}) = \frac{f_{c(b)}(p_T^{real})}{f_{c(b)}(p_T^{c(b)})} \times \epsilon_{c(b)}(p_T^{c(b)}), \tag{5.50}$$

where

- p_T^{real} and $p_T^{c(b)}$ are the effective bin center of electron p_T in real data and simulation for charm (bottom) production.

- $f_{c(b)}(p_T)$ is the fit function for the obtained $\epsilon_{c(b)}$.

Figure 5.72 and 5.73 show ϵ_{data}, ϵ_c and ϵ_b as a function of electron p_T in RUN5 and RUN6, respectively. Here, black points correspond to ϵ_{data}, red points correspond to ϵ_c and blue points
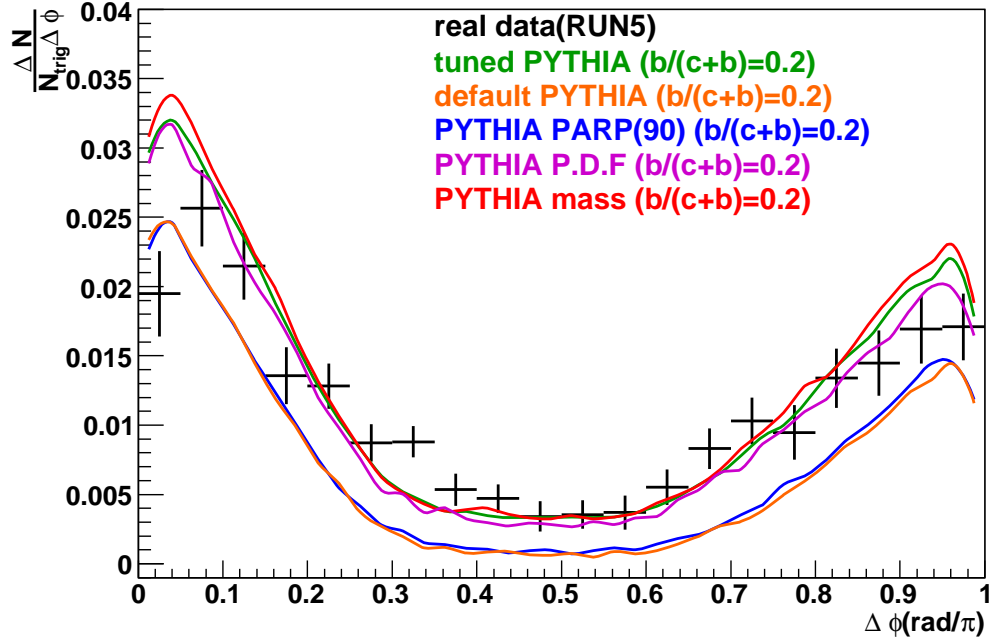
Figure 5.71: The correlation function of electrons and hadrons, when the trigger electrons were from heavy flavor. Black points show the result in RUN5 data obtained at SectionC and various lines show the result at PYTHIA with the parameter sets.

correspond to ϵ_b. In Fig. 5.72 and 5.73, data points move near bottom values as electron p_T increases. This fact indicates the fraction of the electrons from bottom increases with electron p_T. Results are summarized in Table 5.25
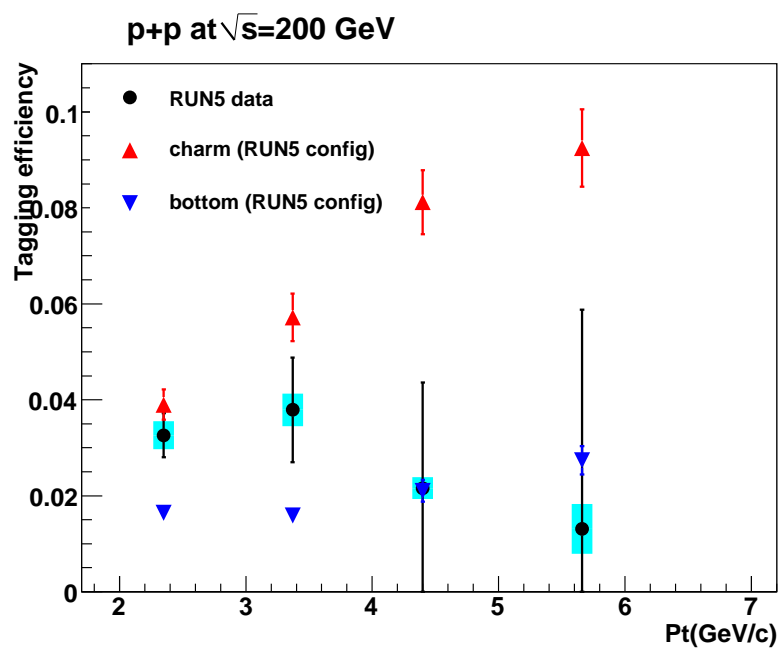
Figure 5.72: ϵ_c, ϵ_b and ϵ_{data} as a function of electron p_T in RUN5.
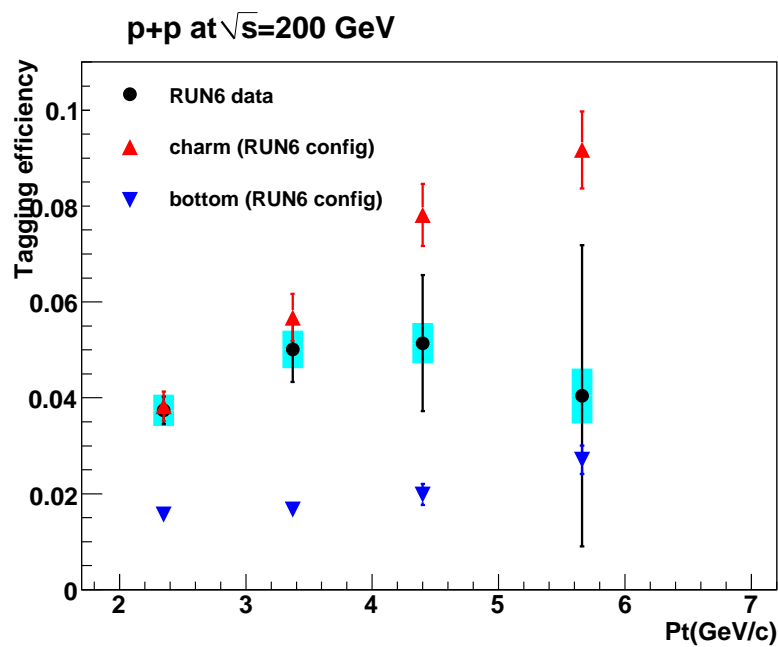
Figure 5.73: ϵ_c, ϵ_b and ϵ_{data} as a function of electron p_T in RUN6.

Table 5.19: Detail of charm and bottom decay for electron p_{T} 2-3 GeV/c

channel	N_{tag} (part)/(all)	N_{ele} (part)/(all)	ϵ
D^0			
$D^0 \to e^+ K^- \nu_e$	38.96%	29.64%	$4.68 \pm 0.09\%$
$D^0 \to e^+ K^{*-} \nu_e$	15.24%	3.73%	$14.57 \pm 0.34\%$
$D^0 \to e^+ \pi^- \nu_e$	4.34%	5.24%	$2.95 \pm 0.19\%$
$D^0 \to e^+ \rho^- \nu_e$	2.04%	0.52%	$13.88 \pm 0.81\%$
$D^0 \to e^+ other$	1.23%	0.51%	$8.67 \pm 0.83\%$
D^+			
$D^+ \to e^+ \bar{K}^0 \nu_e$	25.23%	38.55%	$2.33 \pm 0.07\%$
$D^+ \to e^+ \bar{K}^{*0} \nu_e$	6.00%	4.70%	$4.55 \pm 0.31\%$
$D^+ \to e^+ \pi^0 \nu_e$	2.00%	3.32%	$2.15 \pm 0.21\%$
$D^+ \to e^+ \rho^0 \nu_e$	0.25%	0.36%	$2.52 \pm 1.14\%$
$D^+ \to e^+ other$	1.91%	2.02%	$3.37 \pm 0.37\%$
D_s			
$D_s \to e^+ \phi \nu_e$	0.45%	0.89%	$1.80 \pm 0.73\%$
$D_s \to e^+ \eta \nu_e$	3.70%	7.66%	$1.72 \pm 0.14\%$
$D_s \to e^+ \eta' \nu_e$	0.30%	0.67%	$1.60 \pm 0.69\%$
$D_s \to e^+ other$	0.35%	0.82%	$1.52 \pm 0.47\%$
Λ_c			
$\Lambda_c \to e^+ \Lambda \nu_e$	-0.40%	0.31%	$-4.63 \pm 2.67\%$
$\Lambda_c \to e^+ other$	-1.60%	1.05%	$-5.44 \pm 1.25\%$
B^0			
$B^0 \to e^+ D^- \nu_e$	3.27%	6.20%	$0.89 \pm 0.15\%$
$B^0 \to e^+ D^{*-} \nu_e$	0.50%	21.21%	$0.04 \pm 0.09\%$
$B^0 \to e^+ other$	4.39%	5.88%	$1.26 \pm 0.17\%$
B^+			
$B^+ \to e^+ D^0 \nu_e$	7.16%	6.72%	$1.80 \pm 0.15\%$
$B^+ \to e^+ D^{*0} \nu_e$	21.30%	22.93%	$1.57 \pm 0.08\%$
$B^+ \to e^+ other$	2.95%	6.47%	$0.77 \pm 0.17\%$
B_s			
$B_s \to e^+ total$	15.87 %	10.81%	$2.49 \pm 0.12\%$
$Bhad \to e^+$	10.51%	10.10%	$1.76 \pm 0.12\%$
$B \to c \to e$	34.05%	9.69%	$5.95 \pm 0.18\%$

Table 5.20: The effect of $D^+/D^0, D_s/D^0, \Lambda_c/D^0$ changes on ϵ_c

electron p_T	$\Delta(\epsilon_c)/\epsilon_c$ $2 < p_T < 3$ GeV/c	$\Delta(\epsilon_c)/\epsilon_c$ $3 < p_T < 4$ GeV/c	$\Delta(\epsilon_c)/\epsilon_c$ $4 < p_T < 5$ GeV/c	$\Delta(\epsilon_c)/\epsilon_c$ $5 < p_T < 7$ GeV/c
$D^\pm/D^0$	2.7%	3.6%	3.3%	4%
D_s/D^0	2.0%	1.9%	2.0%	2.0%
Λ_c/D^0	1.7%	1.5%	1.0%	0.4%

Table 5.21: The effect of B_s/B^0 and B baryons/B^0 changes on ϵ_b

electron p_T	$\Delta(\epsilon_c)/\epsilon_c$ $2 < p_T < 3$ GeV/c	$\Delta(\epsilon_c)/\epsilon_c$ $3 < p_T < 4$ GeV/c	$\Delta(\epsilon_c)/\epsilon_c$ $4 < p_T < 5$ GeV/c	$\Delta(\epsilon_c)/\epsilon_c$ $5 < p_T < 7$ GeV/c
B_s/B^0	2.5%	2.5%	3.7 %	4.5 %
B baryons/B^0	0.5%	1%	2.5 %	3 %

Table 5.22: Branching ratio of D and B hadrons in P.D.G and EvtGen. The assigned uncertainties for the branching ratios and these effect on the ϵ_c and ϵ_b electron p_T 2-3 GeV/c

charmed hadrons channel	Branching Ratio EvtGen	Branching ratio P.D.G	$\delta(Br)/Br$	$\delta(\epsilon_c)/\epsilon_c$
D^0				
$D^0 \to e^+ K^- \nu_e$	3.50±0.11%	3.51%±0.11%	3.10%	0.29%
$D^0 \to e^+ K^{*-} \nu_e$	2.25±0.16%	2.17%±0.16%	7.10%	0.81%
$D^0 \to e^+ \pi^- \nu_e$	0.34±0.06%	0.28%±0.02%	17.60%	0.16%
$D^0 \to e^+ \rho^- \nu_e$	0.22±0.03%	0.19%±0.04%	13.60%	0.21%
$D^0 \to e^+ other$	0.45±0.35%	0.56%±0.35%	77.80%	0.56%
$D^0 \to e^+$ total				1.06%
D^+				
$D^+ \to e^+ \bar{K}^0 \nu_e$	9.00±0.50%	8.60%±0.50%	5.60%	0.73%
$D^+ \to e^+ \bar{K}^{*0} \nu_e$	5.50±0.50%	8.60%±0.50%	5.40%	0.07%
$D^+ \to e^+ \pi^0 \nu_e$	0.44±0.07%	0.44%±0.07%	16.30%	0.21%
$D^+ \to e^+ \rho^0 \nu_e$	0.28±0.06%	0.22%±0.04%	21.40%	0.02%
$D^+ \to e^+ other$	1.46±0.7%	1.12%±0.7%	48.70%	0.05%
$D^+ \to e^+$ total				0.77%
D_s				
$D_s \to e^+ \phi \nu_e$	2.42±0.50%	2.50%±0.30%(l^+)	20.70%	0.09%
$D_s \to e^+ \eta \nu_e$	3.07±0.8%	3.10%±0.60%	26.10%	1.01%
$D_s \to e^+ \eta' \nu_e$	1.06±0.4%	1.08%±0.35%	47.20%	0.17%
$D_s \to e^+ other$	0.37±0.37%	100.00%	0.46%	
$D_s \to e^+$ total				1.13%
Λ_c				
$\Lambda_c \to e^+ \Lambda \nu_e$	1.8±0.6%	2.1%±0.6%	33.30%	0.24%
$\Lambda_c \to e^+ other$	2.7±1.8%	2.4%±1.8%	66.70%	1.76%
$\Lambda_c \to e^+$ total				1.77%
total				2.48%
bottomed hadrons channel	Branching Ratio EvtGen	Branching ratio P.D.G	$\delta(Br)/Br$	$\delta(\epsilon_b)/\epsilon_b$
B^0				
$B^0 \to e^+ D^- \nu_e$	2.07±0.2%	2.12%±0.2%	9.70%	0.28%
$B^0 \to e^+ D^{*-} \nu_e$	5.70±0.35%	5.35%±0.2%	6.10%	1.25%
$B^0 \to e^+ other$	2.6±0.5%	2.93%±0.5%	19.20%	0.28%
$B^0 \to e^+$ total				1.31%
B^+				
$B^+ \to e^+ D^0 \nu_e$	2.24±0.22%	2.15%±0.22%	10.20%	0.04%
$B^+ \to e^+ D^{*0} \nu_e$	6.17±0.5%	6.50%±0.5%	7.70%	0.12%
$B^+ \to e^+ other$	2.49±0.7%	2.25%±0.67%	26.90%	0.93%
$B^+ \to e^+$ total				0.94%
B_s				
$B_s \to e^+$ total	7.9±3%	7.9%±2.4%	37.00%	1.80%
$Bhad \to e^+ others$	7.5±4.0%	8.5%±4.0%	40.0%	0.2 %
total				2.42%

Table 5.23: Inclusive resonance D production in B decays at PDG and EvtGen

	P.D.G 06 (%)	EvtGen (%)
$B \to e\nu X$	10.24 ± 0.15	10.6
$B \to D^{\pm}X$	22.8 ± 1.4	32.4
$B \to D^0 X$	63.7 ± 1.4	68.2
$B \to D^{*\pm}X$	22.5 ± 1.5	26.2
$B \to D^{*0}X$	26.0 ± 2.7	25.7
$B \to D^{(*)}D^{(*)}barX$	$7.1 + 2.7 - 1.7$	7.7

Table 5.24: Summary of ϵ_c and ϵ_b

ϵ_c electron p_{T}	simulation statistics	EvtGen+PYTHIA	geometrical acceptance	total
2.0-3.0 GeV/c	1.7%	7.6%	3%	8.3%
3.0-4.0 GeV/c	2.2%	7.9%	3%	8.7%
4.0-5.0 GeV/c	1.6%	7.5%	3%	8.3%
5.0-7.0 GeV/c	2.1%	8.0%	3%	8.8%

ϵ_b electron p_{T}	simulation statistics	EvtGen+PYTHIA	geometrical acceptance	total
2.0-3.0 GeV/c	3.5%	7.5%	3%	8.8%
3.0-4.0 GeV/c	5.0%	7.3%	3%	9.4%
4.0-5.0 GeV/c	4.8%	9.1%	3%	10.7%
5.0-7.0 GeV/c	3.8%	9.6%	3%	10.7%

Table 5.25: ϵ_{data}, ϵ_c and ϵ_b

electron p_{T}	ϵ_{data}	ϵ_c	ϵ_b
RUN5			
2.35GeV/c	$0.0326 \pm 0.0046 \pm 0.0029$	0.0390 ± 0.0031	0.0164 ± 0.0014
3.37GeV/c	$0.0379 \pm 0.0109 \pm 0.0034$	0.0571 ± 0.0050	0.0159 ± 0.0015
4.40GeV/c	$0.0216 \pm 0.0220 \pm 0.0023$	0.0812 ± 0.0067	0.0210 ± 0.0023
5.66GeV/c	$0.0131 \pm 0.0457 \pm 0.0052$	0.0924 ± 0.0081	0.0274 ± 0.0030
RUN6			
2.35GeV/c	$0.0374 \pm 0.0029 \pm 0.0033$	0.0382 ± 0.0031	0.0156 ± 0.0014
3.37GeV/c	$0.0501 \pm 0.0068 \pm 0.0039$	0.0567 ± 0.0049	0.0167 ± 0.0015
4.40GeV/c	$0.0514 \pm 0.0142 \pm 0.0042$	0.0781 ± 0.0065	0.0198 ± 0.0022
5.66GeV/c	$0.0404 \pm 0.0314 \pm 0.0057$	0.0917 ± 0.0080	0.0271 ± 0.0029

Chapter 6

Result

The spectrum of electrons from semi-leptonic decay of heavy flavor and tagging efficiency, ϵ_{data}, ϵ_c and ϵ_b are obtained as described in the previous chapter. $(b \rightarrow e)/(c \rightarrow e + b \rightarrow e)$ is determined using ϵ_{data}, ϵ_c and ϵ_b in Sec. 6.1. The reconstructed signals in real data are compared with these in simulation in Sec. 6.2. The electron spectra for charm and bottom are obtained from the ratio, $(b \rightarrow e)/(c \rightarrow e + b \rightarrow e)$, and the spectrum of single electrons in Sec. 6.3. Total cross section of bottom is also measured by integrating this spectrum.

6.1 $(b \rightarrow e)/(c \rightarrow e + b \rightarrow e)$ Results

The fraction of the contribution of bottom quark in the single non-photonic electrons $((b \rightarrow e)/(c \rightarrow e + b \rightarrow e))$ is obtained from ϵ_{data}, ϵ_c and ϵ_b using following equation.

$$\frac{b \rightarrow e}{c \rightarrow e + b \rightarrow e} = \frac{\epsilon_c - \epsilon_{data}}{\epsilon_c - \epsilon_b}. \tag{6.1}$$

The obtained values of $(b \rightarrow e)/(c \rightarrow e + b \rightarrow e)$ in RUN5 and RUN6 are combined. When the results in RUN5 and RUN6 are combined, following two issues should be taken carefully. First, a part of systematic errors of RUN5 and RUN6 are correlated. Second, a physical boundary exits in the value of $(b \rightarrow e)/(c \rightarrow e + b \rightarrow e)$, that is $0 < (b \rightarrow e)/(c \rightarrow e + b \rightarrow e) < 1$. BLUE (Best Linear Unbiased Estimate) method and Bayes' principle are applied to take into account such conditions [134, 135]. The combined mean values and standard deviations are determined using the BLUE method under the condition that there is no physical boundary. Then, Bayes' principle is applied to take into account the physical constraint.

6.1.1 BLUE Method in Correlation Analysis

The BLUE method is applied to combine the results in RUN5 and RUN6. Error sources are summarized in Table 6.1. The definition of the types of errors is described in Sec.5.6.4. In Table 6.1, the correlated systematic errors is tagged as B and they are assumed to have 100% correlation. With this assumption, the relation between correlated and uncorrelated errors in

Table 6.1: Summary of error source

error source	run5/6 correlation (Type)
statistics	0 % (A)
signal count	0% (A)
cocktail calculation	100%(B)
PISA geometry	0% (B)
simulation statistics	0% (A)
Event generator	100%(B)

BLUE to become simple as follows.

$$(\sigma^{corr})^2 = \rho \sigma_{run5} \sigma_{run6}, \tag{6.2}$$

$$\sigma^{corr} = \sqrt{\sigma_{run5}^{sys-B} \sigma_{run6}^{sys-B}}, \tag{6.3}$$

$$\sigma_{runi}^{uncorr} = \sqrt{(\sigma_{runi})^2 - (\sigma^{corr})^2}. \tag{6.4}$$

From the above equations, the weighted average and combined error are obtained as follows.

$$<r> = \frac{r_{run5}(\sigma_{run6}^{uncorr})^2 + r_{run6}(\sigma_{run5}^{uncorr})^2}{(\sigma_{run5}^{uncorr})^2 + (\sigma_{run6}^{uncorr})^2}, \tag{6.5}$$

$$\sigma = \sqrt{\frac{\sigma_{run5}^2 \sigma_{run6}^2 - (\sigma^{corr})^4}{(\sigma_{run5}^{uncorr})^2 + (\sigma_{run6}^{uncorr})^2}}, \tag{6.6}$$

$$\sigma^{stat} = \frac{\sqrt{(\sigma_{run6}^{stat})^2 (\sigma_{run5}^{uncorr})^4 + (\sigma_{run5}^{stat})^2 (\sigma_{run6}^{uncorr})^4}}{(\sigma_{run5}^{uncorr})^2 + (\sigma_{run6}^{uncorr})^2}, \tag{6.7}$$

$$\sigma^{sys} = \sqrt{\sigma^2 - (\sigma^{stat})^2}. \tag{6.8}$$

(χ^2/ndf) of the combination is 3.0/4, which indicates that the results in RUN5 and RUN6 are consistent.

6.1.2   Physical Constraint

The ratio, $(b \to e)/(c \to e + b \to e)$ which we want to determine in this analysis has physical boundary, $0 \le (b \to e)/(c \to e + b \to e) \le 1$. Bayes' principle is applied to take into account the effect of the physical constraint [46, 47]. Bayes' principle is

$$f(r \mid \epsilon) = \frac{L(\epsilon \mid r)g(r)}{\int_{r'} L(\epsilon \mid r')g(r')dr'}. \tag{6.9}$$

Here, ϵ is the outcome of experiment (tagging efficiency in this analysis) and r is an unknown parameter that we want to determine $((b \to e)/(c \to e + b \to e)$ in this analysis). $f(r \mid \epsilon)$ is the posterior probability density function when experimental value ϵ is given. Since $f(r \mid \epsilon)$

includes all knowledge about r, we can determine the error of r when we get $f(r \mid \epsilon)$. $L(\epsilon \mid r)$ is the likelihood function, that is the joint probability density function for the data given a certain value of r. $g(r)$ is the prior probability density function. Since the statistics does not give us any information about $g(r)$, we must assume the distribution of $g(r)$ reasonably. We assume that $(b \to e)/(c \to e + b \to e)$ has uniform distribution from 0 to 1 in this analysis. Since the obtained error for ϵ obey Gaussian, $f(r \mid \epsilon)$ becomes

$$
\begin{aligned}
f(r \mid \epsilon) &= A \times \exp\{-(r - r_0)/2\sigma_r^2\} \quad (0 \le r \le 1), \\
f(r \mid \epsilon) &= 0 \quad (0 > r \mid\mid r > 1).
\end{aligned}
\tag{6.10}
$$

Here, r_0 is the obtained r from the combination of RUN5 and RUN6 analysis and σ_r is the obtained deviation from r the combination. A is a normalization factor so that the integral value of $f(r \mid \epsilon)$ becomes 1.

The variables, x_1 and x_2 are defined as following equations.

$$
\begin{aligned}
\int_0^{x_1} f(r \mid \epsilon) dr &= \int_{x_2}^1 f(r \mid \epsilon) dr = (1 - \alpha)/2, \\
\int_{x_1}^{x_2} f(r \mid \epsilon) dr &= \alpha. \\
\alpha &= 0.6827
\end{aligned}
\tag{6.11}
$$

Deviation from x_1 and x_2 to mean value are considered as the standard deviation.

6.1.3 Lower and Upper Limit

90% C.L is determined for the highest and the lowest elecctron p_T range ($2.0 < p_\mathrm{T} < 3.0$ GeV/c and $5.0 < p_\mathrm{T} < 7.0$ GeV/c), since the mean value obtained by the BLUE analysis is close to the boundary.

Probability density function is defined as bellow.

$$
\begin{aligned}
f(r) &= A \times \exp(-(r - r_0)^2/2\sigma^2) \quad (0 < r < 1), \tag{6.12} \\
r_0 &= \frac{\epsilon_c - \epsilon_{data}}{\epsilon_c - \epsilon_b}, \tag{6.13} \\
\sigma &= \sqrt{\sigma_{stat}^2 + \sigma_{sys}^2}. \tag{6.14}
\end{aligned}
$$

Here, A is a normalization factor to have integrated value becomes 1. σ_{stat} is statistical error of ϵ_{data} without the consideration of the boundary. σ_{sys} is also systematic errors of ϵ_{data}, ϵ_c and ϵ_b without the consideration of the boundary.

90% C.L is determined from this probability density fucntion. The values at which integrated probability density function becomes 50% from the boundary are also determined as the mean values.

6.1.4   The Combined Result

Figure 6.1 shows the combined result about the bottom fraction, $(b \to e)/(c \to e + b \to e)$ as a function of electron p_T with FONLL prediction [77, 82]. In this figure, black points show the the obtained $(b \to e)/(c \to e + b \to e)$. Red line show the central value in FONLL prediction and pink solid and dotted lines show the uncertainty of FONLL calculation. Pink solid lines in Fig. 6.1 show $(b \to e)/(c \to e + b \to e)$ of the FONLL prediction when the correlation of the uncertainty about cross sections of charm and bottom are maximum. Pink dotted lines show $(b \to e)/(c \to e + b \to e)$ of the FONLL prediction when the correlation of the uncertainty about cross sections of charm and bottom are anti-maximum. The results are also summarized in Table 6.2. FONLL is almost consistent with the obtained result within the theoretical uncertainty.

It is worth to note that the point at lowest p_T has a small value. This suggests majority of interested yield of 'single non-photonic electron', that is the electron after the subtraction of all possible background and what we have been measured, can be explained as semi-leptonic $c \to e$ decay. It provides the proof that the indirect measurement of heavy flavor via electrons performed at PHENIX is really measurement of heavy flavor.

Table 6.2: Result of $(b \to e)/(c \to e + b \to e)$ in RUN5 and RUN6

2.35 GeV/c	< 0.41 (90% C.L) 0.19 (50% point)
3.37 GeV/c	$0.26^{+0.14}_{-0.13}$(stat)$^{+0.11}_{-0.11}$(sys)
4.40 GeV/c	$0.63^{+0.18}_{-0.21}$(stat) $\pm$ 0.08(sys)
5.66 GeV/c	> 0.33 (90% C.L) 0.71 (50% point)

6.2   Comparison of the Data with Simulation

The invariant mass (M_{eh}) distributions of extracted signals in the data shown at Fig 5.58 and 5.59 are compared with those generated by PYTHIA and EvtGen simulation. The distributions are normalized by number of the single non-photonic electrons. An agreement of the simulation results with the data provide the confidence for this analysis method and the result.

Figure 6.2 to 6.7 show the invariant mass distributions of extracted signals in the data and the simulation at each electron p_T range in RUN5 and RUN6. In these figures, black points are the data points. Red points show the result of PYTHIA and EvtGen simulation only for charm production and blue points show the result of PYTHIA and EvtGen simulation only for bottom production. Green points show the result of the simulation which is obtained by combining the charm and bottom contributions according to the obtained $(b \to e)/(c \to e + b \to e)$ values.

The agreement of simulation (green) and real data is good. χ^2/ndf values which are calculated in $0.4 < M_{eh} < 5.0$ GeV/c^2 are summarized in Table 6.3. Uncertainty of simulation is NOT included in these (χ^2/ndf).
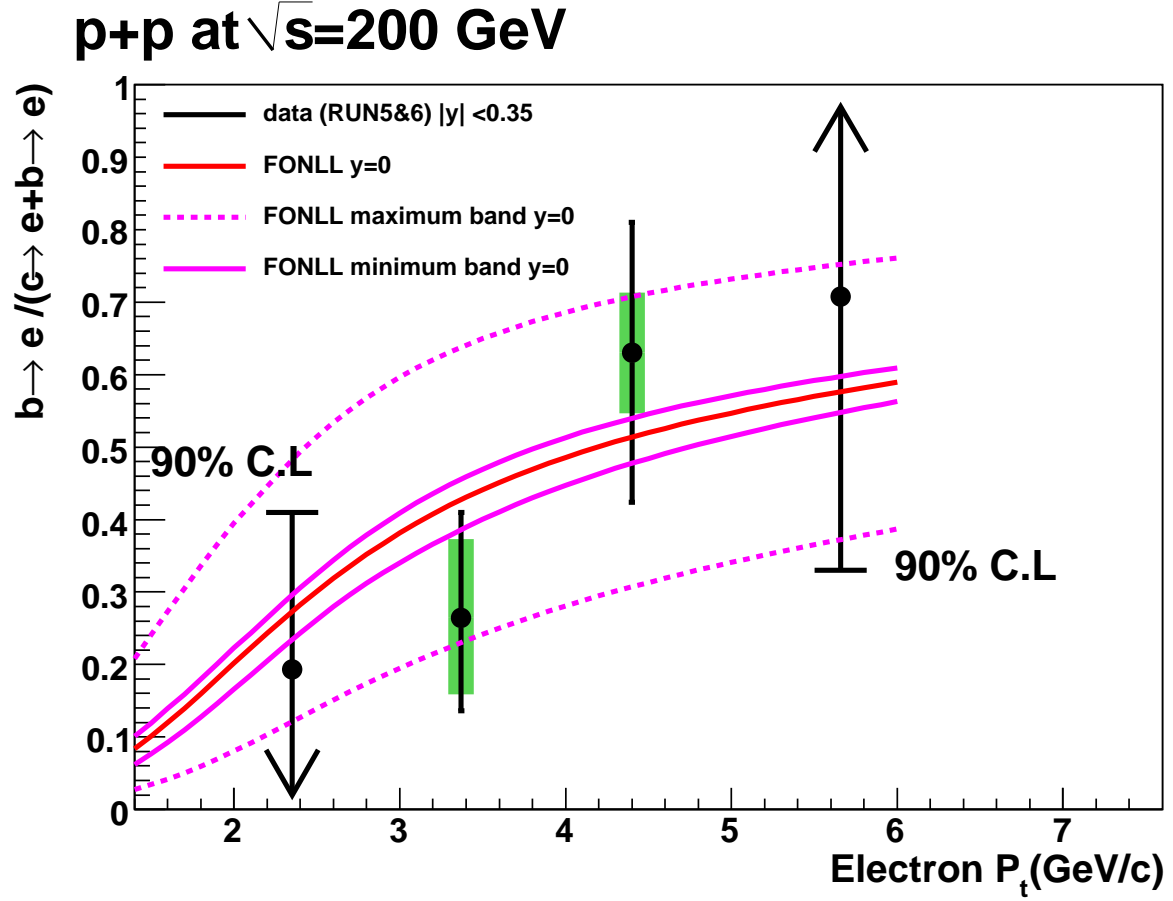
Figure 6.1: $(b \to e)/(c \to e + b \to e)$ in the electrons from heavy flavor as a fiction of electron p_T in RUN6 and RUN5 with FONLL calculation. Black points show the result in RUN6 and RUN5. Red lines are FONLL prediction and pink solid and dotted lines are uncertainty of FONLL prediction.

Table 6.3: χ^2/ndf (theoretical uncertainty is NOT included)

electron p_T	$\chi^2/ndf(\text{RUN5})$	$\chi^2/ndf(\text{RUN6})$
2.0-3.0 GeV/c	20.3/22	17.2/22
3.0-4.0 GeV/c	15.5/22	21.2/22
4.0-5.0 GeV/c	28.0/22	23.1/22
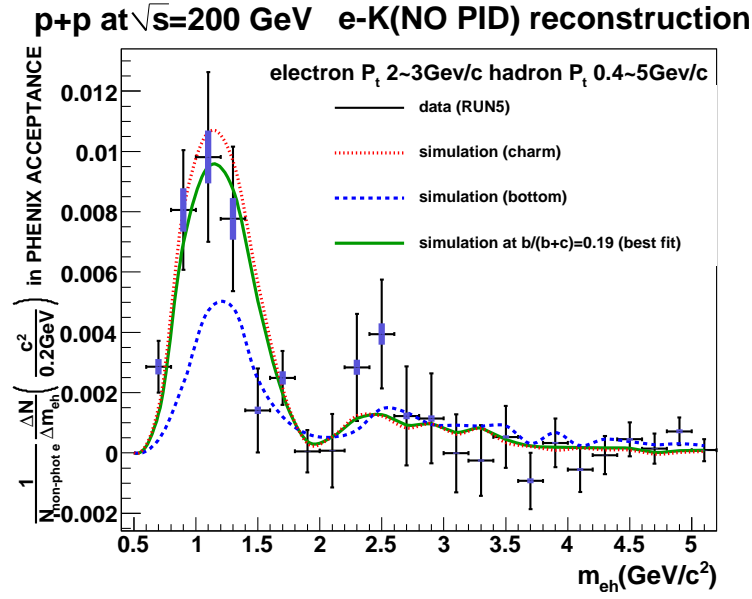
Figure 6.2: Comparison of the data with PYTHIA and EvtGen simulation about subtracted invariant mass distributions in RUN5. Electron p_T range is 2.0-3.0 GeV/c.
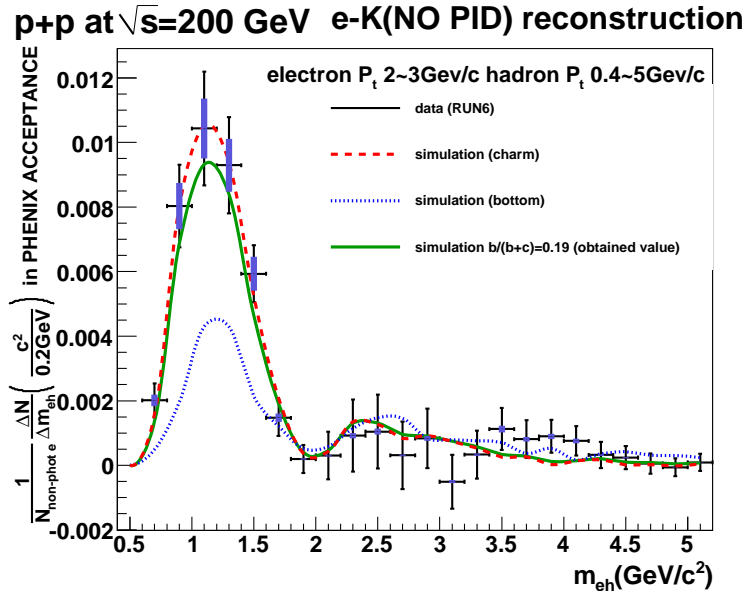
Figure 6.3: Comparison of the data with PYTHIA and EvtGen simulation about subtracted invariant mass distributions in RUN6. Electron p_T range is 2.0-3.0 GeV/c.
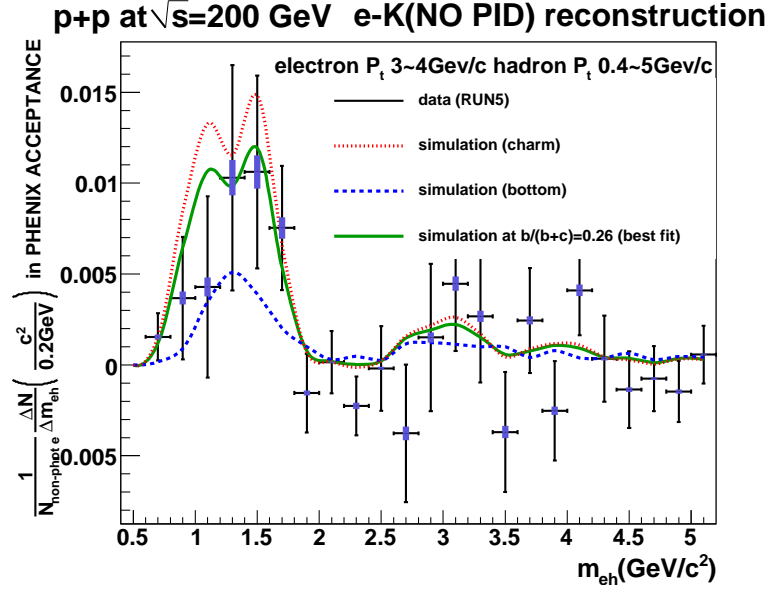
Figure 6.4: Comparison of the data with PYTHIA and EvtGen simulation about subtracted invariant mass distributions in RUN5. Electron p_T range is 3.0-4.0 GeV/c.
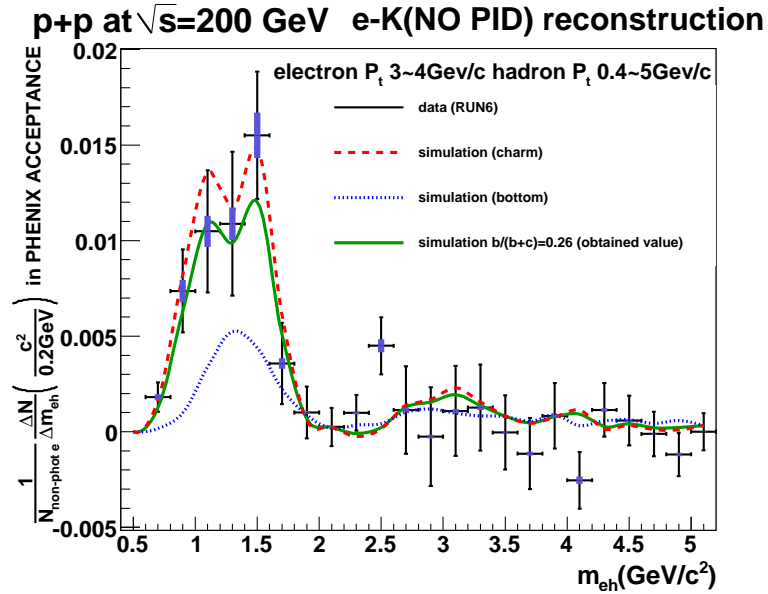
Figure 6.5: Comparison of the data with PYTHIA and EvtGen simulation about subtracted invariant mass distributions in RUN6. Electron p_T range is 3.0-4.0 GeV/c.
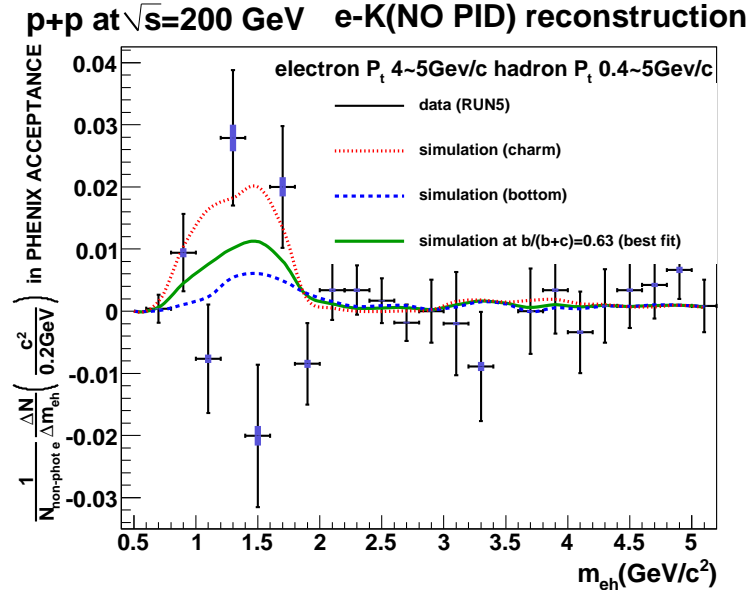
Figure 6.6: Comparison of the data with PYTHIA and EvtGen simulation about subtracted invariant mass distributions in RUN5. Electron p_T range is 4.0-5.0 GeV/c.
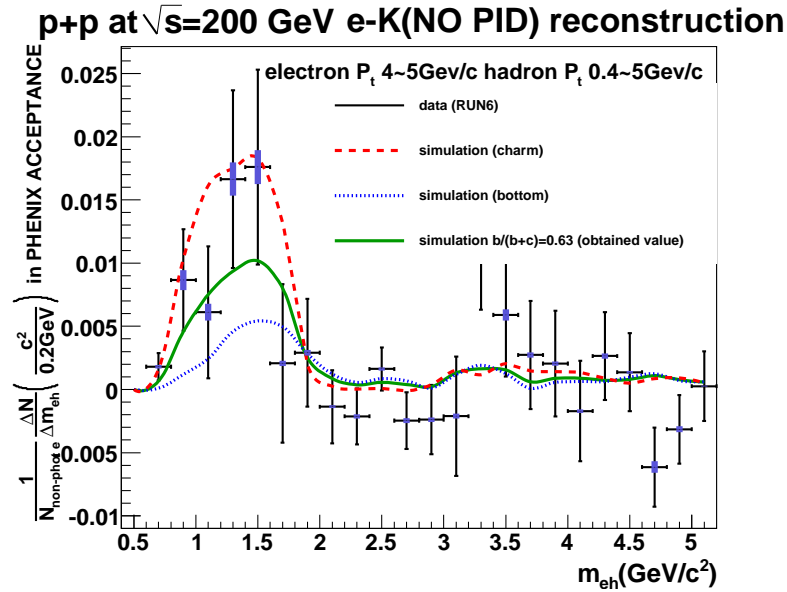
Figure 6.7: Comparison of the data with PYTHIA and EvtGen simulation about subtracted invariant mass distributions in RUN6. Electron p_T range is 4.0-5.0 GeV/c.

6.3 Cross Section of Bottom

Cross section of bottom is obtained using the spectrum of the electrons from heavy flavor and the ratio, $(b \to e)/(c \to e + b \to e)$.

6.3.1 Invariant Cross Section of Electrons from Charm and Bottom

The differential invariant cross section of the electrons from semi-leptonic decay of charm and that from bottom are obtained by (electron spectrum from heavy flavor) $\times$ $(c(b) \to e)/(c \to e + b \to e)$. $(b \to e)/(c \to e + b \to e)$ is obtained in the four electron p_T range, 2-3GeV/c, 3-4GeV/c, 4-5GeV/c and 5-7GeV/c. The spectrum of the single non-photonic electrons is merged into these electron p_T range to make the same bin width as $(b \to e)/(c \to e + b \to e)$. The yield at the electron p_T, where $(b \to e)/(c \to e + b \to e)$ is obtained, is calculated as follows.

$$Y(p_T^{real}) = \frac{f(p_T^{real})}{f(p_T^0)} \times Y(p_T^0). \tag{6.15}$$

Here, p_T^{real} is the bin values of electron p_T where $(b \to e)/(c \to e + b \to e)$ is obtained, p_T^0 is the bin values where the electron spectrum is rebined, $f(p_T)$ is the fit function of the electron spectrum and $Y(p_T)$ is the electron yield.

Figure 6.8 shows the invariant cross section of single electrons from charm and those from bottom with FONLL calculation. The spectrum of single electrons (circles) is also shown as a reference. The results are also summarized in Table 6.4.

Table 6.4: Invariant cross section of electrons from charm and bottom

electron p_T	cross section (mb GeV$^{-2}c^3$)	data/FONLL
2.35 GeV/c	> 3.30 (90% C.L) 4.52 (50%) $\times 10^{-6}$	> 1.49 (90% C.L) 2.03 (50%)
3.37 GeV/c	$4.17^{+0.73+0.41}_{-0.83-0.46} \times 10^{-7}$	$2.05^{+0.36+0.20}_{-0.41-0.22}$
4.40 GeV/c	$3.49^{+1.95}_{-1.70} \pm 0.66 \times 10^{-8}$	$1.16^{+0.65}_{-0.56} \pm 0.22$
5.66 GeV/c	< 1.11 (90% C.L) 0.48 (50%) $\times 10^{-8}$	< 2.48 (90% C.L) 1.08 (50%)
bottom		
2.35 GeV/c	< 2.30 (90% C.L) 1.08 (50%) $\times 10^{-6}$	< 2.74 (90% C.L) 1.29 (50%)
3.37 GeV/c	$1.49^{+0.83+0.73}_{-0.73-0.66} \times 10^{-7}$	$0.99^{+0.55+0.48}_{-0.48-0.43}$
4.40 GeV/c	$5.95^{+1.70}_{-1.95} \pm 1.10 \times 10^{-8}$	$1.87^{+0.54}_{-0.61} \pm 0.34$
5.66 GeV/c	> 0.54 (90% C.L) 1.17 (50%) $\times 10^{-8}$	> 0.90 (90% C.L) 1.93 (50%)

6.3.2 Total Cross Section of Bottom

Total cross section of bottom is obtained from the spectrum of the electron from bottom. The procedure to get total cross section of bottom can be written by following equations.

$$\left.\frac{d\sigma_{b\bar{b}}}{dy}\right|_{y=0} = \frac{1}{BR(b \to e)} \frac{1}{C_{e/B}} \frac{d\sigma_{b \to e}}{dy}, \tag{6.16}$$

$$\sigma_{b\bar{b}} \quad = \quad \int_y dy \frac{d\sigma_{b\bar{b}}}{dy} \sim R \times \frac{d\sigma_{b\bar{b}}}{dy}\bigg|_{y=0}. \tag{6.17}$$

The procedures to calculate above equations are following.

- $b \to c \to e$ subtraction and p_T extrapolation to obtain $d\sigma_{b\to e}/dy$.

- Kinematical correction $(C_{e/B})$

- Branching ratio correction.

- Rapidity extrapolation. R is a correction factor for rapidity extrapolation

Differential cross section of single electrons from bottom shown in Fig 6.8 is integrated from $p_\mathrm{T} = 3$ GeV/c to $p_\mathrm{T} = 5$ GeV/c. The points at $2 < p_\mathrm{T} < 3$ GeV/c and $5 < p_\mathrm{T} < 7$ GeV/c is dropped off for this integral, since confidence level is only determined at these region.

$$\frac{d\sigma^{b\to e+b\to c\to e}}{dy}\bigg|_{y=0} (3 < p_\mathrm{T} < 5 \ GeV/c) = 0.0048^{+0.0018}_{-0.0016}(\mathrm{stat})^{+0.019}_{-0.018}(\mathrm{sys})\mu\mathrm{b}. \tag{6.18}$$

p_T Extrapolation

$b \to c \to e$ subtraction and p_T extrapolation are done by using PYTHIA and FONLL calculation. Figure 6.9 shows invariant cross sections of the electrons from bottom with FONLL calculation and PYTHIA with $1.5 < k_\mathrm{T} < 10$ GeV/c. Solid lines show the electron from $b \to c \to e$ and $b \to e$ and dotted lines show the electron from $b \to e$. In Fig 6.9 black line show FONLL calculation and other lines show PYTHIA with $1.5 < k_\mathrm{T} < 10$ GeV/c. The distribution of the simulations are normalized at 4-5 GeV/c points. Correction factor is determined from the simulation as follows.

$$\frac{(d\sigma^{b\to e})/(dy)_{|y=0}}{(d\sigma^{b\to e+b\to c\to e})/(dy)_{|y=0}(3 < p_\mathrm{T} < 5 \ GeV/c)}. \tag{6.19}$$

Obtained correlation factors from simulation are summarized in Table 6.5. We take 16.8 as the correction factor for the p_T extrapolation and $b \to c \to e$ subtraction. We assigned 2.0 as systematic error to cover PYTHIA simulation and FONLL results.

Kinematical Correction

The kinematical correlation factor, $C_{e/B}$ is applied to account for the difference in rapidity distribution of the electron from bottom and B hadron.
PYTHIA simulation is used to determine a kinematical correction factor, $C_{e/B}$.
Figure 6.10 shows the rapidity distribution of B hadron and the electrons from bottom at PYTHIA. Black points show the rapidity distribution of the electrons and red points show that of B hadron. Figure 6.11 shows the ratios of the rapidity distributions of the electrons over that of B hadron shown at Fig.6.10. $C_{e/B}$ is determined by straight line fit of this ratios. We use 0.88 as $C_{e/B}$.
Systematic error is not assigned for this correction, since this correction factor is determined by pure kinematics.

Table 6.5: Correction factors for p_T extrapolation and $b \to c \to e$ subtraction

simulation	Correction factor
PYTHIA $k_T 1.5$	18.6
PYTHIA $k_T 2.5$	16.9
PYTHIA $k_T 3.5$	15.9
PYTHIA $k_T 5.0$	15.3
PYTHIA $k_T 7.5$	14.9
PYTHIA $k_T 10.0$	14.7
FONLL p_T scaling	18.1
FONLL p_T scaling (max)	18.8
FONLL p_T scaling (min)	17.0

Table 6.6: Electron branching ratios of bottom hadrons

hadron	BR(e)
$B^{+(-)}$	10.8± 0.4
B^0	10.1± 0.4
B_s	7.9± 2.4
B baryons	8.6± 2.5

Branching ratio

Inclusive $BR(b \to e)$ is calculated from the production ratios of B hadron and their exclusive electron branching ratios. Their exclusive electron branching ratios are summarized in Table 6.6. As a result, inclusive $BR(b \to e)$ is determined to be $10.0\% \pm 1\%$. This assignment is conservative and also cover LEP result, 10.8%.

$d\sigma_{b\bar{b}}/dy_{|y=0}$ and $d\sigma^{b \to e}/dy_{|y=0}$ are obtained from above correction factors. The results are as follows.

$$\left. \frac{d\sigma^{b \to e}}{dy} \right|_{y=0} = 0.081^{+0.030}_{-0.027}(\text{stat})^{+0.034}_{-0.027}(\text{sys})\mu\text{b}. \tag{6.20}$$

$$\left. \frac{d\sigma_{b\bar{b}}}{dy} \right|_{y=0} = 0.92^{+0.035}_{-0.031}(\text{stat})^{+0.39}_{-0.36}(\text{sys})\mu\text{b}. \tag{6.21}$$

Figure 6.12 shows $d\sigma^{b \to e}/dy_{|y=0}$ with FONLL prediction as a function of rapidity. Figure 6.13 shows $d\sigma_{b\bar{b}}/dy_{|y=0}$ with FONLL prediction as a function of rapidity. The FONLL prediction is very consistent with the experimental result.

Rapidity Extrapolation

Total cross section of bottom is obtained by extrapolating rapidity of B hadron. The correction factor for rapidity extrapolation is determined by using the simulation as follows

$$R = \frac{\int dy \frac{d\sigma}{dy}(B \quad hadron)}{\int_{-0.5}^{0.5} dy \frac{d\sigma}{dy}(B \quad hadron)}. \tag{6.22}$$

The correction factor by rapidity distribution of B hadron at PYTHIA is 3.30. NLO calculation for heavy quark production (HVQMNR) is also used for rapidity extrapolation [41], since PYTHIA is just LO calculation. Figure 6.14 show rapidity distribution of bottom quark at HVQMNR using CTEQ5M as parton distribution function for example.

Generated rapidity distribution at HVQMNR is that of bare b quark, while we should integrate cross section for rapidity of B hadron. Generated rapidity distribution of bare b quark is expected to differ from that of bare b quark slightly by the fragmentation process.
The correction factor for the difference in the rapidity distribution between bare b quarks and B hadrons is estimated by the similar way to determine $C_{e/B}$. 0.96 is used for the correction for the fragmentation of bare b into B hadrons.
Therefore the rapidity correction is done as follows.

$$R = \frac{\int dy \frac{d\sigma}{dy}(B \quad hadron)}{\int_{-0.5}^{0.5} dy \frac{d\sigma}{dy}(B \quad hadron)} = \frac{\int dy \frac{d\sigma}{dy}(bare \quad b)}{\int_{-0.5}^{0.5} dy \frac{d\sigma}{dy}(bare \quad b)} \times \frac{1}{0.96}. \tag{6.23}$$

The correction factor is calculated by using HVQMNR at various conditions. Results are summarized in Table 6.7. CTEQ5M value, 3.44 is used as the correction factor. Systematic error for the correction factor is assigned 0.25 to cover the results at various conditions. $\sigma_{b\bar{b}}$ is obtained from the correction factor for rapidity extrapolation. The result is:

$$\sigma_{b\bar{b}} = 3.16^{+1.19}_{-1.07}(\text{stat})^{+1.37}_{-1.27}(\text{sys})\mu\text{b}. \tag{6.24}$$

The FONLL predicts $\sigma_{b\bar{b}} = 1.87^{+0.99}_{-0.67}\mu\text{b}$ and agrees with the experimental result.

Table 6.7: Correction factors for rapidity extrapolation

simulation condition	Correction factor(bare b)	Correction factor(B hadron)
CTEQ4M(PDF)	3.37	3.51
CTEQ5M1(PDF)	3.22	3.35
CTEQ5M(PDF)	3.30	3.44
CTEQ5HQ(PDF)	3.37	3.51
GRVHO(PDF)	3.44	3.58
CTEQ5M(PDF) b mass 4.5 GeV	3.20	3.33
PYTHIA		3.30
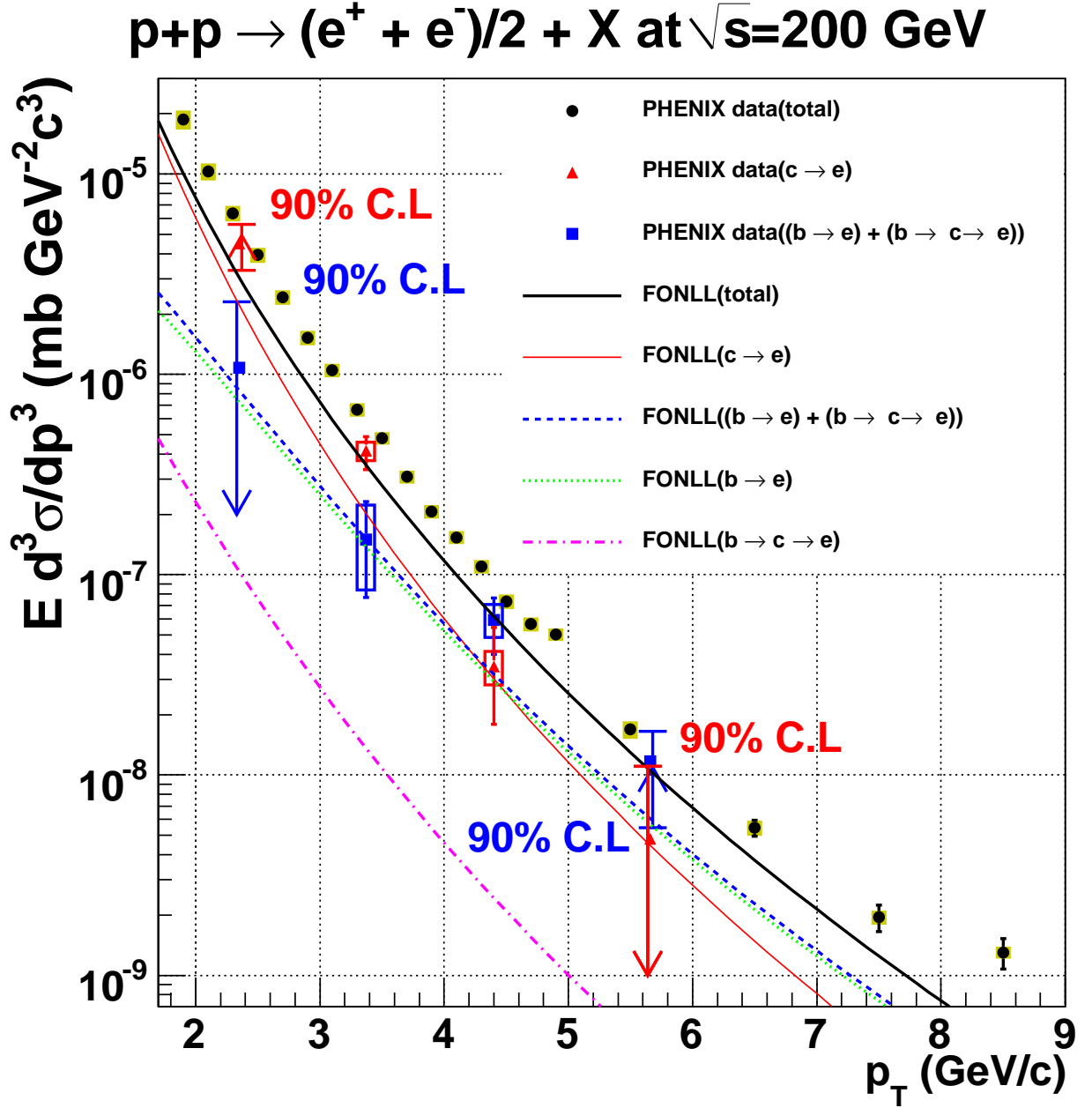
Figure 6.8: Invariant cross sections of electrons from charm and bottom with FONLL calculation.
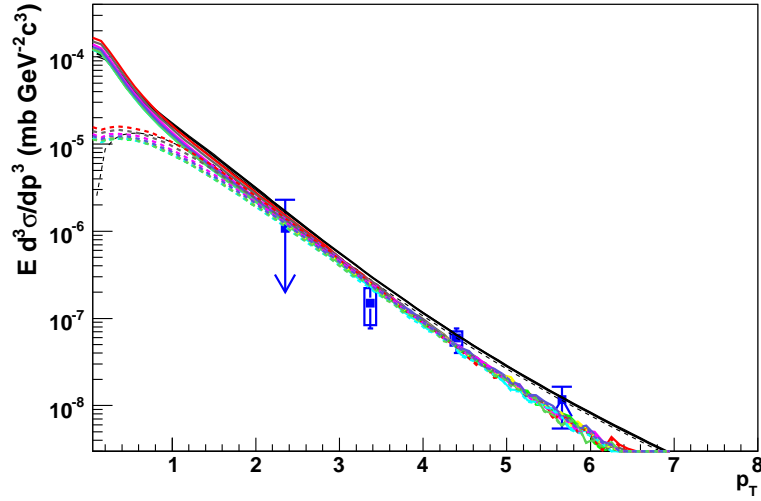
Figure 6.9: Invariant cross sections of electrons from bottom from FONLL calculation and PYTHIA. The simulations include electron from $b \rightarrow c \rightarrow e$ and $b \rightarrow e$. Black line show FONLL calculation. Other lines show PYTHIA with $1.5 < k_{\mathrm{T}} < 10$ GeV/c. Dotted lines show electron from $b \rightarrow e$.
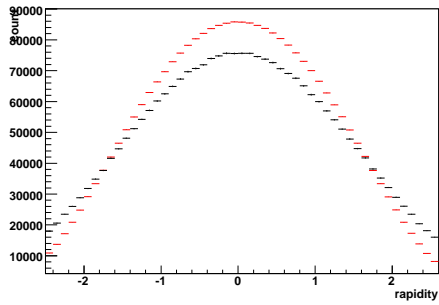
Figure 6.10: Rapidity distribution of B hadron and electrons from bottom at PYTHIA. Black points show the distribution of electrons and blue points show that of B hadron.
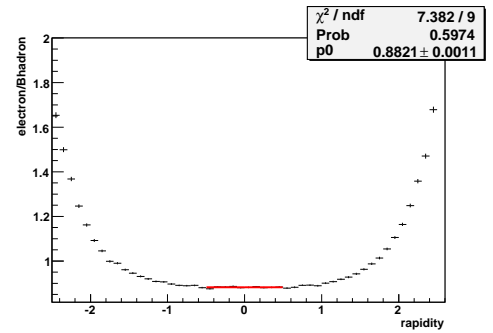
Figure 6.11: Ratios of the rapidity distributions shown at Fig.6.10
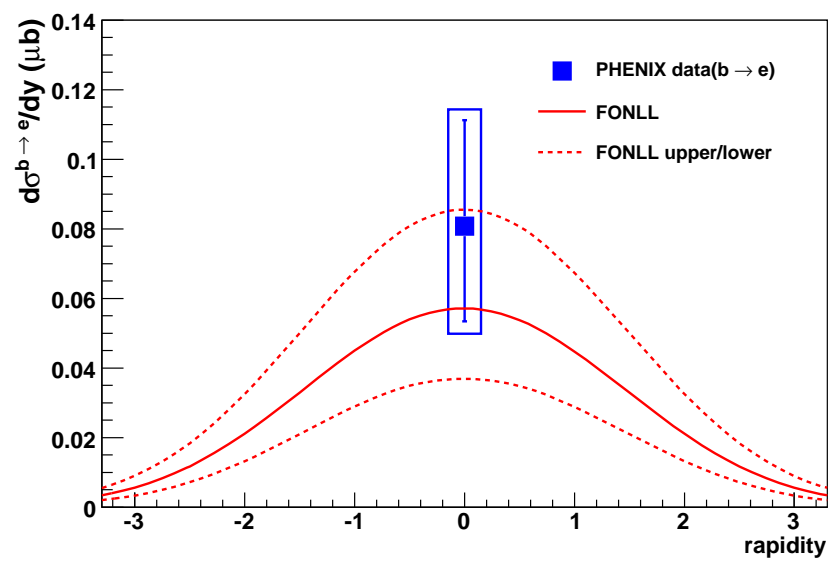
Figure 6.12: $d\sigma^{b\to e}/dy_{|y=0}$ with FONLL prediction as a function of rapidity.
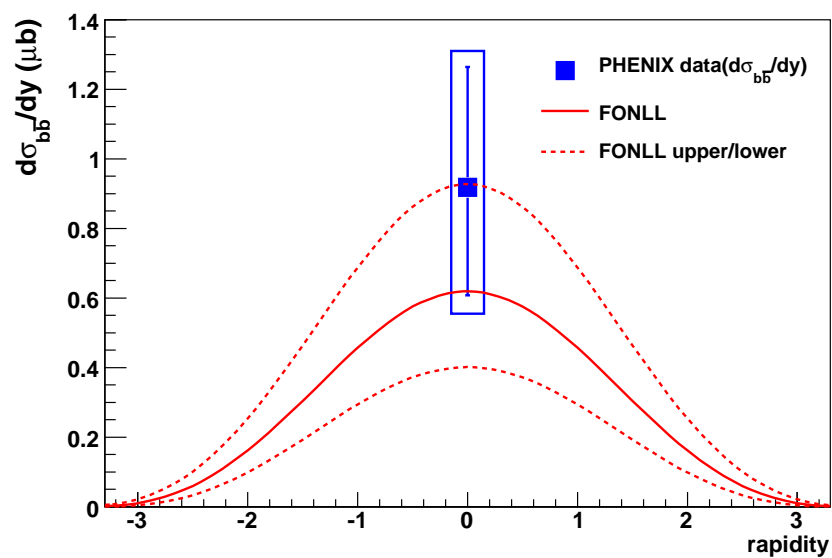
Figure 6.13: $d\sigma_{b\bar{b}}/dy_{|y=0}$ with FONLL prediction as a function of rapidity.
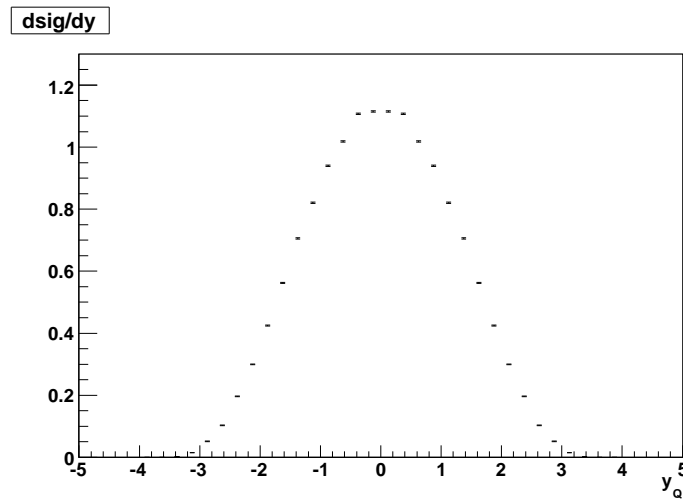
Figure 6.14: Rapidity distribution of bottom quark at HVQMNR using CTEQ5M as parton distribution function.

Chapter 7

Discussion

In this chapter, we discuss implications of the experimental results on the electrons from semi-leptonic decay of heavy flavors (single non-photonic electrons) in $p + p$ and Au+Au collisions. The measured p_{T} distributions of single electrons from charm and bottom are compared with pQCD calculation in Sec. 7.1. Total cross section of bottom is compared with the measured result via di-electron spectrum in PHENIX in Sec. 7.2. Total cross sections of charm and bottom in world data measured in hadron colliders are presented in Sec. 7.3. An implications of the R_{AA} and v_2 in Au+Au collisions are discussed based on the measured ratio, $(b \rightarrow e)/(c \rightarrow e + b \rightarrow e)$, in Sec. 7.4. The R_{AA} and v_2 in Au+Au collisions are compared with latest theoretical models in Sec. 7.5 Finally, important measurements about heavy flavor in the near future are discussed in Sec. 7.6.

7.1 Comparison with Perturbative QCD

The measured yield of heavy flavor in $p + p$ collisions provides a good test of perturbative QCD. For this purpose, the ratios of measured yield over the FONLL prediction are studied. Figure 7.1 the ratios, data/FONLL of single non-photonic electrons as a function of electron p_{T}. The dotted lines in Fig 7.1 represent uncertainties in the FONLL calculations. The FONLL calculation reproduce the measured yield of single non-photonic electrons within its uncertainty. Most of single non-photonic electrons for $p_{\mathrm{T}} < 2$ GeV/c originates from charm as shown in Sec. 6.1.4. Therefore, Fig 7.1 indicates the ratio data/FONLL for charm production is ~ 2.

Figure 7.2 the ratios, data/FONLL of the electrons from charm (upper panel) and bottom (lower panel) separately as a function of electron p_{T}. The FONLL prediction for charm production agrees with the data within the theoretical uncertainty and the ratio of data/FONLL is ~ 2. The uncertainty of FONLL for bottom production is less than that for charm production due to large mass of bottom. The FONLL prediction for bottom production also agrees with the data and the ratio of data/FONLL is ~ 1.

The similar tendency can be found in $p + \bar{p}$ collisions at $\sqrt{s} = 1.96$ GeV at Tevatron. Figure 7.3 and 7.4 shows the ratio, (measured results at CDF)/FONLL , of D and B hadrons as a function of heavy flavored hadron p_{T}, respectively [80, 69, 70, 79]. Maximum values of FONLL calculations for charm production are consistent with the measured results at CDF and
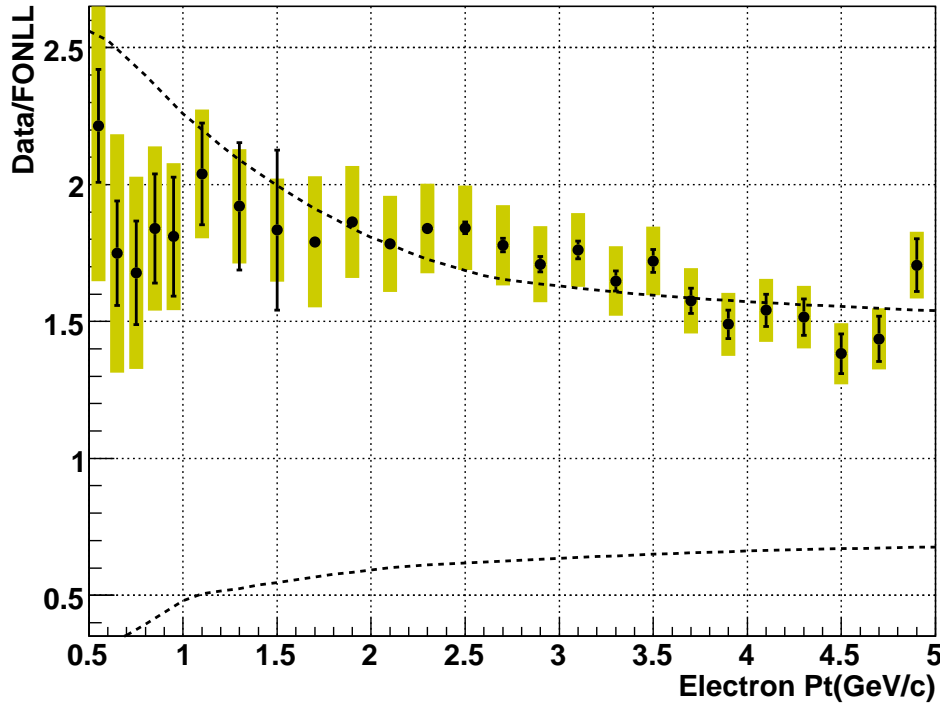
Figure 7.1: The ratios, data/FONLL of single non-photonic electrons as a function of electron p_T. The dotted line represent uncertainties in the FONLL calculations.

the ratio is $\sim$ 1.5-2.0. FONLL calculations for bottom production agrees with the measured results at CDF within its uncertainty and The ratio of data/FONLL is $\sim$ 0.8-1.2.

The ratios of (experimental results)/FONLL are $\sim$ 2 for charm production and $\sim$ 1 for bottom production at RHIC and Tevatron. Such difference can be understood in terms of a better convergence of the pQCD calculation for bottom production. It is worth to note that compared variables are not bare quarks but hadrons or these decay electrons and p_T distribution of hadrons (these decay electrons) in FONLL agrees with the measured results. This fact supports not only pQCD but also theoretical treatment of fragmentation process works well.

7.2   Comparison with Di-electron Measurement

PHENIX has measured the electron-positron pair mass spectrum in $p + p$ collisions at $\sqrt{s} =$ 200 GeV, from which the production cross section of heavy flavors is also obtained [171]. This measurement provides a good cross check for measurements to the results from single non-photonic electrons.

Figure 7.5 shows measured e^+e^- pair yield per $p + p$ collision in PHENIX acceptance. Combinatorial and correlated background are already subtracted. In Fig. 7.5 a cocktail of
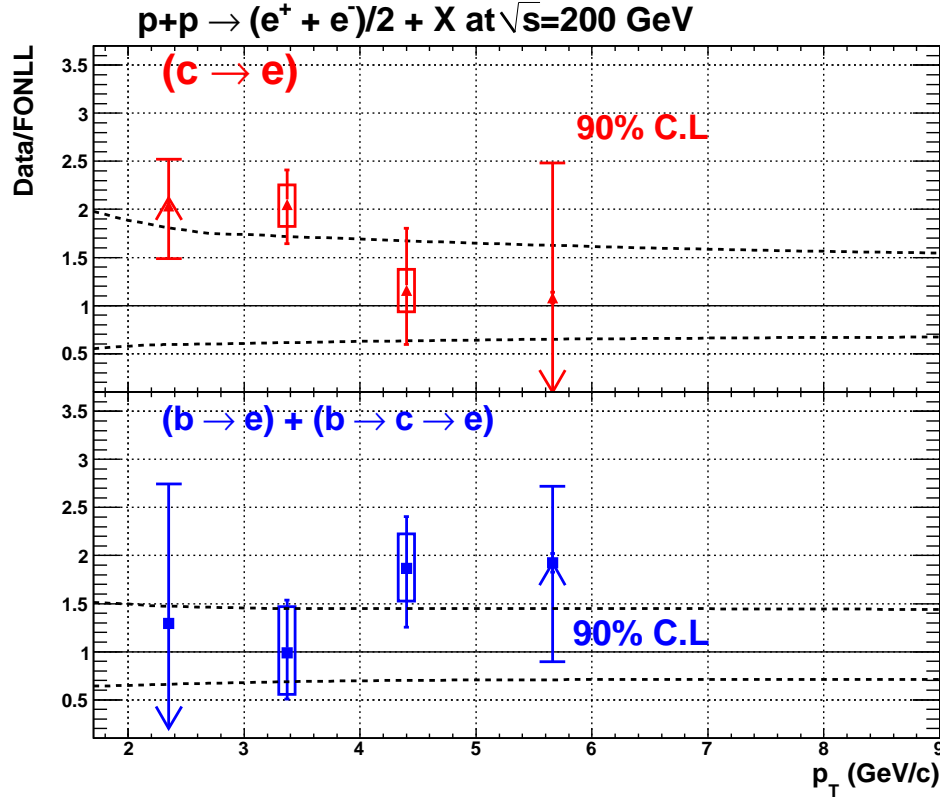
Figure 7.2: The ratios, data/FONLL of single non-photonic electrons from charm (upper panel) and bottom (lower panel) as a function of electron p_T. The dotted lines represent uncertainties in the FONLL calculations.

known sources discussed in Sec. 5.6.1 is also shown. The cocktail calculations account for the continuum in the mass region below ~ 1 GeV/c^2 and vector meson peaks. Except for the quarkonium peaks, the e^+e^- pair in the mass range above 1.1 GeV/c^2 is dominated by single non-photonic electron pairs correlated through flavor conservation.

Figure 7.6 shows the e^-e^+ pair yield remaining after the subtraction of the cocktail originated from the light particles and the quarkonium. The remaining contributions are from $c\bar{c} \rightarrow e^+e^-$, $b\bar{b} \rightarrow e^+e^-$ and Drell-Yan process. To extract contribution from $c\bar{c}$, the e^+e^- pair yield in the range from 1.1 to 2.5 GeV/c^2 is integrated. Integrated yield is extrapolated to zero e^+e^- pair mass by using the di-electron spectrum from $c\bar{c}$ simulated by PYTHIA. Contributions from $b\bar{b}$ and Drell-Yan process are estimated and subtracted. The extrapolated e^+e^- yield is converted cross section of charm. Total cross section of charm is obtained as $\sigma_{c\bar{c}} = 544 \pm 39(\text{stat}) \pm 142(\text{sys}) \pm 200(model)\mu\text{b}$, by using rapidity distribution from NLO pQCD calculation [154]. This result is compatible with the result from single non-photonic electron at PHENIX which gives $\sigma_{c\bar{c}} = 567 \pm 57(\text{stat}) \pm 224(\text{sys})\mu\text{b}$ [115].

Cross section of $b\bar{b}$ is also evaluated from di-electron spectrum as follows. The e^+e^- pair distribution after subtraction of Drell-Yan is fitted using the e^+e^- pair distributions from charm and bottom which are produced by PYTHIA. The obtained total cross section of bottom is
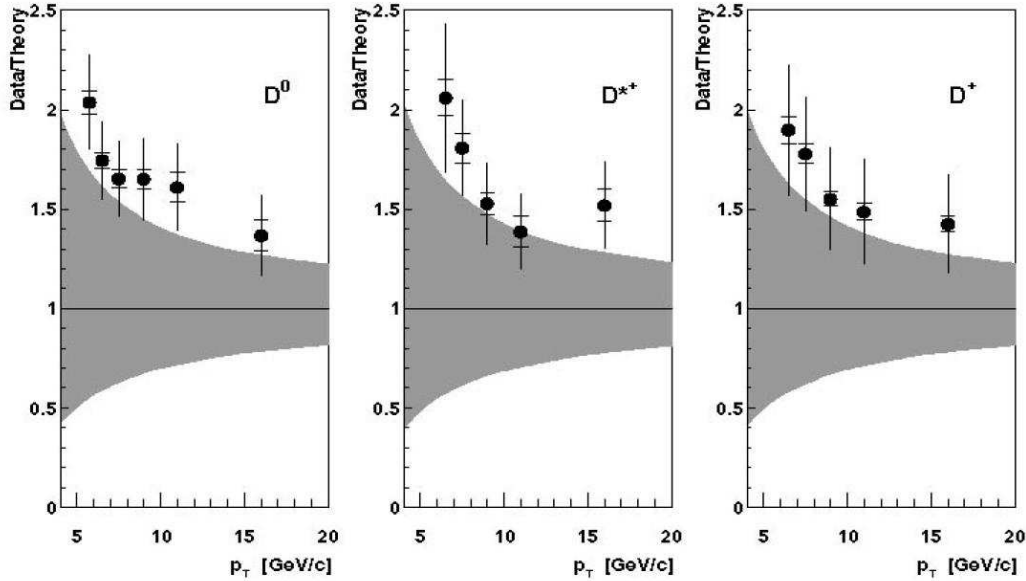
Figure 7.3: The ratios, (CDF data)/(FONLL) of D^0 (left panel), D^{*+} (middle panel) and D^+ (right panel). as a function of hadron p_T. The shadow area represent uncertainties in the FONLL calculations [80].

$\sigma_{b\bar{b}} = 3.9 \pm 2.5(\text{stat})^{+3}_{-2}(\text{sys})\mu\text{b}$. This result is consistent with the result from the spectrum of the single electrons obtained in this thesis.

7.3   Heavy Flavor Production in Hadron Collider

Figure 7.7 and 7.8 show the total cross sections of charm and bottom from the spectrum and di-electron analysis with other experiments in hadron collider as a function of $\sqrt{s}$ [72, 73, 74, 75, 76, 118], respectively. The CDF experiment for bottom production published to the limited rapidity range, $\sigma_{b\bar{b}}(|\ y\ |< 0.6)$. The result of CDF is extrapolated to the cross section, assuming the rapidity distribution given by HVQMNR. In Fig. 7.7 and Fig. 7.8, smooth lines represent cross section of charm and bottom calculated by NLO pQCD and dotted lines represent uncertainties in NLO pQCD.

Dependence of the cross section of heavy flavor production on $\sqrt{s}$ predicted by NLO pQCD agrees with world data including the result obtained in this thesis. This agreement indicates charm and bottom production in hadron collider is well understood by pQCD. The understanding of heavy flavor production supports the expectation that heavy flavors are only produced in the initial stage in the heavy ion collision. Therefore, measurements in $p + p$ collisions in this thesis provide important baselines for the study of the medium created in RHIC.
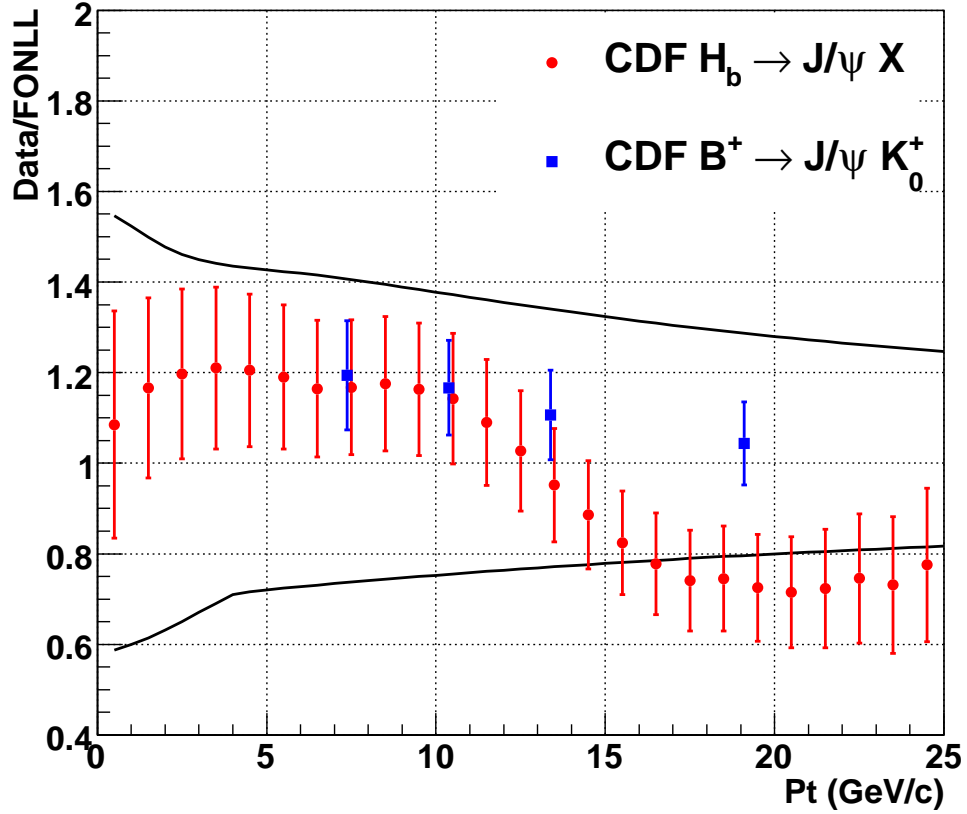
Figure 7.4: The ratios, data/FONLL of single non-photonic electrons from charm (upper panel) and bottom (lower panel) as a function of electron p_T. The dotted lines represent uncertainties in the FONLL calculations [69, 70, 79].

7.4 Interpretation of Results in Au+Au Collisions

In this section, the existence of the energy loss and flow of bottom in the hot and dense medium created at RHIC based on the R_{AA} and v_2 of the single electrons in Au+Au collisions and the measured $(b \to e)/(c \to e + b \to e)$.

The R_{AA} and v_2 of non-photonic electrons reported by PHENIX include the contribution from J/ψ, Υ and Drell-Yan process [114]. Their contributions are small but not negligible as discussed in Sec. 5.6.1. The medium modification of these contribution should be different from that of bare heavy quarks due to the different physical process in the medium. Therefore, the contribution from J/ψ, Υ and Drell-Yan process should be subtracted from the experimental result for the apple to apple comparison. The procedure to correct R_{AA} and v_2 of non-photonic electrons is described in Appendix. G. Figure 7.9 shows the corrected R_{AA} and v_2 of single non-photonic electrons in Au+Au collisions. Upper panel in Figure 7.9 shows the R_{AA} of the single non-photonic electrons in 0-10% central Au+Au collisions. Lower panel in Fig. 7.9 shows the v_2 of the single non-photonic electrons.
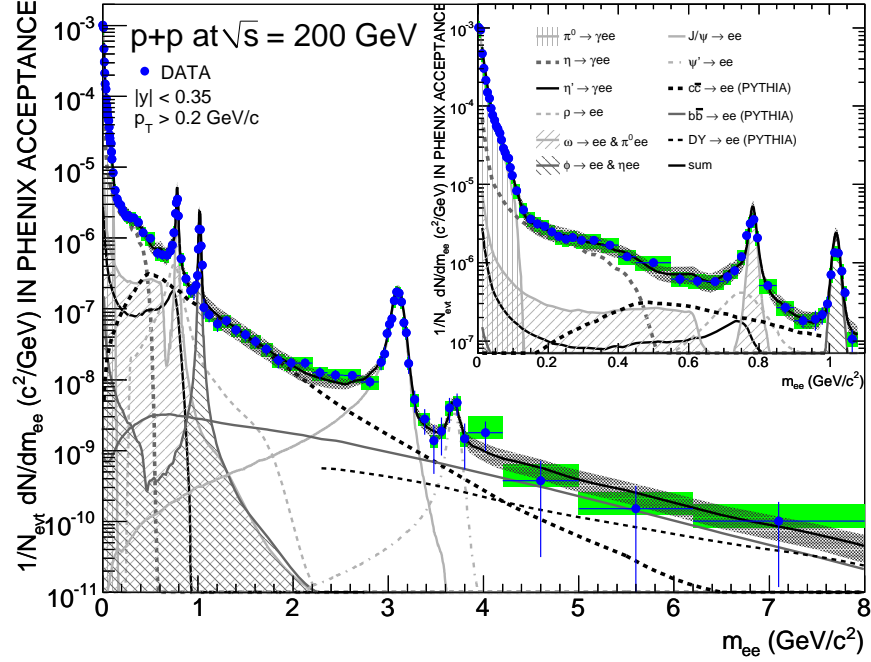
Figure 7.5: The e^-e^+ pair yield per $p+p$ collision in PHENIX acceptance with a cocktail of known sources.

7.4.1   Ratio of Bottom over Charm

The fraction of bottom in single non-photonic electrons, $(b \rightarrow e)/(c \rightarrow e + b \rightarrow e)$, is parameterized as a function of electron p_T assuming the shape of p_T distribution in FONLL. The absolute value is determined by the least-square fitting to the experimental results of $(b \rightarrow e)/(c \rightarrow e + b \rightarrow e)$ using Eq. F.1. The used fit method is described in Appendix. F. Figure 7.10 shows the resulting ratios of the single electrons from bottom over charm. Red line represents the best fit result and blue lines show 1σ uncertainties. The obtained absolute value of cross section from the fit is defined as the initial state of heavy flavor in heavy ion collisions for the comparison of $R_{AA}(p_T)$ and $v_2(p_T)$.

7.4.2   Modification of Bottom in the Medium

The magnitude of energy loss of bottom in the medium is expected to be much smaller than that of charm due to the large mass of bottom. The existence of significant bottom modification in the medium has been an open question when $(b \rightarrow e)/(c \rightarrow e + b \rightarrow e)$ has not been measured. In this subsection, the existence of significant bottom modification in the medium is shown from the measured $(b \rightarrow e)/(c \rightarrow e + b \rightarrow e)$.

For the purpose, we consider only energy loss of charm, that is, we assume that bottom quarks do not lose their energy in the medium. In this case, possible minimum values of R_{AA} of single non-photonic electrons are $(b \rightarrow e)/(c \rightarrow e + b \rightarrow e)$ in $p+p$ collisions, corresponding to the case which R_{AA} of the electrons from charm $\rightarrow 0$. Figure 7.11 shows R_{AA} of single non-photonic electrons in Au+Au collisions compared to possible minimum values, $(b \rightarrow e)/(c \rightarrow e + b \rightarrow$
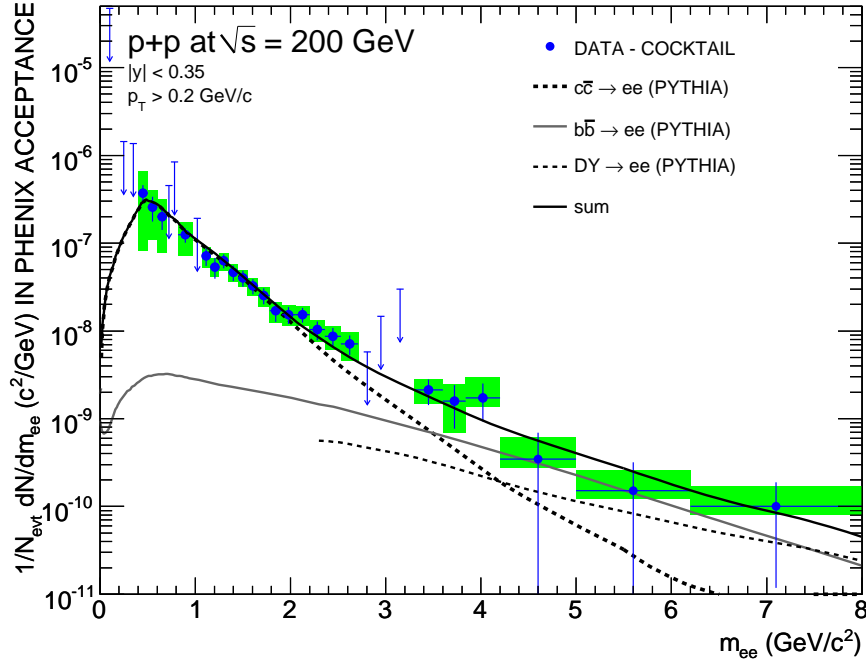
Figure 7.6: The e^-e^+ pair yield remaining after subtraction of the cocktail.

e) (solid line). Dotted lines in Fig 7.11 represent the uncertainties of $(b \to e)/(c \to e + b \to e)$ which is obtained in the previous subsection. Above 4.5 GeV/c, significant deviation ($> 3\sigma$) exists between the measured R_{AA} and possible minimum values where bottom do not lose energy. This deviation indicates not only charm but also bottom lose a certain fraction of their energy in the medium.

7.4.3 Contribution from Bottom in Au+Au Collisions

The contribution from bottom in Au+Au collisions becomes important for the discussion of $v_2(p_T)$ of in single non-photonic electrons. The contribution from bottom in single non-photonic electrons in Au+Au collisions should be larger than the measured value in $p+p$ collisions, since the suppression magnitude of bottom in the medium is expected to be much smaller than that of charm.

To evaluate the contribution of bottom in Au+Au collisions from the measured $(b \to e)/(c \to e + b \to e)$ in this thesis, a model calculation based on Langevin equation is done. A detailed implementation and procedure for the model calculation are described in Appendix. H. In this subsection, the procedure is briefly summarized and the result is shown.

The procedure in the model calculation is as follows.

- Generation of heavy quarks

- Simulation of space time evolution of heavy quarks in the medium

- Hadronization of bare heavy quarks
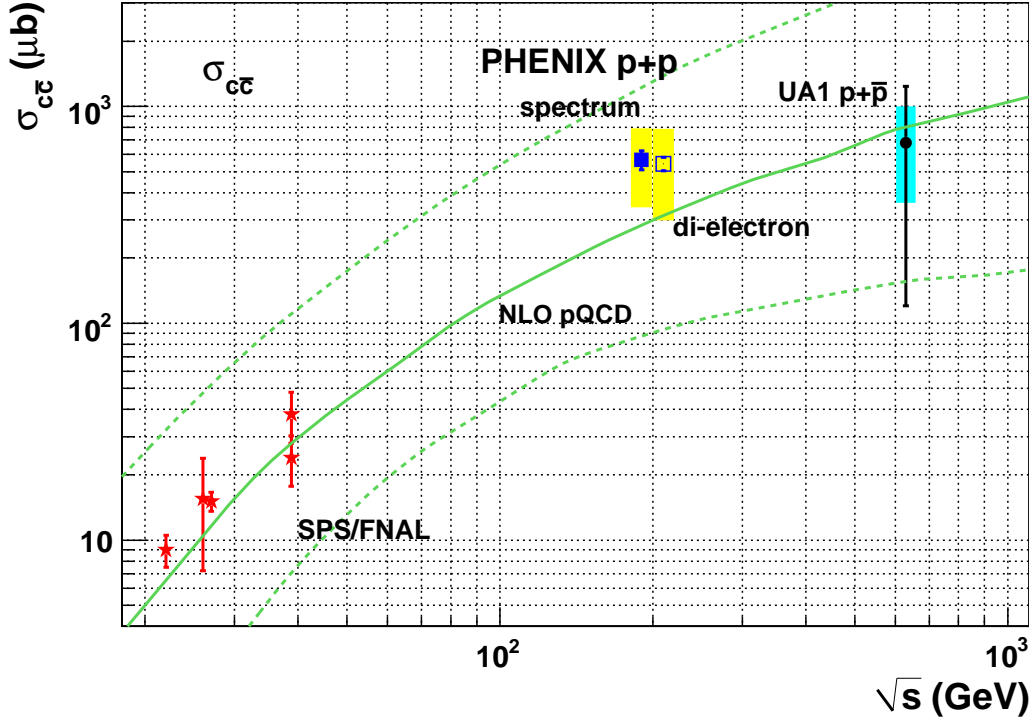
Figure 7.7: Total cross section of charm with other experiments as a function of $\sqrt{s}$ [118].

- Semi-leptonic decay of heavy flavored hadrons

The shape of p_{T} distribution of generated charm and bottom quarks are taken from the FONLL calculations. The absolute value of cross section is normalized according to $(b \to e)/(c \to e + b \to e)$ as described in Sec. 7.4.1.

Especially, understanding of space time evolution of heavy quarks in the medium is important since the difference of the medium modification between charm and bottom is generated in this stage. Monte-Carlo simulation using Langevin equation is applied for the description of the space time evolution. Heavy quarks are produced only in the initial hard collisions and it takes many collisions to change the momentum of heavy quark substantially due to their large mass compared with temperature of the medium (~ 200 MeV). Therefore, heavy quarks can be described as Brownian particle and the Langevin equation is a good approximation to model the motion of the heavy quarks in the medium [140, 141, 144].

The interaction between heavy quarks and the medium is represented in terms of drag force and diffusion coefficients in Langevin equation. The following relation is assumed for the drag coefficient.

$$\gamma = \alpha \frac{T^2}{M}, \tag{7.1}$$

where M is mass of heavy quark and α is the dimensionless free parameter which is independent of other parameters. Eq. 7.1 is motivated by the result from the AdS/CFT correspondence.
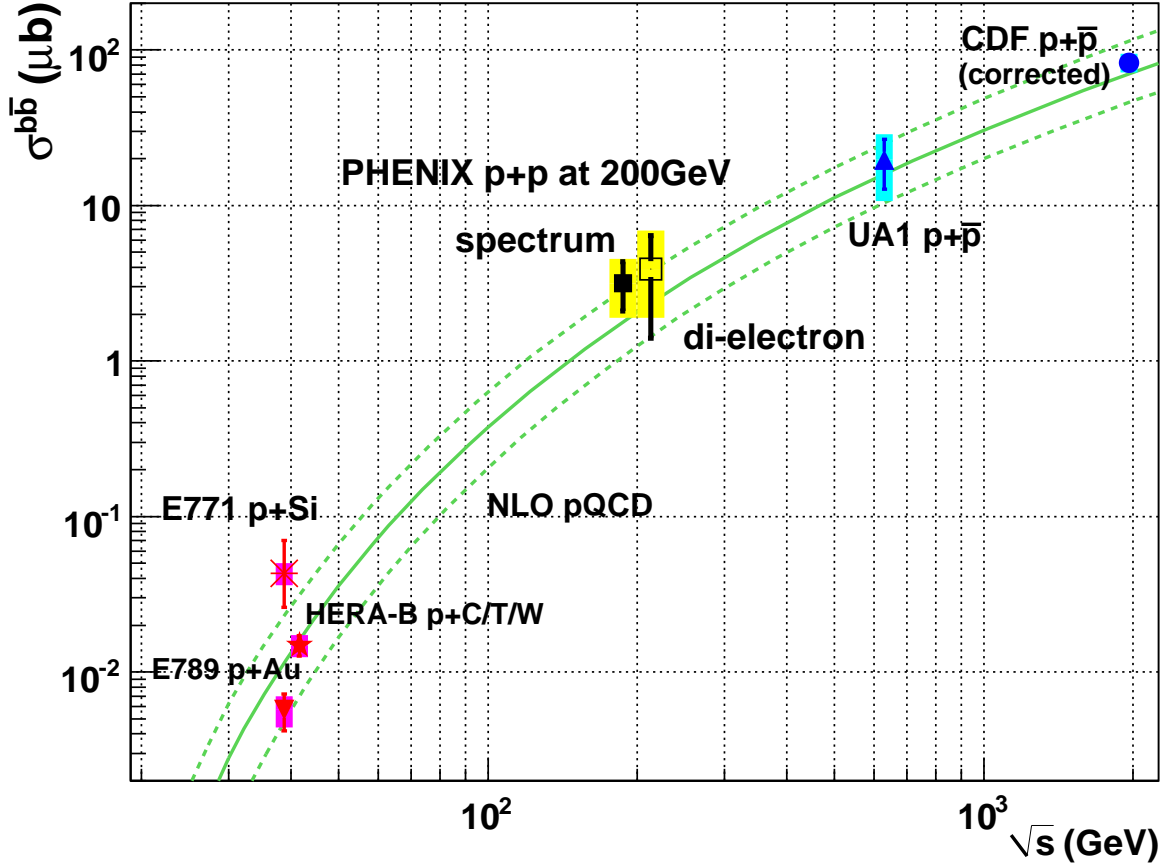
Figure 7.8: Total cross section of bottom with other experiments as a function of $\sqrt{s}$ [72, 73, 74, 75, 76].

This drag coefficient represents the strongly coupling limit of QGP because the AdS/CFT correspondence is valid under such condition as discussed in Sec. 2.2.3.

The magnitude of drag force (free parameter α) is constrained by the fit for the experimental $R_{AA}(p_T)$ and $v_2(p_T)$. The fit method is described in Appendix. F and H.5

Figure 7.12 shows $R_{AA}(p_T)$ and $v_2(p_T)$ of the decay electrons with the drag force defined in Eq. 7.1 (AdS/CFT) which are the results of the fit at the 3 ratios of $(b \rightarrow e)/(c \rightarrow e + b \rightarrow e)$, best fit and $\pm 1\sigma$. The blue solid line shows the result of $R_{AA}(p_T)$ and $v_2(p_T)$ at the best fit ratio of $(b \rightarrow e)/(c \rightarrow e + b \rightarrow e)$. The green dashed line and magenta dotted line show the result at the $\pm 1\sigma$ ratios of $(b \rightarrow e)/(c \rightarrow e + b \rightarrow e)$. The fit results are summarized in Table H.1. As a result, the experimental results are successfully reproduced with $\gamma = 2.1^{+0.4}_{-0.6} \frac{T^2}{M}$ including the uncertainty of the ratio of bottom over charm.

$(b \rightarrow e)/(c \rightarrow e + b \rightarrow e)$ in Au+Au collisions is evaluated as a function of electron p_T from the fit result of the magnitude of drag force (α). Figure 7.13 shows the evaluated $(b \rightarrow e)/(c \rightarrow e + b \rightarrow e)$ in Au+Au collisions. The dotted lines represent 1σ uncertainties.
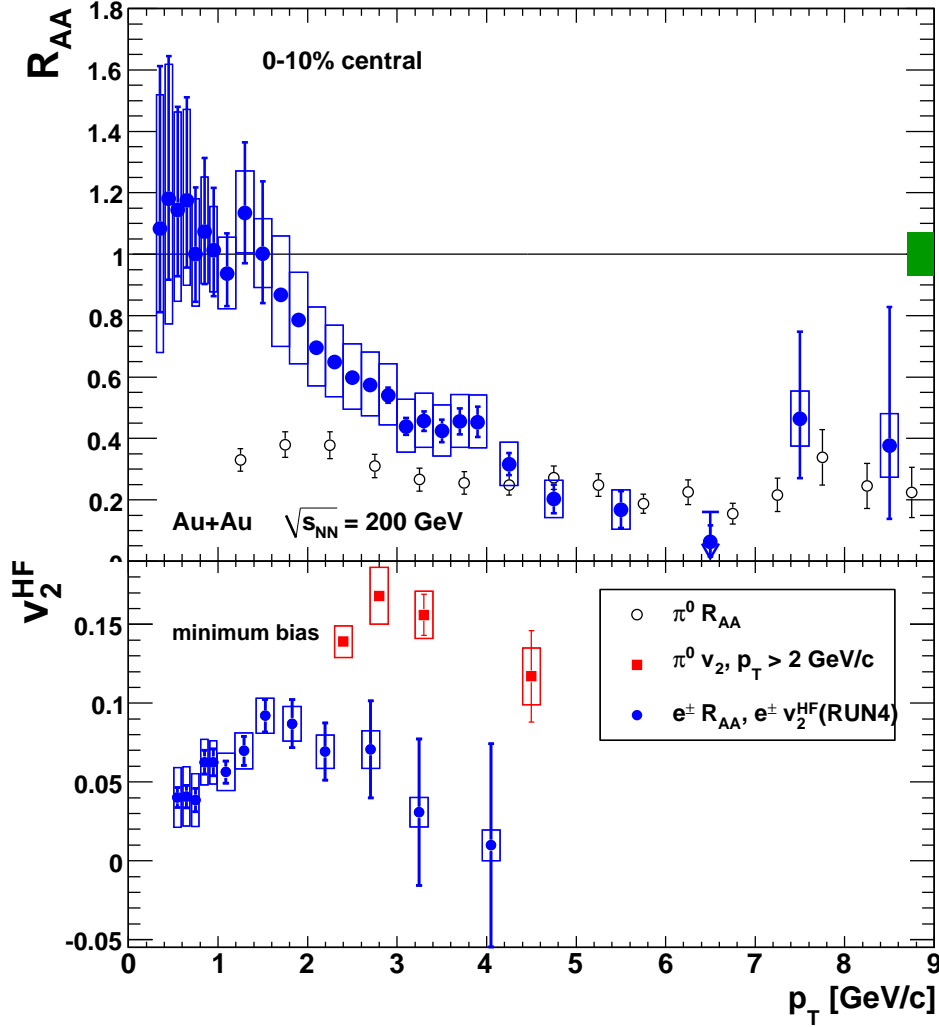
Figure 7.9: Upper panel:R_{AA} of the electrons from semi-leptonic decay of heavy flavor. Lower panel:v_2 of the electrons from semi-leptonic decay of heavy flavor.

Fig. 7.13 indicates the contribution from bottom dominates in single non-photonic electrons above $p_T \sim 2$ GeV/c. The decreasing $v_2(p_T)$ of single non-photonic electrons at $p_T > 2$ GeV/c can be understood as the effect of increasing contribution of bottom, since $v_2(p_T)$ of bottom is much smaller than that of charm. In addition, Fig. 7.13 suggests most of single non-photonic electrons is originated from bottom at $p_T > 3$ GeV/c. This fact directly leads to that the existence and magnitude of bottom flow can be studied by measurement of $v_2(p_T)$ at $p_T > 3$ GeV/c. It is difficult to obtain a strong physics message about bottom flow from the current measured $v_2(p_T)$, due to limited statistics in Au+Au collisions. However, more precise result about $v_2(p_T)$ of single non-photonic electrons will be obtained at the PHENIX experiment in the near future. The existence and magnitude of bottom flow will be revealed based on the coming result and the measured $(b \rightarrow e)/(c \rightarrow e + b \rightarrow e)$. The measured $(b \rightarrow e)/(c \rightarrow e + b \rightarrow e)$ in $p + p$ collisions provides an important base line for such discussion.
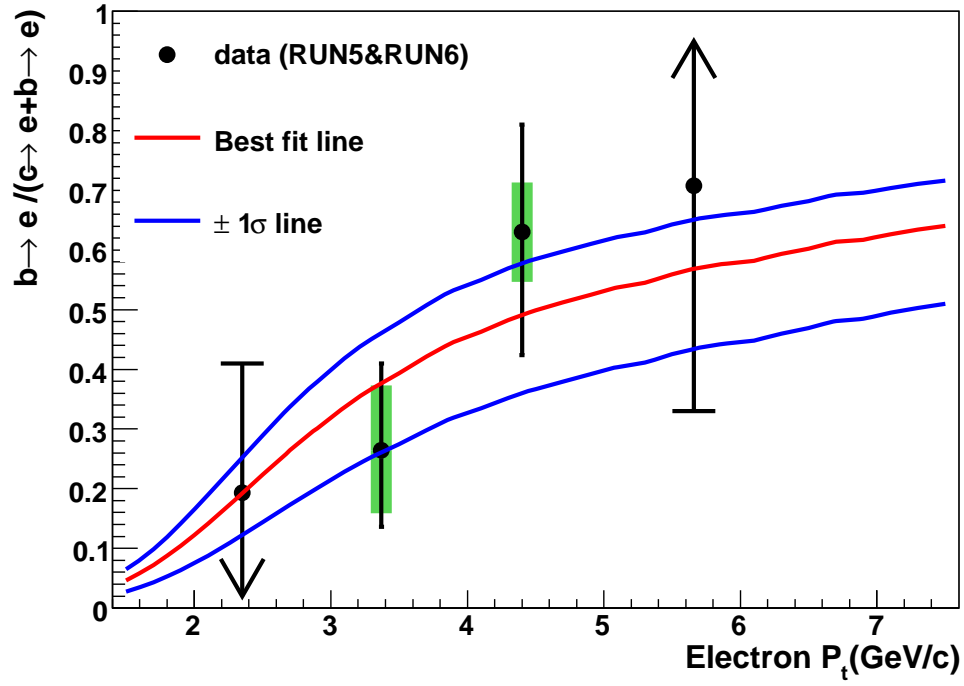
Figure 7.10: The ratio of the electrons from bottom over charm to use the comparison of $R_{AA}(p_T)$ and $v_2(p_T)$ which is obtained by the least-square fit using Eq. F.1.
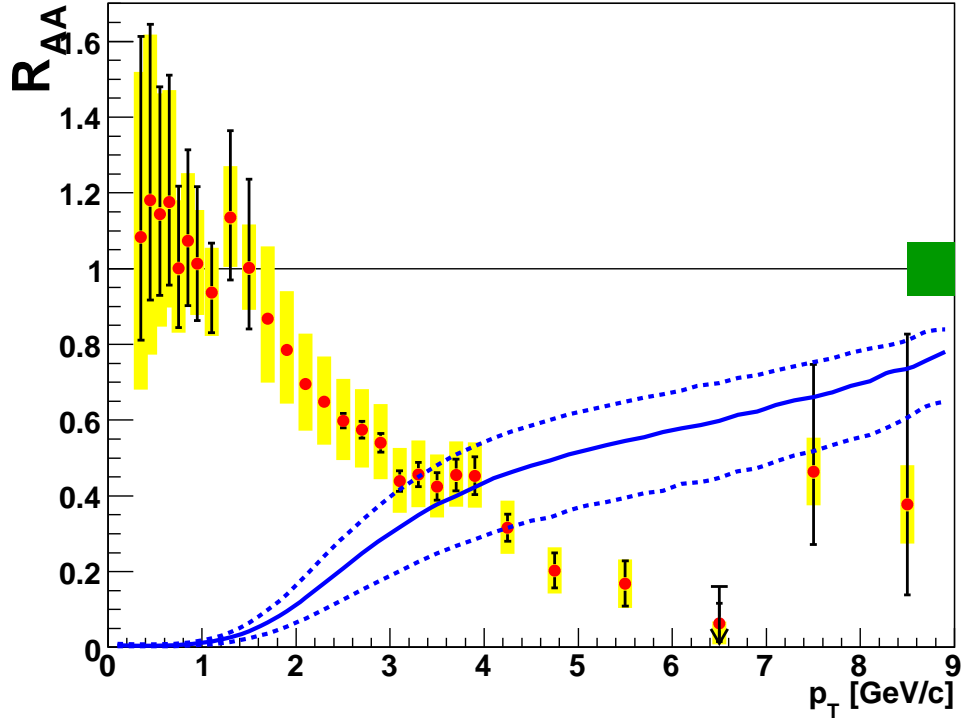
Figure 7.11: R_{AA} of single non-photonic electrons in Au+Au collisions compared to possible minimum values, $(b \rightarrow e)/(c \rightarrow e + b \rightarrow e)$ (solid line). Dotted lines represent the uncertainties of $(b \rightarrow e)/(c \rightarrow e + b \rightarrow e)$
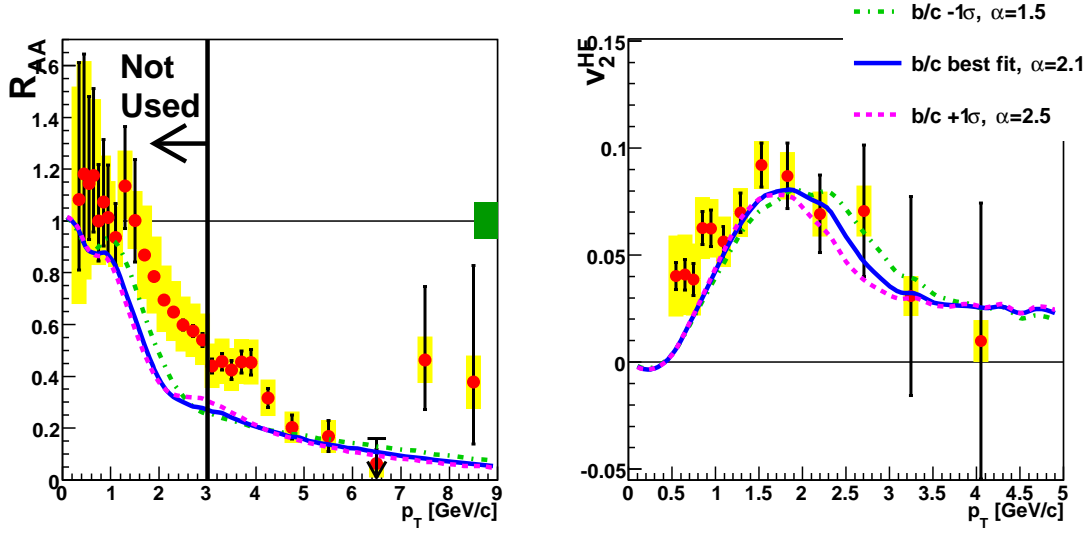
Figure 7.12: $R_{AA}(p_T)$ and $v_2(p_T)$ of single electrons which are the fit results for $R_{AA}(p_T)$ and $v_2(p_T)$ at the 3 ratios of $(b \to e)/(c \to e + b \to e)$, best fit and $\pm 1\sigma$. The drag force is defined in Eq. 7.1 (AdS/CFT). Data points of $R_{AA}(p_T)$ with $p_T < 3$ GeV/c are not used for the fit.
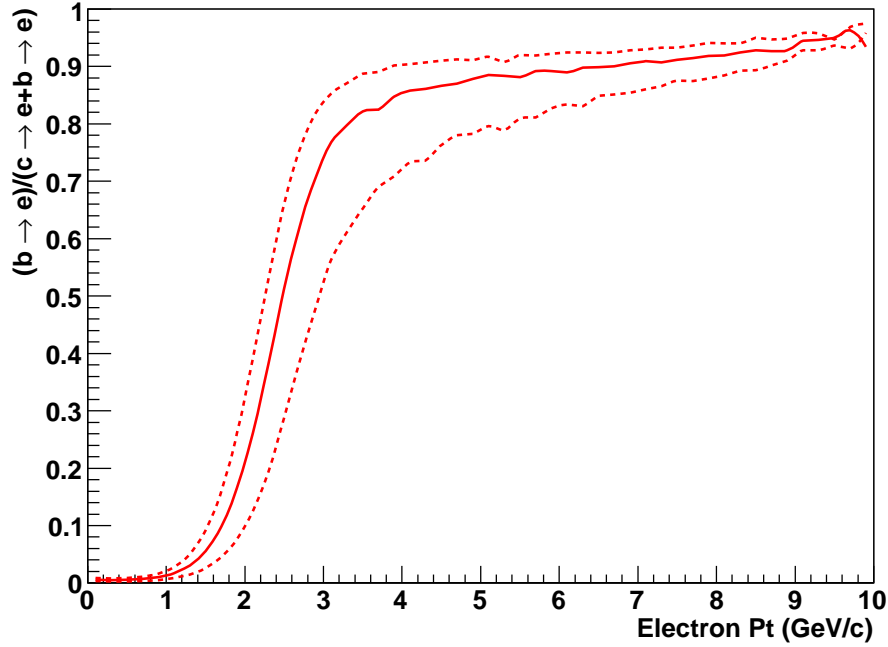
Figure 7.13: The evaluated $(b \to e)/(c \to e + b \to e)$ in Au+Au collisions. The dotted lines represent 1σ uncertainties.

7.5   The Latest Theoretical Calculations

There are latest theoretical predictions which are based on the microscopic interaction and are compatible with the experimental results. Such models provide not only the information of the medium, but also the possible scenarios of the microscopic interaction of heavy quarks.

7.5.1   Resonance Model

The main feature of this model is to assume that resonant D- and B-like states exist in QGP in the temperature of 1-2T_c [141, 142]. The existence of such resonance state is motivated by the existence of hadronic resonances in QGP suggested by the lattice QCD calculation [173, 174]. The interaction of heavy quarks with light quarks in QGP is strongly enhanced via the resonance state compared with pQCD. Treatment of heavy quark transport in the medium is similar with the calculation described in Sec. H.2. The drag and diffusion coefficients are given in the microscopic calculation by resonance model. The charm and bottom quarks are hadronized including coalescence process at the freeze-out time. Then the heavy flavored hadrons are decayed into the electrons via semi-leptonic decay. The treatment of these process are also similar with the calculation described in Sec. H.3. $R_{AA}(p_T)$ and $v_2(p_T)$ of decay electrons are calculated with this model. Figure 7.14 shows the calculated $R_{AA}(p_T)$ and $v_2(p_T)$ of decay electrons with the experimental result.

7.5.2   Potential Model

The feature of this model is to adopt the results from the lattice QCD calculation to treat the interaction of heavy quarks. Although lattice QCD is a powerful tool in the non-perturbative QCD calculation, lattice QCD can not be used for the dynamical process. Therefore, a combination of a reduced T-matrix approach and lattice QCD calculation is used to treat the dynamical scattering process of heavy quarks [143]. The reduced interaction kernel in T-matrix approach is identified as a 2-body potential which is extracted from lattice QCD calculation. There is still open issues about the extraction method of the 2-body potential from the lattice calculation [143]. The largest uncertainty in the model is this extraction method. The drag and diffusion coefficients are given by T-matrix calculation. Treatment of quark transport, hadronization and decay processes is the same as in Sec. 7.5.1. $R_{AA}(p_T)$ and $v_2(p_T)$ of decay electrons are calculated from this model. The calculated $R_{AA}(p_T)$ and $v_2(p_T)$ are shown in Fig 7.14. The $R_{AA}(p_T)$ and $v_2(p_T)$ calculated by resonance model and potential model almost agree with the data.

7.5.3   Thermalization Time

Figure 7.15 shows thermalization time τ_{HQ} of charm and bottom quark calculated using resonance model, potential model and the used model in Sec. 7.4.3 (AdS/CFT based fit) as a function of temperature. Figure 7.16 shows the spatial diffusion constant in units of the thermal wave length, $1/2\pi T$ calculated by resonance model and potential model with the used

model in Sec. 7.4.3 (AdS/CFT based fit) as a function of temperature. In Fig. 7.15 and 7.16, the results based on AdS/CFT fit are obtained in Appendix. H.6.

Contrary to both AdS/CFT based fit and the resonance model, the lattice QCD based potential model provides an increase of the thermalization time and the spatial diffusion constant of heavy quarks with increasing temperature. This indicates the potential model predicts QGP becomes weak coupling state with increasing temperature. The potential model seems to be the most realistic approach for the interaction of the heavy quark in the medium among the three models, and the temperature dependence agrees with the picture where QGP becomes a weakly coupled gas at sufficiently large temperature due to color screening effect. The AdS/CFT correspondence is valid at a strongly coupled region as already described and the assumed D- and B-like resonance will dissolve at high temperature. Therefore, the reason of the contracted temperature dependence of the AdS/CFT correspondence and the resonance model could be considered to be that the AdS/CFT correspondence and the resonance model are plausible only at the near critical temperature.

There is an interesting discussion about the nature of the medium, η/s related to the spatial diffusion constant. This consideration is described in Appendix. I.

7.5.4 Dissociation Model

In Ref. [163], a conceptually different approach is introduced to reproduce the magnitude of $R_{AA}(p_T)$ of decay electrons. Since the formation time (τ_{form}) of D and B meson (1.6 fm for D meson with 10 GeV/c and 0.4 fm for B meson with 10 GeV/c) is less than the lifetime of QGP, c and b quarks are assumed to hadronize to D and B meson in QGP in this model. The D and B meson in QGP dissociate into c and b quarks via the collisional interaction in QGP. Heavy quarks lose a large fraction of their energy via these fragmentation and dissociation process. Such mechanism becomes more important for heavy quarks with low p_T, since $\tau_{form} \propto p_T$. The largest uncertainty in the model is the treatment of the fragmentation process, which may be modified in the medium (e.g. coalescence process, modified fragmentation functions etc). Figure 7.17 shows the calculated $R_{AA}(p_T)$ of decay electrons in dissociation model with the experimental result. This model have the remarkable feature that the magnitude of the suppression of B meson becomes larger than that of D meson above $\sim$10 GeV/c.

7.6 Toward Further Understanding

The measured $(b \to e)/(c \to e + b \to e)$ suggests more precise result about $v_2(p_T)$ of single non-photonic electrons at high p_T will reveal the existence and magnitude of bottom flow as described in Sec. 7.4.3. Therefore, more statistics in Au+Au collisions is important to the understand the behavior of bottom in the medium.

Various theoretical models are proposed for the interpretation of the interaction of heavy quarks in the medium and some of these succeed to reproduce the experimental results as discussed in Sec. 7.5. More theoretical and experimental studies are necessary to build up a unified picture of interaction of heavy quarks in the medium. Especially, separate measurement of the B- and D-hadrons in Au+Au collisions, more precise measurement in d+Au collisions,

more statistics at high $v_2(p_T)$ and measurement at the medium with higher temperature are most important topics. These measurement will be done at PHENIX with the new detector, Silicon Vertex Detector and the experiments at LHC in the near future.
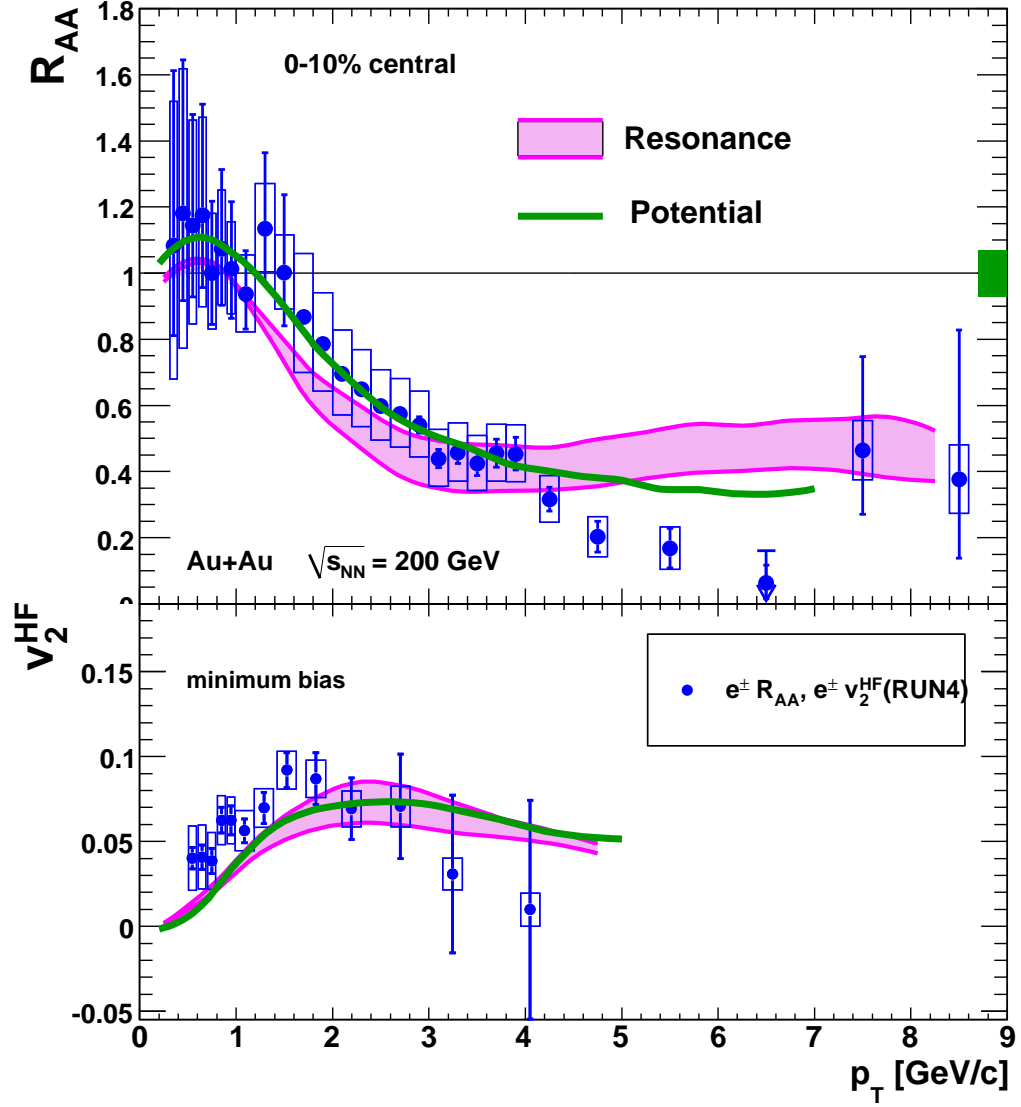
Figure 7.14: $R_{AA}(p_{\mathrm{T}})$ and $v_2(p_{\mathrm{T}})$ of the electrons from heavy flavor in resonance and potential models [141, 143] with the experimental result.
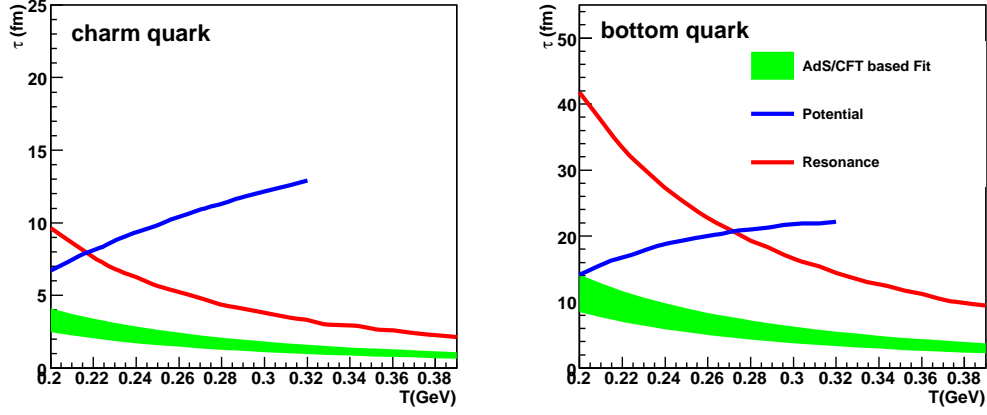
Figure 7.15: Thermalization time τ_{HQ} of charm and bottom quark calculated by resonance model and potential model with τ_{HQ} given by Eq. H.26 as a function of temperature.
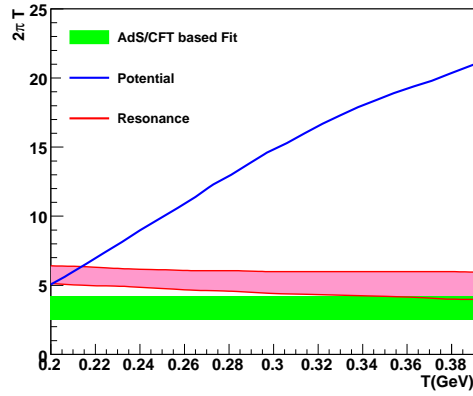
Figure 7.16: The spatial diffusion constant in units of the thermal wave length, $1/2\pi T$ calculated by resonance model and potential model with D_s given by Eq. H.25 as a function of temperature.
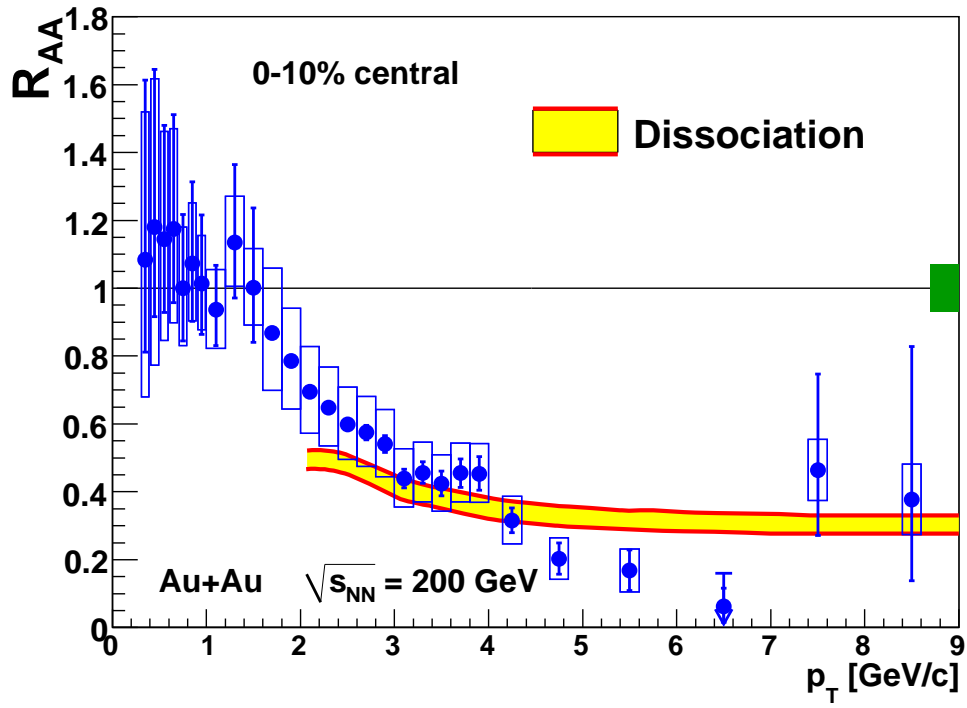
Figure 7.17: The calculated $R_{AA}(p_T)$ and $v_2(p_T)$ of decay electrons in dissociation model with the experimental result.

Chapter 8

Conclusion

Measurement of the electrons from semi-leptonic decay of heavy flavor (single non-photonic electrons) in $p + p$ collisions at $\sqrt{s}$=200 GeV has been carried out with the PHENIX detector in the RHIC Year-2005 and Year-2006 run. It provides a good test of pQCD due to the large mass and a test of theoretical treatments of fragmentation process. Measurement of heavy flavor in $p + p$ collisions also provides the important base line of the interpretation of the result of heavy flavor in Au+Au collisions at RHIC, since heavy flavor is only produced in the initial collisions.

A strong suppression at high p_T and azimuthal anisotropy of the single electrons have been observed in central Au+Au collisions. Measured single electrons include contribution from both charm and bottom. The magnitude of energy loss of bottom in the hot and dense medium is expected to be much smaller than that of charm due to the large difference of their masses. In addition, since the thermalization time of bottom should be larger than that of charm, the magnitude of flow of bottom is expected to be much smaller than that of charm. This fact indicates charm quarks lose a large fraction of their energy and flow in the matter created in Au+Au collisions. On the other hands, the existence of bottom modification (energy loss and flow) in the medium has been an open question without the determination of $(b \rightarrow e)/(c \rightarrow e + b \rightarrow e)$.

The measurement of the fraction of bottom contribution in the single non-photonic electrons provides a precise test of perturbative QCD, since the fraction allows us to compare p_T distributions of charmed and bottomed hadrons with these in pQCD separately. Especially, p_T distribution about bottomed hadrons is important due the a better convergence for bottom production. The fraction also provides the important base line to discuss at the behavior of bottom quarks in the medium created in Au+Au collisions.

The first measurement aiming to determine the fraction of charm and bottom in single non-photonic electrons via a new method, partial reconstruction of $D/\bar{D} \rightarrow e^{\pm} K^{\mp} X$ decay, has been also carried out in $p+p$ collisions in the RHIC Year-2005 and Year-2006 run. The fraction of bottom contribution in the single non-photonic electrons is determined experimentally. It is found that there is the considerable contribution from bottom in the single non-photonic electrons above 3 GeV/c. The first spectra of single non-photonic electrons from charm and bottom are measured based on the fraction of bottom at RHIC. p_T distribution predicted in pQCD agrees with the measured spectra within its uncertainty and the ratio, (data/pQCD) is ~ 2 for charm

production and ~ 1 for bottom production. The same tendency can be found at Tevatron. The total cross section of bottom is also determined to $\sigma_{b\bar{b}} = 3.16^{+1.19}_{-1.07}(\text{stat})^{+1.37}_{-1.27}(\text{sys})\mu\text{b}$. It is found that the perturbative QCD predictions of charm and bottom production are consistent with the measurement at PHENIX.

The existence of energy loss of bottom quarks in the medium created in Au+Au collisions is found based on the measured $(b \rightarrow e)/(c \rightarrow e+b \rightarrow e)$ in $p+p$ collisions. The contribution from bottom in single non-photonic electrons in Au+Au collisions should be larger than the measured value in $p+p$ collisions due to the difference of expected suppression patterns between charm and bottom. The contribution of bottom in Au+Au collisions is evaluated from the measured $(b \rightarrow e)/(c \rightarrow e+b \rightarrow e)$ and a model calculation based on Langevin equation. As a result, most of single non-photonic electrons in Au+Au collisions may be originated from bottom at $p_{\mathrm{T}} > 3$ GeV/c. This result directly leads to that the existence and magnitude of bottom flow can be studied by measurement of $v_2(p_{\mathrm{T}})$ at $p_{\mathrm{T}} > 3$ GeV/c. The existence and magnitude of bottom flow will be revealed from the coming result in the near future. The measured $(b \rightarrow e)/(c \rightarrow e+b \rightarrow e)$ in $p+p$ collisions provides an important base line for such discussion.

The mechanism of the such strong interaction of heavy quarks in the medium is still under debate. The initial nuclear effect, the temperature dependence of the magnitude of the interaction and separate measurement of $R_{AA}(p_{\mathrm{T}})$ and $v_2(p_{\mathrm{T}})$ for D and B mesons are necessary to understand the mechanism. Therefore, separate measurement of the B and D hadrons in Au+Au collisions, more precise measurement at d+Au collisions, more statistics at high $v_2(p_{\mathrm{T}})$ and measurement at the medium with higher temperature are most important subjects. These measurement will be done at PHENIX with the new detector, Silicon Vertex Detector and the experiments at LHC in the near future.

Acknowledgment

First of all, I would like to thank my supervisor, Prof. H. Hamagaki, for his essential advice and comments about the experiment and physics. His abundant knowledge and precise suggestion always guided me. He has helped me not only with his advice but also with support to concentrate on the research. Without his help, I could not accomplish this work. I would like to express my sincere thanks to Prof. K. Ozawa for his kind supports for the analysis and a great deal of encouragements. I could learn many techniques of the experiments and analysis from him and could enjoy the research and my life in BNL with his support. I would like to express my deep thanks to Prof. Y. Akiba for his many incisive comments and suggestions. He introduced me to single electron analysis and this work benefited especially from his idea and suggestions. I wish to thank Dr. T. Gunji for his encouragement for the completion of this work. His abundant knowledge of the RICH detector and electron analysis helped me.

I would like to express my thanks to Prof. T. Sakaguchi for his great help with the operation of the RICH detector and thoughtful advice on the data analysis. I am obliged to Dr. S. Kametani for the help with my early work and computing environment. I with to thank Dr. F. Kajihara for his abundant experience of the single electron analysis. This work is largely motivated with the his work on the single electron. I with to thank Dr. T. Isobe for his abundant knowledge of the EMCal detector. I with to thank Dr. S. Oda for his kind help and abundant experience of electron analysis.

I wish to acknowledge for all the collaborators of the PHENIX experiment. I am much obliged to the previous and present spokespersons, Prof. W. A. Zajc and Prof. B. V. Jacak for their heartful administration of the collaboration. I am grateful to the Year-2005 and Year-2006 RUN coordinators, Prof. J. Lajoie and Prof. A. Deshpande for their great leadership. I would like to thank Dr. J. Haggerty for his great work with the experiment. I would like to express my thanks to the conveners of the Heavy/Light Working Group, Prof. M. J. Leitch, Dr. R. G. de Cassagnac, Prof. T. K. Hemmick, Dr. A. Lebedev, Dr. A. Toia and Dr. X. Wei for many constructive comments and suggestions on the analysis. I would like to appreciate the other members of Paper Preparation Group 094 and single electron analysis group, Dr. S. Butsyk, Dr. R. Averbeck, Dr. A. Dion, Dr. S. Sakai and Dr. D. Hornback for their help and valuable physics discussion on this analysis. I am obliged to Dr. C. Pinkenburg, Dr. D. P. Morrison and Dr. J. T. Mitchel for their marvelous assistance on the analysis environment at BNL.

I wish to express my appreciation to the past and present member of our group, Dr. M. Inuzuka, Dr. K. Kino, Dr. T. Horaguchi, Mr. N. Kurihara, Mr. S. Saito, Mr. Y. Yamaguchi, Mr. Y. Aramaki, Mr. S. Sano, Mr. A. Takahara, Mr. R. Akimoto and Mr. Y. Hori for their help, interesting discussions and the friendship. I could really enjoy my daily life at Japan

Appendix A

Data Tables

Table A.1: Invariant cross section of single non-photonic electrons from heavy flavor decays at y=0.

p_{T} (GeV/c)	cross section (mb GeV$^{-2}c^3$)	stat error	sys error
0.55	0.00433	0.000404	0.00111
0.65	0.00218	0.000237	0.000542
0.75	0.00132	0.000148	0.000275
0.85	0.000911	9.87e-005	0.000149
0.95	0.000572	6.87e-005	8.47e-005
1.1	0.00033	3e-005	3.82e-005
1.3	0.000141	1.71e-005	1.53e-005
1.5	6.51e-005	1.04e-005	6.7e-006
1.7	3.29e-005	2.92e-007	4.41e-006
1.9	1.87e-005	1.55e-007	2.06e-006
2.1	1.03e-005	9.17e-008	1.01e-006
2.3	6.36e-006	6.32e-008	5.66e-007
2.5	3.94e-006	4.56e-008	3.31e-007
2.7	2.43e-006	3.36e-008	2e-007
2.9	1.52e-006	2.52e-008	1.23e-007
3.1	1.05e-006	1.93e-008	7.97e-008
3.3	6.65e-007	1.48e-008	5.12e-008
3.5	4.8e-007	1.16e-008	3.5e-008
3.7	3.08e-007	9.05e-009	2.32e-008
3.9	2.07e-007	7.22e-009	1.6e-008
4.1	1.54e-007	5.87e-009	1.15e-008
4.3	1.1e-007	4.82e-009	8.28e-009
4.5	7.35e-008	3.84e-009	5.91e-009
4.7	5.66e-008	3.28e-009	4.42e-009
4.9	5.03e-008	2.85e-009	3.58e-009
5.5	1.69e-008	1.02e-009	1.69e-009
6.5	5.45e-009	5.09e-010	4.64e-010
7.5	1.95e-009	2.91e-010	1.54e-010
8.5	1.3e-009	2.24e-010	8.82e-011

Table A.2: The Data/FONLL ratios of single non-photonic electron yield at y=0.

p_T (GeV/c)	cross section	stat error	sys error
0.55	2.21	0.206	0.567
0.65	1.75	0.19	0.435
0.75	1.68	0.189	0.35
0.85	1.84	0.199	0.3
0.95	1.81	0.217	0.268
1.1	2.04	0.185	0.236
1.3	1.92	0.233	0.208
1.5	1.83	0.293	0.189
1.7	1.79	0.0159	0.24
1.9	1.86	0.0155	0.205
2.1	1.78	0.0159	0.175
2.3	1.84	0.0183	0.164
2.5	1.84	0.0213	0.155
2.7	1.78	0.0246	0.146
2.9	1.71	0.0283	0.138
3.1	1.76	0.0324	0.134
3.3	1.65	0.0367	0.127
3.5	1.72	0.0416	0.126
3.7	1.58	0.0463	0.119
3.9	1.49	0.0521	0.115
4.1	1.54	0.0589	0.115
4.3	1.52	0.0666	0.114
4.5	1.38	0.0722	0.111
4.7	1.44	0.0831	0.112
4.9	1.71	0.0967	0.121
5.5	1.3	0.0788	0.13
6.5	1.45	0.135	0.123
7.5	1.56	0.233	0.124
8.5	2.83	0.488	0.192

Table A.3: Result of $(b \to e)/(c \to e + b \to e)$ in RUN5 and RUN6

electron p_T	$(b \to e)/(c \to e + b \to e)$
2.35 GeV/c	< 0.41 (90% C.L) 0.19 (50% point)
3.37 GeV/c	$0.26^{+0.14}_{0.13}(stat)^{+0.11}_{0.11}(sys)$
4.40 GeV/c	$0.63^{+0.18}_{-0.21}(stat) \pm 0.08(sys)$
5.66 GeV/c	> 0.33 (90% C.L) 0.71 (50% point)

Table A.4: Invariant cross section of electrons from charm and bottom

electron p_{T}	cross section (mb GeV$^{-2}c^3$)	data/FONLL
charm		
2.35 GeV/c	> 3.30 (90% C.L) 4.52 (50%) $\times 10^{-6}$	> 1.49 (90% C.L) 2.03 (50%)
3.37 GeV/c	$4.17^{+0.73+0.41}_{-0.83-0.46} \times 10^{-7}$	$2.05^{+0.36+0.20}_{-0.41-0.22}$
4.40 GeV/c	$3.49^{+1.95}_{-1.70} \pm 0.66 \times 10^{-8}$	$1.16^{+0.65}_{-0.56} \pm 0.22$
5.66 GeV/c	< 1.11 (90% C.L) 0.48 (50%) $\times 10^{-8}$	< 2.48 (90% C.L) 1.08 (50%)
bottom		
2.35 GeV/c	< 2.30 (90% C.L) 1.08 (50%) $\times 10^{-6}$	< 2.74 (90% C.L) 1.29 (50%)
3.37 GeV/c	$1.49^{+0.83+0.73}_{-0.73-0.66} \times 10^{-7}$	$0.99^{+0.55+0.48}_{-0.48-0.43}$
4.40 GeV/c	$5.95^{+1.70}_{-1.95} \pm 1.10 \times 10^{-8}$	$1.87^{+0.54}_{-0.61} \pm 0.34$
5.66 GeV/c	> 0.54 (90% C.L) 1.17 (50%) $\times 10^{-8}$	> 0.90 (90% C.L) 1.93 (50%)

Appendix B

Comparison Between Real Data and Simulation in RUN6

B.1 eID varibles

The distributions of the variables used for the electron identification from the PISA simulation are compared to these of the real data in RUN6. The used cuts for each variable comparison are described in Sec. 5.3.5.

Figure B.1, B.2 and B.3 show the distributions of RICH variables, n0, disp and chi2/npe0 at each RICH sector, respectively. In addition, Figure B.4, B.5 and B.6 show the distributions of EMCal variables at each sector, emcsdphi_e, emcsdz_e and prob, respectively. Figure B.7 and B.8 show mean and sigma values of ecore/mom distributions as a function of electron p_{T}. In Fig. B.1-B.8, black squares show the results from the real data in RUN6 and red circles show these from the PISA simulation with RUN6 tuning parameters and CM++ field. The distribution in simulation is normalized by the number of entries at each sector. The distributions of the simulation and these of the real data match well.
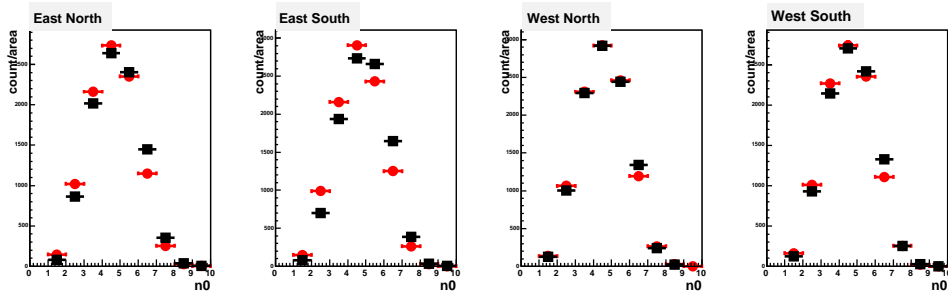
Figure B.1: The distribution of n0 with the standard eID cut without n0 cut and the $0.5 < p_{\mathrm{T}} < 5$ GeV/c cut in the real data (square) and simulation (circle).
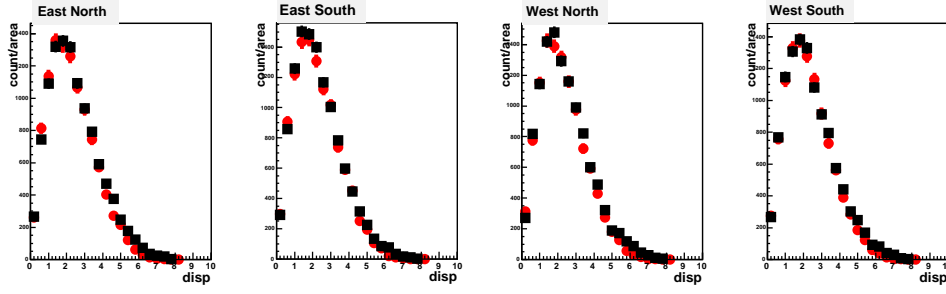
Figure B.2: The distribution of disp with the standard eID cut without disp cut and the 0.5< p_T <5 GeV/c cut in the real data (square) and simulation (circle).
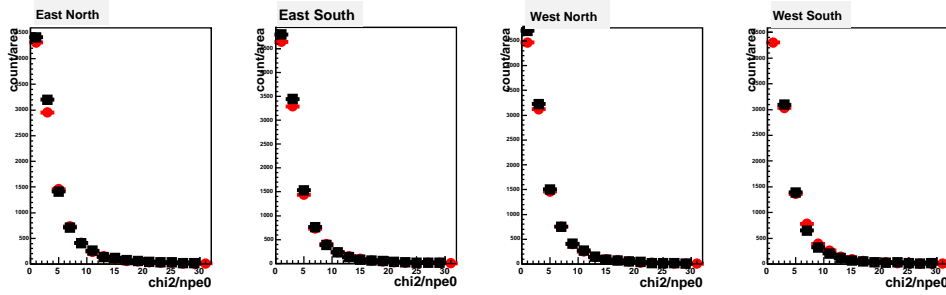
Figure B.3: The distribution of chi2/npe0 with the standard eID cut without chi2/npe0 cut and the 0.5< p_T <5 GeV/c cut in the real data (square) and simulation (circle).

B.2 Geometrical Acceptance

The distributions of phi, zed of the simulation are compared with these of the real data for the electron samples selected by the standard eID and a transverse momentum with 0.5< p_T <5 GeV/c. Figure B.9 shows the distributions of phi at North (top panel) and South (bottom panel)sector, and Figure B.10 shows the distributions of zed at East (top panel) and West (bottom panel) sector. In Fig. B.9 and B.10, black squares show the real data in RUN6 and red circles show the PISA simulation with RUN6 tuning parameters and CM++ field. The distributions of simulation are normalized by number of entries in the reference regions, where are little low efficiency, dead or noisy area. In Fig B.9 and B.10, the used reference region to normalize is region 1.
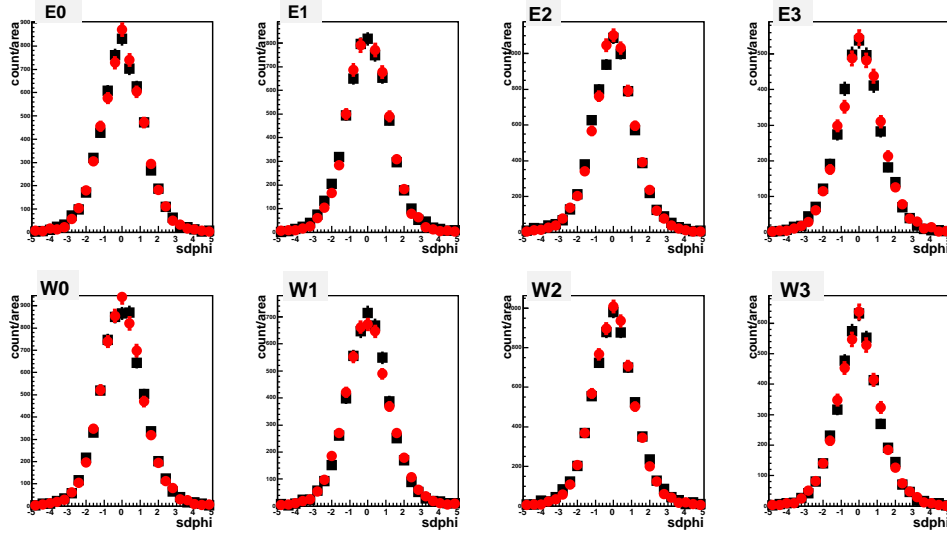
Figure B.4: The distribution of emcsdphi_e with the standard eID cut without emcsd-phi(z)_e cut and the 0.5< p_T <5 GeV/c cut in the real data (square) and simulation (circle).
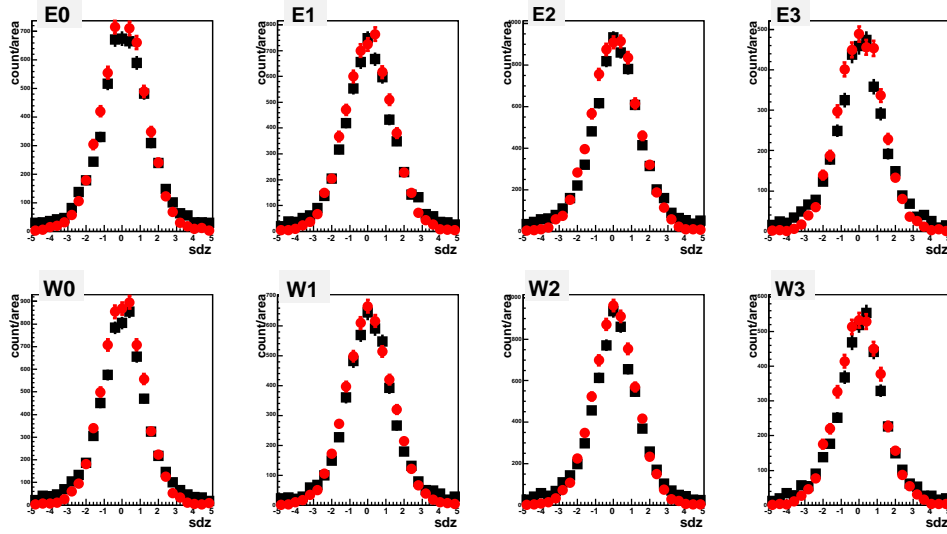
Figure B.5: The distribution of emcsdz_e with the standard eID cut without emcsd-phi(z)_e cut and the 0.5< p_T <5 GeV/c cut in the real data (square) and simulation (circle).
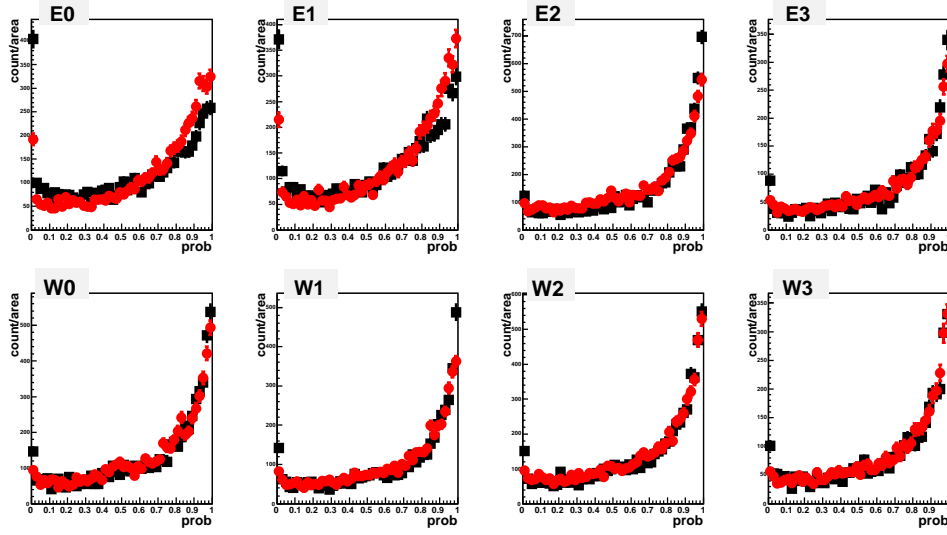
Figure B.6: The distribution of prob with the standard eID cut without prob cut and the $0.5 < p_T < 5$ GeV/c cut in the real data (square) and simulation (circle).
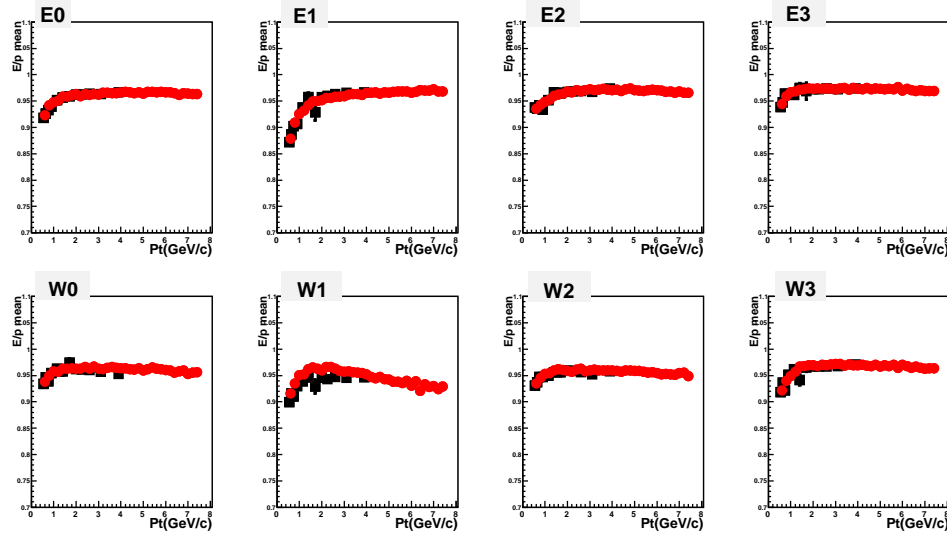
Figure B.7: The mean value of ecore/mom distribution with the standard eID cut as a fiction of electron p_T in the real data (square) and simulation (circle).
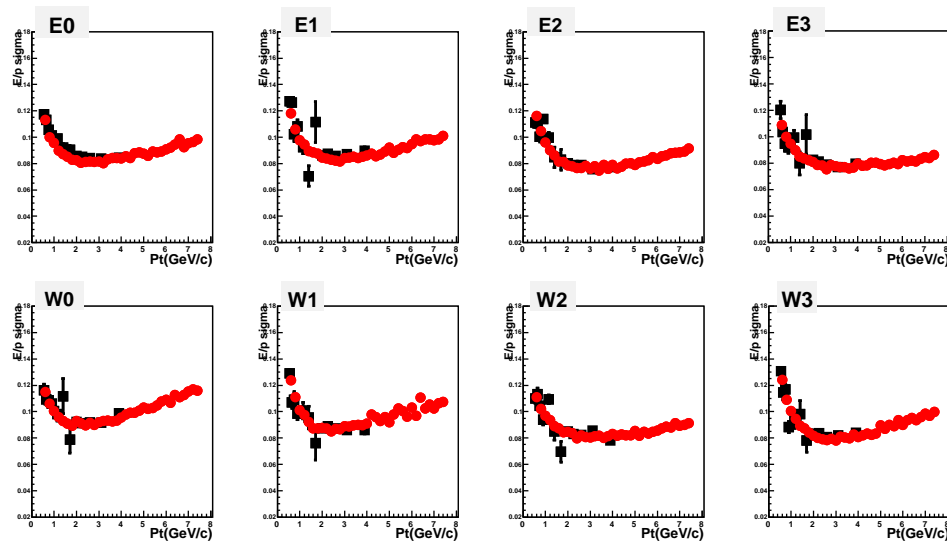
Figure B.8: The sigma value of ecore/mom distribution with the standard eID cut as a fiction of electron p_T in the real data (square) and simulation (circle).
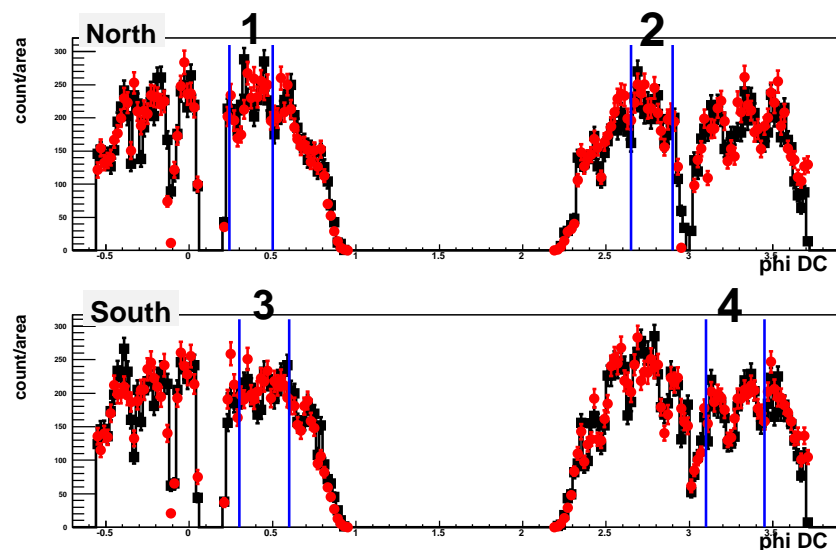
Figure B.9: The distribution of phi with the standard eID cut and the 0.5< p_T <5 GeV/c cut in the real data in RUN6 (square) and simulation (circle).
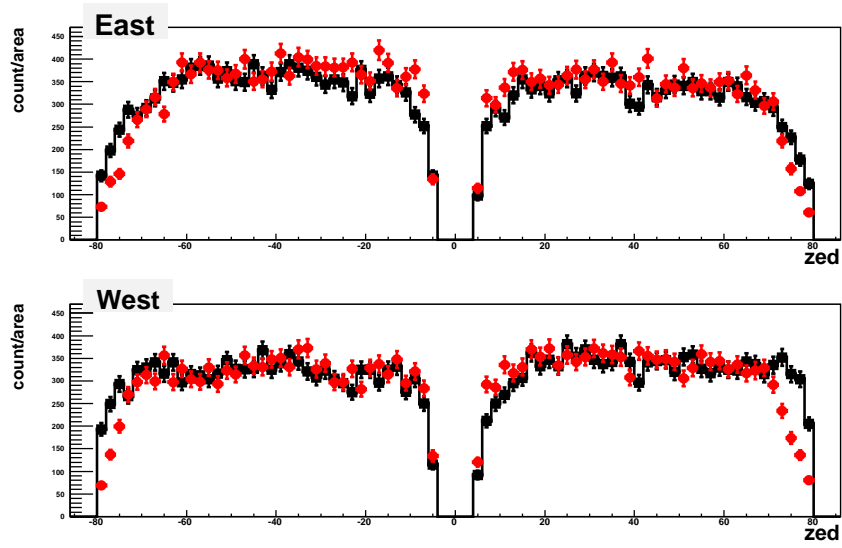
Figure B.10: The distribution of zed with the standard eID cut and the $0.5< p_{\mathrm{T}} <5$ GeV/c cut in the real data in RUN6 (square) and simulation (circle).

Appendix C

Correlation Function of Electron and Hadron

C.1 Correlation Function in Real Data

Acceptance filter is NOT applied when we study the correlation function

Two particle correlations with respect to the azimuthal angular difference, which is called 'correlation function' is studied in this chapter. The one of two particle is called 'trigger particle' and the other is called 'associated particle'. Correlation function is defined as the measured yield of the assocated particles as a function of the azimuthal angular difference. Correlation function of trigger electrons and associated hadrons is studied to compare with PYTHIA simulation. Since charge asymmetry of electing hadron pairs have little PYTHIA parameter dependence, the comparison with real data between PYTHIA should be done for other observables to study the tuning status of PYTHIA. For this purpose, we choose the correlation function between the trigger non-photonic electrons and the associated hadrons.

The condition of analysis cut for trigger electrons is described at Sec 5.3.4. p_T range of the selected trigger electrons is $2.0 < p_T < 5.0$ GeV/c and that of the selected associated hadrons is $0.4 < p_T < 5.0$ GeV/c.

Figure C.1 shows the raw number of the associated hadrons as a funtion of the azimuthal angle with respect to the trigger electron, $\Delta N/\Delta\phi$, per the number of the trigger electrons, where the trigger electrons are inclusive electrons. Black points shows the $\Delta N/\Delta\phi$ in ERT triggered events in RUN5. Red points show the $\Delta N/\Delta\phi$ in mixing events. $\Delta N/\Delta\phi$ in mixing events is considered as the background to take into account the effect of geometrical acceptance. $\Delta N/\Delta\phi$ in mixing events is normalized by the number of the trigger electrons.

Figure C.2 shows the $\Delta N/\Delta\phi$ distribution per the number of the trigger electrons, where the trigger electrons are the photonic electrons. Black points show the $\Delta N/\Delta\phi$ in ERT triggered events in RUN5 and red points show the background used by the mixing event mothod. The photonic electrons are identified by the invariant mass distribution of di-electron. When the associated electron is found in the associated particles, we calculate the invariant mass of the trigger electrons and the associated electrons. The trigger electrons is identified as the photonic

201
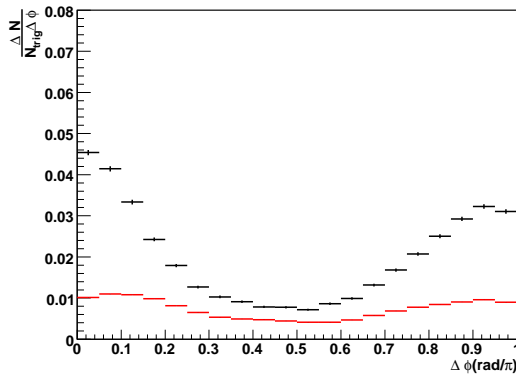
Figure C.1: The $\Delta N/\Delta \phi$ distribution per the number of the trigger electrons, when the trigger electrons were the inclusive electrons.Black points shows the $\Delta N/\Delta \phi$ in real events and red points show the background.
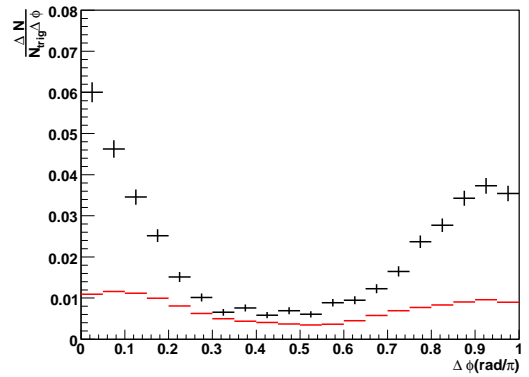
Figure C.2: The $\Delta N/\Delta \phi$ distribution per the number of the trigger electrons, when the trigger electrons were the photonic electrons.Black points shows the $\Delta N/\Delta \phi$ in real events and red points show the background

electron trigger, when the invariant mass is bellow $0.08\,\mathrm{GeV}/c^2$. When we make the background for the photonic electron trigger by mixing events, the photonic trigger electrons are selected by the above method to take account for the acceptance bias by the selection of the photonic electrons.

The correlation functions of the inclusive and the photonic electron-hadrons are obtained by the subtraction of the background $\Delta N/\Delta \phi$ distribution. The correlation function of electrons from heavy flavor - hadrons is obtained as follows.

$$C_{HQ}(\Delta \phi) = (C_{incl}(\Delta \phi) - (1 - R_{HQ}) \times C_{phot}(\Delta \phi))/R_{HQ}.$$

Here,

- $C_{HQ}(\Delta \phi)$ is the correlation function, where the trigger electrons are from heavy flavor.

- $C_{incl}(\Delta \phi)$ is the correlation function, where the trigger electrons are inclusive electrons

- $C_{phot}(\Delta \phi)$ is the correlation function, where the trigger electrons are photonic electrons

- R_{HQ} is the fraction of electrons from heavy flavor in the inclusive electrons.

Figure C.3 shows the correlation functions of electron-hadrons, where the trigger electrons are inclusive (black), photonic (red) and heavy flavor (blue).

C.2   PYTHIA tuning status

The PYTHIA tuning status is studied by the comparison of the correlation function of heavy flavor electrons and hadrons between in RUN5 data and PYTHIA simulation. The correlation function is obtained in PYTHIA simulation by the similar way in the analysis at real data.
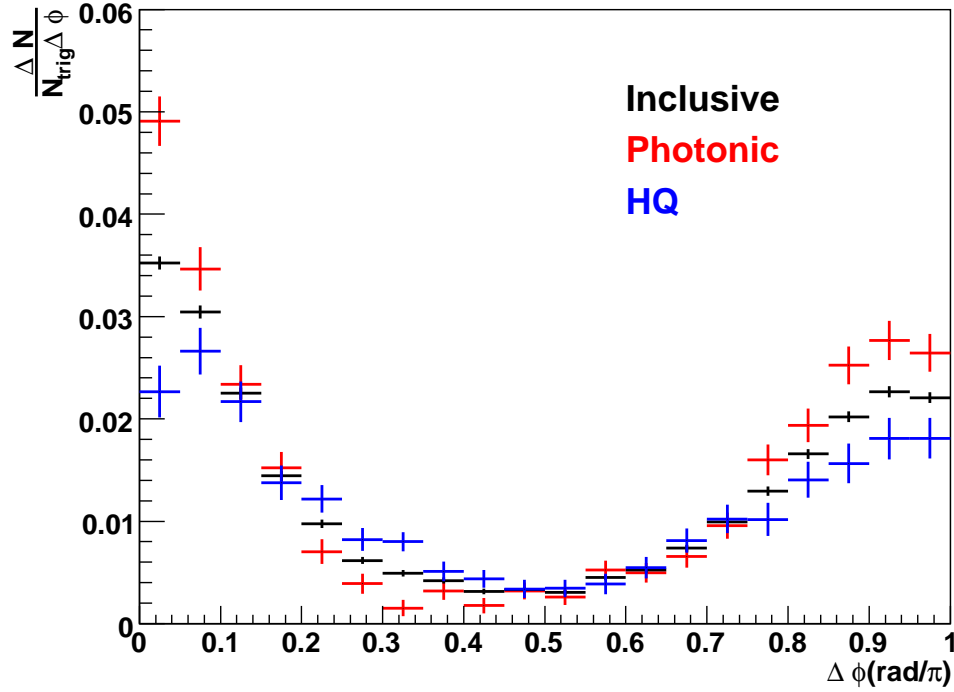
Figure C.3: The correlation function of electron-hadrons when the trigger electrons are inclusive (black), photonic (red) and heavy flavor (blue).

Figure C.4 shows the correlation function of electrons and hadrons in the PYTHIA simulation, where the trigger electrons are from charm and bottom. Red line shows the correlation function in the case of charm production and blue line shows that in the case of bottom production. For the comparison with real data and PYTHIA, the obtained PYTHIA results are mixed up as follows.

$$C_{HQ}(\Delta\phi) = R_b(C_b(\Delta\phi) + (1 - R_b)C_c(\Delta\phi)).$$

Here,

- $C_{HQ}(\Delta\phi)$ is the correlation function, where the trigger electrons are from heavy flavor.

- $C_{c\ (b)}(\Delta\phi)$ is the correlation function, where the trigger electrons are from charm (bottom)

- R_b is $\frac{N_{b\to e}}{N_{c\to e} + N_{b\to e}}$.

We set R_b to 0.2 from this analysis for the comparison with real data. Figure C.5 shows the correlation function of electrons and hadrons, where the trigger electrons are from heavy flavor. Black points show the result in RUN5 data and green line shows the result in PYTHIA. The PYTHIA simulation agrees with the real data. This indicated the tuning for PYTHIA simulation is well.
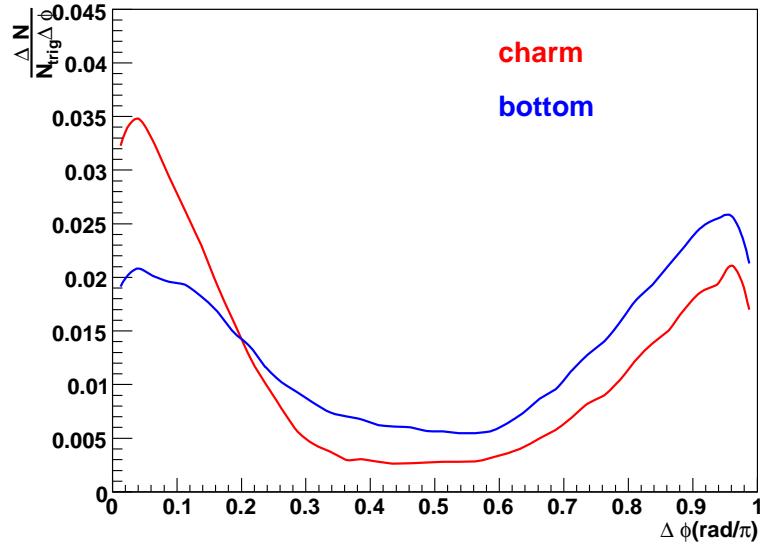
Figure C.4: The correlation function of electrons and hadrons at the tuned PYTHIA, when the trigger electrons were from charm and bottom. Red line shows the correlation function in the case of charm production and blue line shows that in the case of bottom production.
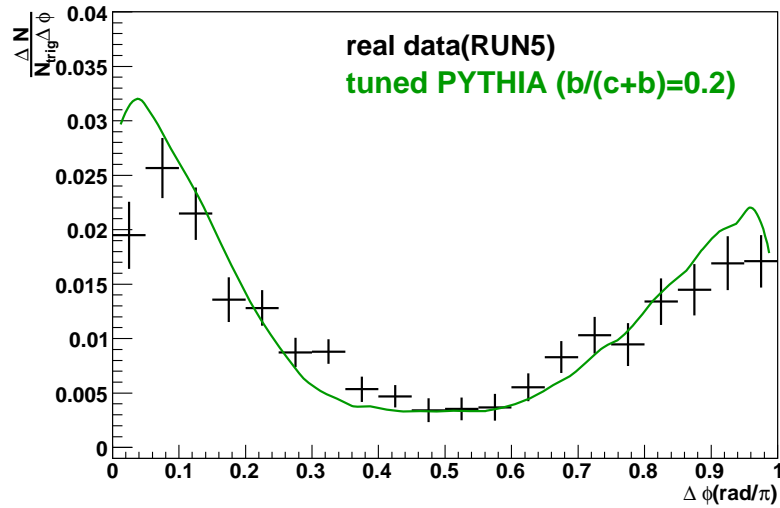
Figure C.5: The correlation function of electrons and hadrons, where the trigger electrons are from heavy flavor. Black points show the result at RUN5 data obtained and green line shows the result at PYTHIA when we set R_b to 0.2.

Appendix D

Centrality Information

Collision centrality, which is an observable corresponded to impact parameter b, is determined by information by BBC and ZDC in PHENIX. Au+Au collisions at $\sqrt{s_{NN}} = 200$ GeV are categorized into 9 centrality groups, 0%-10%, 10%-20%, 20%-30%, 30%-40%, 50%-60%, 60%-70%, 70%-80% and 80%-92.3%. 0%-10% collisions are most central collisions and 80%-92.3% collisions are most pheripheral collisions. Impact parameter (b), the number of binary collisions (N_{coll}) and the number of participants (N_{part}), which corresponds to each centrality group, are determined according to the Glauber Model [132]. The results are summarized in Table D.1.

Table D.1: Results of Glauber Calculations for Au+Au collisions at $\sqrt{s_{NN}} = 200$ GeV.

Centrality (%)	b (fm)	N_{part}	N_{coll}
0-10	3.1	325	955
10-20	5.7	234	603
20-30	7.4	167	374
30-40	8.7	114	220
40-50	9.9	74	120
50-60	11.0	46	61
60-70	11.9	26	29
70-80	12.8	13	12
80-92.3	14.1	6	5

Appendix E

Details of ϵ_c and ϵ_b

Table E.1: Detail of charm and bottom decay for electron p_T 3-4 GeV/c

channel	N_{tag} (part)/(all)	N_{ele} (part)/(all)	ϵ
D^0			
$D^0 \to e^+ K^- \nu_e$	46.71%	29.46%	$8.06 \pm 0.18\%$
$D^0 \to e^+ K^{*-} \nu_e$	11.84%	3.11%	$19.31 \pm 0.73\%$
$D^0 \to e^+ \pi^- \nu_e$	4.65%	5.77%	$4.10 \pm 0.36\%$
$D^0 \to e^+ \rho^- \nu_e$	1.29%	0.45%	$14.63 \pm 1.70\%$
$D^0 \to e^+ other$	0.91%	0.44%	$10.39 \pm 1.74\%$
D^+			
$D^+ \to e^+ \bar{K}^0 \nu_e$	21.57%	39.47%	$2.78 \pm 0.13\%$
$D^+ \to e^+ \bar{K}^{*0} \nu_e$	6.08%	4.05%	$7.64 \pm 0.64\%$
$D^+ \to e^+ \pi^0 \nu_e$	1.84%	3.79%	$2.47 \pm 0.35\%$
$D^+ \to e^+ \rho^0 \nu_e$	0.14%	0.32%	$2.20 \pm 2.31\%$
$D^+ \to e^+ other$	1.60%	1.92%	$4.23 \pm 0.72\%$
D_s			
$D_s \to e^+ \phi \nu_e$	0.44%	0.73%	$3.04 \pm 1.56\%$
$D_s \to e^+ \eta \nu_e$	3.91%	7.80%	$2.55 \pm 0.26\%$
$D_s \to e^+ \eta' \nu_e$	0.58%	0.57%	$5.18 \pm 1.49\%$
$D_s \to e^+ other$	0.16%	0.82%	$0.98 \pm 0.90\%$
Λ_c			
$\Lambda_c \to e^+ \Lambda \nu_e$	-0.57%	0.26%	$-11.24 \pm 5.15\%$
$\Lambda_c \to e^+ other$	-1.15%	1.04%	$-5.63 \pm 2.34\%$
B^0			
$B^0 \to e^+ D^- \nu_e$	4.56%	5.93%	$1.41 \pm 0.22\%$
$B^0 \to e^+ D^{*-} \nu_e$	0.76%	23.28%	$0.06 \pm 0.12\%$
$B^0 \to e^+ other$	5.48%	5.29%	$1.90 \pm 0.26\%$
B^+			
$B^+ \to e^+ D^0 \nu_e$	8.31%	6.55%	$2.33 \pm 0.22\%$
$B^+ \to e^+ D^{*0} \nu_e$	29.43%	25.17%	$2.14 \pm 0.12\%$
$B^+ \to e^+ other$	3.64%	5.86%	$1.14 \pm 0.26\%$
B_s			
$B_s \to e^+ \text{total}$	16.69 %	11.62%	$2.63 \pm 0.16\%$
$Bhad \to e^+ others$	11.41%	10.82%	$1.93 \pm 0.17\%$
$B \to c \to e$	19.71%	5.48%	$6.60 \pm 0.34\%$

Table E.2: Detail of charm and bottom decay for electron p_{T} 4-5 GeV/c

channel	N_{tag} (part)/(all)	N_{ele} (part)/(all)	ϵ
D^0			
$D^0 \to e^+ K^- \nu_e$	46.18%	29.62%	$10.79 \pm 0.18\%$
$D^0 \to e^+ K^{*-} \nu_e$	10.54%	3.42%	$21.30 \pm 0.69\%$
$D^0 \to e^+ \pi^- \nu_e$	3.97%	5.52%	$4.97 \pm 0.38\%$
$D^0 \to e^+ \rho^- \nu_e$	1.02%	0.49%	$14.53 \pm 1.62\%$
$D^0 \to e^+ other$	1.14%	0.47%	$16.78 \pm 1.76\%$
D^+			
$D^+ \to e^+ \bar{K}^0 \nu_e$	23.71%	39.07%	$4.20 \pm 0.13\%$
$D^+ \to e^+ \bar{K}^{*0} \nu_e$	5.62%	4.40%	$8.83 \pm 0.60\%$
$D^+ \to e^+ \pi^0 \nu_e$	2.03%	3.58%	$3.93 \pm 0.34\%$
$D^+ \to e^+ \rho^0 \nu_e$	0.21%	0.34%	$4.33 \pm 2.23\%$
$D^+ \to e^+ other$	1.33%	1.95%	$4.73 \pm 0.71\%$
D_s			
$D_s \to e^+ \phi \nu_e$	0.37%	0.80%	$3.20 \pm 1.49\%$
$D_s \to e^+ \eta \nu_e$	3.71%	7.70%	$3.33 \pm 0.27\%$
$D_s \to e^+ \eta' \nu_e$	0.32%	0.62%	$3.63 \pm 1.49\%$
$D_s \to e^+ other$	0.37%	0.81%	$3.16 \pm 0.90\%$
Λ_c			
$\Lambda_c \to e^+ \Lambda \nu_e$	-0.36%	0.32%	$-7.89 \pm 4.81\%$
$\Lambda_c \to e^+ other$	-0.16%	0.88%	$-1.30 \pm 2.55\%$
B^0			
$B^0 \to e^+ D^- \nu_e$	5.79%	5.84%	$2.08 \pm 0.28\%$
$B^0 \to e^+ D^{*-} \nu_e$	-0.48%	23.89%	$-0.04 \pm 0.15\%$
$B^0 \to e^+ other$	5.34%	5.09%	$2.20 \pm 0.34\%$
B^+			
$B^+ \to e^+ D^0 \nu_e$	7.40%	6.40%	$2.43 \pm 0.28\%$
$B^+ \to e^+ D^{*0} \nu_e$	31.15%	25.89%	$2.53 \pm 0.14\%$
$B^+ \to e^+ other$	1.61%	5.65%	$0.60 \pm 0.33\%$
B_s			
$B_s \to e^+ total$	19.83 %	11.97%	$3.48 \pm 0.20\%$
$Bhad \to e^+ others$	14.67%	10.79%	$2.86 \pm 0.21\%$
$B \to c \to e$	14.69%	4.47%	$6.91 \pm 0.46\%$

Table E.3: Detail of charm and bottom decay for electron p_T 5-7 GeV/c

channel	N_{tag} (part)/(all)	N_{ele} (part)/(all)	ϵ
D^0			
$D^0 \to e^+ K^- \nu_e$	50.38%	29.51%	$13.60 \pm 0.22\%$
$D^0 \to e^+ K^{*-} \nu_e$	9.46%	3.20%	$23.53 \pm 0.84\%$
$D^0 \to e^+ \pi^- \nu_e$	2.72%	5.77%	$3.75 \pm 0.44\%$
$D^0 \to e^+ \rho^- \nu_e$	1.27%	0.48%	$21.16 \pm 1.89\%$
$D^0 \to e^+ other$	1.03%	0.43%	$19.32 \pm 2.15\%$
D^+			
$D^+ \to e^+ \bar{K}^0 \nu_e$	22.03%	39.60%	$4.43 \pm 0.15\%$
$D^+ \to e^+ \bar{K}^{*0} \nu_e$	4.38%	4.10%	$8.51 \pm 0.73\%$
$D^+ \to e^+ \pi^0 \nu_e$	2.11%	3.77%	$4.46 \pm 0.37\%$
$D^+ \to e^+ \rho^0 \nu_e$	0.20%	0.33%	$4.87 \pm 2.67\%$
$D^+ \to e^+ other$	1.33%	1.91%	$5.53 \pm 0.85\%$
D_s			
$D_s \to e^+ \phi \nu_e$	0.41%	0.74%	$4.42 \pm 1.81\%$
$D_s \to e^+ \eta \nu_e$	3.46%	7.66%	$3.59 \pm 0.32\%$
$D_s \to e^+ \eta' \nu_e$	0.46%	0.57%	$6.32 \pm 1.90\%$
$D_s \to e^+ other$	0.58%	0.80%	$5.79 \pm 1.07\%$
Λ_c			
$\Lambda_c \to e^+ \Lambda \nu_e$	-0.32%	0.28%	$-9.09 \pm 6.70\%$
$\Lambda_c \to e^+ other$	0.51%	0.85%	$4.79 \pm 3.30\%$
$\Lambda_c \to e^+ total$	0.19 %	1.13%	$1.37 \pm 2.98\%$
B^0			
$B^0 \to e^+ D^- \nu_e$	5.55%	5.81%	$2.59 \pm 0.25\%$
$B^0 \to e^+ D^{*-} \nu_e$	2.80%	24.29%	$0.31 \pm 0.13\%$
$B^0 \to e^+ other$	7.30%	5.08%	$3.89 \pm 0.30\%$
B^+			
$B^+ \to e^+ D^0 \nu_e$	8.80%	6.34%	$3.75 \pm 0.24\%$
$B^+ \to e^+ D^{*0} \nu_e$	27.02%	26.10%	$2.80 \pm 0.13\%$
$B^+ \to e^+ other$	1.47%	5.55%	$0.71 \pm 0.29\%$
B_s			
$B_s \to e^+ total$	21.74 %	12.21%	$4.82 \pm 0.17\%$
$Bhad \to e^+ others$	14.94%	10.57%	$3.83 \pm 0.20\%$
$B \to c \to e$	10.38%	4.04%	$6.95 \pm 0.42\%$

Appendix F

Fit Method Including Systemateic Uncertainies

This chapeter describes appiled fit method to take into account the correlation of systematic uncertainties.

The uncertainties of the measured points are categorized into type A (p_T-uncorrelated, statistical + systematic, σ_i), type B (p_T-correlated, σ_{bi}) and type C (normalization, T_{AB} in this calculation σ_c) as discussed in Sec. 5.6.4, where the σ's represent the standard deviations of the assumed Gaussian distributed uncertainties. In order to consider the such correlated uncertainties, the fit is done by minimizing a following variable [122].

$$\chi^2 \equiv \left[\sum_{i=1}^{n} \frac{(y_i + \sum_j \epsilon_{bj}\sigma_{bj} + \epsilon_c\sigma_c - \mu_i(\mathbf{q}))^2}{\tilde{\sigma_i}^2} \right] + \sum_j \epsilon_{bj}^2 + \epsilon_c^2, \tag{F.1}$$

where $y_1, y_2, ..., y_n$ are the experimental results and $\mu_1(\mathbf{q}), \mu_2(\mathbf{q}), ..., \mu_n(\mathbf{q})$ are the theoretical predictions with parameter sets, $\mathbf{q}$. σ_{bj} represent jth standard deviation in type B systematic uncertainties. ϵ_{bj} and ϵ_c are the fractions of the type B and C systematic uncertainties that all points are moved together, that is, ϵ_{bj} and ϵ_c are normalized uncertainty to have Gaussian form with $\sigma = 1$. $\tilde{\sigma}_i$ is a quadrature sum of statistical error and type A systematic error basically. When the statistical error and p_T-correlated errors have some relation, $\tilde{\sigma}_i$ is modified to take into account the such relation. The minimum χ^2 ($\chi_{min}^2(\mathbf{q})$) is searched for each $\mathbf{q}$ in Eq. H.3 by varying $\epsilon_{bj}, \epsilon_c$. Then, the parameter set which gives the minimum $\chi_{min}^2(\mathbf{q})$ is regarded as the best fit values.

For any fixed values of ϵ_{bj} and ϵ_c, Eq. F.1 follows the χ^2 distribution with n+1+j degrees of freedom, for testing the theoretical predictions $\mu_i(\mathbf{q})$, because it is the sum of n+1+j Gaussian distributed random variables. The best fit, χ_{min}^2, the minimum of χ^2 should follow the χ^2 distribution with n-1 degrees of freedom.

F.1 $R_{AA}(p_\text{T})$ and $v_2(p_\text{T})$ Comparison

We try to find the drag force which reproduces the experimental $R_{AA}(p_\text{T})$ and $v_2(p_\text{T})$ by the least-square fit using Eq. F.1.

In this fit, we consider 2 type B uncertainties and 1 type C uncertainty:

- σ_{b1}: The type B systematic uncertainty of R_{AA}

- σ_{b2}: The type B systematic uncertainty of v_2

- σ_c: The type C systematic uncertainty of R_{AA}

The uncertainties in $R_{AA}(p_{\mathrm{T}})$ and $v_2(p_{\mathrm{T}})$ are correlated via the type B uncertainties in the electron spectrum in Au+Au collisions. Since it is found this correlated uncertainty is small, this correlation is neglected for the simplicity. $\sigma_{b1(2)}$ is assumed to have 100% correlation with p_{T} for the simplicity. For the $v_2(p_{\mathrm{T}})$ fitting, we use statistical error as $\tilde{\sigma}_i$.

F.2 Fit Method for R_{AA}

There is the relation between the statistical error and p_{T} correlated systematic error from the nature of the statistical error. To take into account the relation, the following $\tilde{\sigma}_i$is applied.

Let us consider a simple example, where the experimental observable can be expressed as follows.

$$y = C_1 \times C_2 \times ... \times C_n \times y_0 = a \times y_0, \tag{F.2}$$

where, $C_1...C_n$ are systematic correction factors, a is the overall correction factors, y_0 is the raw yield and y is the experimental observable. In this case, statistical error of y, σ_y can be written as follows.

$$\sigma_y = a \times \sigma_{y_0}, \tag{F.3}$$

Where, σ_{y_0} is the statistical error of y_0. When y move to y' $(= y + \sum_j \epsilon_{bj}\sigma_{bj} + \epsilon_c\sigma_c)$ due to the change of systematic correction $(a \to a')$ as described in Eq. F.1, statistical error of y' becomes as follows.

$$\sigma_{y'} = a' \times \sigma_{y_0} = \frac{a'}{a}\sigma_y \tag{F.4}$$

$$= \frac{y + \sum_j \epsilon_{bj}\sigma_{bj} + \epsilon_c\sigma_c}{y}\sigma_y. \tag{F.5}$$

Therefore, in the case which the experimental observable can be expressed in Eq. F.2, we should use $\tilde{\sigma}_y = (y + \sum_j \epsilon_{bj}\sigma_{bj} + \epsilon_c\sigma_c)/y\sigma_y$ in Eq. F.1 instead of σ_y.

As a nest step, $\tilde{\sigma}_y$ of $R_{AA}(p_{\mathrm{T}})$ is considered. Statistical error of $R_{AA}(p_{\mathrm{T}})$ above 3 GeV/c is determined by the spectrum of single non-photonic electrons in Au+Au collisions. The spectrum of single non-photonic electrons is obtained as follows.

$$Y = a \times N - B, \tag{F.6}$$

where N is raw yield of the inclusive electrons, a is the overall correction factor, B is the yield of background electrons and Y is the value of the spectrum of single non-photonic electrons. We assume the change of the value of the spectrum, $Y \to Y'$ by varying ϵ_{b1} in Eq. F.1 is the change of the correlation factor, $a \to a'$ for the simplicity. This assumption is almost justified

in the $R_{AA}(p_T)$ analysis. Therefore, when the spectrum Y is moved to Y', the statistical error becomes as follows.

$$\frac{Y' + B}{Y + B} a(\Delta N)_{stat} = \frac{Y' + B}{Y + B}(\Delta Y)_{stat} \tag{F.7}$$

The statistical error of R_{AA} can be written from the scaling error, ϵ_c and Eq. F.7 with the signal to the background ratio in the measured electrons $(R_{NP} = Y/B)$ as follows.

$$\sigma_{Y_{stat}} \times \left(\frac{\frac{R_{AA}(i)}{R_{AA}(i) + \epsilon_{b1}\sigma_{b1}} R_{NP} + 1}{R_{NP} + 1} + \frac{\epsilon_c \sigma_c}{R_{AA}} \right) \tag{F.8}$$

Therefore, $\tilde{\sigma}_Y$ defined in Eq. F.8 is used instead of σ_Y.

Appendix G

R_{AA} and v_2 Correction
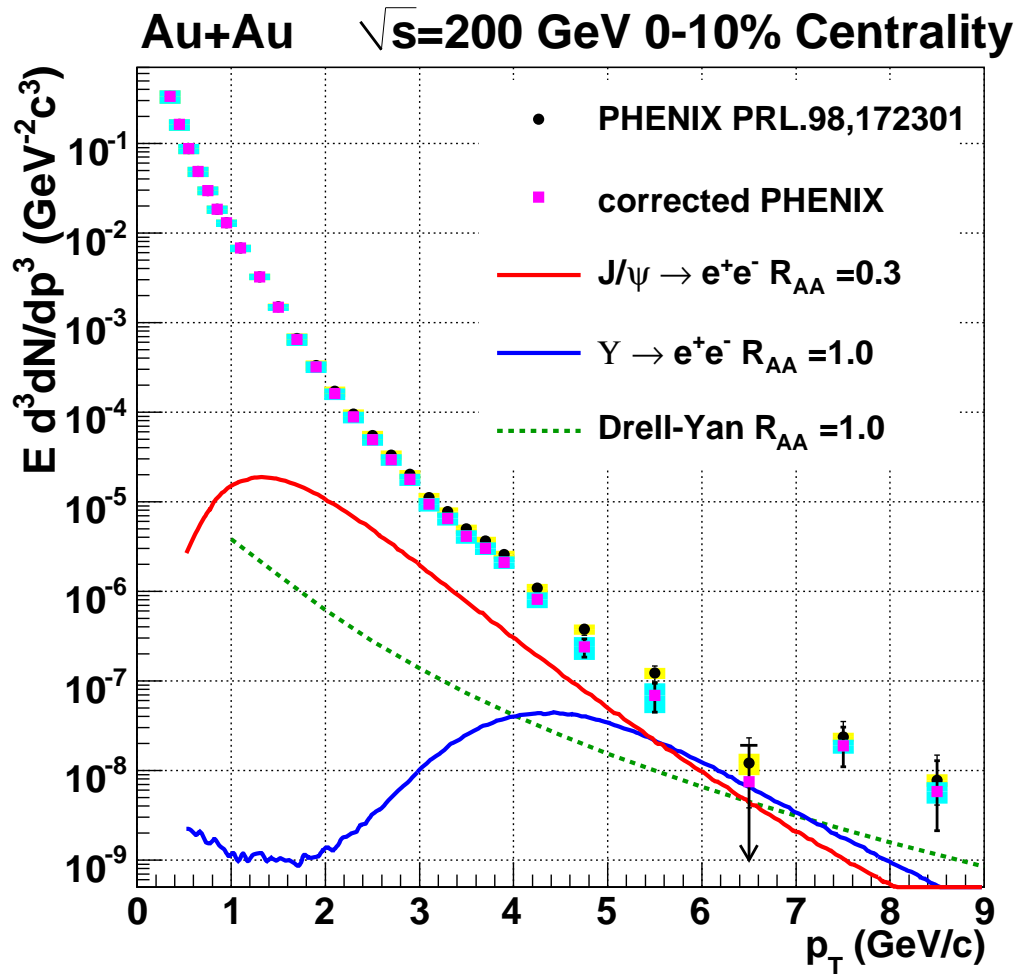
Figure G.1: The spectra of the electrons from heavy flavor measured in PHENIX [114], additional non-photonic background (J/ψ, Υ and Drell-Yan process), and the electrons from semi-leptonic decay of heavy flavor in 0-10% central Au+Au collisions.
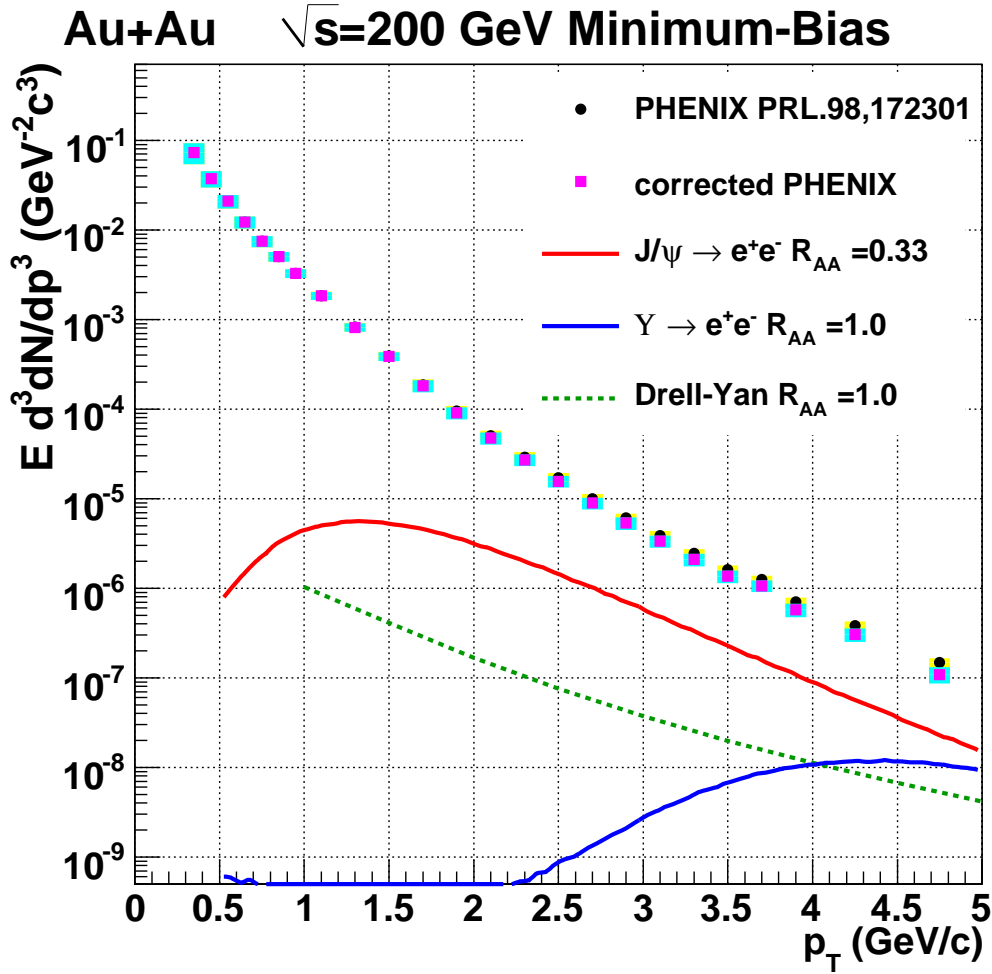
Figure G.2: The spectra of the electrons from heavy flavor measured in PHENIX [114], additional non-photonic background (J/ψ, Υ and Drell-Yan process), and the electrons from semi-leptonic decay of heavy flavor in minimum bias Au+Au collisions.

The R_{AA} and v_2 of non-photonic electrons reported by PHENIX include the contribution of the electrons from J/ψ, Υ and Drell-Yan process [114]. The contribution from J/ψ, Υ and Drell-Yan process should be subtracted from the experimental result in this chapter.

Figure G.1 shows the spectrum of the non-photonic electrons in 0-10% central Au+Au collisions measured in PHENIX [114], which includes single non-photonic electrons from heavy flavor and the contributions from non-photonic background (J/ψ, Υ and Drell-Yan process). It has been observed the yield of J/ψ is suppressed in Au+Au collisions compared with that in p+p collisions at PHENIX [120]. In Fig. G.1, R_{AA} of J/ψ is assumed to be 0.3 according to the experimental result. 50% systematic error is assinged for the contribution of J/ψ to cover p_T dependance of R_{AA} measured in PHENIX [120]. While the yields of Υ and Drell-Yan process have not been measured at RHIC in Au+Au collisions, the yields of Υ and Drell-Yan process are expected not to be suppressed [162]. R_{AA} of Υ and Drell-Yan process is assumed to be one. 70% and 75% systematic error are assinged for contribution of Υ and Drell-Yan

process including the uncertainty of the yield of Υ and Drell-Yan in p+p collisions and the uncertainty of R_{AA}. The spectrum of single non-photonic electrons in 0-10% central Au+Au collisions is obtrained by the subtraction of non-photonic background (J/ψ, Υ and Drell-Yan process) from the spectrum of the non-photonic electrons reported by PHENIX. R_{AA} of the single non-photonic electrons is obtained from the spectrum of the single non-photonic electrons in p+p and Au+Au collisions.

To obtain v_2 of single non-photonic electrons from that of non-photonic electrons in minimum-bias Au+Au collisions reported by PHENIX, the spectrum of single non-photonic electrons in minimum-bias Au+Au collisions is also obtained in similar way in 0-10% central collisions. Figure G.2 shows the spectrum of the non-photonic electrons in minimum-bias Au+Au collisions measured in PHENIX [114], which includes single non-photonic electrons from heavy flavor and the contributions from non-photonic background (J/ψ, Υ and Drell-Yan process). R_{AA} of J/ψ is assumed to be 0.33 according to the experimental result [120]. R_{AA} of Υ and Drell-Yan process is assumed to be one in the same case of 0-10% central collisions. There is small contribution of J/ψ and Υ above 3 GeV/c. v_2 of non-photonic electrons measured in PHENIX [114] is also corrected to take account to the effect of electrons from J/ψ and Υ. The v_2 of the electrons from J/ψ and Υ is assumed to be zero, since the v_2 of J/ψ is currently consistent with zero [121]. The deviation of the corrected v_2 from the original v_2 is included into systematic error of the corrected v_2.

Appendix H

Model Calculation Based on Langevin Equation

A model calculation is done to study the medium property and underling physics from the $R_{AA}(p_T)$ and $v_2(p_T)$ of the single non-photonic electrons from charm and bottom, where the obtained ration of b/c+b is used in this model calculation.

The procedure is as follows.

- Generation of heavy quarks

- Simulation of space time evolution of heavy quarks in the medium

- Hadronization of bare heavy quarks

- Semi-leptonic decay of heavy flavored hadrons

Especially, understanding of space time evolution of heavy quarks in the medium is important since what we want to know is the information of the medium via the interaction of the heavy quark and the medium. Monte-Carlo simulation using Langevin equation is applied for the description of the space time evolution. Heavy quarks are produced only in the initial hard collisions and it takes many collisions to change the momentum of heavy quark substantially due to their large mass compared with temperature of the medium ($\sim$ 200 MeV). Therefore, heavy quarks can be described as Brownian particle and the Langevin equation is a good approximation to model the motion of the heavy quarks in the medium [140, 141, 144]. The interaction between heavy quarks and the medium is represented in terms of drag force and diffusion coefficients in Langevin equation. The magnitude of drag force and diffusion coefficients will be constrained to reproduce the experimental $R_{AA}(p_T)$ and $v_2(p_T)$. In this section, drag force and diffusion coefficients which reproduce the results of the single non-photonic electrons are studied.

H.1   Initial Condition of Heavy Quarks

The bulk thermalization time is assumed to be τ_0 ($= \sqrt{t^2 - z^2}$) = 0.6 fm [152, 153]. The space and momentum distribution of heavy quarks at τ_0 is defined as the initial condition.

The momentum distribution of heavy quarks at τ_0 is assumed to be the distribution at which heavy quarks are generated, since there is not significant interaction for heavy quarks before τ_0. Heavy quarks are assumed to stream freely in the transverse direction before τ_0.
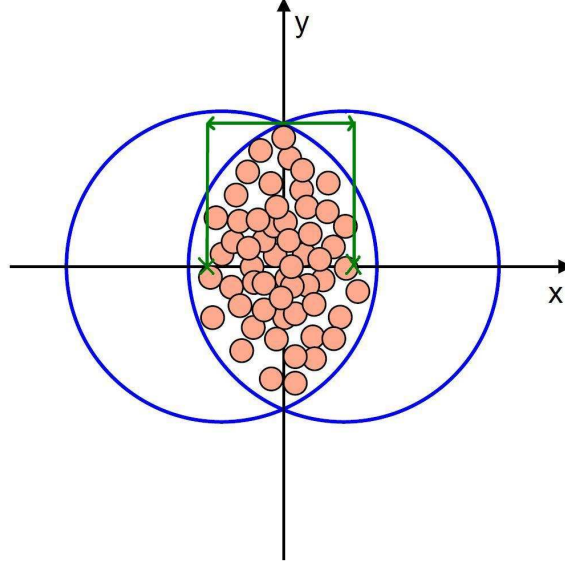
Figure H.1: Conceptual view of the heavy ion collision and coordinate system.

In the heavy ion collisions, the space distribution of generated heavy quarks is determined by the geometry of the collisions, because heavy quark is produced only in the initial hard collision and the yield is scaled by the number of nucleon-nucleon collisions as described in Sec. 2.3.6. The initial positions of heavy quarks are calculated according to the Glauber model [136] discussed in Sec. 2.1.2. The space distribution of heavy quarks in transverse plane $(n_{in}^r(x, y))$ is represented as

$$n_{in}^r(x, y) \propto \rho_A(x - b/2, y) \times \rho_B(x + b/2, y). \tag{H.1}$$

Here, $\rho_{A(B)}$ is nuclear density function and b is the impact parameter of the collision. Reaction plane of the collision is defined as (x,z) plane with the impact parameter to be parallel to the x-axis. Figure H.1 shows the conceptual view of the heavy ion collision and coordinate system. Impact parameter (b) is used 3.1 fm for 0-10% centrality events. For Minimum Bias events, events with the impact parameter corresponding to each centrality are merged accoring to Table D.1 in Appendix D, where the production of heavy qurak is assumed to be N_{coll} scaling. The nuclear density function is parameterized by a Woods-Saxon function defined in Eq. 2.1. Figure H.2 shows the space distribution in transverse plane of heavy quarks generated according to Eq.H.1 for 0-10% centrality events and Minimum-Bias events. For the distribution in z direction, it is assumed that spatial rapidity, $y_S = \frac{1}{2} \ln \frac{t+z}{t-z}$, has the same value with the rapidity in momentum space.

The initial momentum spectra of charm and bottom are determined by FONLL calculation [77]. The absolute values of cross section of charm and bottom are normalized according to the experimental results obtained in this thesis, which is discussed in Sec. 7.4.1.
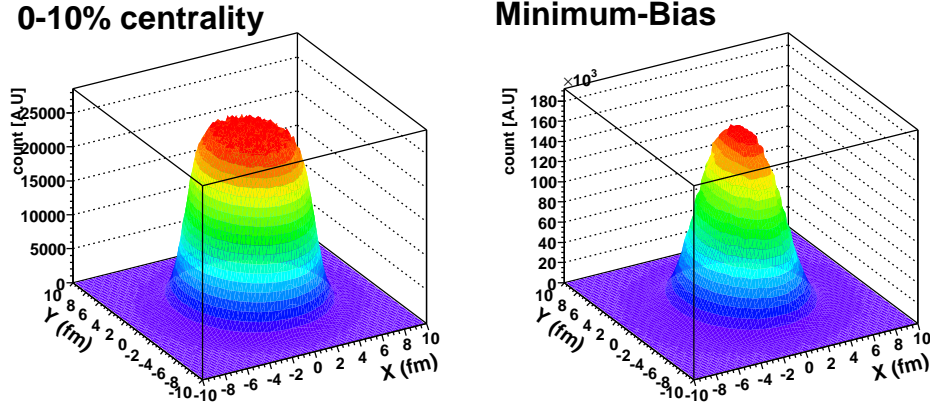
Figure H.2: The distribution in transverse plane of the initial position of heavy quark generated according to Eq.H.1 for 0-10% centrality events and Minimum-Bias events.

Figure H.3 shows FONLL calculation of the p_T distribution of charm and bottom at mid-rapidity ($| y | < 0.5$) in p+p $\sqrt{s} = 200$ GeV collisions [82]. The azimuthal distribution is assumed to be flat.

Initial nuclear effects such as shadowing and Cronin effect are not considered for simplicity in this calculation. Such effects are not large as discussed in Sec. 2.2.1, while these should be considered for the precise description.
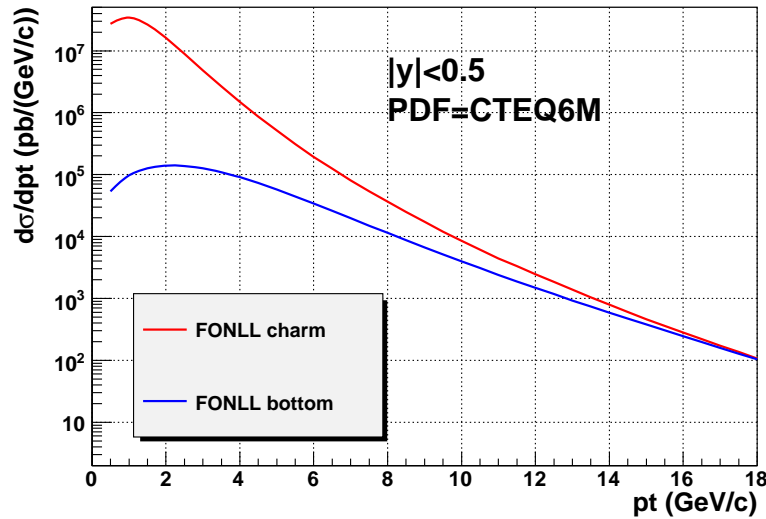
Figure H.3: FONLL calculation of the p_T distribution of charm and bottom at mid-rapidity ($| y | < 0.5$) in p+p $\sqrt{s} = 200 GeV$ collisions [82].

H.2   Space Time Evolution of Heavy Quarks

The hot and dense medium created with heavy ion collisions is assumed to be thermalized at $\tau_0 = 0.6$ fm and then the medium follows the space-time evolution [152, 153]. Heavy quarks propagate the hot and dense medium. Relativistic hydrodynamics has been applied for the description of the space-time evolution of the medium from τ_0 to the freeze-out, which is the background of the motion of heavy quarks. Hydrodynamical calculations succeed in reproduction of the observed light particle spectra in low p_{T}, azimuthal anisotropy of the light particles and multiplicity well [150, 151, 152, 153]. In this model calculation, the results of the relativistic hydrodynamical calculation are used to describe the evolution of the medium, which are taken from Ref. [152, 153].

The relativistic hydrodynamical calculation is characterized by local temperature ($T(\mathbf{x}, t)$), energy density ($e(\mathbf{x}, t)$), flow velocity ($\mathbf{v}(\mathbf{x}, t)$) and fraction of QGP ($f_{qgp}(\mathbf{x}, t)$). The critical temperature and the thermal freeze-out temperature are assumed to be 170 MeV and 100 MeV, respectively. Figure H.4 shows the calculated temperature profile at $z = 0$ in 0-10% central Au+Au collisions. Each panel corresponds to the temperature field at each proper time. The hydrodynamical calculation in the centrality corresponding to the impact parameter are used as the model calculation for Minimum Bias events.

The end time of space time evolution of heavy quarks is determined by the fraction of QGP ($f_{qgp}(\mathbf{x}, t)$). $f_{qgp}(\mathbf{x}, t)$ is s calculated by the relativistic hydrodynamics at each local point. The fraction of QGP is defined as,

$$f_{qgp}(\mathbf{x}, t) \equiv \frac{e - e_{had}}{e_{QGP} - e_{had}}. \tag{H.2}$$

Here, e_{QGP} (e_{had}) is the maximum (minimum) value of the energy density at local grid. The evolution of heavy quark is stopped when $f_{qgp}(\mathbf{x}, \mathbf{t})$ becomes bellow 0.5 and then heavy quarks are hadronized.

Space time evolution of generated heavy quarks in the medium is simulated by Monte-Carlo calculation according to relativistic Langevin equation. The relativistic Langevin equation in the rest frame of the background fluid is written as,

$$\Delta \mathbf{x}(t) = \frac{\mathbf{p}}{E} \Delta t, \tag{H.3}$$

$$\Delta \mathbf{p}(t) = -\gamma \mathbf{p} \Delta t + \xi(t) \Delta t. \tag{H.4}$$

Here, $\Delta \mathbf{x}$ and $\Delta \mathbf{p}$ are deviations of space and momentum of heavy quarks in a discrete step of time, Δt. γ is the drag coefficient and ξ represents random momentum kick that is uncorrelated in time. ξ is assumed to have Gaussian shape and is characterized by the following equations.

$$< \xi_i(t) > = 0, \tag{H.5}$$

$$< \xi_i(t) \xi_j(t') > = D_p \delta_{ij} \delta(t - t'), \tag{H.6}$$

where D_p is the diffusion coefficient in momentum space. γ and D_p are related from the relativistic Kramers equation and the requirement for the equation to have the Jutter distribution

as a stationary solution [145, 147]. The relation is as follows.

$$\gamma + \frac{dD_p}{d(p^2)} = \frac{D_p}{2ET}.$$
(H.7)

The relation between γ and D_p is reduced to more simple form called as Einstein's fluctuation-dissipation relation when D_p is independent of momentum.

$$\gamma = \frac{D_p}{2ET}$$
$$\sim \frac{D_p}{2MT}(E \to M).$$
(H.8)

In the non-relativistic limit, the spatial diffusion constant ($D_{sx} \equiv (<x^2> - <x>^2)/2\Delta t$) is written in terms of γ as follows.

$$D_s = \frac{T}{M\gamma}.$$
(H.9)

The thermal relaxation time of heavy quarks (τ_{HQ}) is obtained as the inverse of drag coefficient (γ).

$$\tau_{HQ} \sim \frac{1}{\gamma}$$
(H.10)

The parametric dependence of drag coefficient (momentum, temperature and so on) is governed by the microscopic interaction of heavy quark with the medium, and it has not been understood. In this model calculation, we concentrate on the phenomenological understanding of the interaction and the medium property. Therefore, we assume the parametric dependence of drag coefficient with one free parameter and the free parameter is constrained with the experimental results. The following two relations are assumed for the drag coefficient.

$$\gamma = \alpha\frac{T^2}{M},$$
(H.11)
$$\gamma = \alpha\frac{T^2}{E},$$
(H.12)

where $M(E)$ is mass (energy) of heavy quark and α is the dimensionless free parameter which is independent of other parameters.

The two relations represent the two extreme cases. Eq. H.11 is motivated by the result from the AdS/CFT correspondence. The drag coefficient can be expressed as bellow according to the AdS/CFT correspondence [145, 165, 166, 167].

$$\gamma \sim 2\frac{T^2}{M} \propto \frac{T^2}{M}.$$
(H.13)

This drag coefficient represents the strongly coupling limit of QGP because the AdS/CFT correspondence is valid under such condition as discussed in Sec. 2.2.3.

In the other hand, Eq. H.12 is motivated by the perturbative QCD calculation of collisional process [169, 144]. This drag coefficient represents the week coupling regime of QGP, where perturbative collisional process is dominant.

The corresponding diffusion coefficient D_p is obtained from the generalized fluctuation-dissipation relation in Eq H.7 as follows.

$$D_p = \alpha \frac{2T^3}{M}(E+T) \qquad \text{(AdS/CFT)}, \tag{H.14}$$

$$D_p = \alpha 2T^3 \qquad \text{(pQCD)}. \tag{H.15}$$

The evolution of heavy quarks is analyzed numerically according to Eq. H.3 and H.4 in the rest frame of the medium fluid. And then heavy quarks are transformed in the laboratory frame, to take into the account the medium fluid. This process is continued until the end time of space time evolution determined above.

H.3   Hadronization Process

Since the experimental observable is not bare quark but hadron, the hadronization process should be considered in the model calculation to compare with the experimental result. As discussed in Sec. 2.2.3, the quark coalescence (recombination) model has received renewed interest in the context of RHIC data, by providing a successful explanation of two phenomena observed in intermediate p_T hadron spectra, the constituent quark number scaling of the elliptic flow and the large baryon-to-meson ratios [155, 156]. It is natural to apply it to the hadronization of heavy quarks as well. Since the fraction of baryons containing heavy quarks over meson is rather small, the hadronization to heavy flavored meson is only considered here.

Since the probability of the hadronization of heavy quarks via coalescence process becomes small at high p_T where the phase-space density of light-quark to coalesce becomes very small, the hadronization of heavy quarks via usual fragmentation process discussed in Sec .2.3.2 becomes dominant process at high p_T ($p_T > 3$ GeV/c). Thus, the total D (B)-meson spectrum takes the following form

$$\frac{dN_{D(B)}^{tot}}{d^2\mathbf{p_T}} = \frac{dN_{D(B)}^{coal}}{d^2\mathbf{p_T}} + \frac{dN_{D(B)}^{frag}}{d^2\mathbf{p_T}} \tag{H.16}$$

The yield of heavy flavored mesons produced via quark coalescence process is modeled according to the following equation [157, 158].

$$\frac{dN_M}{d^2\mathbf{p_T}} = \frac{g_M}{(\Delta y)^2} \int d^2\mathbf{r}_{Q\mathrm{T}} d^2\mathbf{r}_{q\mathrm{T}} d^2\mathbf{p}_{Q\mathrm{T}} d^2\mathbf{p}_{q\mathrm{T}} \times \left.\frac{dN_Q}{d^2\mathbf{r}_{Q\mathrm{T}}d^2\mathbf{p}_{Q\mathrm{T}}}\right|_{|y|<\Delta y/2} \left.\frac{dN_q}{d^2\mathbf{r}_{q\mathrm{T}}d^2\mathbf{p}_{q\mathrm{T}}}\right|_{|y|<\Delta y/2}$$

$$\times \int dy_{SQ} dy_Q dy_{Sq} dy_q \delta(y_{SQ}-y_Q)\delta(y_{Sq}-y_q) f_M(x_Q,x_q;p_Q,p_q)\delta(\mathbf{p_T}-\mathbf{p}_{Q\mathrm{T}}-\mathbf{p}_{q\mathrm{T}}), \tag{H.17}$$

where Q and q denote heavy quark (c,b) and light quark (u,d,s), respectively. Δy is rapidity range and g_M is statistical factor to take into account the internal quantum numbers (spin and color). $f_M(x_Q,x_q;p_Q,p_q)$ is the coalescence probability function which depends on the overlap of heavy and light quark in momentum and coordinate space. Here, we assume a uniform distribution as follows [159],

$$f_M(x_Q,x_q;p_Q,p_q) = \frac{9\pi}{2\Delta_x^3\Delta_p^3}\Theta(\Delta_x^2-(x_Q-x_q)^2)\Theta(\Delta_p^2-\frac{(p_Q-p_q)^2}{4}\frac{(M_Q-m_q)^2}{4}). \tag{H.18}$$

Here, Δ_x, Δ_p are the covariant spatial and momentum coalescence radii, and they are related with each other by the uncertainty relation $\Delta_x \Delta_p \sim 1$. In this calculation, we take 0.24 GeV as Δ_p [157].

The heavy quark distribution function $(\frac{dN_Q}{d^2\mathbf{r}_{QT}d^2\mathbf{p}_{QT}})$ is directly taken from the output of the Langevin simulations discussed in the previous section.

The light-quark distributions $(\frac{dN_q}{d^2\mathbf{r}_{qT}d^2\mathbf{p}_{qT}})$ are taken from the successful application of the coalescence model of Ref. [160] to light hadron observables at RHIC. Figure H.5 shows the light-quark distributions in momentum space $(\frac{dN_q}{d^2\mathbf{p}_{qT}})$ to be use in the calculation of Eq. H.17. Black line shows the distribution of u and d quark and red dotted line shows that of s quark. The light-quark above 1.7 GeV/c is considered as mini-jet parton and the p_{T} distribution is assumed to have power-law form, where that p_{T} distribution is tuned to reproduce observed jet quenching for high p_{T} charged particles [159, 160]. The light-quark bellow 1.7 GeV/c is considered as thermalized partons in QGP and the p_{T} distribution is assumed to have exponential form. To take into account collective flow of QGP, these partons are boosted by a flow velocity $\mathbf{v}_{\mathrm{T}} = \beta(\mathbf{r}_{\mathrm{T}}/R)$, depending on their transverse radial positions $\mathbf{r}_{\mathrm{T}}$. Here, R is the transverse size of the QGP (8fm) at hadronization, and β is the collective flow velocity of QGP and is taken to be $0.5c$ [160].

In addition, the p_{T} distribution of light-quarks is assumed to have the following relation with respect to the azimuthal direction in momentum space and the magnitude of momentum to take into account the effect of the elliptic flow of light quarks in the medium.

$$\frac{dN_q}{d^2\mathbf{p}_{qT}} \propto 1 + 2v_2(p_{\mathrm{T}})\cos(2\phi) \tag{H.19}$$

$v_2(p_{\mathrm{T}})$ is taken from Ref. [161] which reproduces the elliptic flow of light flavored hadron. Figure H.6 shows the assumed $v_2(p_{\mathrm{T}})$ of light-quarks to use the calculation.

The remaining c and b quarks from coalescence process are hadronized using δ-function fragmentation [141]. While δ-function fragmentation is not accurate treatment for the fragmentation, the result via δ-function fragmentation almost agrees with the experimental result.

Finally, the D and B mesons are decayed into electrons via semi-leptonic decay. This process is done by using EvtGen simulation as done in the analysis of experimental data.

H.4 Numerical Result

The numerical results of the model calculation are shown in this section. $R_{AA}(p_{\mathrm{T}})$ and $v_2(p_{\mathrm{T}})$ are determined in this calculation as follows.

$$R_{AA}(p_{\mathrm{T}}) = \frac{N_{out}(p_{\mathrm{T}})}{N_{in}(p_{\mathrm{T}})}, \tag{H.20}$$

$$v_2(p_{\mathrm{T}}) = <\cos 2\phi > (p_{\mathrm{T}}). \tag{H.21}$$

Here, $N_{in(out)}(p_{\mathrm{T}})$ is the input (output) yield of the calculation. Input electron yield is determined as the yield of decay electrons of D (B) mesons from hadronization of input heavy quark via δ-function fragmentation.

Figure H.7 and H.8 show $R_{AA}(p_T)$ and $v_2(p_T)$ of charm and bottom quarks calculated by the drag force defined in Eq. H.11 with various values of one free parameter, respectively. $R_{AA}(p_T)$ results are calculated for 0-10% centrality events ($b = 3.1$ fm) and $v_2(p_T)$ results are calculated for Minium-Bias events to compare the experimental results. The magnitude of suppression at high p_T and $v_2(p_T)$ become larger as the drag force become stronger. In addition the magnitude of suppression at high p_T and $v_2(p_T)$ of charm quark are larger than these of bottom quark. These tendencies are expected.

Figure H.9 and H.10 are the same as Fig. H.7 and H.8, however the used drag force is defined in Eq. H.12. The tendency of $R_{AA}(p_T)$ and $v_2(p_T)$ with the drag force defined in Eq. H.12 is the almost same as the result with the drag force in Eq. H.11.

Figure H.11 and H.12 show $R_{AA}(p_T)$ and $v_2(p_T)$ of single electrons from charm and bottom quarks calculated by the drag force defined in Eq. H.11, respectively. Figure H.13 and H.14 are the same as Fig. H.11 and H.12, however the used drag force is defined in Eq. H.12. $R_{AA}(p_T)$ of electrons below 3 GeV/c is strongly enhanced than $R_{AA}(p_T)$ of quarks. This behavior is the effect of coalescence process which make p_T of hadrons larger by $0.5 \sim 1$ GeV/c than that of quarks. The magnitude of $v_2(p_T)$ is also enhanced than that of quarks and this is also from coalescence process.

These numerical results nicely demonstrate the magnitude of suppression and $v_2(p_T)$ of charm quarks are much larger than these of bottom quarks.

H.5   Comparison between Experimental Results and Model Calculation

In this section, free parameters in the model calculation are constrained within the obtained experimental uncertainties. First, the ratio of absolute value of cross section of input bottom over that of charm is constrained according to the experimental result, which is obtained in this thesis. The fit result for $(b \to e)/(c \to e + b \to e)$ is described in Sec. 7.4.1. Then, we perform a simultaneous least-squares fit about $R_{AA}(p_T)$ and $v_2(p_T)$ to the model calculation $(R_{AA}(p_T, \gamma), v_2(p_T, \gamma))$. Since the data points of $R_{AA}(p_T)$ in $1.7 < p_T < 3$ GeV/c have a very small statistical uncertainty, the free parameter in the model which gives the minimized χ^2 (χ^2_{min}) is almost determined by the shape of $R_{AA}(p_T)$ in $1.7 < p_T < 3$ GeV/c. However, the effect of coalescence process is dominant in $R_{AA}(p_T)$ in $1.7 < p_T < 3$ GeV/c, which is not from the medium property and what we want to know. Therefore, the data points above $p_T > 3$ GeV/c are used for the $R_{AA}(p_T)$ fit to extract the medium property.

$R_{AA}(p_T)$ and $v_2(p_T)$ of single non-photonic electrons ($R_{AA}^{mix}(p_T)$ and $v_2^{mix}(p_T)$) to compare with the experimental results are determined according to the constrained ratios, $(b \to e)/(c \to e + b \to e)$.

To take into the account the uncertainty of the absolute value of charm and bottom cross section, we prepare three kinds of sets of ($R_{AA}^{mix}(p_T)$ and $v_2^{mix}(p_T)$), which correspond to the results with three kinds of values of $(b \to e)/(c \to e + b \to e)$ that are best fit value and $\pm 1\sigma$ as shown in Fig. 7.10. The least square fit using Eq. F.1 are performed for these 3 $R_{AA}^{mix}(p_T)$ and $v_2^{mix}(p_T)$ set.

Figure H.15 shows $R_{AA}(p_T)$ and $v_2(p_T)$ of the decay electrons with the drag force defined in Eq. H.11 (AdS/CFT) which are the results of the fit at the 3 ratios of $(b \to e)/(c \to e + b \to e)$, best fit and $\pm 1\sigma$. The blue solid line shows the result of $R_{AA}(p_T)$ and $v_2(p_T)$ at the best fit ratio of $(b \to e)/(c \to e + b \to e)$. The green dashed line and magenta dotted line show the result at the $\pm 1\sigma$ ratios of $(b \to e)/(c \to e + b \to e)$. The fit results are summarized in Table H.1. As a result, the experimental results are successfully reproduced with $\gamma = 2.1^{+0.4}_{-0.6}\frac{T^2}{M}$ including the uncertainty of the ratio of bottom over charm.

Table H.1: Fit result using the drag force defined in Eq. H.11 (AdS/CFT).

$(b \to e)/(c \to e + b \to e)$	α	χ^2/NDF	ϵ_{b1}	ϵ_{b2}	ϵ_c
best fit	2.1	32.2/23	-2.0	-1.4	-0.7
-1σ	1.5	37.4/23	-2.2	-1.5	-0.6
+1σ	2.5	28.8/23	-1.8	-1.3	-0.6

Figure H.16 also shows the calculated $R_{AA}(p_T)$ and $v_2(p_T)$ with drag force is defined in Eq. H.12 (pQCD). In Fig. H.16, the meaning of the each line is the same in Fig. H.15. Table H.2 is the same as Table H.1, however the used drag force is defined at Eq. H.12 (pQCD). As a result, the experimental results are successfully reproduced with $\gamma = 5.3^{+0.6}_{-0.9}\frac{T^2}{E}$. About factor 2 large α is necessary with the drag force defined in Eq. H.12 to reproduce the experimental results, compared with the drag force defined in Eq. H.11.

In Fig. H.15 and Fig. H.16, there is a deviation of $R_{AA}(p_T)$ below 3 GeV/c between the model calculation and the experimental result. More accurate treatment of coalescence process, fragmentation process and initial nuclear effect are needed for the description of heavy flavor in the medium below 3 GeV/c. In addition, the more realistic parametric form of the drag force will be necessary for the complete reproduction of the experimental results.

Table H.2: Fit results using the drag force defined in Eq. H.12 (pQCD).

$(b \to e)/(c \to e + b \to e)$	α	χ^2/NDF	ϵ_{b1}	ϵ_{b2}	ϵ_c
best fit	5.3	45.8/23	-2.1	-1.3	-0.2
-1σ	4.4	54.7/23	-2.2	-1.3	-0.6
+1σ	5.9	40.3/23	-2.2	-1.4	-0.6

H.6 Result of Model Calculation

Based on the Langevin calculations, the drag force is constrained within the experimental uncertainties as follows.

$$\gamma = 2.1^{+0.4}_{-0.6}\frac{T^2}{M}, \tag{H.22}$$

$$\gamma = 5.3^{+0.6}_{-0.9}\frac{T^2}{E}. \tag{H.23}$$

The result of Eq. H.22 is compatible with the result, $\gamma \sim 2\frac{T^2}{M}$, from AdS/CFT correspondence [145, 166, 167]. This fact may suggest the medium is deconfined and strongly coupled matter, since the AdS/CFT correspondence is only valid in such condition [168].

Comparison between the result of Eq. H.23 with pQCD calculation is interesting because Eq. H.23 is motivated by the perturbative QCD calculation of collisional process (weak coupling region). The drag force calculated by 3-color, 3-flavor NLO pQCD is given as follows [172]

$$\gamma = \frac{g_s^4}{3\pi}\frac{T^2}{M}\left(\ln\frac{1}{g_s} + 0.07428 + 1.9026g_s + O(g_s^2)\right), \tag{H.24}$$

where g_s is the coupling constant in QCD. Figure H.17 shows the diffusion constant in momentum space as a function of g_s where the results are in the leading order calculation and the next-leading order calculation [172]. The result indicates the convergence of the pQCD calculation is poor above $g_s \sim 0.1$. $g_s \sim 2$ is required from the comparison between Eq. H.23 and Eq. H.24. Eq. H.24 becomes clearly unreliable for $g_s \sim 2$. This fact means that higher order pQCD or the non-perturbative treatment are necessary to describe the experimental result.

The obtained drag force in Eq. H.22 is converted to thermalization time (τ_{HQ}) and the spatial diffusion constant (D_s) of heavy quarks using Eq. H.10 and Eq. H.9.

$$D_s = \frac{1}{2.1^{+0.4}_{-0.6}T} \tag{H.25}$$

$$\tau_{HQ} = \frac{M}{2.1^{+0.4}_{-0.6}T^2} \tag{H.26}$$

With typical value $T = 200$ MeV, $M_{charm} = 1.25$ GeV and M_{bottom}=4.3 GeV, τ_{charm} and τ_{bottom} are $2.9^{+1.2}_{-0.5}$ fm and $10.1^{+4.0}_{-1.6}$ fm, respectively. τ_{charm} is shorter than the typical lifetime of QGP, $\tau_{QGP} \sim 6$ fm. Therefore, the experimental results indicate charm quarks are thermalized in the QGP. In addition, the obtained τ_{charm} is much smaller than LO pQCD calculation(~ 35fm) [141]. The non-perturbative treatment is necessary to reproduce such τ_{charm} from the microscopic interaction.
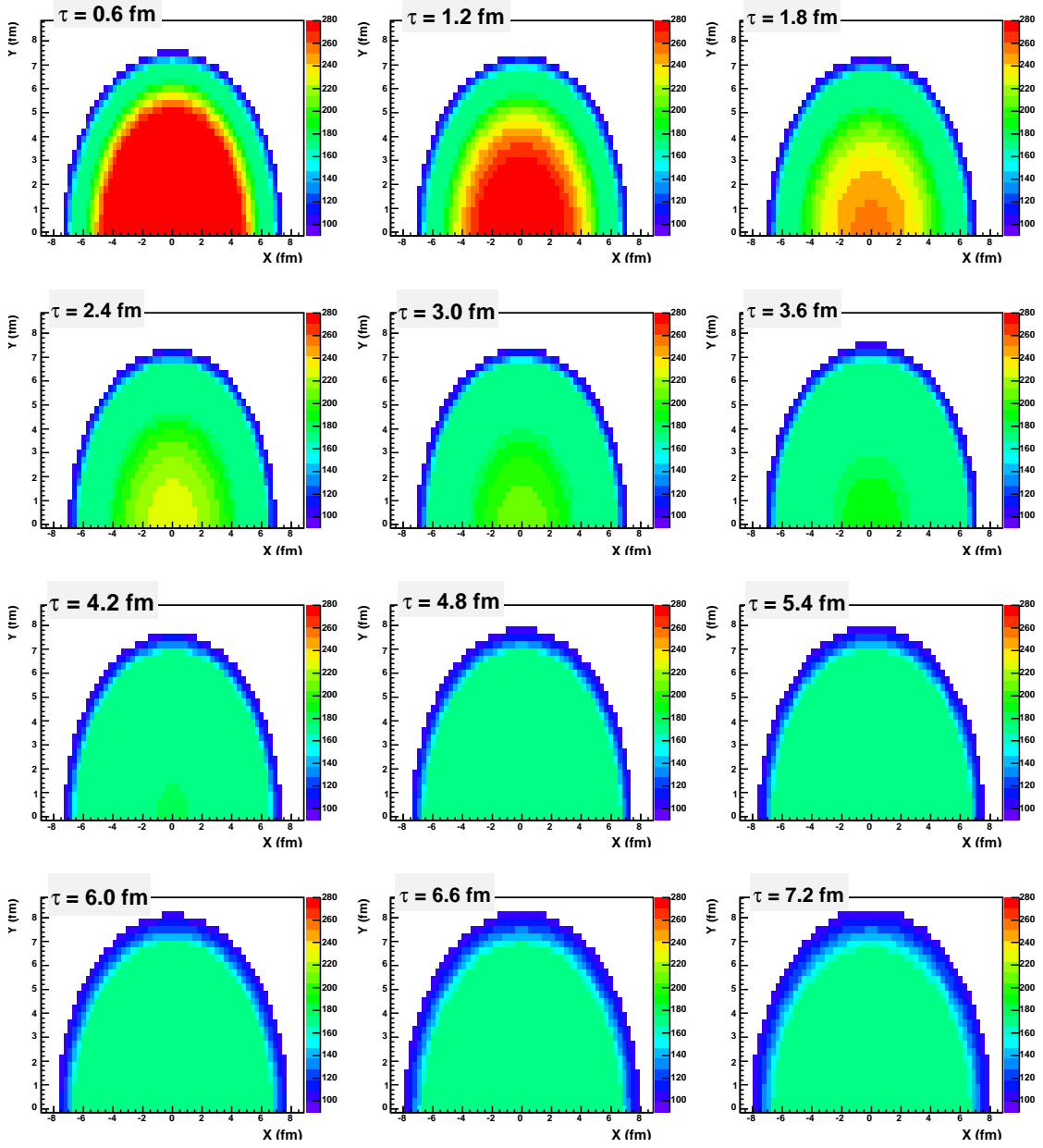
Figure H.4: The calculated temperature profile at $z = 0$ in 0-10% central Au+Au collisions [152, 153]. Each panel indicates time evolution of the matter.
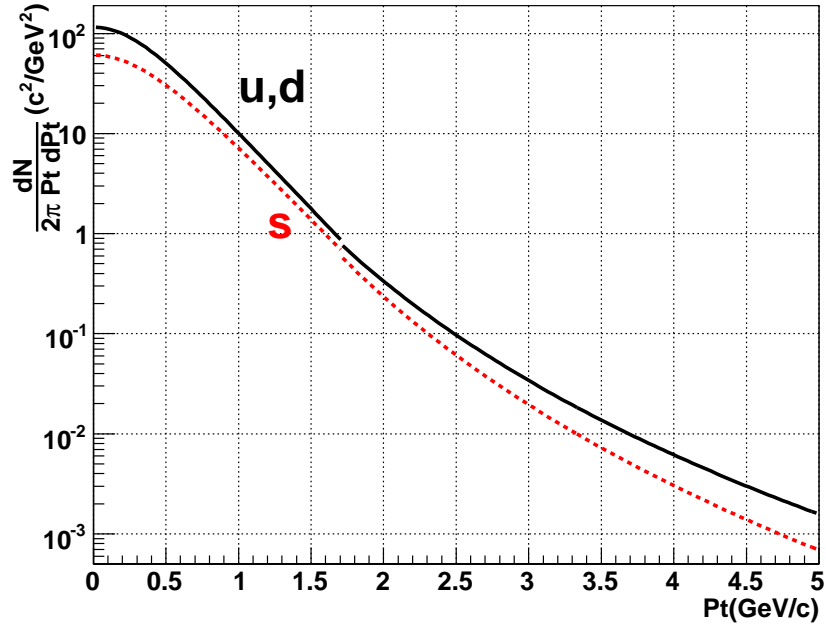
Figure H.5: The light-quark distributions to use the calculation of Eq. H.17. Black line shows the distribution of u and d quark and red dotted line shows that of s quark.
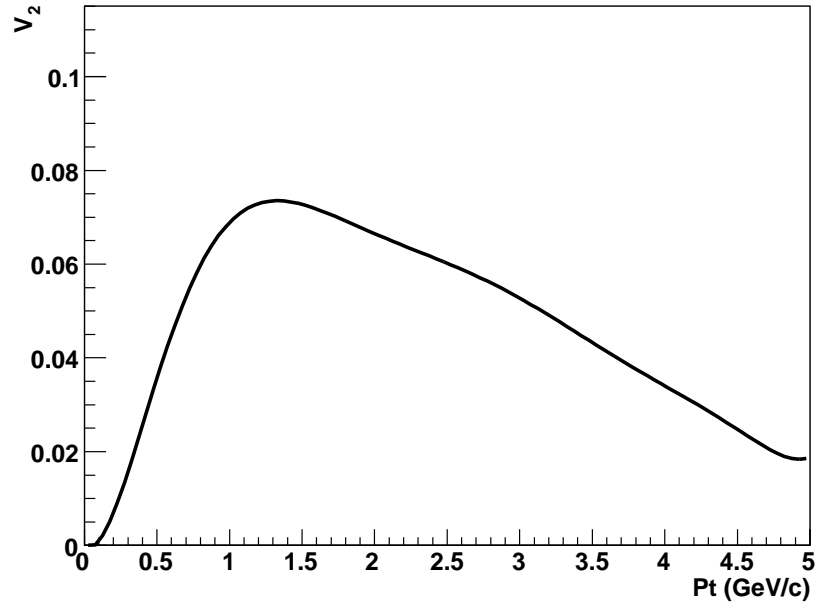
Figure H.6: The assumed $v_2(p_T)$ of light-quarks to use the calculation [161].
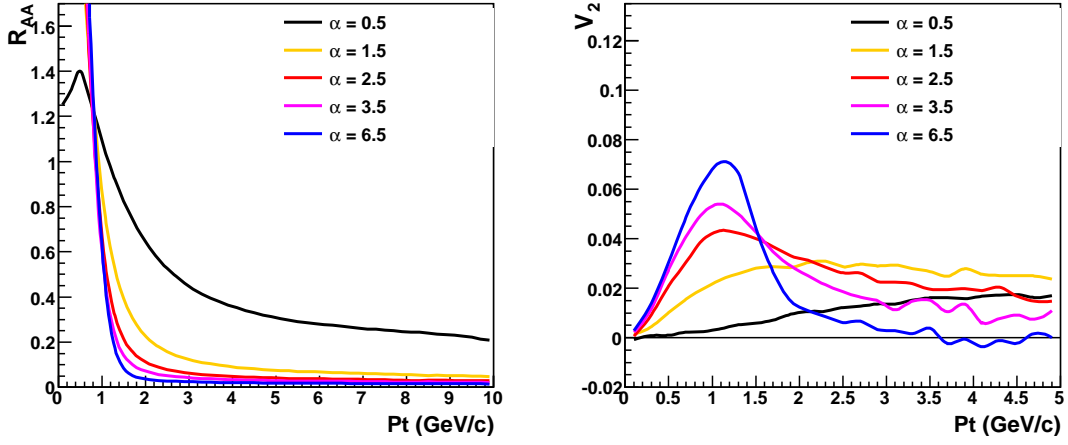
Figure H.7: $R_{AA}(p_T)$ and $v_2(p_T)$ of charm quarks calculated by the drag force defined in Eq. H.11 (AdS/CFT). Calculated conditions correspond 0-10% centrality events for $R_{AA}(p_T)$ and Minimum Bias events for $v_2(p_T)$.
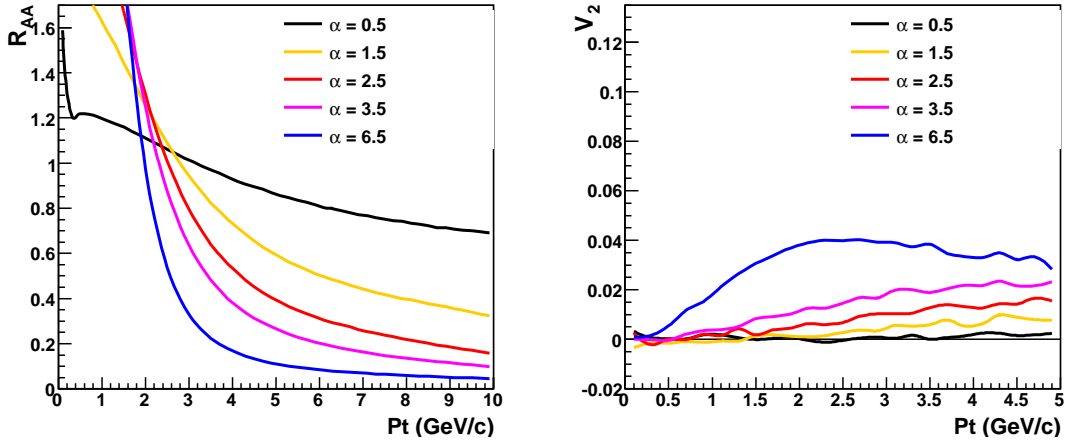
Figure H.8: $R_{AA}(p_T)$ and $v_2(p_T)$ of bottom quarks calculated by the drag force defined in Eq. H.11 (AdS/CFT). Calculated conditions correspond 0-10% centrality events for $R_{AA}(p_T)$ and Minimum Bias events for $v_2(p_T)$.
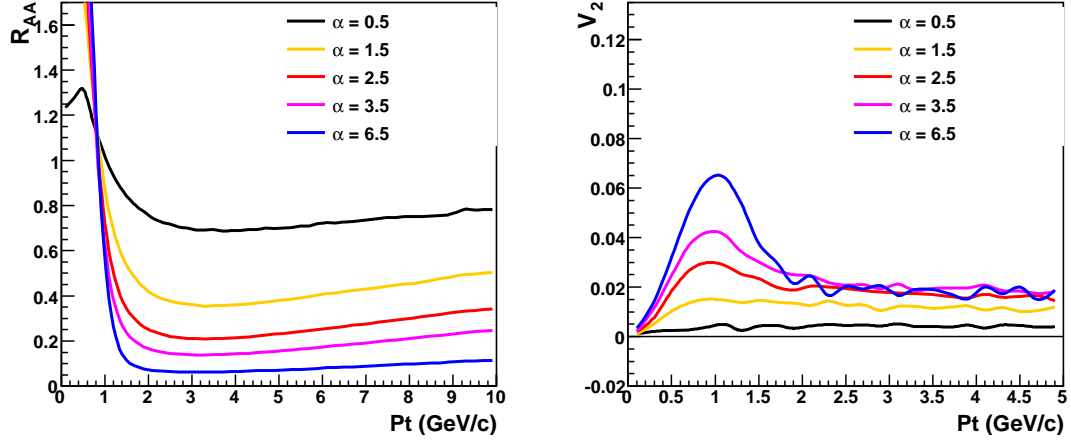
Figure H.9: $R_{AA}(p_T)$ and $v_2(p_T)$ of charm quarks calculated by the drag force defined in Eq. H.12 (pQCD).
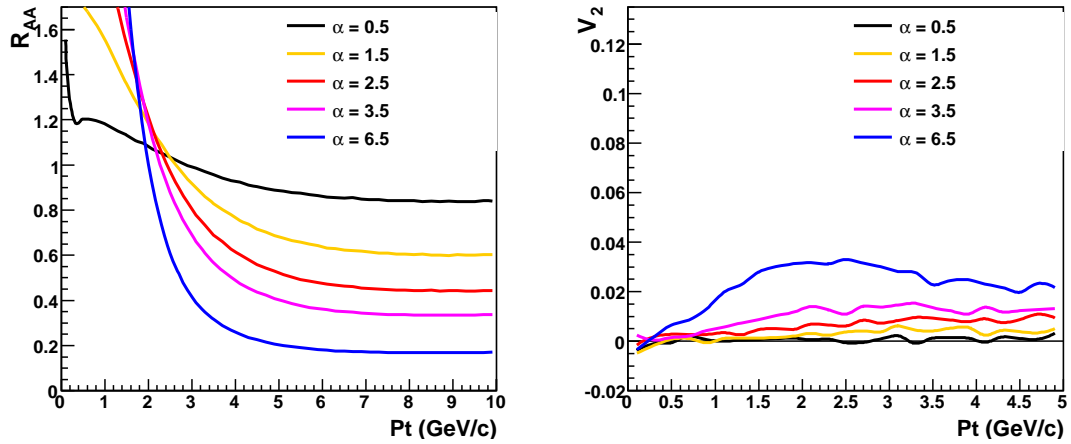
Figure H.10: $R_{AA}(p_T)$ and $v_2(p_T)$ of bottom quarks calculated by the drag force defined in Eq. H.12 (pQCD).
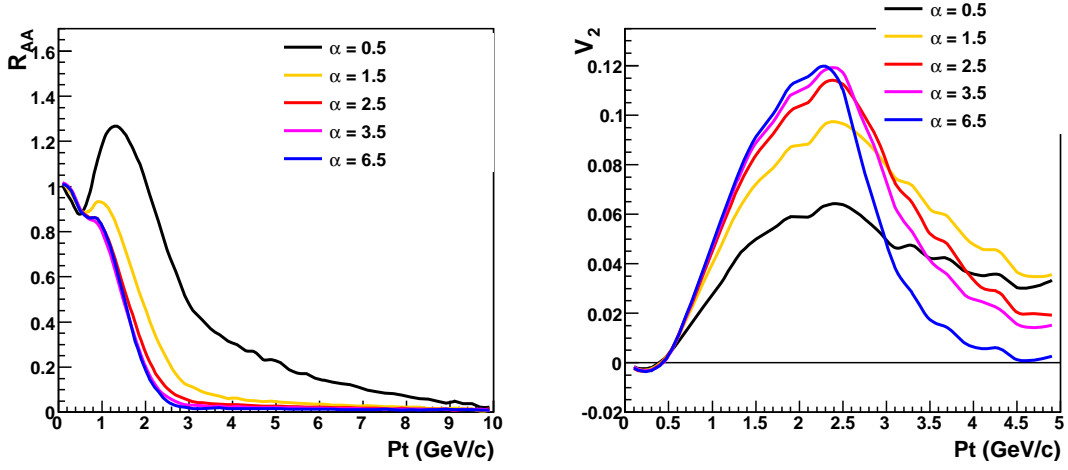
Figure H.11: $R_{AA}(p_T)$ and $v_2(p_T)$ of electrons from charm quarks calculated by the drag force defined in Eq. H.11 (AdS/CFT). Calculated conditions correspond 0-10% centrality events for $R_{AA}(p_T)$ and Minimum Bias events for $v_2(p_T)$.
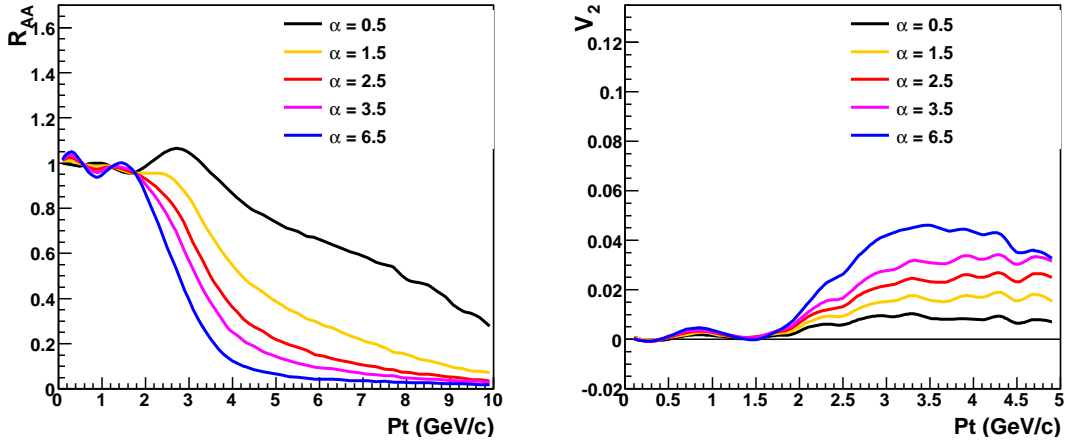
Figure H.12: $R_{AA}(p_T)$ and $v_2(p_T)$ of electrons from bottom quarks calculated by the drag force defined in Eq. H.11 (AdS/CFT). Calculated conditions correspond 0-10% centrality events for $R_{AA}(p_T)$ and Minimum Bias events for $v_2(p_T)$.
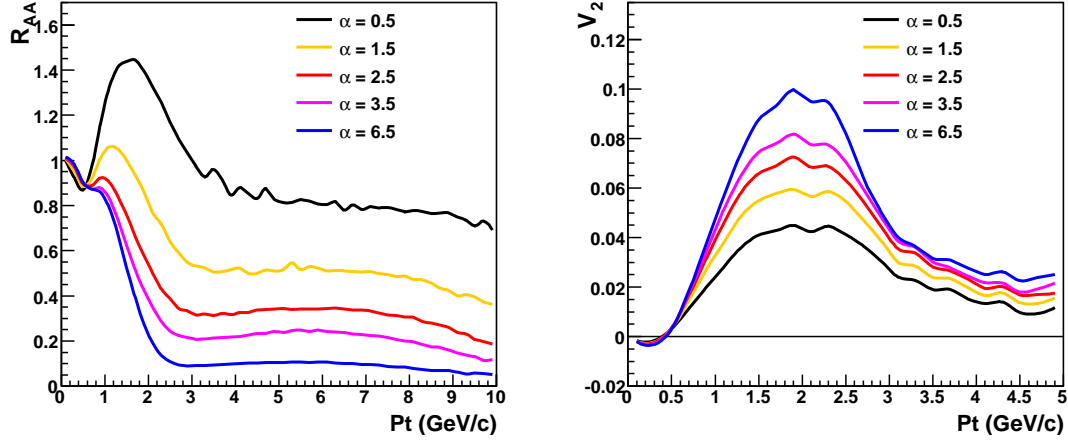
Figure H.13: $R_{AA}(p_{\mathrm{T}})$ and $v_2(p_{\mathrm{T}})$ of electrons from charm quarks calculated by the drag force defined in Eq. H.12 (pQCD).
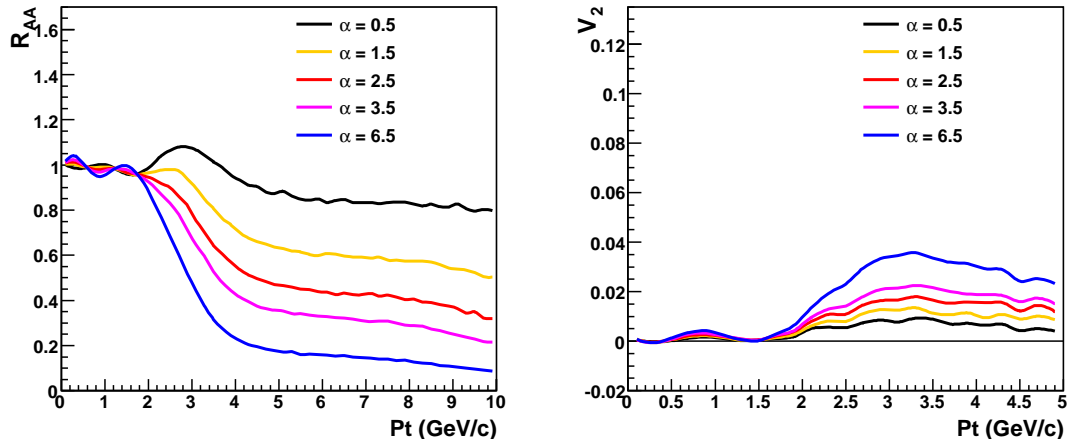
Figure H.14: $R_{AA}(p_{\mathrm{T}})$ and $v_2(p_{\mathrm{T}})$ of electrons from bottom quarks calculated by the drag force defined in Eq. H.12 (pQCD).
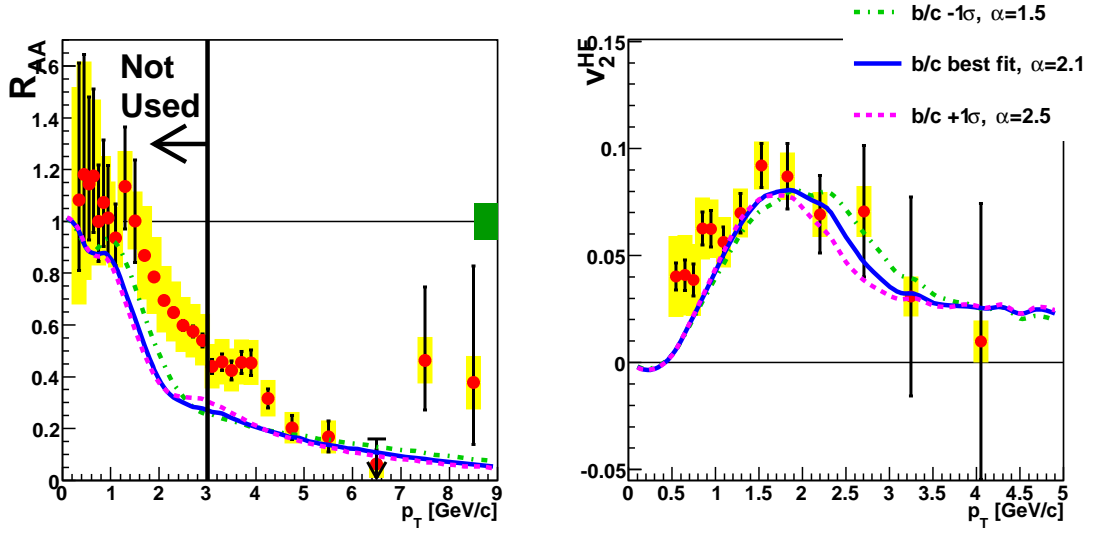
Figure H.15: $R_{AA}(p_T)$ and $v_2(p_T)$ of single electrons which are the fit results for $R_{AA}(p_T)$ and $v_2(p_T)$ at the 3 ratios of $(b \to e)/(c \to e + b \to e)$, best fit and $\pm 1\sigma$. The drag force is defined in Eq. H.11 (AdS/CFT). Data points of $R_{AA}(p_T)$ with $p_T < 3$ GeV/c are not used for the fit.
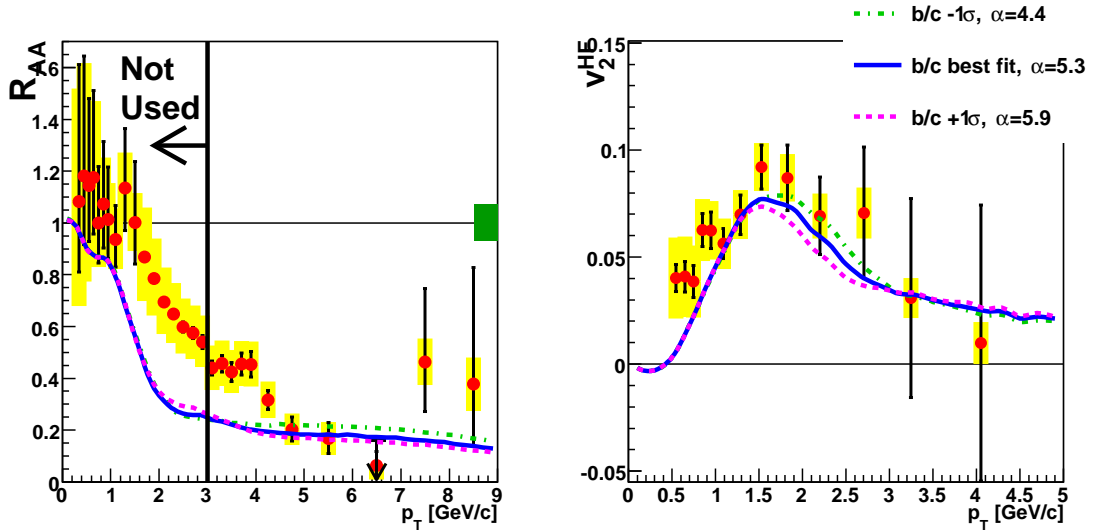
Figure H.16: $R_{AA}(p_T)$ and $v_2(p_T)$ of single electrons which are the fit results for $R_{AA}(p_T)$ and $v_2(p_T)$ at the 3 ratios of $(b \to e)/(c \to e + b \to e)$, best fit and $\pm 1\sigma$. The drag force is defined in Eq. H.11 (pQCD). Data points of $R_{AA}(p_T)$ with $p_T < 3$ GeV/c are not used for the fit.
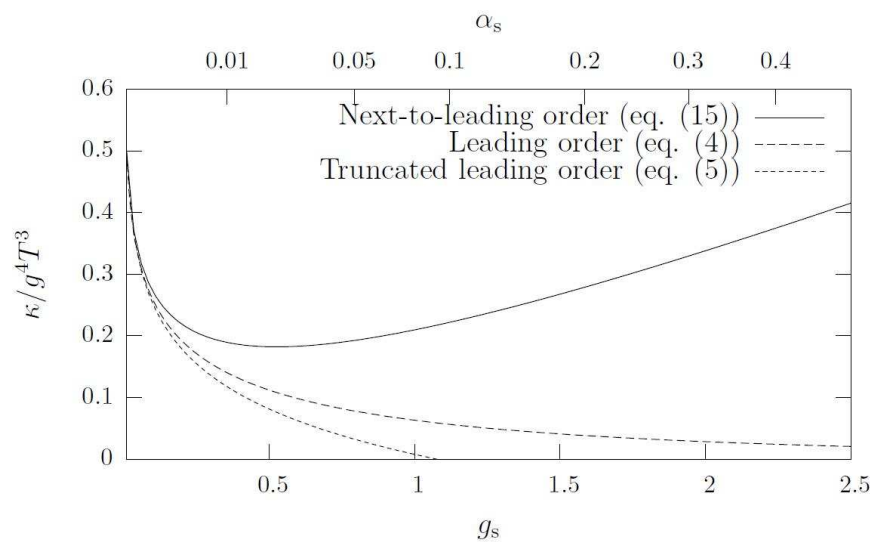
Figure H.17: The diffusion constant in momentum space as a function of g_s a calculated by 3-color, 3-flavor NLO pQCD with leading order calculation [172]

Appendix I

Shear Viscosity

The ratio of shear viscosity to entropy density, which characterize the hydrodynamical property of the medium, is related to the spatial diffusion constant D_s. A kinetic theory for an ultra-relativistic gas provides the relation of η/s [175, 176].

$$\frac{\eta}{s} \sim \frac{1}{5}TD_s. \tag{I.1}$$

Leading-order pQCD calculation of elastic scattering also provides the relation as follows [144, 177].

$$\frac{\eta}{s} \sim \frac{1}{6}TD_s \tag{I.2}$$

Eq. I.1 and Eq. I.2 are compatible and these equations are believed to be valid in the weak-coupling limit. It is not clear whether Eq. I.1 and Eq. I.2 are plausible in the strongly coupled matter, while in Ref. [144], Eq. I.2 are expected to be largely independent of its perturbative assumption due to the cancellation of the higher order correction. Using Eq. I.1, Eq. I.2 and Eq. H.25, the ratio of shear viscosity to entropy density, η/s is given as bellow.

$$\frac{\eta}{s} \sim \frac{0.8 - 1.7}{4\pi}. \tag{I.3}$$

This result is very close to the conjectured quantum lower bound $1/4\pi$. Such η/s indicates the created medium at RHIC is near a prefect fluid and strongly coupled matter.

On the other hand, the relation between η/s and D_s in the strong coupling limit is estimated using the AdS/CFT correspondence and the assumed proportionality $\eta/s \propto D_s$ from the kinetic theory in Ref [175].

$$\frac{\eta}{s} \sim \frac{1}{2}TD_s \tag{I.4}$$

The significantly smaller coefficient in Eq. I.1 and Eq. I.2 compared to that in Eq. I.4 could be understood to reflect the expected underestimation of the shear viscosity if a gas estimate is applied in a liquid-like regime [176]. Using Eq. I.4, η/s becomes as bellow.

$$\frac{\eta}{s} \sim \frac{2.5 - 4.2}{4\pi} \tag{I.5}$$

This result is also close to the conjectured quantum lower bound $1/4\pi$.

Finally, by combining Eq. I.3 and Eq. I.5, we obtain,

$$\frac{\eta}{s} \sim \frac{0.8 - 4.2}{4\pi} \tag{I.6}$$

When we find more realistic relation between η/s and D_s, more precise η/s will be obtained.

Figure I.1 shows the compilation of η/s density for various substances [178]. Green line shows the result in Eq. I.6. $T_c = 170$ MeV and $T = 210$ MeV are assumed according to the used hydrodynamical calculations for the $(T\text{-}T_c)/T_c$. $T = 210$ MeV is the mean temperature of the matter in which heavy quarks moved. Since the temperature of the matter depends on the time, the error of $(T\text{-}T_c)/T_c$ is determined from the highest temperature and T_c. Upper 3 symbols show η/s of atomic He, molecular N_2 and H_2O [179] as a function of temperature with the fixed pressures. The fixed pressures are their critical pressures, that is, 0.227455 MPa for He, 3.39 MPa for N_2 and 22.06 MPa for H_2O [179]. Red triangles shows the case for pure-glue lattice QCD calculations [180]. η/s of the matter created at RHIC is remarkably small compared to other matters and the very small η/s is one of most striking features of the matter.

The result in Eq. I.6 is compatible with the lattice QCD calculation. The lattice QCD calculation predicts η/s becomes large with increasing temperature, which is the expected behavior from the discussion in Sec. 7.5.2. The temperature dependence of η/s may be revealed from the experiments at LHC and the interaction of heavy quarks in the medium will be studied more precisely.
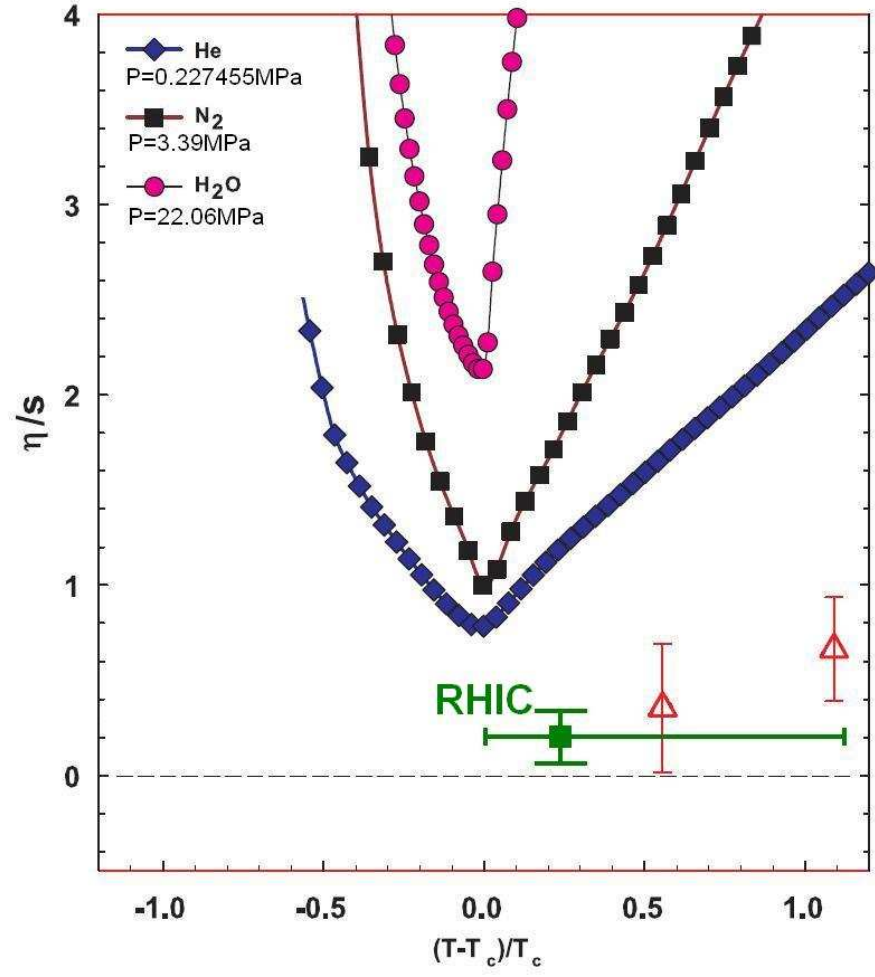
Figure I.1: The compilation of the ratio of shear viscosity to entropy density for various substances [180, 179].

Bibliography

[1] D. J. Gross and F. Wilczek, Phys. Rev. Lett. **30** (1973) 1343.

[2] J. C. Collins and M. J. Perry, Phys. Rev. Lett. **30** (1975) 1353.

[3] K. Yagi, T. Hatsuda and Y. Miake, Quark-Gluon Plasma, (Cambridge University Press, 2005).

[4] W. Greiner, S. Schramm and E. Stein, Quantum Chromodynamics, (Springer, 2002).

[5] H. Satz, Nucl. Phys. **A 418**, (1984) 448.

[6] F. Kasch *et al.*, Nucl. Phys. **A 478**, (2000) 447.

[7] F. Kasch, PoSCPOD **07**, (2007) 026.

[8] K. Rajagopal, Nucl. Phys. **A 661**, (1999) 150.

[9] J. Peter *et al.*, arXiv:0705.1930 (2007).

[10] T. D. Lee, Nucl. Phys. **A 538**, (1992) 3.

[11] L. Mclerran, Rev. Mod. Phys. **58**, (1986) 1021.

[12] R. J. Glauber and G. Matthiae, Nucl. Phys. **B21**,(1970) 135.

[13] J. D. Bjorken, Phys. Rev. **D27**,(1983) 140.

[14] PHENIX Collaboration K. Adcox *et al.*, Nucl. Phys. **A 757**, (2005) 184.

[15] STAR Collaboration J. Adams *et al.*, Nucl. Phys. **A 757**, (2005) 102.

[16] PHOBOS Collaboration B. B. Adcox *et al.*, Nucl. Phys. **A 757**, (2005) 28.

[17] BRAHMS Collaboration I. Arsene *et al.*, Nucl. Phys. **A 757**, (2005) 1.

[18] J. W. Cronin *et al.*, Nucl. Phys. **D11**,(1975) 3105.

[19] J. J. AUBERT *et al.*, Phys. Lett. **B 123**, (1983) 275.

[20] M. Arneodo *et al.*, Nucl. Phys. **B 441**, (1995) 12.

[21] M. Gyulassy, M. Plumer, *et al.*, Phys. Lett. **B 243**, (1990) 432.

[22] X. N. Wang, M. Gyulassy, *et al.*, Phys. Rev. Lett **68**, (1992) 1480.

[23] STAR Collaboration, J. Adams *et al.*, Phys. Rev. Lett. **93** (2004) 252301.

[24] M. Gyulassy, X. N. Wang, Nucl. Phys. **B 420** (1994) 583.

[25] A. Dainese, C. Loizides, and G. Paic, Nur. Phys. J. C**38** (2005) 461.

[26] R. Baier, Y. L. Dokshitzer, A. H. Mueller, S. Peigne, and D. Schiff, Nucl. Phys. **B 484** (1997) 265.

[27] M. Gyulassy, P. Levai and I. Vitev, Phys. Rev. Lett **85**, (2000) 5535.
M. Gyulassy, P. Levai and I. Vitev, Nucl. Phys. **B 594** (2001) 371.

[28] I. Vitev, Phys. Lett. **B 639**, (2006) 38.

[29] Z. Lin and C.M. Ko, Phys. Rev. Lett **89**, (2002) 202302.

[30] STAR Collaboration J. Adams *et al.*, Phys. Rev. Lett **92**, (2004) 052302.

[31] PHENIX Collaboration S. S.Adler *et al.*, Phys. Rev. Lett **91**, (2003) 182301.

[32] P. Huovinen *et al.*, Phys. Lett. **B503**, (2001) 58.

[33] Y. Dokshitzer and D. Kharzeev, Phys. Lett. **B519**, (2001) 199.

[34] Y. Dokshitzer *et al.*, Phys. Lett. **B632**, (2006) 81.

[35] N. Armesto *et al.*, Phys. Lett. **B637**, (2006) 362.

[36] S. Wicks *et al.*, Nucl. Phys. **A 784**, (2007) 426.

[37] M. G .Mustafa *et al.*, Phys. Rev. C **72**, (2005) 014905.

[38] M. Djordjevic, Phys. Rev. C **74**, (2006) 064907.

[39] R.Field Acta Phys Polon B **36** (2005) 167

[40] CDF Collaboration T. Affolder *et al.*, Phys.Rev.D **65** (2006) 092002

[41] http://www.ge.infn.it/ ridolfi/

[42] GEANT4 home page
http://geant4.web.cern.ch/

[43] Y.S Tsai, Mod. Phys. **46**,(1974) 815

[44] E. Norrbin, T.'Sjostrand Eur.Phys.J.C **17** (2000) 137

[45] D.Acosta *et al.*, Phys Rev Lett **91** (2003) 241804.

[46] Particle Data Group 2007.

[47] R.D. Cousins, Am, J. Phys **63**,(1995) 398.

[48] L. Gladilin ,hep-ex/9912064

[49] T. Sjostrand, P. Eden, C. Friberg *et al.*, Comput. Phys. Commun. **135** (2001) 238

[50] T. Sjostrand, L. Lonnblad, S. Mrenna, hep-ph/0108264

[51] D. J. Lange, Nucl. Instr. and Meth **A462** (2001) 152.

[52] EvtGen home page
http://www.slac.stanford.edu/ lange/EvtGen/

[53] EvtGen documentation
http://www.slac.stanford.edu/ lange/EvtGen/rel_alpha-00-14-05/Evt.ps.gz

[54] G. Alves *et al.*, Phys Rev Lett**77**,(1996) 2388

[55] CLEO collaboration B. Barish *et al.*, Phys. Rev. Lett **76** (1996) 1570

[56] CLEO collaboration Y. Kubota *et al.*, Phys. Rev. D **54**, (1996) 2004

[57] CLEO collaboration N. E. Adam *et al.*, Phys. Rev. Lett **97**, (2006) 251801

[58] CLEO collaboration S. Dobbs *et al.*, Phys. Rev. D **77**, (2008) 112005

[59] CLEO collaboration G. Brandenburg, *et al.*, Phys. Rev. D **61**, (2000) 072002

[60] CLEO collaboration M. Artuso *et al.*, Phys. Rev. D **70**, (2004) 112001.

[61] BABAR collaboration B. Aubert *et al.*, Phys. Rev. D **69** (2004) 111104.

[62] CLEO collaboration A. H. Mahmood *et al.*, Phys. Rev. D **70** (2004) 032003.

[63] Belle collaboration K. Abe *et al.*, Phys. Rev. D **64**, (2001) 072001.

[64] Belle collaboration R. Seuster *et al.*, Phys. Rev. D **73**, (2006) 032002.

[65] ALEPH collaboration A. Heister*et al.*, Phys. Lett. B **512**, (2001) 30.
OPAL collaboration G. Abbiendi*et al.*, Eur. Phys. J. C **29**, (2003) 463.
SLD collaboration K. Abe*et al.*, Phys. Rev. D **65**, (2002) 092006.

[66] N. Isgur, D. Scora, B. Grinstein and M. B. Wise, Phys. Rev. D **39**, (1989) 799

[67] D. Scora and N. Isgur, Phys. Rev. D **52**, (1995) 072001

[68] J. D. Richman and P. R. Burchat Rev. Mod. Phys. **67**, (1995) 893.

[69] CDF Collaboration A. Abulencia *et al.*, Phys.Rev.D **75** (2007) 012010.

[70] CDF Collaboration D. Acosta *et al.*, Phys.Rev.D **71** (2005) 032001.

[71] CDF Collaboration preliminary
http://www-cdf.fnal.gov/physics/new/bottom/061025.blessed-bxsec-mud0channel/

[72] HERA-B collaboration Phys.Rev.D **73**,052005(2006)

[73] E789 collaboration Phys.Rev.Lett **74**,3118(1995)

[74] E789 collaboration Phys.Rev.Lett **82**,41(1999)

[75] UA1 collaboration Phys.Lett.B **256**,121(1991)

[76] CDF collaboration Phys.Rev.D **71**,032001(2005)

[77] M. Cacciari *et al.*, Phys.Rev.Lett **95** (2005) 122001

[78] M. Cacciari *et al.*, hep-ph/0306212

[79] M. Cacciari *et al.*, hep-ph/0312132

[80] M. Cacciari, hep-ph/0407187.

[81] M. Cacciari *et al.*, JHEP **9805** (1998) 007

[82] M. Cacciari private communication

[83] M. Cacciari *et al.*, Phys.Rev.Lett **89** (2002) 122003

[84] PHENIX Conceptual Design Report, BNL, USA 1993, unpublished.

[85] PHENIX Collaboration D. P. Morrison, *et al.*, Nucl. Phys. **A638**, (1998) 565c.

[86] L. Aphecetche, *et al.*, Nucl. Instrum. Meth. **A499** (2003) 521.

[87] H. Hahn *et al.* Nucl. Instr. and Meth. A **499**, (2003) 245

[88] K. Ikematsu, *et al.*, Nucl. Instrum. Meth. **A411** (1998) 238.

[89] H. Huang *et al.*, Phys. Rev. Lett. **73** (1994) 2982.

[90] PHENIX Collaboration C. Adler *et al.*, Nucl. Instrum. Meth. **A470** (2001) 488.

[91] S. N. White, Nucl. Instrum. Meth. **A409** (1998) 618.

[92] J. Schmalzle *et al.*, IEEE Transactions on Applied Superconductivity, Vol.10 No.1 (2000) 220.

[93] Y. Akiba, *et al.*, Nucl. Instr. and Meth **A433** (1999) 143.

[94] A. J. Baltz *et al.*, Nucl. Instrum. Meth. **A417** (1998) 1. (nucl-ex/9801002)

[95] T. Tamagawa, Master Thesis (1996).

[96] T. Sakaguchi *et al.*, Nucl. Instr. and Meth **A453** (2000) 382.

[97] G. David *et al.*, IEEE Trans. Nucl. Sci. Vol.45 No.3 (1998).

[98] T. C. Awes *et al.*, nucl-ex/0202009.

[99] PHENIX Collaboration S. S. Adler *et al.*, Phys. Rev. C **75**, (2007) 024909.

[100] S. White, AIP Conf. Proc. **792**, (2005) 527.

[101] PHENIX Collaboration S. S. Adler *et al.*, Phys. Rev. Lett **91**, (2003) 241803.

[102] J. T. Mitchell *et al.*, Nucl. Instrum. Meth. **A482** (2002) 491.

[103] A. Chikanian *et al.*, Nucl. Instrum. Meth. **A371** (1996) 480.

[104] J. Myrhiem and L. Bugge, Nucl. Instrum. Meth. **160** (1979) 43.

[105] GEANT Detector description and simulation tool, CERN Program Library Long Write-up W5013, CERN Geneva.

[106] PHENIX Collaboration S. S. Adler *et al.*, Phys. Rev. C **74**, (2006) 024904.

[107] PHENIX Collaboration S. S. Adler *et al.*, nucl-ex/0611007 (2006).

[108] PHENIX Collaboration K. Adcox *et al.*, Phys. Rev. Lett **88**, (2002) 192303

[109] PHENIX Collaboration S. S. Adler *et al.*, Phys. Rev. Lett. **96**, (2006) 202301.

[110] R. Averbeck *et al.*, PHENIX Internal Analysis Note **89** (2001)

[111] PHENIX Collaboration S. S. Adler *et al.*, nucl-ex/0611031 (2006).

[112] PHENIX Collaboration S. S. Adler *et al.*, Phys. Rev. Lett. **96**, (2006) 032001.

[113] PHENIX Collaboration S. S. Adler *et al.*, Phys. Rev. Lett. **94**, (2006) 2323301.

[114] PHENIX Collaboration S. S. Adler *et al.*, Phys. Rev. Lett. **98**, (2007) 172301.

[115] PHENIX Collaboration S. S. Adler *et al.*, Phys. Rev. Lett. **97**, (2006) 252002.

[116] PHENIX Collaboration S. S. Adler *et al.*, Phys. Rev. Lett. **96**, (2006) 032301.

[117] PHENIX Collaboration S. S. Adler *et al.*, Phys. Rev. Lett. **96**, (2006) 032001.

[118] PHENIX Collaboration S. S. Adler *et al.*, Phys. Rev. Lett. **94**, (2005) 082301.

[119] STAR Collaboration B. I. Abelev *et al.*, Phys. Rev. Lett. **98**, (2007) 192301.

[120] PHENIX Collaboration S. S. Adler *et al.*, Phys. Rev. Lett. **98**, (2007) 232301.

[121] C. Silvestre for the PHENIX Collaboration , J. Phys. G **35** (2008) 104136.

[122] PHENIX Collaboration S. S. Adler *et al.*, Phys. Rev. C **77**, (2008) 064907.

[123] PHENIX Collaboration S. S. Adler *et al.*, Phys. Rev. Lett. **98**, (2007) 232002.

[124] PHENIX Collaboration S. S. Adler *et al.*, Phys. Rev. Lett. **91**, (2003) 072303.

[125] PHENIX Collaboration S. S. Adler *et al.*, arXiv:0801.4020

[126] PHENIX Collaboration S. S. Adler *et al.*, Phys. Rev. C **71**, (2005) 034908.

[127] PHENIX Collaboration S. S. Adler *et al.*, Phys. Rev. Lett. **91**, (2003) 172301.

[128] S. Kelly, J. Phys. G. **30**, (2004) S1189.

[129] H. Wohri and C. Lourenco, J. Phys. G. **30**, (2004) S315.

[130] PHENIX Collaboration S. S. Adler *et al.*, Phys. Rev. Lett. **91**, (2003) 072301.

[131] PHENIX Collaboration S. S. Adler *et al.*, Phys. Rev. Lett. **96**, (2006) 032302.

[132] K. Reygers *et al.*, PHENIX Internal Analysis Note **169** (2003)

[133] N.M Knoll and W. Wada, Phys. Rev. **98**, (1955) 1355.

[134] A. Valassi , Nucl. Instrum. Meth. **A500** (2003) 391.

[135] L. Lyons, D. Gibaut and P. Clifford, Nucl. Instrum. Meth. **A270** (1988) 110.

[136] R.J. Glauber, in: Lectures in theoretical physics, ed. W.E. Brittin *et al.*, (Interscience Publishers, New York, 1959) vol. I, p. 315

[137] R. Vogt, Private communication.

[138] M. J. Leitch for the PHENIX Collaboration J. Phys. G **32** (2006) S391.

[139] D. Das for the STAR Collaboration J. Phys. G **35** (2008) 104153.

[140] B. Svetitsky, Phys. Rev. D. **37**, (1998) 2484.

[141] H. van Hees, V. Greco and R. Rapp, Phys. Rev. C. **73**, (2006) 034913.

[142] H. van Hees, V. Greco and R. Rapp, Phys. Rev. C. **71**, (2005) 034907.

[143] H. van Hees, M. Mannarelli, V. Greco and R. Rapp, Phys. Rev. Lett. **73**, (2008) 192301.

[144] G.D. Moore and D. Teaney , Phys. Rev. C. **71**, (2005) 064904.

[145] Y. Akamatsu, T. Hatsuda and T. Hirano, arXiv:0809.1499

[146] P.B. Gossiaux, J. Aichelin and A. Peshier, arXiv:0802:2525

[147] F. Debbasch, K. Mallick and J.P. Rivet, J. of Stat. Phys. **88**, (1997) 945.

[148] H. R. Collard, L. R. B Elton, R. Hofstadter, Landolt-BAornstein, Numerical Data and Functional Relationsships in Science and Technology, New Series, Volume 2, Nuclear Radii, Springer-Verlag, 1967

[149] T. Hirano and K. Tsuda, Phys. Rev. C. **66**, (2002) 054905.

[150] T. Hirano and Y. Nara, Phys. Rev. Lett. **91**, (2003) 082301.

[151] T. Hirano and Y. Nara, Phys. Rev. C. **69**, (2004) 034908.

[152] T. Hirano *et al.*, Phys. Lett. B. **636**, (2006) 299.

[153] T. Hirano *et al.*, Phys. Rev. C. **77**, (2008) 044909.

[154] M. L. Mangano, P. Nason and G.Ridolfi *Nucl. Phys* **B405**, 507 (1993)

[155] R. J. Fries, B. Muller, C. Nonaka and S.A. Bass, Phys. Rev. Lett. **90**, (2003) 202303.

[156] R. C. Hwa and C. B. Yang, Phys. Rev. C. **67**, (2003) 034902.

[157] V. Greco, C.M. Ko and R. Rapp, Phys. Lett. B. **595**, (2004) 202.

[158] C. Dover, U. Heinz, E. Schnedermann, and J. Zimanyi, Phys. Rev. C. **44**, (1991) 1636.

[159] V. Greco, C.M. Ko and P. Levai, Phys. Rev. C. **68**, (2003) 034904.

[160] V. Greco, C.M. Ko and P. Levai, Phys. Rev. Lett. **90**, (2003) 202302.

[161] Shingo Sakai Doctol Thesis

[162] H. Satz J. Phys. G **32**, (2006) R25.

[163] A. Adil and I. Vitev Phys. Lett. B. **649**, (2007) 139.

[164] J. M. Maldacena Adv. Theor. Math. Phys. **2**(1998) 231.

[165] S. S. Gubser Phys. Rev. D. **76**, (2007) 126003.

[166] S. S. Gubser Phys. Rev. D. **74**, (2006) 126005.

[167] C.P. Herzog, A. Karch, P. Kovtun, C. Kozcaz and L.G. Yaffe, JHEP **07**, 013 (2006).

[168] P. K. Kovtun, D. T. Son and A. O. Starinets, Phys. Rev. Lett. **94**, (2005) 111601.

[169] S. Wicks, W. Horowitz, M. Djordjevic and M. Gyulassy, Nucl. Phys. **A784**, 426 (2007).

[170] A. Adare *et al.*(PHENIX Collaboration) arXiv:0706.3034

[171] A. Adare *et al.*(PHENIX Collaboration) arXiv:0802.0050

[172] S. Caron-Huot and G.D. Moore, Phys. Rev. Lett. **100**, (2008) 052301.

[173] G. Aarts, C. Allton, M. B. Oktay, M. Peardon and J. I. Skullerud, Phys. Rev. D. **76**, (2006) 094513.

[174] M. Asakawa, T. Hatsuda and Y Nakahara, Nucl. Phys. **A715**, (2003) 863.

[175] R. Rapp and H. v. Hees arXiv:0803.0901

[176] P. Danielewicz and M. Gyulassy, Phys. Rev. D. **31**, (1985) 53.

[177] P. Arnold, G. D. Moore, and L. G. Yaffe, JHEP **0305**, (2003) 051.

[178] R. A. Lacey and A. Taranenko, PoS C **FRNC2006**, (2006) 021.

[179] L. P. Csernai, J. I. Kapusta and L. D. McLerran, Phys. Rev. Lett. **97**, (2006) 152303.

[180] A. Nakamura and S. Sakai, Phys. Rev. Lett. **94**, (2005) 072305.